

Supramolecular Assemblies of π -Conjugated Phenylenevinylenes in Solid State

**A Thesis
Submitted in Partial Fulfillment of the Requirements
Of the Degree of
Doctor of Philosophy**

By

Mahima Goel

Reg. No. 20083016



Department of Chemistry
INDIAN INSTITUTE OF SCIENCE EDUCATION AND RESEARCH, PUNE
Pune 411008, Maharashtra, India

March 2013

Dedicated to

My Parents

For their endless love, support and encouragement...



भारतीय विज्ञान शिक्षा एवं अनुसंधान संस्थान, पुणे
INDIAN INSTITUTE OF SCIENCE EDUCATION AND RESEARCH (IISER) PUNE
(An Autonomous Institution of Ministry of Human Resource Development, Govt. of India)
Sai Trinity Building, Garware Circle, Pashan Pune - 411 021

Dr. M. Jayakannan

Associate Professor
Department of Chemistry

CERTIFICATE

Certified that the work incorporated in the thesis entitled “*Supramolecular Assemblies of π -conjugated Phenylenevinylenes in Solid State*” Submitted by **Ms. Mahima Goel** was carried out by the candidate under my supervision. The work presented here or any part of it has not been included in any other thesis submitted previously for the award of any degree or diploma from any other University or institution.

Dr. M. Jayakannan

Date:

(Thesis supervisor)

DECLARATION

I declare that this written submission represents my ideas in my own words and where others' ideas have been included; I have adequately cited and referenced the original sources. I also declare that I have adhered to all principles of scientific honesty and integrity and have not misrepresented or fabricated or falsified any idea/data/fact/source in my submission. I understand that violation of the above will be cause for disciplinary action by the institute and can also evoke penal action from the sources which have thus not been properly cited or from whom proper permission has not been taken when needed.

(Mahima Goel)

Date:

Roll. No. 20083016

ACKNOWLEDGEMENTS

I thank, Dr. M. Jayakannan, my research supervisor, for his excellent guidance, constant encouragement, invaluable suggestions, and supporting this work with ideas and criticism. His determination, energy and dedication for research motivated me to do science when I joined IISER. I will be always grateful to him for teaching, guiding and counseling me for all these years of my PhD at IISER, Pune.

I am extremely thankful to Prof. K. N. Ganesh, Director, IISER-Pune for providing all the facilities for carrying out this research work.

I would like to thank my research advisory committee (RAC) members; Dr. V. G. Anand and Dr. B. L. V. Prasad from NCL for their interactive discussions and valuable suggestions.

Special thanks to Dr. Asha, S. K. for her constant support and intellectual scientific discussions.

I would like to thank Dr. Bhoomishankar and Dr. Sujit Ghosh for helping me with single crystal data analysis. All the faculty members in the department of chemistry are kindly acknowledged for extending their research facilities, interactive scientific discussions and teaching me various courses.

I appreciate the support and cooperation from all my present and former lab mates, especially, Amrutha, Jinish, Anil, Bala, Smita, Ananthraj, Pramod, Bapu, Narshima, Rajendra, Bhagyashree, Moumita, Uma, Vivek, Deepak, Rekha, kaushal, Nagesh, Chinmay, Nisha, Senthil, Saibal, Prajitha, Swapnil for their love, care and support which made my life memorable at IISER, Pune.

I would like to thank following people for helping me with instrumentation: Pooja, Swati, Archana, Neeraj, Abhigyan, Sachidanand, Biplabh, Arvind, Anupam, Rekha and Arul. Dr. K. Guruswamy, Dr. P. A. Joy and Dr. K. Krishnamoorthy for extending research facilities from NCL, Pune are kindly acknowledged.

I wish to express my sincere thanks to all my friends at IISER-Pune, especially, Padmashree, Priya, Madhuri, Anandita, Tanpreet di and Veena for friendly chats during tea sessions.

I also thank all the staff members in administration, finance, accounts, stores, library and canteen especially, Ms. Nayana, Mr. Mayuresh, and Mr. Ankush for their immediate help whenever I needed them.

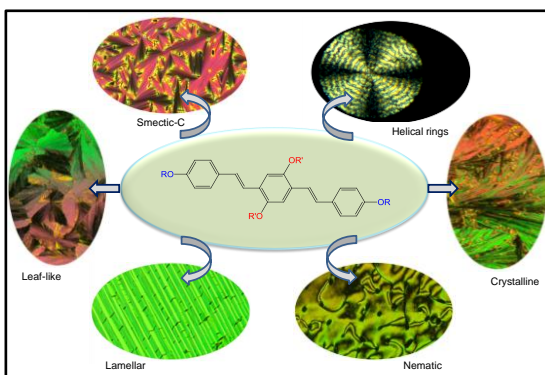
I am deeply indebted to my family for their whole hearted support and encouragement at every step of my life, especially, my papa for his insights and visions which motivated me to do research. I would like to thank my mummy for everything that I have achieved in life, without her none of this would have been possible. Special thanks to Abhinav (my husband) and Guddu bhaiya for all the love and support. And last but not least, I thank Varun (my brother) for his everlasting support and encouragement.

Financial support from Council of Scientific and Industrial Research (CSIR) is greatly acknowledged.

Mahima

SYNOPSIS

π - Conjugated semiconducting oligomers and polymers are emerging as important classes of materials for applications in electronic devices such as light emitting diodes (LEDs), photovoltaics (PVs), field effect transistors (FETs) and so on. *p*- Phenylenevinylenes are one of the most promising π -conjugated materials due to their high luminescence characteristics, thermal and optical stability, solubility in organic solvents, film forming tendency, easy synthetic approaches and so on. It has been now realized that the performance of π -conjugated materials in electronic devices are mainly driven by the precise molecular arrangements in solid state. However, it is rather very challenging to obtain information on the packing of π -conjugated molecules in the solid state due to the non-availability of single crystal structures for these large π -conjugated molecules. It has been a great challenge for synthetic chemists to design appropriate models which could self-organize in solid state (in a solvent free condition) and also produce their single crystal structures so that direct correlation between molecular packing and self-assembly could be established. Hence, design and synthesis of new π - conjugated systems and obtaining control over the supramolecular organization of these electronically active molecules is a major challenge to fine-tune and optimize their electrical properties for better device performance.



To address the above issue, this thesis work is focused on design and development of new π -conjugated phenylenevinylenes and their segmented polymers that can self-assemble via weak non-covalent interactions in the solid state. The design principle was adopted in such a way so that the molecules were constructed using simple hydrocarbon anchoring units and the molecular assemblies were driven by very weak non-covalent forces. A series of oligophenylenevinylenes (OPVs) having tricyclodecanemethylene pendant groups were designed to trace the effect of

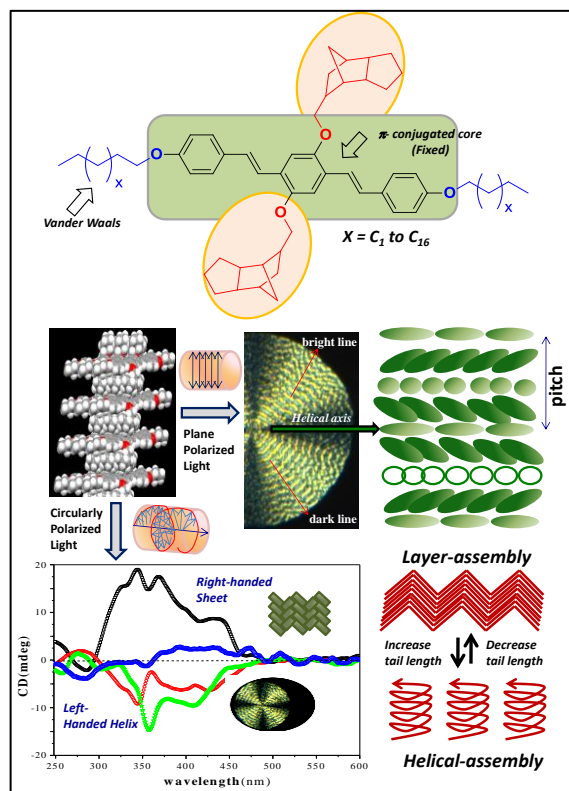
vander Waals and π - π stacking interactions on molecular self-assembly. The role of OPV structures on liquid crystallinity, self-assemblies, herringbone to helical packing and donor-acceptor self-assemblies were explored. In addition to that a large number of single crystal structures were resolved to study the role of planarity and peripheral substitution on solid state packing of this class of OPV molecules.

This thesis has been divided in to four major sections:

1. Helical Supramolecular Assemblies of OPVs: The origin of two dimensional herringbone layers to 3D helical self-assembly in a homologous series of OPVs has been studied.
2. Hierarchical Assemblies of OPV Structural Isomers: The role of OPV backbone planarity, CH/ π hydrogen bond, and positional effect of peripheral substitution, alkyl chain lengths and its orientation were investigated on the various properties such as liquid crystallinity and solid state orders etc.
3. Fluorocarbon versus Hydrocarbon tail in OPVs: Effort was made to synthesize fluorocarbon and hydrocarbon tailed OPV molecules. The role of tail nature on LC mesophases such as smectic, nematic and their H and J aggregates formations were investigated.
4. Donor-acceptor Assemblies of Segmented OPV Polymers: The effect of chemical structure and polymer chain topology on donor acceptor self-assemblies of segmented OPV polymers and perylenebisimide chromophore were studied. The donor-acceptor self-organization was investigated in detail using FRET mechanistic pathways.

This thesis work has been organized in five chapters. Chapter-1 starts with a brief introduction to π -conjugated materials and their application in electronic devices. A detailed literature survey on different types of π -conjugated systems which are commonly used in electronic devices, their properties and limitations have been discussed. This chapter also provides a complete literature survey on supramolecular self-assemblies of π -conjugated molecules in solution and solid state. Towards the end self-organization via liquid crystal approach has been discussed as an important approach for molecular self-assembly of π -conjugates.

In the second chapter, a homologous series of OPVs with tricyclodecanemethylene pendant units in the aromatic core with variable tail length in the longitudinal position was synthesized. Detailed thermal (by DSC) and polarized light microscope (PLM) analysis were done to understand the effect of the structure on solid state packing and mesophase morphologies. OPVs exhibited systematic sigmoidal transition from crystalline to ring-banded textures via cholesteric mesophases. Single-crystal X-ray structures of OPV molecules were resolved to find out the origin of sigmoidal self-assembly at the molecular level. It was found that self-organization of π -conjugated species underwent transformation from 2D herringbone layers to 3D helical twist in the liquid crystalline mesophases. Weak hydrogen bonding CH/ π interactions were found to be an important non-covalent force in the molecular self-assembly. Crystallographic parameters such as pitch and roll angles and their displacements were determined to find out the presence of π - π stacking interaction. The large pitch and roll displacements completely destroyed the aromatic π -stacking interactions among OPV chromophores. Circular dichroism studies were done to confirm the helical structures produced on aligning the chromophores in the LC mesophases. Detailed photophysical characterization was done to establish identical photophysical properties in LC and single crystal domains. The uniqueness of the present approach was that both herringbone and helical assemblies could be easily varied by means of the number of carbon atoms in



mesophases. Single-crystal X-ray structures of OPV molecules were resolved to find out the origin of sigmoidal self-assembly at the molecular level. It was found that self-organization of π -conjugated species underwent transformation from 2D herringbone layers to 3D helical twist in the liquid crystalline mesophases. Weak hydrogen bonding CH/ π interactions were found to be an important non-covalent force in the molecular self-assembly. Crystallographic parameters such as pitch and roll angles and their displacements were determined to find out the presence of π - π stacking interaction. The large pitch and roll displacements completely destroyed the aromatic π -stacking interactions among OPV chromophores. Circular dichroism studies were done to confirm the helical structures produced on aligning the chromophores in the LC mesophases. Detailed photophysical characterization was done to establish identical photophysical properties in LC and single crystal domains. The uniqueness of the present approach was that both herringbone and helical assemblies could be easily varied by means of the number of carbon atoms in

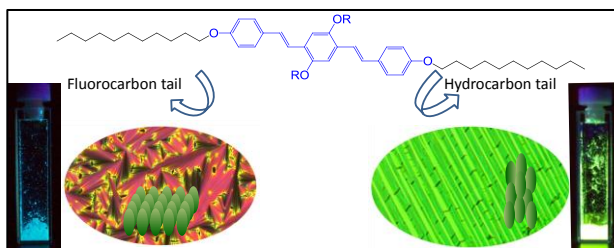
the tails. The overall findings revealed that the CH/ π interaction is a very powerful non-covalent interaction in supramolecular chemistry.

The third chapter describes the role of planarity, peripheral substitution, alkyl chain lengths and its orientation on liquid crystallinity, inter-molecular non covalent forces, pitch and roll displacements and solid state packing of oligophenylenevinylenes (OPVs). A series of structural isomers with identical distyrylbenzene based aromatic core but opposite arrangement of alkyl side chains around the periphery was synthesized. Similarly, another series of higher homologues OPVs with equal substitutions in the longitudinal and vertical directions was also synthesized. DSC studies were done to understand the difference in packing properties with respect to horizontal, vertical and radial substitution of the alkyl chains. Polarized Light Microscope imaging was used to study the influence of molecular structure on its liquid crystalline properties. The increase in the alkyl chain length in the horizontal position induced liquid crystalline properties whereas their vertical structural isomers remained as crystalline solids. Radially substituted OPVs with equal alkyl chain substitutions in both x and y directions exhibited well-ordered two-dimensional lamellar textures. Single crystal XRD analysis was done to understand the role of planarity, alkyl chain length and its orientation on molecular ordering and intermolecular non-covalent interactions. Planar molecules were generally found to be devoid of strong CH/ π and π - π interactions. On the other hand, non-planar molecules exhibited presence of strong CH/ π interactions. The roll and pitch calculations were done to show that in general non planar molecules were more prone to show π - π stacking interactions. Further, OFET devices were constructed to study the effect of liquid crystalline self-assembly on charge carrier mobility. OPVs exhibited hundred folds increase in charge carrier mobility in LC frozen state as compared to drop cast films. This preliminary result showed that the LC mesophase approach was indeed a good concept to explore in OFET applications.

The fourth chapter deals with the role of fluorocarbon tails and hydrocarbon tails on the diverse molecular self-assembly of π -conjugated oligophenylenevinylenes. OPVs were designed with appropriate pendants in the

aromatic core with hydrocarbon or fluorocarbon tails along the long molecular axis. Detailed DSC and PLM analysis was done to understand the difference between molecular packing and mesophase morphology among fluorocarbon (FC) and hydrocarbon (HC) tailed OPVs.

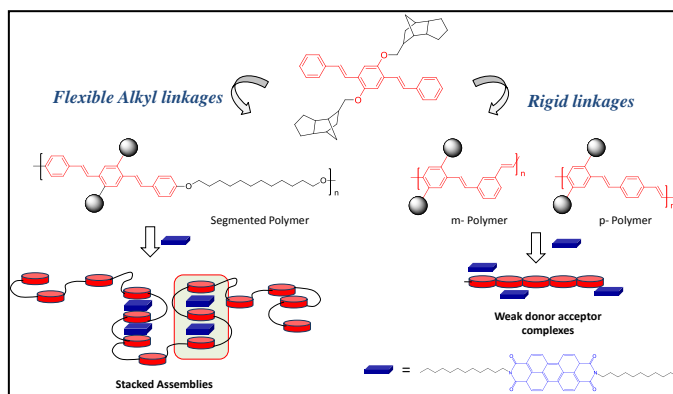
HC-OPVs showed better packing properties than their fluorocarbon counterparts. Fluorocarbon tailed OPVs produced smectic LC



mesophases irrespective of the pendant groups attached in the middle aromatic core. In contrast, in hydrocarbon tailed OPVs, both pendant geometry and along the middle aromatic core determined the molecular self-organization. Effort was made to understand the mechanism of identical smectic self-assembly using variable temperature wide angle XRD patterns. Fluorocarbon tailed OPVs exhibited regular periodicity corresponding to equidistant planes formed in smectic LCs. Small angle variable temperature X-ray diffraction analysis was done to establish smectic A to a more ordered smectic C phase transitions. Photophysical characterizations were carried out to understand the formation of H and J aggregates in these FC and HC-OPVs.

In the fifth chapter, a series of OPV segmented polymers with identical OPV optical chromophores but variable alkyl chain spacers (Poly-n; $n = 4, 8, \text{ and } 12$) were synthesized.

A rigid polymer (m-PPV) was also synthesised by introduction of m-linkages along the polymer back bone. The design strategy was adopted in such a way that all the polymers had almost



identical energy levels but varied only in their topology. The effects of chemical structures and polymer chain topology on donor acceptor self-assemblies of OPV

and perylenebisimide chromophores were also studied. The macroscopic properties of polymers were completely different from their oligomeric OPV analogues. OPVs exhibited strong tendency to self-assemble in to highly order crystalline domains whereas the polymers were amorphous. Photophysical analysis revealed that segmented polymers were superior to rigid polymers and OPVs in forming strong inter-molecular aggregates in solution state. The flexible alkyl spacers facilitated segmented polymer folding. Further, the polymers were found to form D-A arrays with electron deficient perylenebisimide based chromophores. The stability and type of self-assembly in these arrays was highly dependent on the chemical structure and the topology of the polymer backbone. Molar ratio method was used to determine the composition (donor to acceptor ratio) of D-A complexes and their stability or association constants. Segmented polymer formed extended D-A arrays in which the chains folded in stacked fashion to accommodate acceptor perylene units in 3:2 (donor: acceptor) ratio. On the other hand, the rigid polymer was found to form only weak 1:1 complexes. The stability constants revealed that the donor and the acceptor complexes formed by segmented polymer were ten times more stable than their rigid counterparts. Thus, the role of chemical structure and polymer chain topology on donor-acceptor self-assembly was established using the segmented polymer approach.

The last chapter summarizes the outcome of research work carried out in the Ph.D. thesis.

TABLE OF CONTENTS

Chapter 1: Introduction	1-47
1.1. Introduction to Conducting Polymers	2
1.2. Electronic devices based on π -conjugated materials	4
1.2.1. Light Emitting Diodes	4
1.2.2. Photovoltaics	6
1.2.3. Organic Field Effect Transistors	9
1.3. Molecular self-assembly in π -conjugates	11
1.3.1. Hydrogen-bond assisted self-assemblies	12
1.3.2. Aromatic π - π stack induced self-assembly	16
1.4. Liquid Crystalline π -conjugated materials	20
1.5. Solid- State assemblies of π -conjugates	27
1.6. Aim of the thesis	37
1.7. References	39
Chapter 2: Helical Supramolecular Self-assembly of OPVs in solid state.	48-115
2.1. Introduction	50
2.2. Experimental Methods	55
2.2.1. Materials	55
2.2.2. General Procedures	55
2.2.3. Synthesis	57
2.3. Results and Discussion	68
2.3.1. Synthesis and characterization of OPVs	68
2.3.2. Thermal Properties	72
2.3.3. Polarized Light Microscopic studies	76
2.3.4. Rind Banded Structures	80
2.3.5. Single Crystal XRD Analysis of OPV molecules	82
2.3.6. Roll and Pitch Inclinations	86
2.3.7. CH/ π Hydrogen Bonds	91
2.3.8. PLM images in Single crystals and Powder samples	94
2.3.9. Mechanism of Helical rings- <i>The Grandjean Lines</i>	97
2.3.10. Circular Dichroism Analysis	101
2.3.11. Photophysical Analysis	103
2.4. Conclusion	108
2.5. References	109

Chapter 3: Hierarchical Assemblies of OPV Structural Isomers	<i>116-170</i>
3.1. Introduction	118
3.2. Experimental Methods	123
3.2.1. Materials	123
3.2.2. General Procedures	123
3.2.3. Synthesis	126
3.3. Results and Discussion	134
3.3.1. Synthesis and characterization of OPVs	134
3.3.2. Thermal Properties	139
3.3.3. Polarised Light Microscopic Analysis	144
3.3.4. Single crystal XRD Analysis	149
3.3.5. Roll and Pitch displacements	159
3.3.6. Photophysical Analysis	164
3.3.7. Field Effect Transistor Measurements\	165
3.4. Conclusion	167
3.5. References	168
Chapter 4: Fluorocarbon Versus Hydrocarbon tails on the Self-assembly of OPVs	<i>170-211</i>
4.1. Introduction	173
4.2. Experimental Methods	178
4.2.1. Materials	178
4.2.2. General Procedures	178
4.2.3. Synthesis	179
4.3. Results and Discussion	185
4.3.1. Synthesis and characterization of OPVs	185
4.3.2. Thermal Properties	189
4.3.3. Polarised Light Microscopic (PLM) Analysis	193
4.3.4. Variable temperature XRD Analysis	197
4.3.5. Photophysical Analysis	202
4.4. Conclusion	208
4.5. References	209

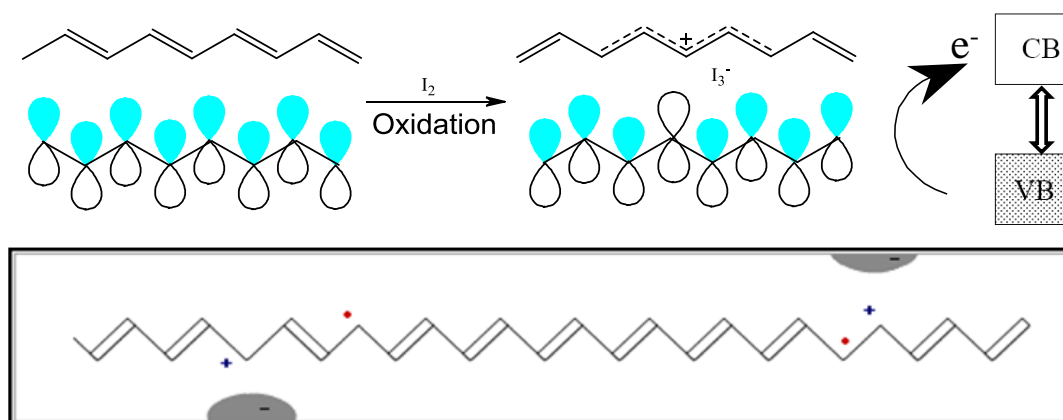
Chapter 5: Donor-acceptor Assemblies of Segmented OPV Polymers and Perylenebisimides	212-253
5.1. Introduction	214
5.2. Experimental Methods	222
5.2.1. Materials	222
5.2.2. General Procedures	222
5.2.3. Synthesis	223
5.3. Results and Discussion	226
5.3.1. Synthesis and characterization of Polymers	226
5.3.2. Molecular weight Determination	228
5.3.3. Thermal Properties	229
5.3.4. Photophysical Characterization	231
5.3.5. Solvent induced Molecular Self-assembly	232
5.3.6. Donor- Acceptor Self-assembly	237
5.3.7. Molar Ratio Method	242
5.3.8. TCSPC Analysis	246
5.4. Conclusion	249
5.5. References	250
 <i>Conclusion and Future directions</i>	 254-261
 <i>List of Publications</i>	 262-264

Chapter 1

Introduction

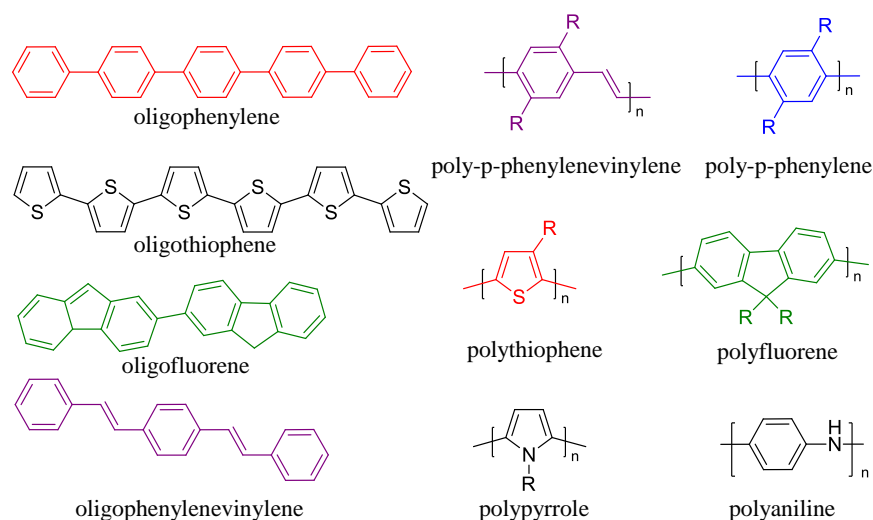
1.1. Introduction to Conducting Polymers

Polymers are important classes of materials for wide range of applications in plastics, textiles, coatings, paints, electric insulation and so on. Properties like high tensile strength, non-wettability, high mechanical strength, elasticity, resistance towards acids and alkalis, facile processibility and easy synthetic procedures make polymers an attractive class of materials. Typically, polymers are insulator in nature; for example, polyethylene, polypropylene and polyvinylchloride have been widely used for electrical insulating applications. Recent discoveries that a selective group of polymers having extended π -conjugation can conduct electricity like metals by three eminent scientists MacDiarmid, Heeger, and Shirakawa changed the entire way of looking at polymers as insulators.¹ Polymeric materials with these special features were used for newer applications in molecular electronics such as light emitting diodes (LEDs), photovoltaic (PVs) and field effect transistor (FETs).²⁻⁶ These polymers could replace metals traditionally used in constructing electronic devices and had added advantages such as better mechanical stability, easy processibility, low density and high impact, which were completely absent in metals or normal inorganic materials. The essential structural feature for a polymer to be conducting was that, it should have extended π -conjugated system. For example, this process has been explained in polyacetylene as shown in the scheme 1.1.



Scheme 1.1. Electrically conducting polyacetylene and mobility of the charges in the backbone.

Polyacetylene is not conducting in its nascent form; however, it could be converted from an insulator to conductor by exposing it to iodine vapour. The chemical oxidation of polyacetylene chains led to removal of an electron from valance band; as a result, radical cation or holes (positive charges) started migrating along the polymer chain. This process converted insulating polyacetylene chains into electrically conducting polymeric material as shown in the scheme 1.1. This breakthrough discovery of conducting polyacetylene was recognized by the award of the Nobel Prize in chemistry in the year 2000. Polyacetylene showed amazingly interesting conducting properties and could be doped to achieve conductivity as high as that of copper. In spite of high conductivity, polyacetylene was air-sensitive and insoluble in common organic solvents. These drawbacks led to the search for other conjugating materials, which could show similar behavior but were stable and processable.⁷⁻⁸



Scheme 1.2. Chemical structures of various conducting oligomers and polymers.

Scheme 1.2 illustrates few oligomers and polymers such as oligophenylene, oligothiophene, oligofluorene, oligophenylenevinylene, poly(*p*-phenylenevinylene), poly(*p*-phenylene), polypyrrole, polythiophene, polyfluorene and polyaniline. All the polymers had different optical (HOMO-LUMO) band gaps due to different π -

conjugated aromatic backbones and hence conducting polymers provided a large variety of structures having different photophysical and optoelectronic properties. Some common conducting polymers and their properties have been summarized^{8b} in table 1.1.

Table 1.1. *Electrical Conductivity, processibility and stability of some important conducting polymers.*

Polymer	Conductivity (S/cm)	Stability	Processibility
Polyacetylene	1000	Poor	Limited
Polypyrrole	500-7500	Good	Limited
Polythiophene	1000	Good	Excellent
Polyphenylene	1000	Poor	Limited
Polyaniline	200	Good	Limited
Polyfluorene	1000	Good	Good
Poly(phenylenevinylene)	1000	Good	Excellent

Since this thesis is focused on soluble π -conjugated materials and their self-assembly, subsequent discussions and reviews are mainly based on systems belonging to polythiophenes, polyphenylenevinylenes and polyfluorenes etc.

1.2. Electronic devices based on π -conjugated materials

Conducting polymers are emerging as potential candidates for various applications since they combine high electrical conductivity and processibility. In 1990, the field received a major boost when Richard Friend and Andrew Holmes discovered electroluminescence (EL) in π -conjugated polymers.⁹⁻¹⁰ They showed that polymers such as poly(phenylenevinylene)s emitted light on applying voltage between two metallic electrodes. This led to first polymer based light-emitting diode and the subsequent introduction of π -conjugated systems in molecular devices.¹¹

1.2.1. Light Emitting Diodes

A polymer light emitting diode works on the principle of the electroluminescence, which involves emission of light when a π -conjugated material is excited by flow of electric current. The schematic diagram for single-layer electro

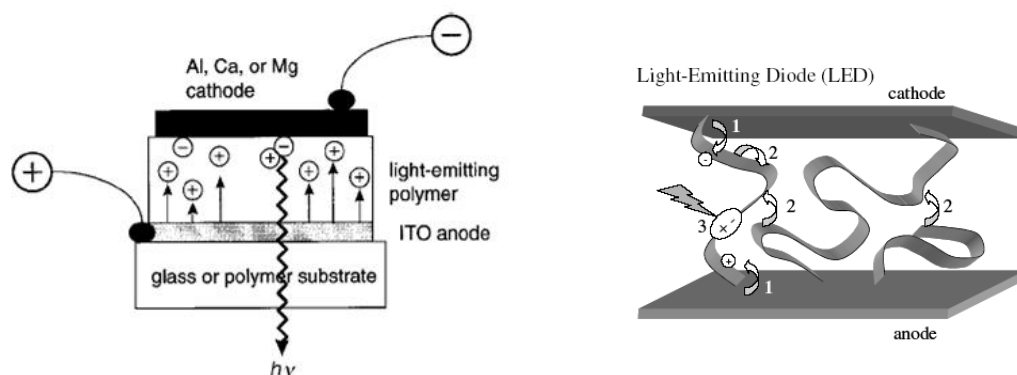
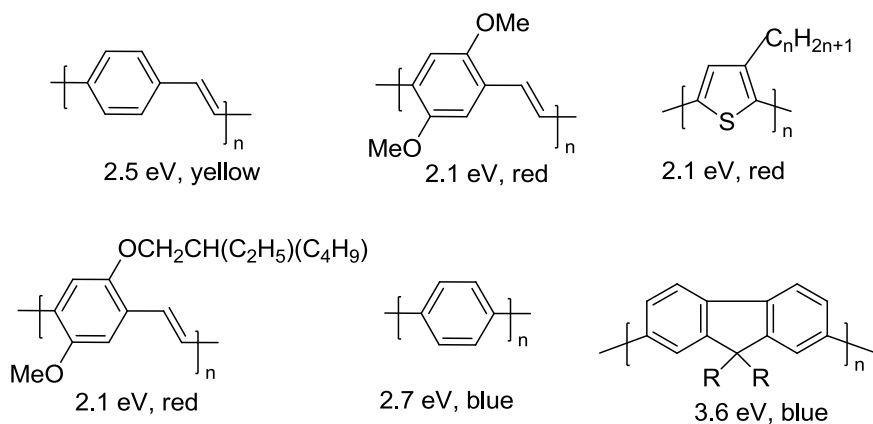


Figure 1.1. Device set up and conduction mechanism of light emission from a PLED.

luminescent device using a polymer layer has been shown in the figure 1.1. A thin film of π -conjugated material is sandwiched between two electrodes. The anode consists of a layer of PEDOT-PSS coated on an ITO patterned glass substrate and the polymer layer is spin casted above it. The cathode¹² is made up of a low-work function material such as calcium, magnesium or aluminium. In a polymer LED, electrons are injected into the LUMO (to form radical anions) and holes into the HOMO (to form radical cations) of the electroluminescent polymer, as diagrammatically represented in figure 1.1. The resulting charges migrate from polymer chain to polymer chain under the influence of the applied electric field. When a radical anion and a radical cation combines on a single conjugated segment, light is emitted.



Scheme 1.3. Polymers with different emission colors and their π - π^* band gaps.

Some examples of π -conjugated polymers used in electroluminescent devices with different emission colors⁴ have been shown in the scheme 1.3. These π -conjugated polymers have significant properties like colour tuning ability, mechanical stability, and flexibility etc.¹³, which were not there in inorganic and organic crystals. π -Conjugated systems also have the added advantages such as brightness, wide viewing angle, high contrast and thin film forming properties. Though, significant advances have been made in the area of PLEDs, there are few challenges that remain to be addressed, such as; (i) control of molecular chain aggregation; (ii) enhancement of electroluminescence intensities, (iii) photo and thermal stability of the materials and (iv) longer lifetime for the devices and so on.

1.2.2. Photovoltaics

The general device setup for an organic solar cell is similar to that of a light emitting diode.¹⁴ An organic solar cell consists of an electron donating (D) and electron acceptor (A) layer. Upon absorption of light, an electron is transferred from an electron donor (p-type semiconductor) to electron acceptor (n-type semiconductor). This photoinduced electron transfer results in the formation of radical cation of the donor ($D^{\bullet+}$) and the radical anion of the acceptor ($A^{\bullet-}$) as shown in the figure 1.2. The photogenerated charges are then transported and collected at opposite electrodes leading to the flow of current.¹⁵

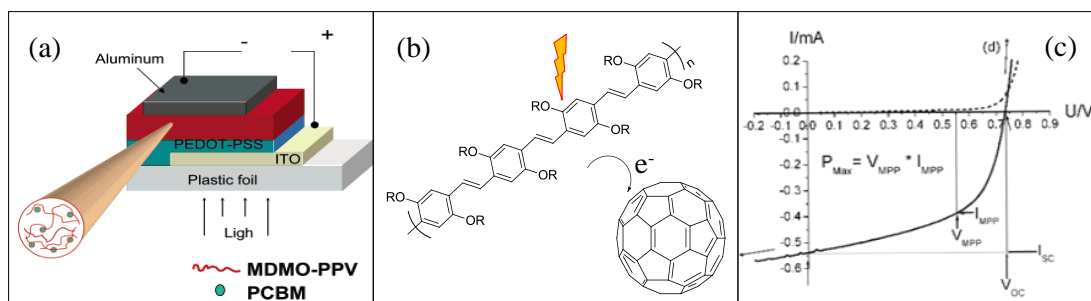
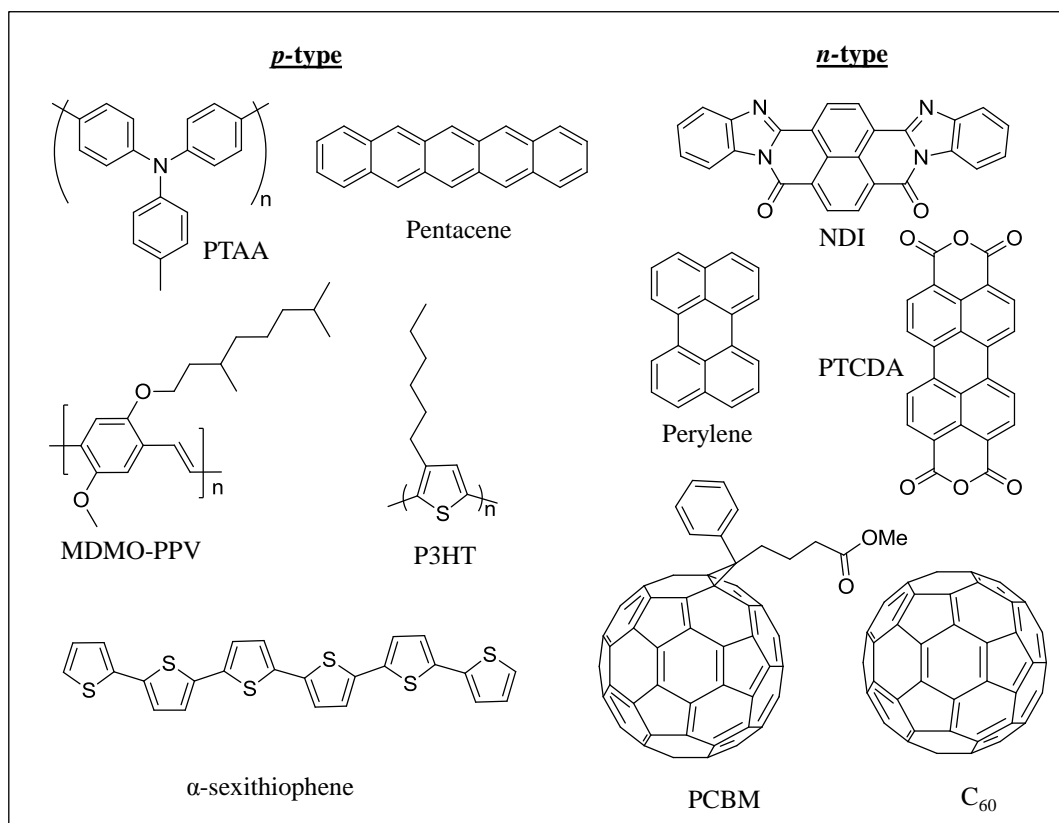


Figure 1.2. (a) Device set up of a solar cell. (b) Electron transfer from donor to acceptor. (c) Current-voltage (I - V) curves of an organic solar cell (dark-dashed; illuminated,-full line)(Adopted from Hoppe et al. *J. Mater. Res.* **2004**, 19, 1924-1945; Gunes et al. *Chem. Rev.* **2007**, 107, 1324-1338).

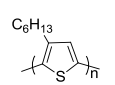
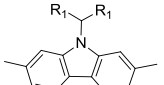
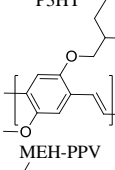
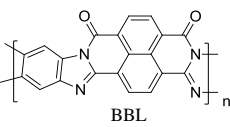
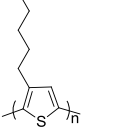
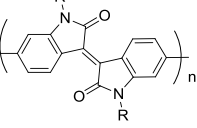
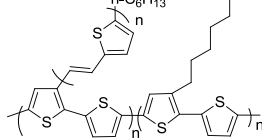
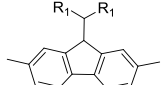


Scheme 1.4. Various conjugated polymers and oligomers used in organic solar cells.

The chemical structures of various conjugated polymers and oligomers commonly used for solar cell applications have been summarized in the scheme 1.4. Important examples of hole conducting donor-type semiconducting polymers are (i) derivatives of phenylenevinylene backbones such as poly[2-methoxy-5-(3,7-dimethyloctyloxy)-1,4-phenylenevinylene] (MDMO-PPV), (ii) derivatives of thiophene chains such as poly(3-hexylthiophene) (P3HT), and (iii) derivatives of fluorene backbones such as (poly(9,9'-dioctylfluorene-*co*-bis-*N,N'*-(4-butylphenyl)-1,4-phenylenediamine)(PFB). Small oligomers such as phthalocyanine, pentacene, α -sexithiophene and (E,E,E,E)-1,4-bis[(4-styryl)styryl]-2-methoxy-5-(2'-ethyl hexoxy)benzene have also been used successfully for solar cell devices. Buckminster fullerene C₆₀ and its derivative PCBM (1-(3-methoxycarbonyl)propyl-1-phenyl[6,6]C₆₁) are among the most commonly used *n*-type semiconducting materials in organic solar cells. Buckminster fullerene C₆₀ can be electrochemically

reduced up to 6 electrons, but it has limited solubility. PCBM is a soluble derivative of C_{60} and has been widely used in polymer/fullerene solar cells due to its solubility. Among the other popular n-type π -conjugated acceptors are perylene and its derivatives. Some recent examples of π -conjugated donor and acceptor systems and their solar cell device data¹⁶ have been summarized in the table 1.2.

Table 1.2. π -Conjugated donors and acceptors and their solar cell device data.

Donor	Acceptor	V_{OC} (V)	J_{SC} (mA/cm ²)	FF (%)	ECE (%)
 P3HT	 PC-PDI	0.58	0.91	55	0.29
 MEH-PPV	 BBL	0.94	1.95	35	1.00
 P3HT	 Poly II	0.55	0.98	35	0.19
 PF-PDI	 PC-PDI	0.76	1.77	43	0.58

The low cost of synthesis, easy processing of films for large surface displays and high absorption coefficients made π -conjugated materials good chromophores for solar cell applications. Bulk-heterojunction solar cells based on MDMO-PPV as a donor and PCBM as an acceptor showed excellent power conversion efficiencies exceeding 2.5%.¹⁷ PCBM has high electron mobility compared to many other organic or polymer materials that can be deposited by spin coating.

Nevertheless, there are many limitations that need to be addressed before any major practical application of bulk-heterojunction polymer-fullerene solar cells. A recent study based on MDMO-PPV/PCBM solar cells revealed appreciable

degradation under accelerated lifetime testing conditions (increased temperature).¹⁸ At high temperatures, PCBM molecules diffused through the MDMO-PPV matrix and formed large crystals leading to increased phase segregation.¹⁸ Therefore, development of new combinations of materials with easy synthetic approaches, better color tuning properties, increased photostability and better energy conversion efficiencies are some of the major challenges to be addressed.

1.2.3. Organic Field Effect Transistors

Organic field-effect transistors consisting of organic π -conjugated molecules as active layers are emerging next generation solid state electronics.¹⁹ Two metal electrodes called source and drain are placed on the top of the π -conjugated layers at each ends. Electrode materials are typically chosen from a variety of materials including metals (e.g., Au, Ag), heavily doped silicon and metallic conductive oxides (e.g., indium tin oxide), etc. An insulator separates the active layer from the gate electrode, and three terminals drain, source, and gate electrodes constitute the OFET configuration.²⁰ The device set-up of an OFET has been shown in figure 1.3.

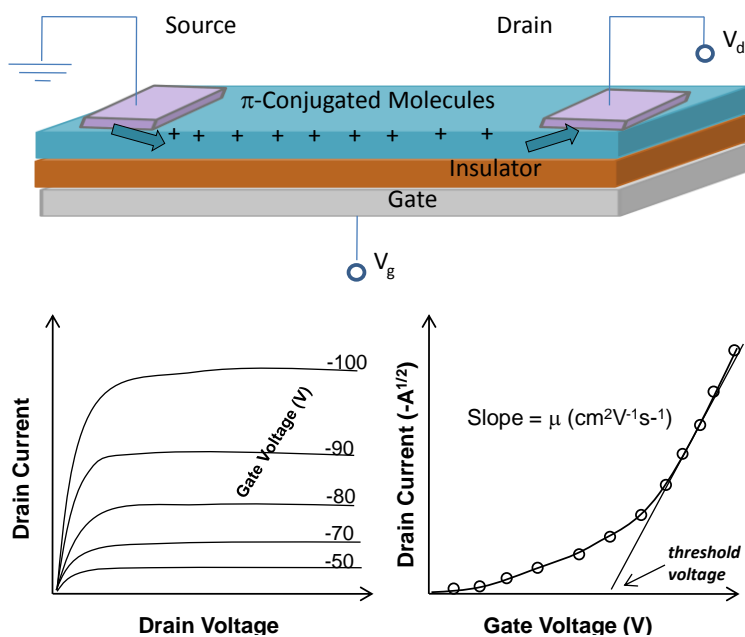


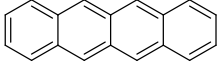
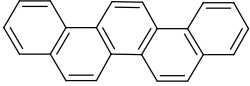
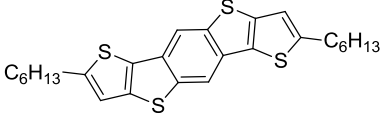
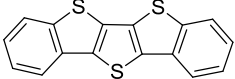
Figure 1.3. OFETs device configuration and typical I-V characteristics.

The mobility of the OFET is determined by the effective flow of charges from the source electrode to the drain electrode through the π -conjugated active layer. In this process, charge carrier accumulation is highly localized at the interface between the organic semiconductor and the gate dielectric. Therefore, OFET could be regarded as a capacitor in which the semiconductor layer and the gate electrode act as electrodes to sandwich the gate insulator. In figure 1.3, a typical OFET data output for the plots of drain current (I_D) vs drain voltage (V_D) for various applied gate voltage (V_G) are shown for π -conjugated molecules. The drain current is expressed as:²⁰

$$I_D = \{WC_i/ 2L\} \times \{\mu (V_G - V_T)^2\}$$

where, C_i is the capacitance per unit area of the dielectric layer, V_T is the threshold voltage, and μ is the field-effect mobility. From the plot of gate voltage versus square root of drain current, the field-effect mobility could be calculated. The intersection point in the x-axis provides the threshold voltages of the devices. The molecular structures, mobilities and packing motifs of some representative π -conjugated materials²¹ have been summarized in the table 1.3.

Table 1.2. Structures of π -conjugates, packing mode and OFETs mobility.

Structure	Packing mode	Mobility ($\text{cm}^2\text{V}^{-1}\text{s}^{-1}$)
	Herringbone	2.4
	Herringbone	1.1
	π -stacking	1.7
	Herringbone	1.8

The mobility of the first polymer OFETs was around $10^{-5} \text{ cm}^2\text{V}^{-1}\text{s}^{-1}$, since then a rapid progress has been made in OFETs based on π -conjugated systems. The highest mobility of thin film transistors based on π -conjugated systems has been reported to reach $10 \text{ cm}^2\text{V}^{-1}\text{s}^{-1}$ and in single crystals up to $15\text{-}40 \text{ cm}^2\text{V}^{-1}\text{s}^{-1}$.²¹ Incorporation of the electron-rich element such as sulphur was an important pathway to organic semiconductors with high performance. Planar or planar-like conjugated structures were generally found to be optimum for organic semiconductors with high mobility.²¹

Although, a considerable amount of advancement and progress has been made in the field of LEDs, devices such as photovoltaics and organic field effect transistors remained far behind in terms of practical applications. Real devices with good performances for commercialization needed serious efforts in terms of understanding basic molecular structures of materials being used. It was realized that the π -conjugated materials used for these devices were synthetically good, but their poor solid state packing resulted in extremely low efficiencies. Therefore, apart from designing suitable chemical structures, self-organization of molecules in solid state remained a major challenge before real introduction of π -conjugates for molecular electronics.

1.3. Molecular self-assembly in π -conjugates

Supramolecular assembly utilizing weak non-covalent forces for making organized molecular architectures is one of the most promising approaches for self-assembly of π -conjugates.²²⁻²⁴ Weak non-covalent forces have been extensively studied in π -conjugated systems for molecular self-organization. Among the various secondary interactions, hydrogen bonds,²⁵ π - π stacking,²⁶⁻²⁹ vander Waals,³⁰⁻³² hydrophobic effects³³ and metal-ligand interactions³⁴⁻³⁶ have turned out to be the most important for self-assembly of π -conjugated molecules. These non-covalent forces are considerably weaker than covalent interactions ranging from 2 kJ mol^{-1} for dispersion interactions to 300 kJ mol^{-1} for 'ion-ion' interactions.²³ The details summarizing the relative strength of these forces have been provided in the table 1.4.

Table 1.4. Summary of supramolecular interactions, their relative strengths and some common examples.

Interaction	Strength (kJ/mol)	Example
Ion-ion	200-300	Tetrabutylammonium chloride
Ion-dipole	50-200	Sodium [15] crown-5
Dipole-dipole	5-50	Acetone
Hydrogen bonding	4-120	Base pairs in DNA
Cation- π	5-80	K^+ in Benzene
π - π	0-50	Benzene/graphite
van der Waals	$< 5 \text{ kJmol}^{-1}$ but varies depending on surface area	Argon, packing in molecular crystals
Hydrophobic	depends to solvent-solvent interaction energy	Cyclodextrin inclusion compounds
CH/ π	$0.8 \text{ kcal mol}^{-1}$	Benzene (gaseous state)

Among the various non-covalent interactions, hydrogen bonding and π - π stacking are most important tools employed for self-organizing systems based on π -conjugates. Therefore, the following sections are focused on the self-assemblies of π -conjugated materials based on polyphenylenevinylenes, polyfluorenes, poly thiophenes and perylenebisimide derivatives via H-bonding and π - π stacking interactions.

1.3.1. Hydrogen-bond assisted self-assemblies

Hydrogen bonding interactions can be considered a master key for molecular self-assembly due to its directionality and relatively predictable strength. A large number of functional units such as phenols, amines, trans-amides, sulphonamides, etc. dimerise through a single H-bond. These groups can be attached to the terminal ends of the building blocks for making large self-assembled structures. Similarly, carboxylic acids, cis and trans amides, oxalamides and urea groups have been incorporated in π -conjugated backbone for dimerization through two hydrogen bonds. Tridentate H-bonding units such as diaminotriazine exhibited significantly higher stabilities as compared to bidentate hydrogen bonding groups. Functional units that form four hydrogen bonds (quadruple hydrogen bonding units) have

become extremely popular in π -conjugated materials because of high stability imparted to supramolecular assemblies. Supramolecular organization of these electronically active π -conjugated molecules through hydrogen bonding interactions³⁷⁻⁴⁸ have been extensively utilized for fine-tuning and optimizing their electronic properties.

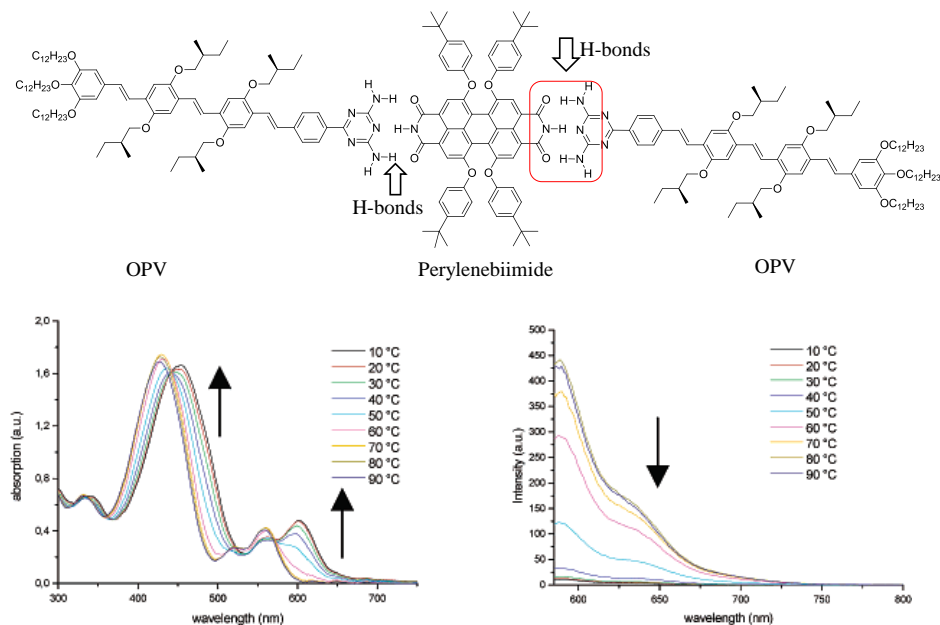


Figure 1.4. Assembly of OPV and perylenebisimide derivatives. UV-vis (left) and fluorescence spectra (right) of the triad in methylcyclohexane (Adopted from Schenning et al. *J. Am. Chem. Soc.* **2002**, 124, 10252-10253).

Figure 1.4 shows hierarchical self-assembly of p-type oligo(*p*-phenylene vinylene) and n-type perylene bisimide into chiral fibers⁴⁹ in which a diaminotriazine hydrogen bonding motif has been utilized. Perylene bisimide acceptor has two complementary binding sites for the diaminotriazine hydrogen-bonded moiety of OPV molecule. Upon photoillumination of these fibers, electron transfer takes place leading to charge separation within the aggregated dyes. These assemblies showed photoinduced electron transfer that is useful for solar cell applications.

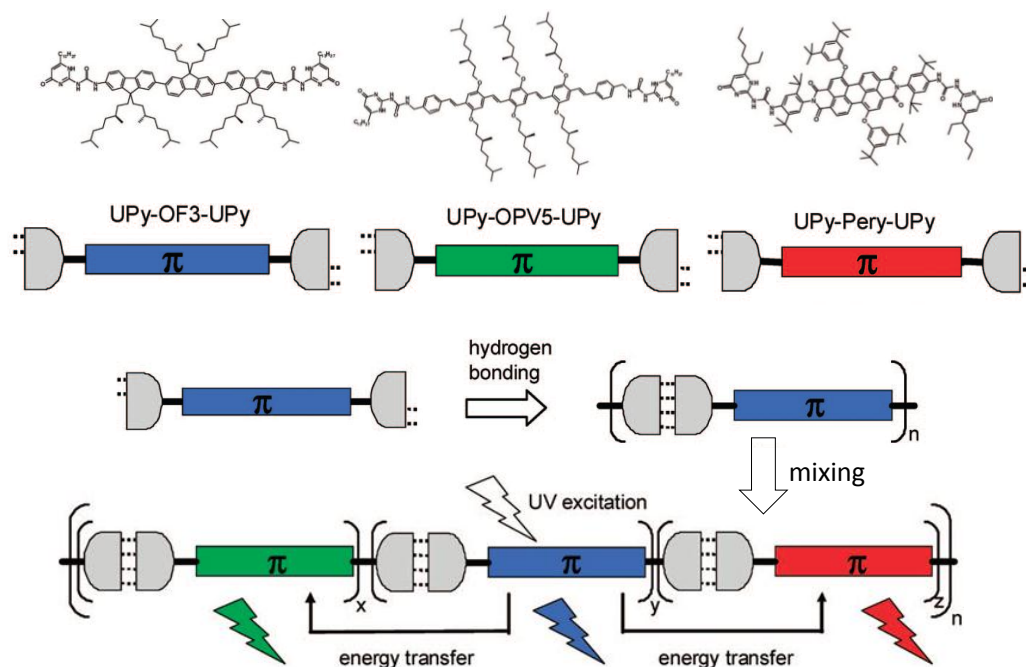


Figure 1.5. Chemical structures of di-UPy functionalized chromophores and a schematic illustration of white photoluminescence (Adopted from Abbel et al. *J. Am. Chem. Soc.* **2009**, *131*, 833-843).

Meijer and co-workers were the first to describe a series of quadruple hydrogen bonding 2-ureido-4[1H]-pyrimidinone derivatives that can dimerise by forming four hydrogen bonds.^{50a-c} These 2-ureido-4[1H]-pyrimidinone hydrogen bonding groups have been utilized for making supramolecular copolymers based on π -conjugated oligomers as shown in the figure 1.5. Three different π -conjugated oligomers; a blue-emitting oligofluorene, a green-emitting oligophenylene vinylene and a red-emitting perylene bisimide were functionalized with self-complementary quadruple hydrogen bonding ureidopyrimidinone (UPy) units at both ends. The molecules self-assembled in solution and in the bulk, forming supramolecular white emissive polymers.^{50c} Light emitting diodes based on these supramolecular polymers were also prepared from all three types of pure materials, yielding blue, green, and red devices, respectively. At suitable mixing ratios of these three compounds, white electroluminescence was observed.

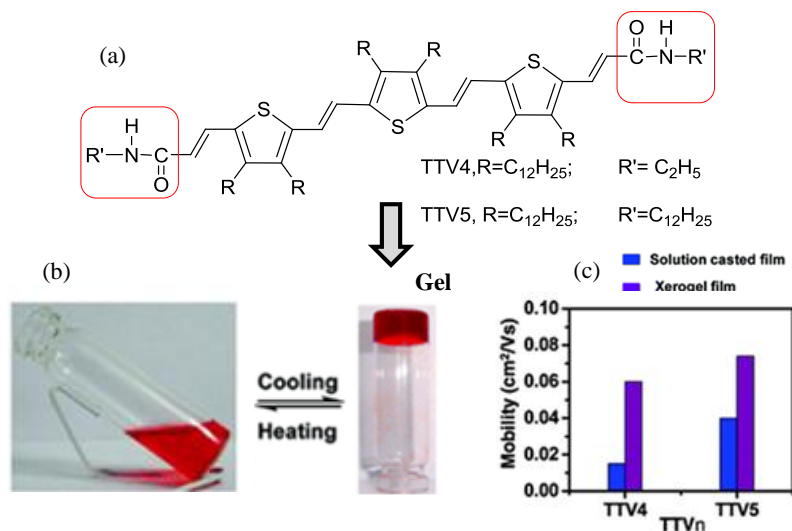


Figure 1.6. Molecular structure (a), photographs of TTV4 gel in decane during heating/cooling (b) and mobility data of TTV4 (c) (Adopted from Prasanthkumar *et al. J. Am. Chem. Soc.* **2010**, 132, 8866-8867).

Ajayaghosh and co-workers^{51a-d} have developed a variety of self-assembled materials based on oligo-phenylenevinylenes with different sizes, shapes, and properties. They have shown that solvent-assisted gel formation with functional organic molecules leading to one-dimensional fibers in oligophenylenevinylenes and oligothiophenes. Such fibers have improved electronic properties and are potential soft materials for organic electronic devices, particularly in bulk heterojunction solar cells. Further, trithiylenevinylenes with amide terminal groups were reported to be self-assembled as organogels in decane (see figure 1.6). The charge carrier mobility was found to be high for a sample from a decane gel when compared to that obtained from that of the chloroform solution.^{51d}

Yagai *et al.* demonstrated an example of synthetic rigid π -conjugating molecule based on oligophenylene vinylenes utilized to make self-assembled nano rings and nano coils (see figure 1.7). The molecule consisted of a barbituric acid

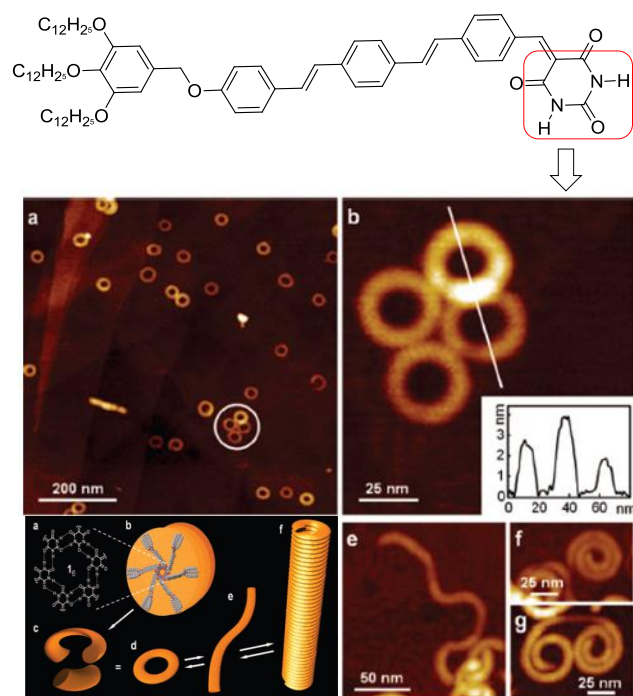


Figure 1.7. Schematic illustration for organization of barbituric acid substituted OPV in to nanorings, open-ended nanofibers, and nanocoils. (Adopted from Yagai et al. *J. Am. Chem. Soc.* **2009**, *131*, 5408 -5410).

(BAR) hydrogen bonding head group and a wedge-shaped tridodecyloxybenzyl (TDB) tail.⁵² Closed ring-shaped nanostructures (nanorings) were visualized by atomic force microscopy (AFM) when the molecule was drop-casted or spin-coated onto highly oriented pyrolytic graphite (HOPG) from a methylcyclohexane solution.

1.3.2. Aromatic π - π stack induced self-assembly

The strong attractive interactions between π -systems are known as π - π interactions or π - π stacking.²⁷ These interactions play a central role in controlling diverse phenomenon from biology to chemistry such as vertical base-base interactions in the double helical structure of the DNA, intercalation of the drugs in DNA, tertiary structures of the proteins, complexation of the host guest systems and the packing of the aromatic molecules in crystals. The origin of these interactions can be explained by using a simple model of charge distribution in a π system as

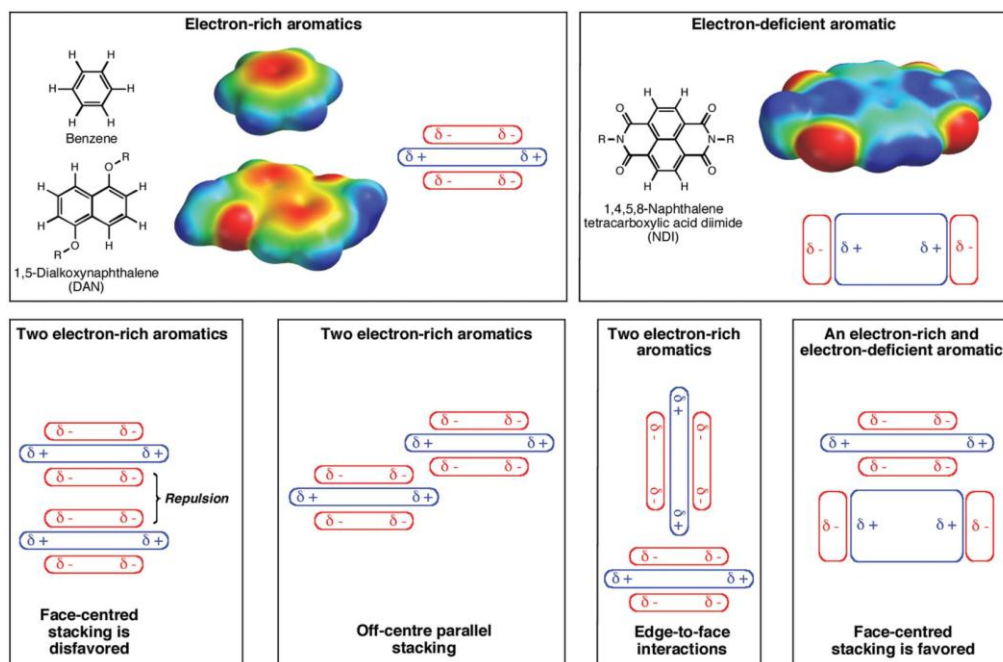


Figure 1.8. Various modes of π - π stacking in electron rich and electron deficient aromatics (Adopted from Martinez et al. *Chem. Sci.* **2012**, 3, 2191-2201).

proposed by Hunter and Sanders.⁵³ This model is known as polar/ π model. According to this model, in electron rich aromatic systems, the π electron density creates a quadrupole moment with partial negative charge above and below the aromatic plane and a partial positive charge around the periphery (see figure 1.8). Therefore, in electron rich aromatic systems, face centered stacking is disfavored due to large electrostatic repulsions.⁵³ To avoid these large electrostatic repulsive forces, aromatic cores in the adjacent molecules slide out from under one another leading to off-centered parallel stacking or perpendicular edge to face interactions. On the other hand, aromatic systems that have strongly electron-withdrawing groups polarize the π -electron density away from the aromatic core. A reversal in the direction of the overall quadrupole moment results in a central area of relative electron deficiency so that a partial positive charge is present above and below the aromatic faces and a partial negative charge around the periphery. These electron deficient systems can undergo strong electrostatic attraction with electron-rich aromatic systems, leading to

face centered pairing.²⁵ The face-centered stacking phenomenon between aromatics with differential polarization is known as ‘ π -stacking’ or ‘ π - π interaction’ or ‘aromatic donor-acceptor interaction’.³⁸

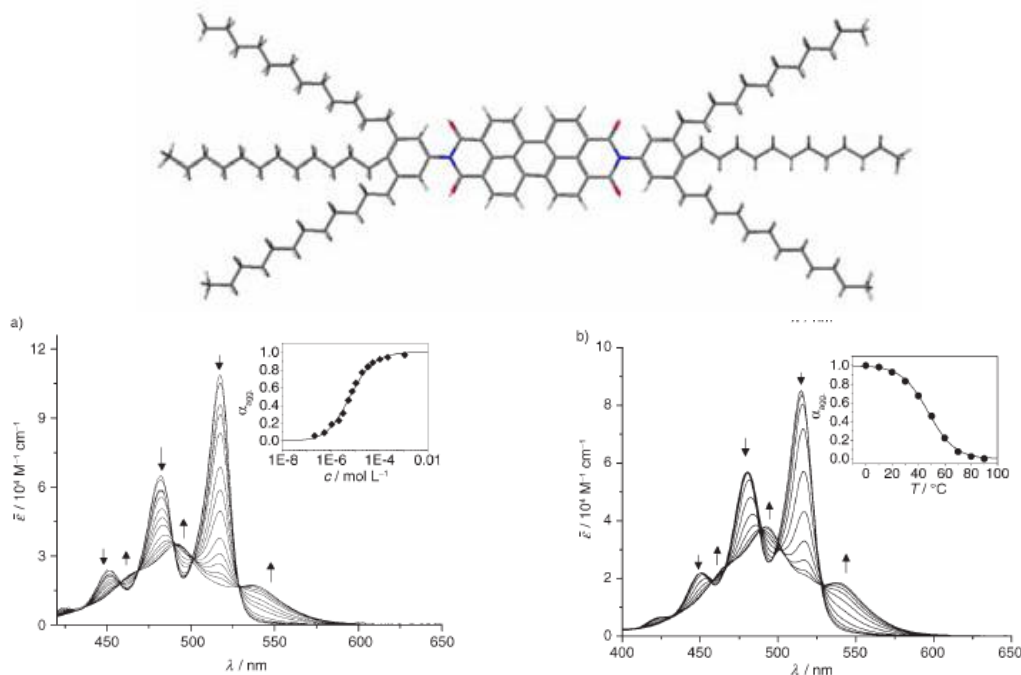


Figure 1.9. (a) Concentration-dependent UV/Vis absorption spectra of perylenebisimide derivative (2) in MCH at room temperature. (b) Temperature-dependent UV/Vis absorption spectra of 2 from 0 to 90 °C. (Adopted from Chen et al. *Chem. Eur. J.* 2007, 13, 436-449).

π - π stacking interactions have been widely studied in the self-assembly of π -conjugated systems such as benzene, naphthalene,⁵⁴ acenes, triphenylenes,⁵⁵⁻⁵⁶ hexabenzocoronenes,⁵⁷ perylene bisimide,⁵⁸⁻⁶³ naphthalene bisimide dyes,⁶⁴ and phthalocyanines.⁶⁵ The molecular self-assembly via π -stacking interactions is determined by several factors such as the electronic nature of the π -conjugated systems, the size and shape of aromatic core and peripheral substituents attached to the π -conjugated core. Chen et al.⁶⁶ reported an example of a new, highly soluble perylene bisimide (PBI) dye (see figure 1.9) which formed extended fluorescent aggregates in hexane utilizing π - π stacking interactions. The highest aggregation constant in hexane enabled the formation of aggregated species as shown by

transition from non-aggregated to aggregated state in the absorption spectra in figure 1.9a and figure 1.9b. The aggregation behavior was found to be concentration and temperature dependent.

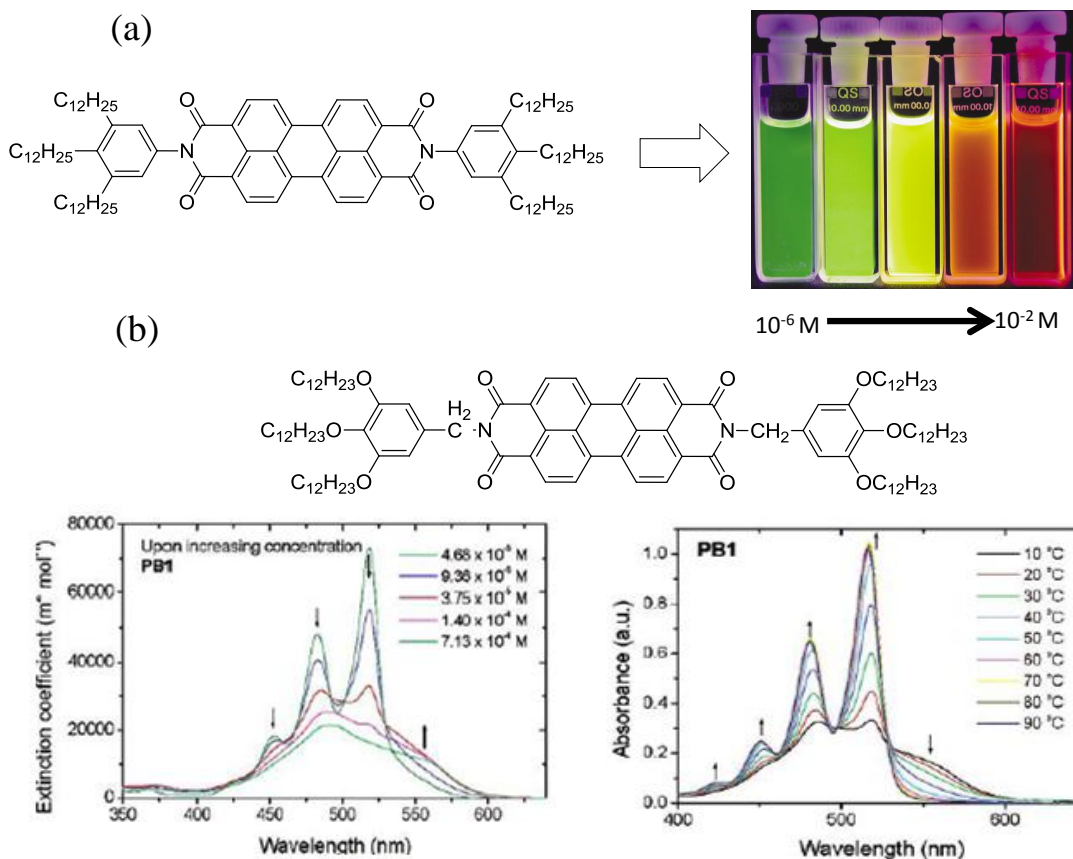


Figure 1.10. (a) Concentration-dependent luminescence of perylene bisimide dye in toluene. (Adopted from Wurthner et al. *Chem. Commun.* **2004**, 1564-1579). (b) Temperature-dependent UV/Vis absorption spectra from 0 to 90 °C. (Adopted from Herrikhuyzen et al. *J. Am. Chem. Soc.* **2004**, 126, 10021-10027).

Figure 1.10a represents another example of a strongly luminescent perylene bisimide dye that exhibits concentration dependent luminescent properties in toluene. In dilute solutions (10^{-6} M), the green emission corresponded to the presence of non-aggregated monomers. As the concentration of the dye increased, strong π - π stacking interactions led to aggregation of dye molecules giving rise to red emission.⁶⁷ Figure 1.10b exhibits an example of an electron-deficient (n-type) perylene bisimide molecule forming supramolecular stacks in apolar methylcyclohexane (MCH)

solution. The aggregation phenomenon was confirmed by the presence of aggregated peaks in the concentration and temperature-dependent absorption studies.⁶⁸

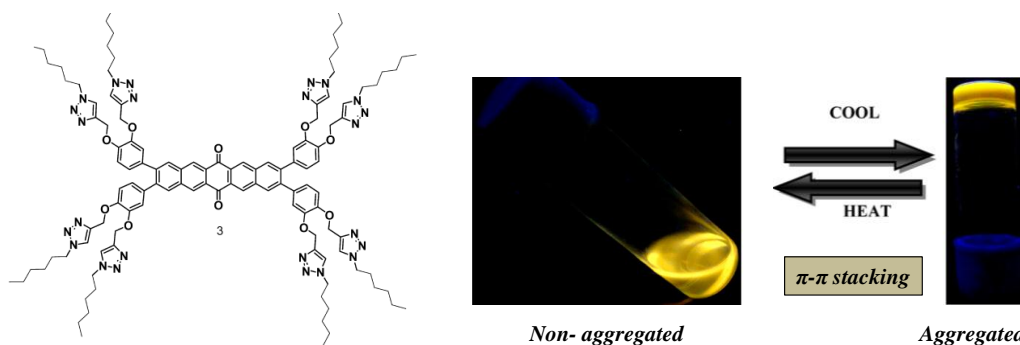


Figure 1.11. Chemical structure and photographs of gel of pentacenequinone derivative formed in toluene/DCM (Adopted from Bhalla et al. *Appl. Mater. Interfaces* **2013**, 5, 672-679).

Acenes such as pentacene and its derivatives are also among widely studied for self-assembling π -conjugated systems in solid state. An example of a pentacenequinone derivative⁶⁹ that forms stable thermoreversible organogels via strong π - π stacking interactions has been illustrated in the figure 1.11. Photographs of gel under 365 nm UV light formed in toluene/DCM (8:2) solvent implement sol phase transition by heating-cooling depict strong π - π stacking among molecules.

Though, unique supramolecular assemblies have been obtained by using hydrogen bonding and π - π interactions in solution state, these self-assemblies were predominantly solvent assisted processes. The concentration and temperature of the solution played an important role in determining equilibrium between individual molecules and aggregated stacks. The presence or absence of solvent greatly affected the stability of aggregates and hence transfer of these solution based assemblies to solid state device films is a major limitation of such solution based systems.

1.4. Liquid Crystalline π -conjugated materials

Liquid crystal aligning of π -conjugated molecules is an attractive methodology to make ordered molecular assemblies via solvent less processes.⁷⁰⁻⁷⁴

The molecules are heated to melt and wide varieties of molecular assemblies can be attained by cooling the samples under appropriate conditions. The outcome of the self-assemblies is visualized as nematic, smectic, cholesteric or columnar textures. These LC textures provide information about alignment of molecules in one dimensional, two dimensional, or three dimensional arrangements. Liquid crystal (LC) is a state of matter that has properties between those of conventional liquid and solid crystal.⁸⁰⁻⁸¹ Liquid crystals are fluidic in nature, like a liquid, but also exhibit a degree of molecular order like crystalline solids as shown in the figure 1.12. Such an intermediate state of matter is called a "mesophase". Broadly, liquid crystals can be divided into two categories: thermotropic or lyotropic. Thermotropic LCs exhibit a phase transition into the LC phase as a function of temperature. Lyotropic LCs exhibit phase transitions as a function of both temperature and concentration of the LC molecules in a solvent. Depending on the type of ordering in mesogens, liquid crystals are mainly classified in to four different phases known as nematic, smectic, cholesteric and columnar phases.

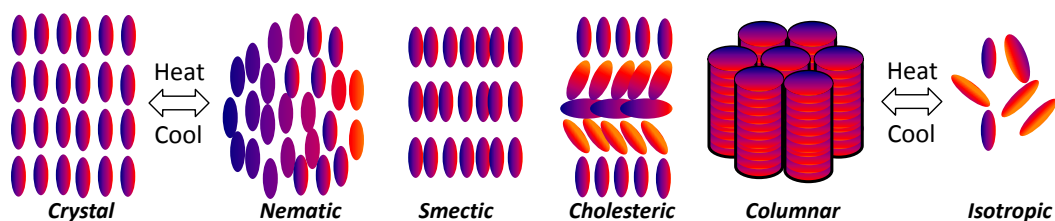


Figure 1.12. Schematic diagrams depicting orientation of molecules in crystalline, nematic, smectic, cholesteric, columnar and isotropic phases.

Nematic phase: The arrangement of mesogens in a nematic phase has been shown in the figure 1.12. In a nematic phase, the molecules tend to be parallel to each other. The molecules lack positional order, but self-align to have long range directional order with their long axes roughly parallel to each other. Thus, the molecules are free to flow and their center of mass positions are randomly distributed like a liquid, but the long-range directional order is preserved. Nematic phases are generally observed at higher temperatures.

Smectic (A and C) phase: In addition to orientational order, the molecules in smectic phases are arranged in layers. The molecules in each smectic layer are randomly distributed, but, oriented in same direction. Depending on the orientation of the molecules with respect to smectic layer normal, this phase can be divided in to smectic A or smectic C. In smectic A, the long molecular axis of the mesogens is parallel to the layer normal; however, in smectic C mesophases, the molecules are tilted with respect to layer normal by a tilt angle θ . The layer thickness of the smectic C phase is related to tilt angle as $d = l \cos \theta$. The ordering of the smectic A and C phases are both higher than the nematic phase so that they appear at a lower temperatures.

Cholesteric (or chiral nematic) phase: The cholesteric N* phase can be understood as a chiral version of the nematic phase possessing only orientational order of the long molecular axis. This phase consists of local nematic layers, which are continuously twisted with respect to each other giving rise to helical superstructure with a twist axis perpendicular to local director.

Columnar mesophases: Disk-shaped liquid crystalline molecules can orient themselves in a layer-like fashion known as the discotic nematic phase. If the disks pack into stacks, the phase is called a discotic columnar. The columns may be organized into rectangular or hexagonal arrays. Chiral discotic phases similar to the chiral nematic phases have also been reported.

Further, depending on the shape of the molecule, LCs can be classified in to two categories. The molecules having “rod like” molecular shape are known as calamitic liquid crystals. On the other hand, molecules having disc like geometries are called discotic liquid crystals. A schematic model for rod like and disc like liquid crystalline molecules has been shown in the figure 1.13. Among the various new materials for organic electronics, π -conjugated liquid crystals (LCs) are currently viewed as new generation of organic semiconductors.⁷⁵⁻⁷⁹ These materials offer the advantages of controlling the order in the bulk at all length scales from molecular to macroscopic distances. π -conjugated calamitic (rod-like)LCs differ from discotic (disc-like) mesogens in terms of molecular shape, phase symmetry, the

A common structural feature of calamitic π -conjugated mesogens is the presence of a relatively rigid core such as phenyl and biphenyl groups, with flexible alkyl or alkoxy side chains. Oligophenylenevinyls, oligophenylenes, oligothiophenes, oligofluorenes, and oligophenyleneethylene based aromatic cores constitute important classes of calamitic π -conjugated liquid crystals.⁸²⁻⁸⁸ Among these multidimensional nanoarchitectures of oligothiophenes and cooperative conformation transition in oligophenyleneethylenes were found to be more attractive. The chemical structures of a few important rod like π -conjugated liquid crystals have been summarized in the scheme 1.5c

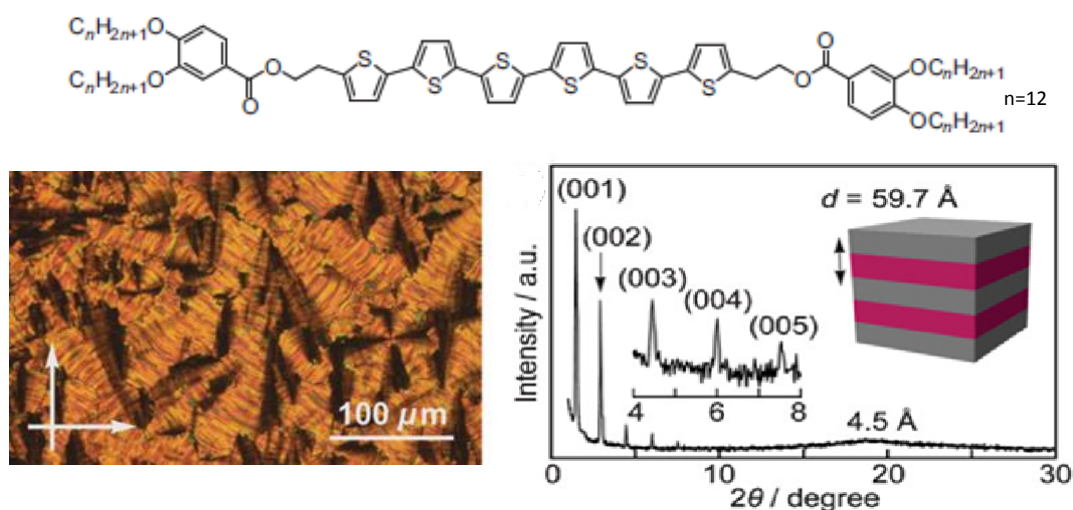
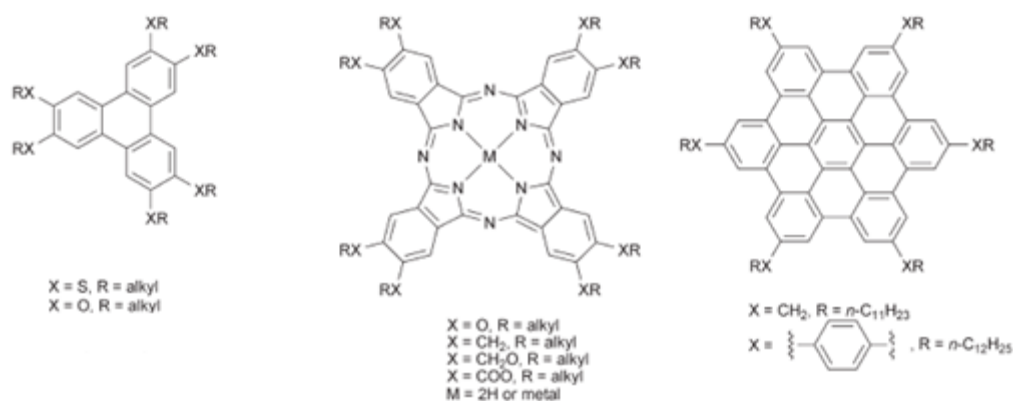


Figure 1.14. Polarized optical photomicrographs and XRD patterns of polythiophene based smectic liquid crystal at 160 °C. (Adopted from Yasuda et al. *Adv. Funct. Mater.* **2009**, *19*, 411-419).

Yasuda et al.⁸⁹ recently reported a series of liquid-crystalline (LC) π -conjugated oligothiophenes bearing three or two alkoxy chains at their extreme ends. These polycatenar oligothiophenes formed various LC nanostructures including smectic, columnar, and micellar cubic phases. Their properties depended on the number and length of the terminal alkoxy chains. For example, tetraalkoxy substitution of the oligothiophene core (see figure 1.14) ensured that the molecules have a calamitic shape and led to the formation of layered smectic LC phases over a wide range of temperatures.

The history of discotic liquid crystals dates back to the year 1977 when Chandrasekhar et al. reported that not only rod-like molecules, but also compounds with disc-like molecular shapes formed liquid crystalline mesophases.⁹⁰ Discotic LCs consists of a large planar conjugated rigid aromatic core and flexible peripheral chains.⁹¹⁻⁹⁶ These molecules self-organized to form stacks and high electron wave function overlap along the stacks in the columnar phases, resulted in high charge carrier mobilities.⁹⁷ The general chemical structures of some of the extensively studied π -conjugated discotic LC materials have been shown in the scheme 1.6.



Scheme 1.6. Chemical structures of commonly used π -conjugated discotic LCs (Adopted from Sergeyev et al. *Chem. Soc. Rev.* 2007, 36, 1902-1929).

Among a large variety of discotic liquid crystals that have been reported, triphenylene,⁹⁸ hexabenzocoronene⁹⁹⁻¹⁰³ and perylene bisimide⁹² derivatives, have been studied for one-dimensional transportation of charge carriers with high mobilities along the columns. Polycatenar oligothiophenes¹⁰⁴ possessing three alkoxy chains at each terminal has been shown in the figure 1.15a. This molecule self-organized into columnar liquid crystalline phase, and one-dimensional columnar stacks could be oriented uniaxially by mechanical shearing in the mesophases. Recently, an interesting example of nematic phase has been reported by Cammidge and coworkers in substituted triphenylenes as shown in the figure 1.15b. An enforced void region in the center of the macrocycle that results from bridging through the triphenylene 3,6-positions excluded simple columnar assembly and gave rise to nematic LC mesophases.¹⁰⁵ Novel discotic LCs by fusing imidazole with

triphenylene aromatic core¹⁰⁶ have also been synthesized (see figure 1.15c) exhibiting interesting columnar discotic mesophases.

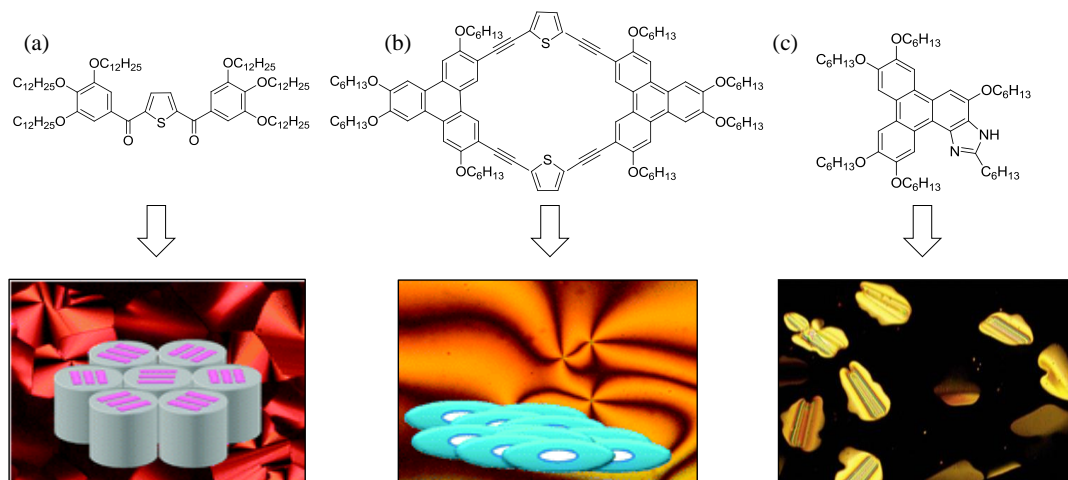


Figure 1.15. (a) Chemical structure and columnar mesophases of π -conjugated oligothiophenes (Yasuda et al. *Chem. Commun.* **2006**, 3399-3401). (b) Nematic mesophases observed in discotic triphenylenes (Zhang et al. *J. Org. Chem.* **2012**, 77, 4288-4297). (c) Chemical structure and optical micrograph of a triphenylenoimidazole mesogen. (Kumar et al. *Tetrahedron Lett.* **2011**, 52, 5363-5367).

Asha and coworkers⁵⁸ synthesized a series of highly fluorescent liquid-crystalline perylenebisimide molecules having amide or ester linkage and end-

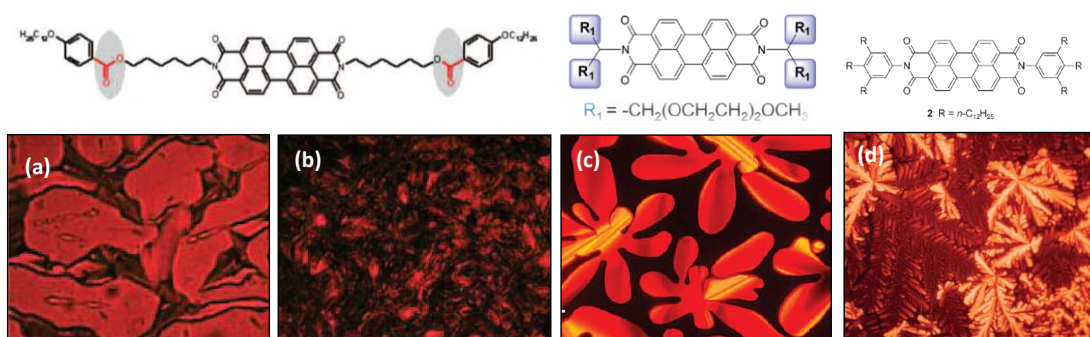


Figure 1.16. (a) Chemical structure and LC mesophases of perylenebisimide derivatives. (Adopted from Jancy et al. *Chem. Mater.* **2008**, 20, 169-181 (a and b); Wicklein et al. *J. Am. Chem. Soc.* 2009, 131, 14442-14453(c); Chen et al. *Chem. Eur. J.* **2007**, 13, 436- 449(d)).

capped tridodecyloxy phenyl units as show in the figure 1.16a. The study indicated that the presence of a single terminal dodecyloxy phenyl substituent has a very stabilizing effect on the overall properties like stability of liquid crystalline phases, stability of aggregates formed, etc., when compared to no terminal dodecyloxy benzyl substitution or tridodecyloxy benzyl substitution. This was true for both the ester as well as amide linkage having monododecyloxy benzene substitution. Thelekkat and coworkers⁴⁰ demonstrated the study of tailor-made liquid crystalline PBIs to elucidate structure-property relationships with respect to thermotropic behavior in *N*-substituted derivatives of PBIs (see figure 1.16b). Symmetrically and unsymmetrically *N*-substituted perylene bisimides were synthesized by two different synthetic strategies. The substituents used involved swallow-tail and linear alkyl or oligooxyethylene (OEG) substituents. The mesophases exhibited characteristic columnar hexagonal packing arising from π - π interactions between cofacially orientated perylene molecules. Wurthner and coworker⁶⁶ synthesized a highly soluble PBI dye which formed extended fluorescent aggregates possessed liquid crystalline properties. In condensed state a hexagonal columnar LC phase (see figure 1.16c) was observed. X-ray diffraction and AFM studies indicated that the columnar stacking is accomplished by rotational displacement among the molecules.

Although, a large amount of research on π -conjugated LCs has been done, but questions like the exact relationships between mesogen structure and its morphology, the rationale behind molecular design for obtaining a specific texture are still debated. Various molecular designs and theories have been proposed for understanding structure property relationships, however, a clear understanding of these relationships is a missing link in the literature and there is still a long way to go.

1.5. Solid- State assemblies of π -conjugates

Typically, organic π -conjugated molecules could pack in three different kinds of packing motifs such as herring bone packing with π - π overlap between adjacent molecules; lamellar packing with one dimensional (1D) π -stacking or lamellar

packing with two dimensional π -stacking.²¹ The molecular arrangements in these three packing motifs have been shown in the figure 1.17. Herringbone arrangement

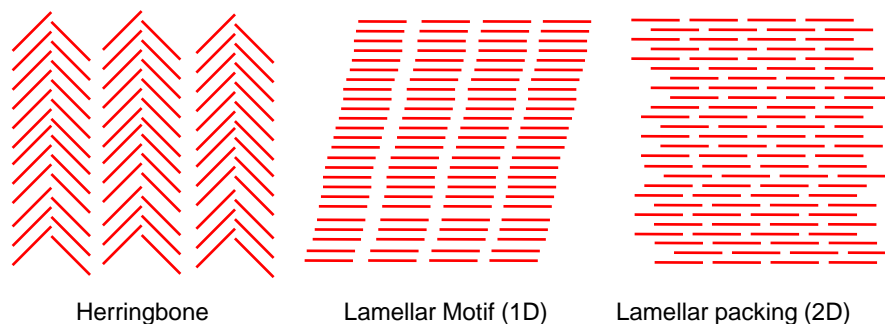


Figure 1.17. Packing of organic π -conjugated molecules in solid state.

is one of the most stable packing for molecules in the solid state, where adjacent stacks of molecules arrange in opposite directions in the unit cell. Long alkyl or alkoxy side chains facilitate lamellar packing due to the crystallization of hydrocarbon tails.

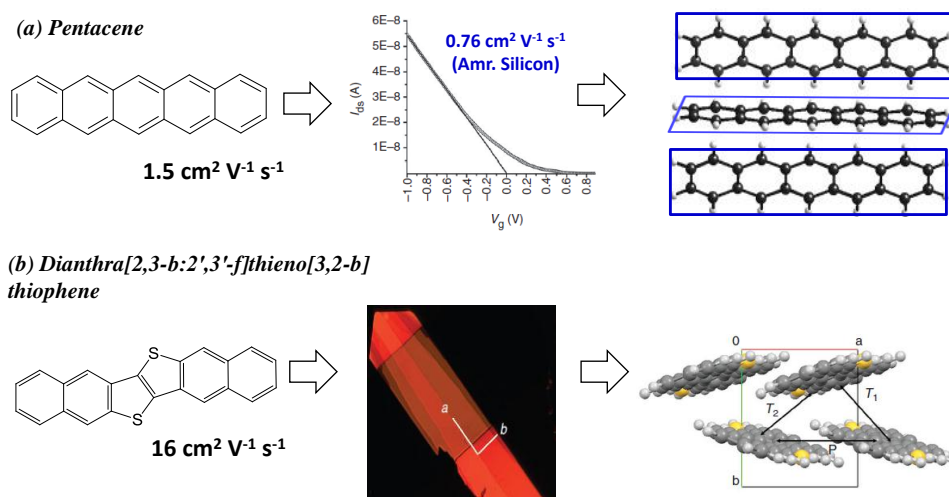


Figure 1.18. (a) FET measurements and single crystal structure of pentacene reflecting herring bone packing. (Adopted from Lin et al. *IEEE Trans. Electron* **1997**, 44, 1325-1331 and Meijer et al. *Nature Mater.* **2003**, 2, 678- 682). (b) Field effect mobility and crystal packing of dianthra[2,3-b:2',3'-f]thieno[3,2-b]thiophene. (Adopted from Sokolov et al. *Nature Comm.* **2011**, 2:437, 1-8).

The solid state packing of π -conjugates have a direct influence on their charge carrier mobilities. Figure 1.18 shows the charge carrier mobilities and molecular arrangements in single crystals of pentacene and dianthra[2,3-b:2',3'-f]thieno[3,2-b] thiophene. Pentacene¹⁰⁷⁻¹⁰⁸ showed mobility up to $1.5 \text{ cm}^2\text{V}^{-1}\text{s}^{-1}$, which was about double the mobilities reported for amorphous silicon. Single crystal structure analysis of pentacene showed that molecules arranged in herringbone motifs. Dianthra[2,3-b:2',3'-f]thieno[3,2-b] thiophene exhibited saturation region hole mobilities as high as $12.3 \text{ cm}^2\text{V}^{-1}\text{s}^{-1}$ and a linear region mobility of $16 \text{ cm}^2\text{V}^{-1}\text{s}^{-1}$ in single crystal OFET devices.¹⁰⁹ The molecules exhibited lamellar ordering which gave rise to such high field effect mobilities.

Oligo-acenes, oligo-thiophenes and oligophenylenes are among the most commonly used π -conjugated materials for organic electronics; therefore it is important to understand the packing motifs of these molecules in solid state. The crystal structures of sexithiophene¹¹⁰ (also pentacene) showed herringbone packing motifs in which the molecules were found to arrange in edge-to-face fashion in two-dimensional (2-D) layers (see figure 1.19A). These molecules showed highest charge carrier mobilities among π -conjugated materials. Few other important examples of unsubstituted π -conjugated oligomers have been summarized in the figure 1.19

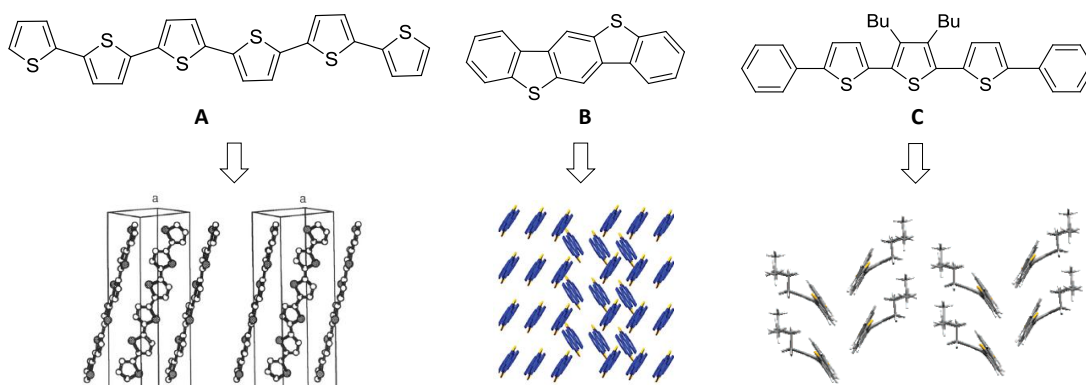


Figure 1.19. Packing motifs of unsubstituted oligomers in their single crystals. A (Adopted from Horowitz et al. *Chem. Mater.* **1995**, 7, 1337-1341); (B) Adopted from Wang et al. *Chem. Rev.* **2012**, 112, 2208-2267); (C) (Adopted from Curtis et al. *J. Am. Chem. Soc.* **2004**, 126, 4318-4328).

A common feature of **A**, **B**, and **C** in figure 1.19 was the absence of side chains or pendent groups in the aromatic core. All the three molecules arranged in herringbone layers. The unit cell for sexithiophene (**A**) belonged to space group P21/n and presented the herringbone packing common to a great deal of planar molecules.¹¹⁰ A butyl substituted derivative of benzo[1,2-b:4,5-b⁰]bis[b]benzothiophene (**C**) exhibited, as seen down the long molecular axis herringbone like structure to give a “lamellar herringbone” packing motif.¹¹¹

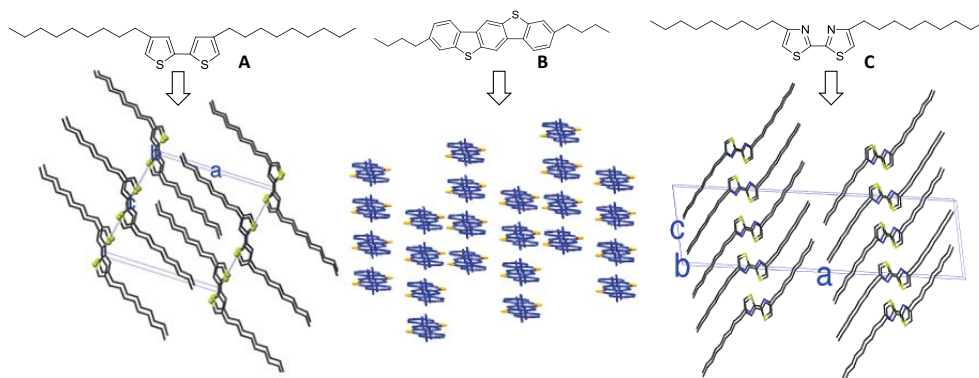


Figure 1.20. Packing motifs of substituted oligomers in their single crystals. (A) and (C) (Adopted from Curtis *et al.* *J. Am. Chem. Soc.* **2004**, 126, 4318-4328). (B) Adopted from Wang *et al.* *Chem. Rev.* **2012**, 112, 2208-2267).

It has been found the nature of the side chains, if present, greatly affected the solid-state packing of conjugated oligomers and polymers. If linear alkyl side chains are present, crystallization of the side chains promotes “lamellar” structure. A few examples of substituted conjugated oligomers have been summarized in the figure 1.20. The structure of nonyl bithiophene (see figure 1.20A) presented lamellar packing and the alkyl side chains were found to be interdigitated.¹¹¹ Interesting lamellar structure was observed in crystals of 1.20B, although the butyl groups were in the end-position instead of the side position.²¹ A view of the packing of nonyl bithiazole, (see figure 1.20C) molecules as seen along the crystallographic *b*-axis, depicted lamellar structure produced at such low degree of polymerization.¹¹¹

A few studies have been done to understand solid state packing of systems based on phenylenevinylene aromatic cores. Vandeveld *et al.* studied the single

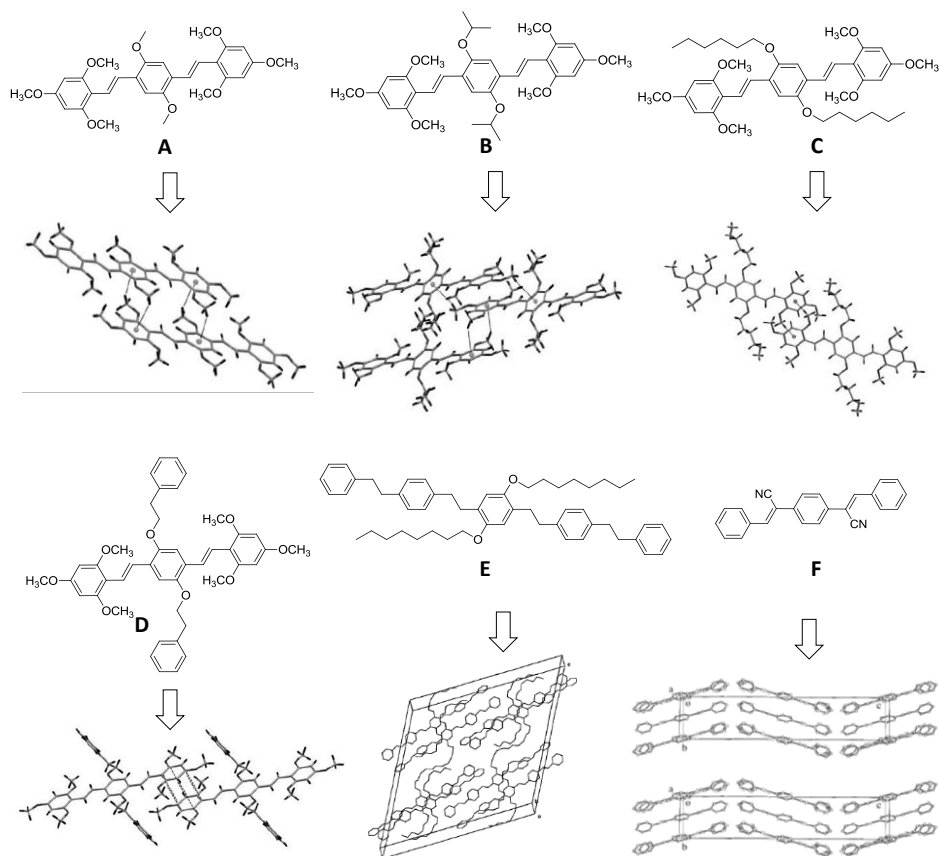
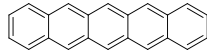
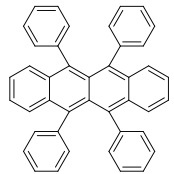
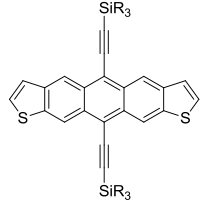


Figure 1.21. Packing motifs and single crystals based on oligophenylenevinylenes. A, B, C and D (Adopted from Vande Velde et al. *Crystal Growth & Design* **2004**, *4*, 823-830); E (Adopted from Gill et al. *Adv. Mater.* **1996**, *8*, 212-214); F (Adopted from Bartholomew et al. *Chem. Mater.* **2000**, *12*, 1422-1430).

crystal structures of *E,E*-1,4-bis[2-(2,4,6-trimethoxyphenyl)ethenyl]-2,5-dimethoxybenzene (1.21A), *E,E*-1,4-bis[2-(2,4,6-trimethoxyphenyl)ethenyl]-2,5-diisopropoxybenzene (1.21B), *E,E*-1,4-bis[2-(2,4,6-trimethoxyphenyl)ethenyl]-2,5-dihexoxybenzene (1.21C), and *E,E*-1,4-bis[2-(2,4,6-trimethoxyphenyl)ethenyl]-2,5-bis(2-phenylethoxy)benzene (1.21D).¹¹² Weak intramolecular hydrogen bond between protons belonging to olefinic bond and the *ortho*-methoxy groups on the adjacent benzene rings led to weak OCH₃- π interactions. The number of such OCH₃- π interactions changed with the structure and length of the side chains. The effects of these interactions explained the crystal formation mechanism in this class of alkoxy

side chain substituted OPVs. Hadziioannou et al. studied five-ring oligo(p-phenylene-vinylene) based liquid crystalline molecule (1.21E).¹¹³ The mesophase morphology was explained in terms of packing arrangement of the molecules in the unit cell. The molecule (1.21E) exhibited nematic textures and crystallized in monoclinic crystal system. The phenyl rings did not show π -stacking and the molecules were arranged in layers parallel to the (010) plane. Bartholomew et al. studied a series distyrylbenzene derivatives.¹¹⁴ The crystal structure of 1,4-bis(1-cyano-2-phenylethenyl)benzene¹¹⁵ has been shown in the figure 1.21F. The molecule crystallised in orthorhombic crystal symmetry (*Pbca*). The molecule was highly nonplanar with cyano groups located neither in the plane of the central nor terminal rings. The molecule exhibited N...H-C contacts and neighboring phenyl rings from different molecules arrange themselves to optimize T-type contacts.

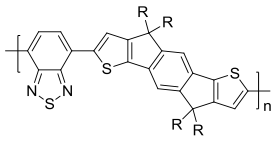
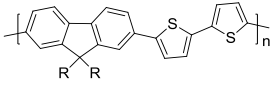
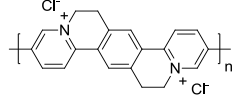
Table 1.5. Structures of π -conjugates, packing mode and OFETs mobility.

Structure	Packing mode	Mobility ($\text{cm}^2\text{V}^{-1}\text{s}^{-1}$)	Solubility
	Herringbone	5.1 and 40.2	Insoluble
	Slipped π -stacking	1.2 – 1.6	Insoluble
	2D π -stacking	1.0 – 1.25	Partially-soluble

The packing of molecules in the solid state in the active layer was found to be directly correlated to their field effect mobilities. OFETs also provide an important insight into the charge transport mechanism of π -conjugated systems. The charge transport mobility of the semiconductor is one of the most important parameters that

determine device performance.¹¹⁵ (see table 1.5). Hence, the understanding the packing of π -conjugated chromophores is very important to correlate the structure-property relationships with OFETs performance.¹¹⁶⁻¹²³ Rigid highly π -conjugated molecules are generally insoluble or poorly soluble in most common solvents. This induces two difficulties in the OFETs: (i) high vacuum sublimation techniques is usually required to fabricate OFET devices and (ii) it is almost impossible to grow single crystal structures of these molecules to trace the type of molecular packing. Among the small molecules, pentacene and its derivatives were found to be the best candidate so far studied for the OFETs. These molecules were found to order in the herringbone fashion. The substitution on the aromatic ring by aryl or alkyl units disturbed the packing of the chromophores.²¹ The mobility of the charges drastically decreased with the variation in the crystal packing. In general, a large number of π -conjugated systems are known to be active in OFETs; however, the lack of crystal structures hampered their structure-property correlation.

Table 1.6. π -Conjugated Polymers and their OFET mobility data.

Structure	Packing mode	Mobility ($\text{cm}^2\text{V}^{-1}\text{s}^{-1}$)	Solubility
	No information	1.2	Soluble
	No information	1.72	Soluble
	No information	2.56	Partially-soluble

Few conducting polymers were also tested for applications in OFETs and their data are summarized in table 1.6. Among the polymers benzothiadiazole-thiophene systems were known to show reasonable charge carrier mobility. However, their tedious synthesis and low molecular weight formation are some of the major hurdles to be addressed.²¹

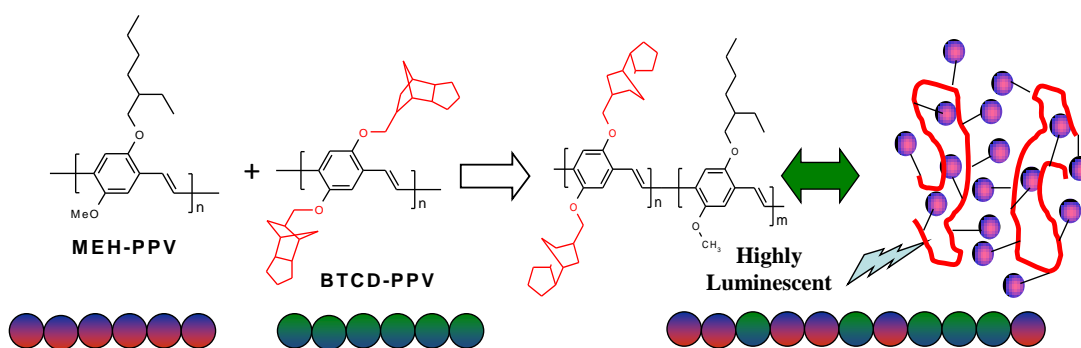


Figure 1.22. Schematic representation of photoluminescent enhancement in rigid bulky-PPV copolymers.

Amrutha et al. from our laboratory had designed and developed novel bulky TCD based PPVs for improved solid state photoluminescence properties.^{32, 124} In this approach, random copolymers of MEH-PPV with 60 % substitution of TCD-units into the PPV backbone were synthesized (see figure 1.22). The introduction of bulky TCD-units into the PPV backbone reduced molecular aggregation and enhanced the solution and solid state photoluminescence characteristics. The rigid bulky-PPV polymers followed Flory-Fox trend for the glass transition and showed photoluminescence enhancement 4-5 times higher than that of MEH-PPV.

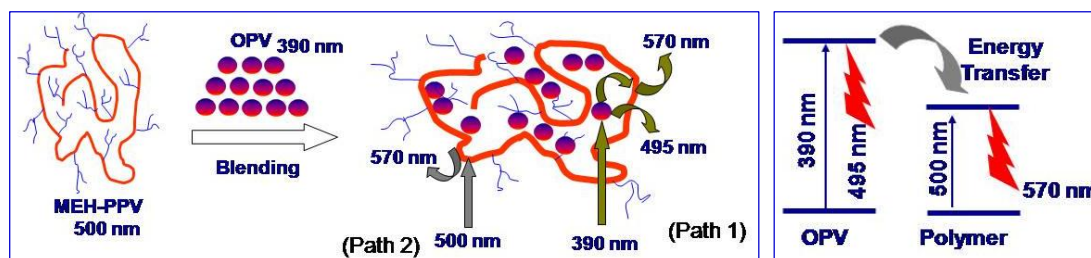


Figure 1.23. Schematic representation of photoluminescent enhancement in polymer-oligomer binary blends.

Subsequently, polymer-oligomer binary blends (figure 1.23) were synthesized by varying the composition of the MEH-PPV and OPVs from 1 to 99 %. Absorption and PL spectroscopic techniques were employed to trace the aggregation properties

in solvents such as toluene, tetrahydrofuran (THF), THF+methanol or THF+water combinations as well as in the solid state.¹²⁵ Through selective PL excitation, both the effect of oligomer-to-polymer energy transfer and luminescent enhancement in MEH-PPV via inter-chain separation were investigated. PL studies revealed that the bulky OPV (BTCD-OPV) increased the emission of the PPV chain via both energy transfer and inter chain separation processes.

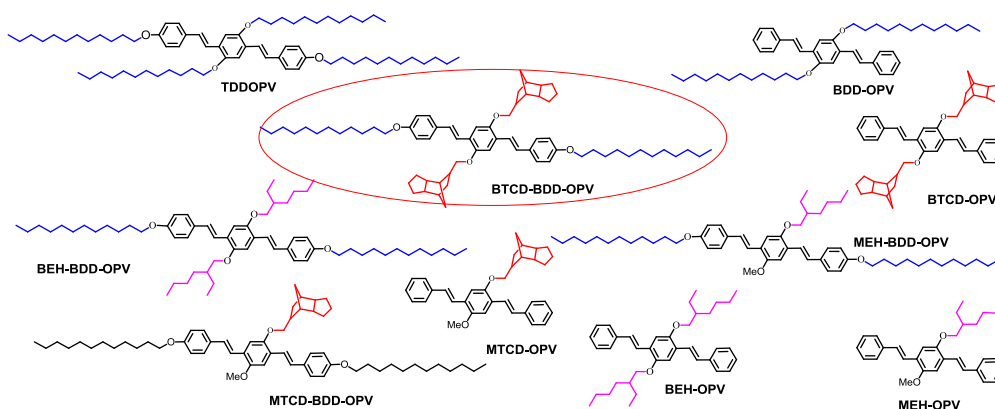


Figure 1.24. Chemical structures of OPVs with different pendent groups.

In an effort to understand the thermotropic liquid crystalline properties in oligomers, a series of bulky/ non-bulky, branched /linear alkyl chain substituted conjugated oligophenylenevinylenes were developed.^{31,125} More than 30 different molecules were synthesized for tracing the role of substituents on thermotropic liquid crystalline behavior of OPVs. The chemical structures of a few representative OPVs have been shown in the figure 1.24. The preliminary investigation revealed that among a dozen of examined OPV structures, OPV molecule with rigid bis-TCD units in the central core and flexible dodecyl chains at the outer phenyl rings (BTCD-BDD-OPV) was found to show very unique ring banded morphology in PLM images, which was the first of its kind in π -conjugated materials. The ring banded morphology of BTCD-BDD-OPV has been shown in the figure 1.25. Electron microscopic (SEM and TEM) analysis confirmed lamella twisting, and the mechanism of ring banded structures. Photophysical studies (excitation and emission

and time dependent fluorescence decay) were carried out to trace the role of π - π interactions in OPV mesogens on the ring banded structures. Therefore, it was shown that the size, shape and nature of the pendant groups attached in the OPV backbone is a crucial factor for inducing liquid crystallinity. Hence, tricyclodecanemethanol (TCD-OH) was established as effective structure directing unit for achieving highly luminescent materials and LC phases compared to that of normal alkyl chains.

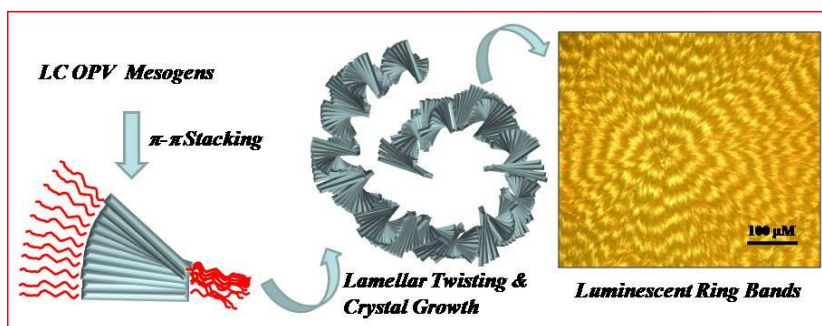


Figure 1.25. Helical twisting and ring banded textures of BTCD-BDD-OPV.

Highly ordered single crystals exhibited high charge carrier mobilities, but, major limitation of these materials is that single crystals cannot be used for large area applications. These rigid highly π -conjugated molecules required high purity, involved tedious multistep synthesis and were generally insoluble or poorly soluble in most common solvents due to their strong intermolecular interactions or the lack of flexible chains. Thus, the use of vacuum sublimation was usually required to fabricate devices containing such materials. High temperature vacuum deposition techniques required for such materials rendered them unsuitable for large area electronics which are feasible only with cheap and easy thin film deposition techniques such as controlled solvent evaporation, spin coating, drop casting or ink jet printing. Hence, construction of highly ordered solid state structures of π -conjugated materials with improved charge carrier mobilities and excellent luminescent characteristics for optoelectronic applications is challenging problems to be addressed.

1.6. Aim of the thesis

From the previous discussions, it is understood that the performance of π -conjugated materials in electronic devices are mainly driven by the molecular arrangements in solid state. Therefore, controlling molecular self-organization and understanding precise intermolecular forces is very important for use of these materials in electronic devices. However, it is rather very challenging to obtain information on the packing of π -conjugated molecules in the solid state due to the non-availability of single crystal structures for these large π -conjugated molecules. It has been a great challenge for synthetic chemists to design appropriate models which could self-organize in solid state (in a solvent free condition) and also produce their single crystal structures so that direct correlation between molecular packing and self-assembly could be established. Hence, design and synthesis of new π -conjugated systems and obtaining control over the supramolecular organization of these electronically active π -conjugated molecules is a major challenge to fine-tune and optimize their electrical properties for better device performances.

This thesis work is focused on design and development of new π -conjugated phenylenevinylenes and their segmented polymers that can self-assemble via weak non-covalent interactions in the solid state. Further, single crystal X-ray structures were resolved to understand the solid state molecular self-assemblies of these π -conjugates. The roles of OPV skeletons on the liquid crystalline properties, planarity versus non-planarity, inter-molecular non covalent forces such as weak CH/ π interactions and π - π stacking, pitch and roll displacements in the crystal lattices and photophysical characteristics were investigated in detail.

The important aspects of the thesis are:

1. Helical Supramolecular Assemblies of OPVs: The origin of two dimensional herringbone layers to 3D helical self-assembly in a homologous series of OPVs has been studied.
2. Hierarchical Assemblies of OPV Structural Isomers: The role of OPV backbone planarity, CH/ π hydrogen bond, and positional effect of peripheral

substitution, alkyl chain lengths and its orientation were investigated on the various properties such as liquid crystallinity and so on.

3. Fluorocarbon versus Hydrocarbon tail in OPVs: Effort was made to synthesize fluorocarbon and hydrocarbon tailed OPV molecules. The role of tail nature on LC mesophases such as smectic, nematic and their H and J aggregates formations was investigated.
4. Donor-acceptor Assemblies of Segmented OPV Polymers: The effect of chemical structure and polymer chain topology on donor acceptor self-assemblies of segmented OPV polymers and perylenebisimide chromophore were studied. The donor-acceptor self-organization was investigated in detail using FRET mechanistic pathways.

In the second chapter, the origin of herringbone to helical self-assembly in custom designed tricyclodecanemethylene OPVs has been studied at molecular level using single-crystal X-ray structures. Weak hydrogen bonding CH/ π interactions were found to be an important non-covalent force in the molecular self-assembly. The third chapter deals with role of OPV backbone planarity and positional effect of peripheral substitutions on solid state packing, liquid crystallinity, intermolecular forces and roll/pitch displacements of a large number of OPVs. In the fourth chapter, fluorocarbon and hydrocarbon tailed OPV molecules with various pendants in the aromatic back bone were synthesised and the role of tail nature on LC mesophases such as smectic, nematic and their H and J aggregates formations was investigated. The fifth chapter describes the synthesis of various segmented OPV polymers. The effect of chemical structure and polymer chain topology on donor acceptor self-assemblies of segmented OPV polymers and perylenebisimide chromophore have been studied using FRET mechanistic pathways. Finally, the overall conclusion of the thesis has been summarized.

1.7. References

1. Shirakawa, H.; Louis, E. J.; MacDiarmid, A. G.; Chiang, C. K.; Heeger, A. J. *J. Chem. Soc., Chem. Commun.* **1977**, 578.
2. Wise, D. L. *Electrical and Optical Polymer Systems: Fundamentals: Methods and Applications* CRC Press, **1998**.
3. Skotheim, T. A. *Handbook of Conducting Polymers*, Marcel Dekker, New York, **1986**.
4. Salamone, J. C. *Polymeric Materials Encyclopedia* CRC Press, **1996**.
5. Nalwa, H. S. *Handbook of Advanced Electronic and Photonic Materials and Devices*, Academic Press, **2000**.
6. Bredas, J. L. *Conjugated Oligomers, Polymers and Dendrimers: From Polyacetylene to DNA*, Proceedings of the Fourth Francqui Colloquium, Brussels, **1998**.
7. Shirakawa, H. *Angew. Chem. Int. Ed.* **2001**, 40, 2574.
8. (a) Sun, S. S.; Sariciftci, N. S. *Organic Photovoltaics: Mechanism, Materials and Devices* CRC Press, **2005**. (b) Saxena, V.; Malhotra, B. D. *Current Appl. Phys.* **2003**, 3, 293-305.
9. Burroughes, N. N.; Bradley, D. D. C.; Brown, A. R.; Marks, N. N.; Mackay, K.; Friend, R. H.; Burns, P. L.; Holmes, A. B. *Nature*, **1990**, 347, 539.
10. Burn, P. L.; Holmes, A. B.; Kraft, A.; Bradley, D. D. C.; Brown, A. R.; Friend, R. H.; Gymer, R. W. *Nature* **1992**, 356, 47.
11. Greenham, N. C.; Moratti, S. C.; Bradley, D. D. C.; Friend, R. H.; Holmes, A. B. *Nature* **1993**, 365, 628.
12. Akcelrud, L. *Prog. Polym. Sci.* **2003**, 28, 875.
13. Mueller, G. *Electroluminescence I (Semiconductors and Semimetals)*, Academic Press, USA, **1999**.
14. Hoppe, H.; Sariciftci, N. S. *J. Mater. Res.* **2004**, 19, 1924-1945. (b) Cheng, Y.J.; Yang, S. H.; Hsu, C. S. *Chem. Rev.* **2009**, 109, 5868-5923.

15. Ouali, L.; Krasnikov, V. V.; Stalmach, U.; Hadziioannou, G. *Adv. Mater.* **1999**, *11*, 1515-1518. (b) Gu'nes, S.; Neugebauer, H.; Sariciftci, N. S. *Chem. Rev.* **2007**, *107*, 1324-1338.
16. Alam, M. M.; Jenekhe, S. A. *Chem. Mater.* **2004**, *16*, 4647-4656. (b) Zhou, E.; Cong, J.; Wei, Q.; Tajima, K. Yang, C.; Hashimoto, K.; *Angew. Chem. Int. Ed.* **2011**, *50*, 2799-2803. (c) Stalder, R.; Mei, J.; Subbiah, J.; Grand, C.; Estrada, L. A.; So, F.; Reynolds, J. R. *Macromolecules* **2011**, *44*, 6303-6310.
17. Shaheen, S. E.; Brabec, C. J.; Sariciftci, N. S.; Padinger, F.; Fromherz, T. *Appl. Phys. Lett.* **2001**, *78*, 841-843.
18. Schuller, S.; Schilinsky, P.; Haunch, J.; Brabec, C. *J. Appl. Phys. A* **2004**, *79*, 37. (b) Yang, X.; Van Duren, J. K. J.; Janssen, R. A. J.; Michels, M. A. J.; Loos, J. *Macromolecules* **2004**, *37*, 2151-2158.
19. Wu, W.; Liu, Y.; Zhu, D. *Chem. Soc. Rev.* **2010**, *39*, 1489-1502.
20. Sun, Y.; Liu, Y.; Zhu, D. *J. Mater. Chem.* **2005**, *15*, 53-65.
21. Wang, C.; Dong, H.; hu, W.; Liu, Y.; Zhu, D. *Chem. Rev.* **2012**, *112*, 2208-2267.
22. Lehn, J. M. *Angew. Chem. Int. Ed. Engl.* **1990**, *29*, 1304-1319.
23. Steed, J.W.; Turner, D.R.; Wallace, K. J. *Core Concepts in Supramolecular Chemistry and Nanochemistry*. John Wiley & Sons, **2007**.
24. Kunitake, A. *Supramolecular Chemistry- Fundamentals and Applications*. Springer-Verlag, Berlin, **2006**.
25. Prins, L. J.; Reinhoudt, D. N.; Timmerman, P. *Angew. Chem. Int. Ed.* **2001**, *40*, 2382 -2426.
26. Waters, M. L. *Curr. Opin. Chem. Biol.* **2002**, *6*, 736-741.
27. Martinez, C. R.; Iverson, B. L. *Chem. Sci.* **2012**, *3*, 2191-2201.
28. Grimme, S. *Angew. Chem. Int. Ed.* **2008**, *47*, 3430-3434.
29. Rubes, M.; Bludsky, O. *Phys. Chem. Chem. Phys.* **2008**, *10*, 2611-2615.
30. Goel, M.; Jayakannan, M. *J. Phys. Chem. B* **2010**, *114*, 12508 -12519;
31. Amrutha,S. R.; Jayakannan, M. *J. Phys. Chem. B* **2009**, *113*, 5083 -5091;

32. Amrutha, S. R.; Jayakannan, M. *Macromolecules* **2007**, *40*, 2380–2391.
33. Stillinger, F. H.; Wasserman, Z. *J. Phys. Chem.* **1978**, *82*, 929-940.
34. Linton, B.; Hamilton, A. D. *Chem. Rev.* **1997**, *97*, 1669-1680.
35. Han, F. S.; Higuchi, M.; Kurth, D. G. *Adv. Mater.* **2007**, *19*, 3928-3931.
36. Knapton, D.; Rowan, S. J.; Weder, C. *Macromolecules* **2006**, *39*, 651-657.
37. Janssen, P. G. A.; Meeuwenoord, N.; Marel, G. V.; Jabbari-Farouji, S.; Schoot, P. V.; Surin, M.; Tomovic, Z.; Meijer, E. W.; Schenning, A. P. H. J. *Chem. Commun.* **2010**, *46*, 109-111.
38. Schenning, A. P. H. J.; Jonkheijm, P.; Peeters, E.; Meijer, E. W. *J. Am. Chem. Soc.* **2001**, *123*, 409-416.
39. Asha, S. K.; Schenning, A. P. H. J. *Chem. Eur. J.* **2002**, *8*, 3353-3361.
40. Wicklein, A.; Lang, A.; Muth, M.; Thelakkat, M. *J. Am. Chem. Soc.* **2009**, *131*, 14442-14453.
41. Babu, S. S.; Praveen, V. K.; Prasanthkumar, S.; Ajayaghosh, A. *Chem. Eur. J.* **2008**, *14*, 9577 -9584.
42. Hirai, Y.; Babu, S. S.; Praveen, V. K.; Yasuda, T.; Ajayaghosh, A.; Kato, T. *Adv. Mater.* **2009**, *21*, 4029-4033.
43. Dudek, S. P.; Pouderoijen, M.; Abbel, R.; Schenning, A. P. H. J.; Meijer, E. W. *J. Am. Chem. Soc.* **2005**, *127*, 11763-11768.
44. Jonkheijm, P.; Zdanowska, A. M. M.; Hoeben, F. J. M.; Feyter, S. D.; Schenning, A. P. H. J.; Schryver, F. C. D.; Meijer, E. W. *Angew. Chem. Int. Ed.* **2004**, *43*, 74-78.
45. Tazawa, T.; Yagai, S.; Kikkawa, Y.; Karatsu, T.; Kitamura, A.; Ajayaghosh, A. *Chem. Commun.* **2010**, *46*, 1076-1078.
46. Kihara, H.; Kato, T.; Uryu, T.; Fréchet, J. M. J. *Chem. Mater.* **1996**, *8*, 961-968.
47. Wilson, A. J. *Nature Chem.* **2011**, *3*, 193-194.
48. Pisula, W.; Tomovic, Z.; Wegner, M.; R.; Pouderoijen, M. J.; Meijer, E. W.; Schenning, A. P. H. J. *J. Mater. Chem.* **2008**, *18*, 2968-2977.

49. Schenning, A. P. H. J.; Herrikhuyzen, J.; Jonkheijm, P.; Chen, Z.; Würthner, F.; Meijer, E. W. *J. Am. Chem. Soc.* **2002**, *124*, 10252-10253.
50. Sijbesma, R. P.; Beijer, F. H.; Brunsveld, L.; Folmer, B. J. B.; Hirschberg, J. H. K. K.; Lange, R. F. M.; Lowe, J. K. L.; Meijer, E. W. *Science* **1997**, *278*, 1601. (b) Hirschberg, J. H. K. K.; Brunsveld, L.; Ramzi, A.; Vekemans, J. A. J. M.; Sijbesma, R. P.; Meijer, E. W. *Nature* **2000**, *407*, 167. (c) Abbel, R.; Grenier, C.; Pouderoijen, M. J.; Stouwdam, J. W.; Leclère, P. E. L. G.; Sijbesma, R. P.; Meijer, E. W.; Schenning, A. P. H. J. *J. Am. Chem. Soc.* **2009**, *131*, 833-843.
51. (a) Babu, S. S.; Prasanthakumar, S.; Ajayaghosh, A. *Angew. Chem. Int. Ed.* **2012**, *51*, 1766-1776. (b) George, S. J.; Ajayaghosh, A.; Jonkheijm, P.; Schenning, A. P. H. J.; Meijer, E. W. *Angew. Chem. Int. Ed.* **2004**, *43*, 3422-3425. (c) Ajayaghosh, A.; George, S. J.; Praveen, V. K. *Angew. Chem. Int. Ed.* **2003**, *115*, 346-349. (d) Saeki, A.; Seki, S.; Ajayaghosh, A. *J. Am. Chem. Soc.* **2010**, *132*, 8866-8867.
52. Yagai, S.; Kubota, S.; Saito, H.; Unoike, K.; Karatsu, T.; Kitamura, A.; Ajayaghosh, A.; Kaneshato, M.; Kikkawa, Y. *J. Am. Chem. Soc.* **2009**, *131*, 5408-5410.
53. Hunter, C. A. *Philos. Trans. R. Soc. London, Ser. A*, **1993**, *345*, 77-85.
54. Park, S. M.; Herndon, W. C. *Tetrahedron Lett.* **1978**, *19*, 2363-2366.
55. Gallivan, J. P.; Schuster, G. B. *J. Org. Chem.* **1995**, *60*, 2423-2429.
56. Boden, N.; Bushby, R. J.; Jesudason, M. V.; Sheldrick, B. *Chem. Commun.* **1988**, *19*, 1342-1343.
57. Kastler, M.; Pisula, W.; Wasserfallen, D.; Pakula, T.; Müllen, K. *J. Am. Chem. Soc.* **2005**, *127*, 4286-4296.
58. Jancy, B.; Asha, S. K. *Chem. Mater.* **2008**, *20*, 169-181.
59. Würthner, F.; Sautter, A. *Chem. Commun.* **2000**, 445-446.
60. Würthner, F.; Chen, Z.; Dehm, V.; Stepanenko, V. *Chem. Commun.* **2006**, 1188-1190.

61. Haas, U.; Thalacker, C. Adams, J. Fuhrmann, J.; Riethmuller, S.; Beginn, U. Ziener, U.; Mo"ller, M.; Dobrawaa, R. and Wu"rthner, F. *J. Mater. Chem.* **2003**, *13*, 767-772.
62. Wurthner, F.; Sautter, A. *Org. Biomol. Chem.* **2003**, *1*, 240-243.
63. Sommer, M.; Huettnerab, S.; Thelakkat, M. *J. Mater. Chem.* **2010**, *20*, 10788-10797.
64. Cubberley, M. S.; Iverson, B. L. *J. Am. Chem. Soc.* **2001**, *123*, 7650-7653.
65. Snow, A. W. in *The porphyrin Handbook, Vol. 17*, (Ed.: K. M. Kadish, K. M. Smith, R. Guilard), Academic press, New York, **2003**, pp.129-176.
66. Chen, Z.; Stepanenko, V.; Dehm, V.; Prins, P.; Siebbeles, L. D. A.; Seibt, J.; Marquetand, P.; Engel, V.; Wurthner, F. *Chem. Eur. J.* **2007**, *13*, 436-449.
67. Wurthner, F. *Chem. Commun.* **2004**, 1564-1579.
68. Herrikhuyzen, J.; Asha, S. K.; Schenning, A. P. H. J.; Meijer, E. W. *J. Am. Chem. Soc.* **2004**, *126*, 10021-10027.
69. Bhalla, V.; Gupta, A.; Kumar, M.; Rao, D. S. S.; Prasad, S. K. *Appl. Mater. Interfaces* **2013**, *5*, 672-679.
70. Wilson, M. R. *Chem. Soc. Rev.* **2007**, *36*, 1881-1888.
71. Tschierske, C. *Chem. Soc. Rev.* **2007**, *36*, 1930-1970
72. Goodby, J. W.; Cowling, V. S. J.; Mackenzie, G.; Martin, P.; Plusquellec, D.; Benvegnu, T.; Boullanger, P.; Lafont, D.; Queneau, Y.; Chamberte, S.; Fitremannf, J. *Chem. Soc. Rev.* **2007**, *36*, 1971-2032.
73. Kato, T.; Hirai, Y.; Nakaso, S.; Moriyama, M. *Chem. Soc. Rev.* **2007**, *36*, 1857-1867.
74. Goodby, J. W. *Chem. Soc. Rev.* **2007**, *36*, 1855-1856.
75. Shimizu, Y.; Oikawa, K.; Nakayamac, K.; Guillond, D. *J. Mater. Chem.* **2007**, *17*, 4223-4229.
76. Garnier, F. *Acc. Chem. Res.* **1999**, *32*, 209-215.
77. Neill, M. O.; Kelly, S. M. *Adv. Mater.* **2003**, *15*, 1135-1146.
78. Breemen, A. J. J. M.; Herwig, P. T.; Chlon, C. H. T.; Sweelssen, J.; Schoo, H. F. M.; Setayesh, S.; Hardeman, W. M.; Martin, C. A.; de Leeuw, D. M.

- ; Valetton, J. J. P.; Bastiaansen, C. W. M.; Broer, D. J.; Popa-Merticaru, A. R.; Meskers, S. C. J. *J. Am. Chem. Soc.* **2006**, *128*, 2336-2345.
79. Theme issue-liquid crystals beyond display applications. *J. Mater. Chem.* **2008**, *18*, 2869-2871.
80. Dierking, I. *Textures of Liquid Crystals*, 2nd ed.; Wiley-VCH Verlag GmbH: Berlin, **2003**.
81. Wang, X. J.; Zhou, Q. F. *Liquid crystalline Polymers*, World Scientific Publishing Co. Pte. Ltd. **2004**.
82. Funahashi, M.; Hanna, J. *Adv. Mater.* **2005**, *17*, 594-598.
83. Hirai, Y.; Babu, S. S.; Praveen, V. K.; Yasuda, T.; Ajayaghosh, A.; Kato, T. *Adv. Mater.* **2009**, *21*, 4029-4033.
84. Kuo, L. C.; Huang, W. T.; Yang, K. H.; Hsu, H. F.; Jin, B. Y.; Leung, M. J. *Phys. Chem. B* **2010**, *114*, 2607-2616.
85. Kloppenburg, L.; Jones, D.; Claridge, J. B.; Loye, H. C.; Bunz, U. H. F. *Macromolecules* **1999**, *32*, 4460-4463.
86. Jin, J.; Smith, D. W.; Glasser, S.; Perahia, D.; Foulger, S. H.; Ballato, J. Kang, S. W.; Kumar, S. *Macromolecules* **2006**, *39*, 4646-4649.
87. Schenning, A. P. H. J.; Kilbinger, A. F. M.; Biscarini, F.; Cavallini, M.; Cooper, H. J.; Derrick, P. J.; Feast, W. J.; Lazzaroni, R.; Leclère, P.; McDonnell, L. A.; Meijer, E. W.; Meskers, S. C. J. *J. Am. Chem. Soc.* **2002**, *124*, 1269-1275.
88. Garnier, F.; Hajlaoui, R.; Kassmi, A. E.; Horowitz, G.; Laigre, L.; Porzio, W.; Armanini, M.; Provasoli, F. *Chem. Mater.* **1998**, *10*, 3334-3339.
89. Yasuda, T.; Ooi, H.; Morita, J.; Akama, Y.; Minoura, K.; Funahashi, M. Shimomura, T.; Kato, T. *Adv. Funct. Mater.* **2009**, *19*, 411-419.
90. Chandrasekhar, S.; Sadashiva, B. K.; Suresh, K. A. *Pramana* **1977**, *9*, 471.
91. Laschat, S.; Baro, A.; Steinke, N.; Giesselmann, F.; Hgele, C.; Scalia, G.; Judele, R.; Kapatsina, E.; Sauer, S.; Schreivogel, A.; Tosoni, M. *Angew. Chem. Int. Ed.* **2007**, *46*, 4832-4887.

92. Sergeyev, S.; Pisulab, W.; Geerts, Y. H. *Chem. Soc. Rev.* **2007**, *36*, 1902-1929.
93. Furchey, J. L.K.; Fayer, M. D. *J. Chem. Phys.* **2006**, *125*, 194901-1 to 194901-7.
94. Kumar, S. *Liq. Cryst.* **2004**, *31*, 1037-1059.
95. Chandrasekhar, S.; Ranganath, G. S. *Rep. Prog. Phys.* **1990**, *53*, 57-84.
(Printed in the UK)
96. Martínez-Haya, B.; Cuetos, A. *Physical Reviews E* **2010**, *81*, 20701-1 to 20701-4.
97. Donovan, K. J. *Proc. Int. Symp. IPAP Conf. Series* **6**, 38-41.
98. Kumar, S. *Current Science*, **2002**, *82*, 256-258.
99. Feng, X.; Marcon, V.; Pisula, W.; Hansen, M. R.; Kirkpatrick, J.; Grozema, F.; Andrienko, D.; Kremer, K.; Müllen, K. *Nature Mater.* **2009**, *8*, 421-426.
100. Kelber, J.; Achard, M. F.; Durola, F.; Bock, H. *Angew. Chem. Int. Ed.* **2012**, *51*, 5200-5203.
101. Schmidt-Mende, L.; Fechtenkötter, A.; Mullen, K.; Moons, E.; Friend, R. H.; MacKenzie, J. D. *Science* **2001**, *293*, 1119 -1122.
102. Pisula, W.; Menon, A.; Steppulat, M.; Lieberwirth, I.; Ui, K.; Tracz, A.; sirringaus, H.; Pahula, T.; Mullen, K. *Adv. Mater.* **2005**, *17*, 684- 689.
103. Craats, A. M.; Warman, J. M.; Fechtenkötter, A.; Brand, J. D.; Harbison, M. A.; Müllen, K. *Adv. Mater.* **1999**, *11*, 1469-1472.
104. Yasuda, T.; Kishimoto, K.; Kato, T. *Chem. Commun.*, **2006**, 3399-3401.
105. Zhang, L.; Hughes, D. L.; Cammidge, A. N. *J. Org. Chem.* **2012**, *77*, 4288-4297.
106. Kumar, S.; Gupta, S. K. *Tetrahedron Letters* **2011**, *52* 5363-5367.
107. Lin, Y. Y.; Gundlach, D. J.; Nelson, S. F.; Jackson, T. N. *IEEE Trans. Electron* **1997**, *44*, 1325-1331.
108. Meijer, E. J.; de Leeuw, D. M.; Setayesh, S.; Veenendaal, E. V.; Huisman, B. H.; Blom, P. W. M.; Hummelen, J. C.; Scherf, U.; Klapwijk, T. M. *Nature Mater.* **2003**, *2*, 678- 682.

109. Sokolov, A. N.; Evrenk, S. A.; Mondall, R.; Akkerman, H. B.; Sánchez-Carrera, R. S.; Granados-Focil, S.; Schrier, J.; Mannsfeld, S. C. B.; Zoombelt, A. P.; Bao, Z.; Aspuru-Guzik, A. *Nature Comm.* **2011**, 2:437, 1-8.
110. Horowitz, G.; Bachet, B.; Yassar, A.; Lang, P.; Demanze, F.; Fave, J.; Garnier, F. *Chem. Mater.* **1995**, 7, 1337-1341.
111. Curtis, M. D.; Cao, J.; Kampf, J. W. *J. Am. Chem. Soc.* **2004**, 126, 4318-4328.
112. Vande Velde, C. M. L.; Chen, L.; Baeke, J. K.; Moens, M.; Dieltiens, P.; Geise, H. J.; Zeller, M.; Hunter, A. D.; Blockhuys, F. *Crystal Growth & Design* **2004**, 4, 823-830.
113. Gill, R. E.; Meetsma, A.; Hadziioannou, G. *Adv. Mater.* **1996**, 8, 212-214.
114. Bartholomew, G. P.; Bazan, G. C.; Bu, X.; Lachicotte, R. J. *Chem. Mater.* **2000**, 12, 1422-1430.
115. Holmes, D.; Kumarasamy, S.; Matzger, A. J.; Vollhardt, K. P. C. *Chem. Eur. J.* **1999**, 5, 3399-3412.
116. Yasuda, T.; Saitoi, M.; Nakakumari, H.; Tsutsui, T. *Jpn. J. Appl. Phys.*, **2006**, 45, L313-L315.
117. Oikawa, K.; Monobe, H.; Nakayama, K.; Kimoto, T.; Tsuchiya, K.; Heinrich, B.; Guillon, D.; Shimizu, Y.; Yokoyama, M. *Adv. Mater.* **2007**, 19, 1864-1868.
118. Meng, H.; Sun, F.; Goldfinger, M. B.; Jaycox, G. D.; Li, Z.; Marshall, W. J.; Blackman, G. S. *J. Am. Chem. Soc.* **2005**, 127, 2406-2407.
119. Payne, M. M.; Parkin, S. R.; Anthony, J. E.; Kuo, C. C.; Jackson, T. N. *J. Am. Chem. Soc.* **2005**, 127, 4986-4987.
120. Naraso; Nishida, J.; Ando, S.; Yamaguchi, J.; Itaka, K.; Koinuma, H.; Tada, H.; Tokito, S.; Yamashita, Y. *J. Am. Chem. Soc.* **2005**, 127, 10142-10143.
121. Ackermann, C. V.; Ackermann, J.; Brisset, H.; Kawamura, K.; Yoshimoto, N.; Raynal, P.; Kassmi, A. E.; Fages, F. *J. Am. Chem. Soc.* **2005**, 127, 16346-16347.

122. Torrent, M. M.; Durkut, M.; Hadley, P.; Ribas, X.; Rovira, C. *J. Am. Chem. Soc.* **2004**, *126*, 984-985.
123. Naraso; Nishida, J.; Kumaki, D.; Tokito, S.; Yamashita, Y. *J. Am. Chem. Soc.* **2006**, *128*, 9598-9599.
124. Amrutha, S. R.; Jayakannan, M. *J. Phys. Chem. B.* **2006**, *110*, 4083.
125. Amrutha, S. R.; Jayakannan, M. *J. Phys. Chem. B.* **2008**, *112*, 1119.

Chapter 2

*Helical Supramolecular Self-assembly of OPVs in
Solid State*

Chapter 2

Helical Supramolecular Self-assembly of OPVs in solid state

The origin of helical self-organization in the π -conjugated oligophenylenevinylenes has been studied at molecular level using single crystal XRD analysis. A homologous series of OPVs with identical aromatic core but increasing number of carbon atoms in the longitudinal position was synthesized. Detailed thermal analysis (by DSC) and polarized light microscope (PLM) analysis revealed that OPVs exhibited systematic sigmoidal transition in the mesophases from crystalline to cholesteric to ring-banded textures with an increase in the methylene units in the alkyl chains. Single-crystal X-ray structures of OPV molecules were resolved to find out the origin of sigmoidal self-assembly at the molecular level. Further, crystallographic parameters such as pitch and roll angles and their displacements were determined to establish the correlation between crystal structures and liquid-crystalline (LC) mesophase morphology. Weak hydrogen bonding CH/ π interactions were proven to be an important non-covalent force in the molecular self-assembly. The findings revealed that the self-organization of π -conjugated species underwent transformation from 2D herringbone layer to 3D helical twist in the liquid crystalline mesophases. The large pitch and roll displacements completely destroyed the aromatic π -stacking interactions among the OPV chromophores. Circular dichroism studies on the OPVs revealed that the helical structures were produced only on aligning the chromophores in the LC mesophases. Photophysical analysis of the OPVs in LC and single crystals revealed that the photophysical properties were identical in both the states. This further confirmed similar type of self-organization in LC and single crystal domains. The uniqueness of the present approach is that both herringbone and helical assemblies could be simply varied by means of the number of carbon atoms in the tails. The overall findings revealed that the CH/ π interaction is a very powerful non-covalent interaction in supramolecular chemistry.

2.1. Introduction

π -Conjugated semiconducting polymers (and oligomers) are futuristic materials for next generation electronics such as light emitting diodes (LEDs), field effect transistors (FETs) and photovoltaics (PVs).¹ The chemical structure and supramolecular-organization of individual molecules (or polymer chains) play a key role in determining the performance of these materials in electronic devices.^{2,3} Therefore, understanding and controlling the supramolecular organization between individual π -conjugated molecules has become one of the most challenging research areas.^{4,5} The detailed literature survey on the self-assemblies of π -conjugated semiconducting systems has already been provided in the introduction in chapter-2. Unfortunately, most of the π -conjugated polymers are amorphous in nature; as a result, understanding the molecular interactions via X-ray diffraction technique becomes almost impossible. π -Conjugated oligomers are important model compounds for understanding the relationships between chemical structure and molecular ordering of long chain π -conjugated polymers. Thus, synthesis of new π -conjugated synthons that produce self-organized assemblies⁶⁻⁸ and studying self-organization at molecular level using single crystal X-ray structures are fundamental challenges in this field.

Oligophenylenes⁹, oligothiophenes¹⁰, oligofluorenes¹¹, oligophenylene ethylene¹² and oligophenylenevinylene¹³ chromophores were reported for self-organization in π -conjugated materials. Among these, multidimensional nano architectures of oligothiophenes^{10d} and cooperative conformation transition in oligophenyleneethylenes^{12d} were found to be more attractive. High luminescence characteristics, thermal and optical stability, solubility in organic solvents, film forming tendency, easy synthetic approaches make OPV-chromophores very unique as compared to other π -conjugates.¹³ Therefore, understanding the self-assembly of these systems at molecular level is of paramount importance. The challenge lies in the fact that most of the π -conjugated oligomers did not form single-crystal structures, and those which produced good crystals were found to be lacking macroscopic self-organization such as liquid crystallinity in the solid state.¹⁴ Wang et

al. published a comprehensive review covering large number of π -conjugated systems to contribute to a better understanding of structure-property relationship of this class of compounds.¹⁵ The importance of the single crystal structures and molecular packing models were explained to facilitate better understanding on chromophore arrangements and their device performances.

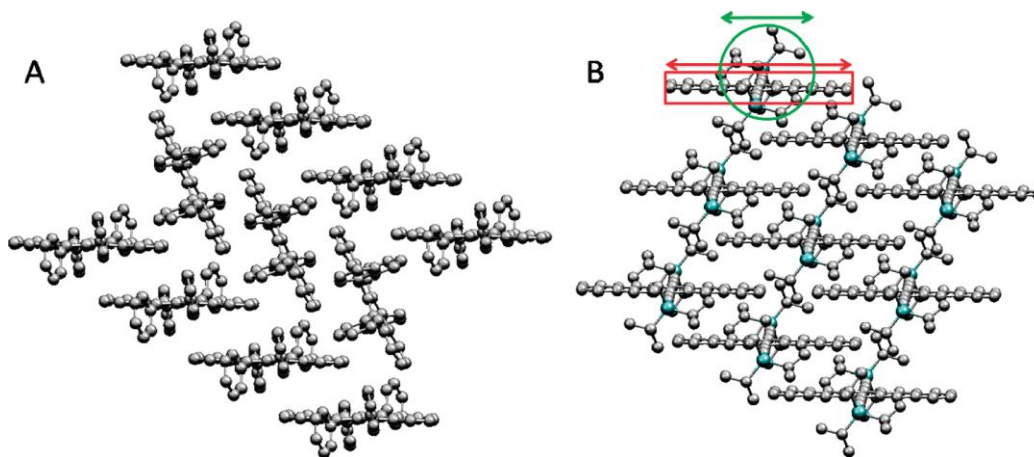


Figure 2.1. Single-crystal X-ray structure of Rubrene (A), and TIPS-PEN (B) (Adopted from Wang et al. *Chem. Rev.* **2012**, 112, 2208 -2267).

Figure 2.1 explains the molecular packing arrangements in rubrene (A) and a substituted acene TIPS-PEN (B). Rubrene (A) exhibited herringbone packing arrangement, but as the length of the substituents changed to approximately half the length of the acene core in (B), the packing motif changed to a two-dimensional lamellar structure.¹⁵ Gao et al. reported that the solid-state molecular packing and fluorescence properties of conjugated linear molecules can be tailored by introducing different side or end functional groups.¹⁶ A new type of linear compound consisting of thiomethyl-terminated OPV (TOPV) was synthesized. This new OPV compound was highly prone to form single crystals. The X-ray structure analysis (see figure 2.2) indicated that it exhibited a rigid planar structure with extended π -conjugated length, which led to strong solid-state fluorescence induced by absorption of one or two photons.

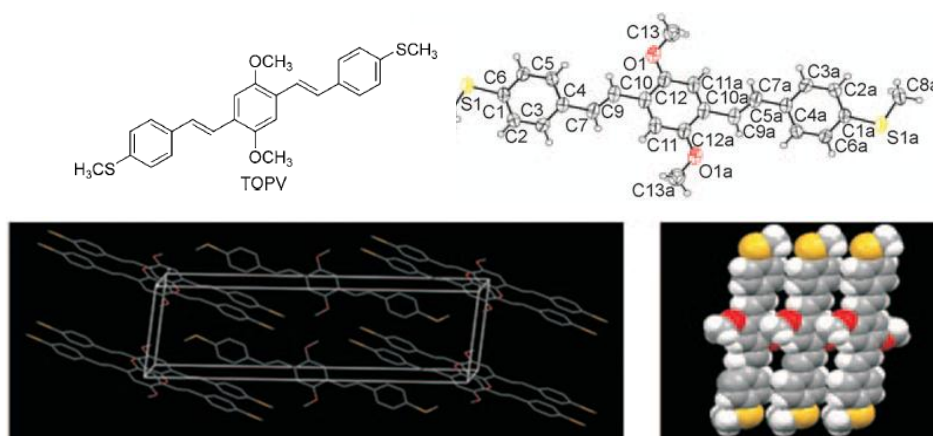


Figure 2.2. Single-crystal X-ray structure of TOPV (Adopted from Gao et al. *Angew. Chem. Int. Ed.* **2010**, *49*, 732-735).

One of the several possible approaches that have been utilized to study self-assembly in these systems is to synthesize liquid crystalline (LC) π -conjugated oligomers, where direct information about the molecular orientations or mesogen alignments can be visualized from LC textures.^{17, 18} Such systems essentially consist of a rigid π -conjugated aromatic core and flexible alkyl side chains giving rise to thermotropic LC materials. The number of carbon atoms in the alkyl side chains can be uniformly varied to synthesize a homologous series of the molecules for the detailed understanding of self-assembling properties. Hydrogen bond inducing skeletons have been attached in the OPV backbone, and both H-bonding and aromatic π -stacking interactions have been utilized for supramolecular LC materials.^{19,20} Jonkheijm et al. reported spectroscopic investigation of hydrogen-bonded molecules and found that an organized shell of solvent played a major role toward self-assembly.²¹ Efforts had been put to self-organize OPVs building blocks via hydrogen bonding,²²⁻²⁵ π - π stacking,²⁶⁻²⁷ and metal-ion interactions,²⁸ and the resultant structures were tested successfully as active layers in electronic devices.²⁹ More often, other interactions like hydrogen bonding and metal-ion interactions were introduced as additional secondary forces to strengthen the aromatic π - π stacking self-assembly.³⁰⁻³¹

Hydrogen bond assisted self-assembly has been found as one of the best tools for making self-assembled suprastructures. However, the non-conjugated chemical linkages such as H-bonding units (or metal-ion units) in the π -conjugated molecules behaved as insulting matrix which further influenced on the performance electronic devices.³² Further, in most cases, it was very difficult to rationalize the extent of π - π stacking and hydrogen bonding interaction in supramolecular structures. It has been now widely realized that retaining the aromatic π - π stacking among the building blocks without compromising on the molecular self-assembly is very much essential for the success of these materials in electronic devices. Alkyl chains assisted self-organization based on weak van der Waals forces is another important secondary interaction; however, it was not explored to its full potential. Therefore, synthesizing pure hydrocarbon materials, without any strongly H-bonding groups that can self-organize in LC domains is an important problem to be addressed. Amrutha et al. from our research group designed and developed a series of bulky/non-bulky, branched/linear alkyl chain substituted conjugated oligo-phenylenevinylenes.³³⁻³⁷ The preliminary investigation revealed that among a dozen of examined OPV structures, OPV molecule with rigid bis-TCD units in the central core and flexible dodecyl chains in the outer phenyl rings (BTCD-BDD-OPV) was found to show very unique ring banded morphology³³ in PLM images, which was the first of its kind in π -conjugated materials. However, the role of π - π stacking interactions in the aromatic core and the van der Waals interactions present in the alkyl tails in determining ring banded liquid crystallinity was not explored. Further, the exact molecular arrangement giving rise to this unique ring banded morphology was not found out. This provided us an opportunity to design OPV building blocks having identical aromatic cores with variable alkyl chains in the longitudinal positions.

In this chapter, the origin of molecular self-organization in the π -conjugated chromophores has been studied. For this purpose, a homologous series of OPVs with identical aromatic core but increasing number of carbon atoms in the longitudinal position was synthesized as shown in the figure 2.3.

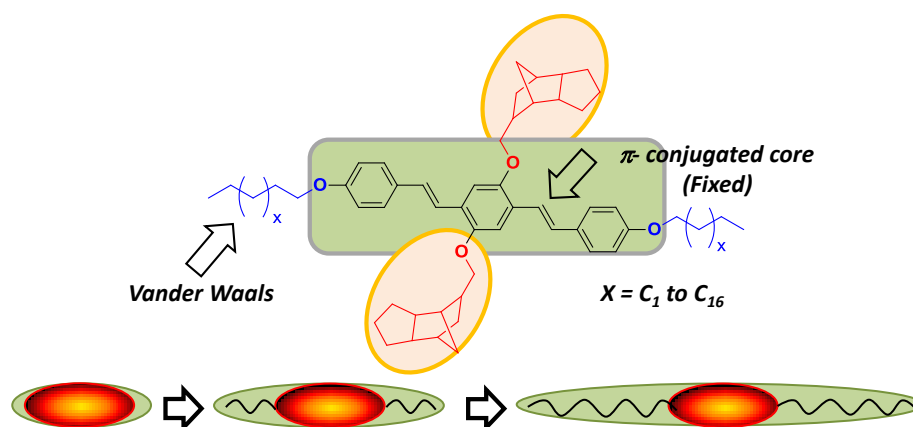


Figure 2.3. Diverse self- organization of OPVs in the solid state.

The structures of the OPV synthons were very carefully chosen with three important components: 1) a distyrylbenzene core as π -acceptor, 2) tricyclodecanemethylene (TCD) bulky units in the middle as C-H donors, and 3) alkyl tails of different lengths as self-assembly directors (see figure 2.3). OPVs molecules showed sigmoidal transition from crystalline solids ($n = 0-4$) to ring banded LC textures ($n = 10-15$) via fan shaped cholesteric textures ($n = 5-9$). Single-crystal X-ray structures of OPV molecules were resolved to trace the origin of sigmoidal self-assembly at the molecular level. The packing changed from herringbone (OPV- 4) to helical self-assembly (OPV-12), and, the presence of multiple CH/ π interactions (in OPV-12) was identified as the main driving force for helical suprastructures. Pitch and roll angles were determined to find out the existence of π - π stacking interactions. The large pitch and roll displacements completely destroyed the aromatic π -stacking interactions among this series of OPV chromophores. Circular dichroism studies on the OPVs revealed that the helical structures were produced only on aligning the chromophores in the LC mesophases. The uniqueness of the present approach is that both herringbone and helical assemblies could be simply varied by means of the number of carbon atoms in the tails. The overall findings revealed that the CH/ π interaction is a very powerful non-covalent interaction in supramolecular chemistry.

2.2. Experimental Methods

2.2.1. Materials: 1, 8-Tricyclodecanemethanol was donated by Celanese Chemicals and Co. and was used without further purification. p-Toulenesulphonylchloride, triethylamine, hydroquinone, triethylphosphite, potassium-t-butoxide (1M in THF), 4-hydroxybenzaldehyde, 1-bromobutane, 1-bromopentane, 1-bromohexane, 1-bromoheptane, 1-bromooctane, 1-bromononane, 1-bromodecane, 1-bromoundecane, 1-bromododecane, 1-bromotridecane, 1-bromotetradecane, 1-bromopentadecane, 1-bromohexadecane, benzaldehyde (**4**), 4-methoxybenzaldehyde (**4a**), 4-ethoxybenzaldehyde (**4b**), 4-propyloxybenzaldehyde (**4c**) were purchased from Aldrich Chemicals. HBr in glacial acetic acid, paraformaldehyde, KI, K₂CO₃ and NaOH were purchased locally. Solvents were purchased locally and purified by standard procedures.

2.2.2. General Procedures: ¹H and ¹³C NMR were recorded using 400 MHz JEOL NMR spectrometer. All NMR spectra were recorded in CDCl₃ containing TMS as internal standard. Infrared spectra were recorded using Bruker FT-IR (ATR mode) spectrophotometer in the range of 4000-600 cm⁻¹. The mass of all the OPVs was determined by using the Applied Biosystems 4800 PLUS MALDI TOF/TOF analyzer. The purity of all OPVs was checked by gel permeation chromatography (GPC), performed by Viscotek triple detector setup in tetrahydrofuran. TGA analysis was done using Perkin Elmer STA 6000 simultaneous thermal analyzer

Differential scanning calorimetry (DSC): Differential scanning calorimetry (DSC) measurements were performed on TA Q20 DSC. A pinch of powdered sample was placed in DSC aluminum pan and crimped. The data were recorded at a heating and cooling rate of 10 °C/min. The first heating cycle data were discarded since they possessed prehistory of the sample.

Polarized Light Microscope (PLM) Analysis: To study the temperature dependent LC textures of all the OPVs, LIECA DM2500 P polarized light microscope equipped with Linkam TMS 94 heating-freezing stage was used. A pinch of sample was placed on the glass substrate, heated to melt at 10 °C/min, and kept isothermally at 20 °C above their melting temperature for 2-3 minutes. The melt was subsequently cooled at 10 °C/min which leads to nucleation and further growth patterns and these images were continuously captured using camera.

Variable Temperature XRD Analysis: Wide angle X-ray diffraction patterns at different temperatures were recorded using Bruker D8 Advance diffractometer with a copper target. The system consisted of a rotating anode generator with a copper

target and a wide angle powder goniometer fitted with a high temperature attachment. Spectra were recorded using Cu K α radiation in the range of $2\theta = 3-50^\circ$ at a heating and cooling rate of 10 $^\circ\text{C}/\text{min}$.

Photophysical Characterization: Photophysical studies were performed in solution, LC frozen films and single crystalline samples. Absorption spectra were recorded using a Perkin Elmer Lambda 45 UV spectrophotometer. Steady state fluorescence emission and excitation spectra were recorded using a Fluorolog HORIBA JOBIN VYON fluorescence spectrophotometer. LC frozen samples were prepared by heating the samples to melt and then cooling to form thin films between two glass cover slips. For single crystalline samples, few single crystals were carefully sealed between two glass coverslips and used for studies. Fluorescence intensity decays were collected by time correlated single photon counting technique (TCSPC) setup from Horiba Jobin Yvon. Diode Laser (375 nm, IBH, UK, NanoLED-375L, with $\lambda_{\text{max}} = 375$ nm) having a FWHM of 102.3 ps was used as sample excitation source. The fluorescence signals were collected in magic angle using a MCP-PMT (Hamamatsu, Japan) detector and the fluorescence decays were collected at emission maxima for all the samples. The quality of fit was judged by fitting parameters such as $\chi^2 \approx 1$, as well as the visual inspection of the residuals.

SEM images were recorded using FEI, QUANTA 200 3D scanning electron microscope. For SEM analysis, the samples were prepared in hot stage (at 10 $^\circ/\text{min}$) under polarised light microscope on glass coverslips (to confirm the formation of textures), subjected to gold coating. CD spectra were recorded in solution, powder and LC frozen films using JASCO J-815 CD spectrophotometer under nitrogen atmosphere.

Single Crystal X-ray Analysis: Bruker APEX duo CCD-X ray diffractometer equipped with graphite monochromator Mo K α radiation ($\lambda=0.71073$ Å) was used for single crystal X-ray analysis of all the OPVs. Good quality crystals were grown in a mixture of DCM and methanol for OPV-4. Chloroform/methanol (2:1 v/v) was used for growing single crystals of OPV-12 (2:1 v/v) and OPV-8. Crystals were subjected to data collection at 100 K. The frames were integrated with Bruker APEX software package. The structures were solved by direct methods and refined with a full matrix least squares techniques using SHELX S v97 programs. The crystallographic parameters for OPV-4, OPV-8 and OPV-12 have been summarized in table 2.1. Crystal structures were visualized using Mercury 3.0 and Materials Studio software. The “pitch” and “roll” angles were measured using Mercury 3.0 program.

Table 2.1. Crystallographic data and refinement parameters for OPVs.

Compound	OPV-12	OPV-8	OPV-4
formula	C ₆₈ H ₉₈ O ₄	C ₆₀ H ₈₂ O ₄	C ₅₂ H ₆₆ O ₄
recrystn solv	DCM/MeOH	Chloroform/MeOH	DCM/MeOH
mol wt	979.50	867.29	755.05
Colour, habit	Yellow green, needle	Yellow green, needle	Yellow green, needle
temp(K)	100	100	100
system	Triclinic	Triclinic	Monoclinic
space group	P-1	P-1	P21/n
a, (Å)	6.508	6.05	6.2129
b, (Å)	8.692	13.2920	9.0972
c, (Å)	26.424	17.1809	37.164
α, (deg)	98.525	85.157	90
β, (deg)	92.656	81.495	93.108
γ, (deg)	99.134	83.001	90
V, Å ³	1451.07	1353.66	2097.42
d _{cacl} , g cm ⁻¹	1.121	1.064	1.19
μ(mm ⁻¹)	0.07	0.06	0.07
GOF	0.984	1.613	1.012
Z	1	1	2
no. of unique reflections	8972	5141	5490
Reflections collected	27196	21421	20608
θ range	1.34 to 24.04	1.34 to 24.04	1.34 to 24.04
No. of refined parameters	651	555	254
R ₁ (on F, I>2σ(I))	0.1317	0.1477	0.1481
wR ₂ (on F ² , all data)	0.4437	0.4398	0.3833

2.2.3. Synthesis

Synthesis of 1, 8-tricyclodecanemethylenetosylate (TCD-OTs): 1,8 Tricyclodecanemethanol (11.6, 0.07 mol) and p-toluenesulfonylchloride (13.3 g, 0.07 mol) were dissolved in DCM (100 ml). Triethylamine (24.4 ml, 0.18 mol) was slowly added to the above solution under ice cold conditions. The above solution was stirred at room temperature for 24 h. The product was extracted in DCM and dried over anhydrous sodium sulphate. It was purified by passing through silica gel

column using 2% ethyl acetate in hexane as eluent. Yield = (79 %). m. p. = 50-52 °C. ¹H-NMR (CDCl₃) δ: 7.81 ppm (d, 2H, Ar-H), 7.37 ppm (d, 2H, Ar-H), 3.84 ppm (m, 2H, -OCH₂), 2.45 -0.79 ppm (m, 18H, cyclic and aliphatic H). ¹³C-NMR (CDCl₃)δ: 144.4, 133.5, 129.7, 127.9 (Ar-C), 73.7(-OCH₂), 45.4, 44.9, 43.3, 41.1, 39.9, 34.1, 28.8, 27.5, 26.8, 26.3, 21.6 ppm (cyclic-C). FT-IR (KBr, cm⁻¹): 2925, 1600, 1508, 1458, 1366, 1229, 1178, 1101, 1027, 959, 831, 821 and 666. GC-MS (MW =320.4): 321.1 (M+1).

Synthesis of 1, 4-bis (1, 8-tricyclodecanemethyleneoxy) benzene (1a): Hydroquinone (4.4 g, 0.04 mol) and NaOH (3.2 g, 0.08 mol) were dissolved in a mixture of water (4.8 mL) and ethanol (40 mL). TCD- tosylate (26.8 g, 0.08 mol) was added and the reaction mixture was refluxed for 24 h. The reaction mixture was poured into large amount of water, extracted in DCM and dried over anhydrous sodium sulphate. It was further purified by passing through silica gel column using 0.5 % ethyl acetate in hexane as eluent. Yield = (45 %). m. p. = 125-126 °C. ¹H NMR (CDCl₃, 400MHz) δ: 6.7 ppm (s, 4H, Ar-H); 3.6 ppm (m, 4H, -OCH₂); 2.5-0.88 ppm (cyclic H, 30 H). ¹³C NMR (CDCl₃, 100 MHz): 153.2, 115.4 (Ar-C), 72.8 (Ar-OCH₂), 45.5, 45.2, 43.7, 41.2, 40.1, 34.5, 28.9, 28.0, 26.9, 26.4 (cyclic-C). FT-IR (KBr, cm⁻¹): 2946, 2866, 2357, 1643, 1508, 1466, 1390, 1282, 1283, 1109, 1028 and 824. GC-MS (MW = 406.60): 407.1 (M+1).

Synthesis of 1, 4-bis (bromomethyl)-2, 5-di-(1, 8-tricyclodecanemethyleneoxy) benzene (2a): 1,4-bis(1,8-tricyclodecanemethyleneoxy)benzene (3.0 g, 7.39 mmol) and *p*-HCHO (0.8 g, 29.30 mmol) were taken in 100 ml of glacial acetic acid and HBr in glacial acetic acid (5.5ml, 20.35mmol) was added using a pressure equalizing funnel. The reaction mixture was then refluxed for 8 h, cooled to room temperature and poured into large amount of water. The product precipitated as white solid, which was repeatedly washed with cold water to remove acidic impurities. The product was filtered and recrystallised from a hot saturated solution of acetone. Yield = (95 %). m. p. = 135-136 °C. ¹H NMR (CDCl₃, 400Hz) δ: 6.8 ppm (s, 2H, Ar-H), 4.5 ppm (s, 4H, -CH₂Br), 3.7 ppm (m, 4H, -OCH₂), 2.5-1 (m, 30H, cyclic H and aliphatic-H). ¹³C NMR δ: (CDCl₃, 100 MHz): 150.6, 127.5, 114.7 (Ar-C), 72.9 (Ar-OCH₂), 45.6, 45.2, 43.8, 41.3, 40.3, 34.6, 29.0, 28.7, 27.9, 27.0, 26.5 (cyclic-C). FT-IR (KBr, cm⁻¹): 2946, 2863, 1510, 1442, 1405, 1313, 1225, 1028 and 688. GC-MS (MW = 592.45): 593.12 (M+1).

Synthesis of 1, 4-bis (tricyclodecanemethyleneoxy)-2, 5-Xylenetetraethyldiphosphonate (3a): 1,4-bis(bromomethyl)-2,5-di-(1,8-tricyclodecanemethyleneoxy)benzene (2.9 g, 5.00 mmol) and triethyl phosphite (1.6

g, 10 mmol) were refluxed at 150 °C and excess triethyl phosphite was removed by applying high vacuum. The product separated as thick yellow oil. Yield = (90 %). ¹H-NMR (CDCl₃, 400 MHz) δ: 6.8 ppm (s, 2H, Ar-H), 3.9 ppm (m, 8H, -PO-OCH₂), 3.6 ppm (m, 4H, Ar-OCH₂), 3.2 ppm (m, 4H, Ar-CH₂P), 2.5-0.8 ppm (m, 42H, aliphatic). ¹³C-NMR (CDCl₃, 100 MHz): 150.3, 119.4, 115 (Ar-C), 72.9 (Ar-OCH₂), 61.9 (P-O-C), 45.6, 45.2, 43.8, 41.3, 40.3, 34.6, 29.0, 28.7, 27.9, 27.0, 26.5 ppm (cyclic-C and aliphatic carbon). FT-IR (cm⁻¹): 2944, 1515, 1472, 1395, 1247, 1219, 1032, 957, 900, 831, 646 and 533.4. GC-MS (MW = 706.83): 707.62 (M+1).

Synthesis of 4-alkoxybenzaldehydes (4a-4p): Benzaldehyde (**4**), 4-methoxybenzaldehyde (**4a**), 4-ethoxybenzaldehyde (**4b**), 4-propyloxybenzaldehyde (**4c**) were purchased from Aldrich Chemicals. The detailed synthesis has been described for 4-decyloxybenzaldehyde and other derivatives were synthesized using similar procedures.

Synthesis of 4-decyloxybenzaldehyde (4j): 4-Hydroxy benzaldehyde (3.6 g, 0.03 mol), anhydrous KI (4.9 g, 0.03 mol) and powdered anhydrous K₂CO₃ (8.3 g, 0.06 mol) were taken in dry acetone (50.0 mL) and refluxed for 2 h under nitrogen atmosphere. 1-Bromodecane (6.8 mL, 0.03 mol) was added drop wise to the above hot reaction mixture. The reaction mixture was further refluxed for 24 h under nitrogen atmosphere. The product was extracted in DCM and dried over anhydrous sodium sulphate. It was further purified by passing through silica gel column using ethyl acetate (2 % v/v) in hexane as eluent. Yield = (84 %). ¹H-NMR (CDCl₃, 400 MHz) δ: 9.85 ppm (s, 1H, Ar-CHO), 7.80 ppm (d, 2H, Ar-H), 6.97 ppm (d, 2H, Ar-H), 4.01 ppm (t, 2H, Ar-OCH₂); 1.79 ppm (m, 2H, Ar-OCH₂CH₂), 1.44 ppm (m, 2H, Ar-OCH₂CH₂CH₂), 1.31-1.25 ppm (12H, aliphatic-H) and 0.86 ppm (t, 3H, -CH₃). ¹³C-NMR (CDCl₃, 100 MHz) δ: 190.8 (-CHO), 164.21, 131.9, 129.63, 114.7 (Ar-C), 68.4 (-OCH₂), 31.84, 29.5, 29.3, 28.9, 25.9, 22.6 and 14.1 (aliphatic). FT-IR (KBr, cm⁻¹): 2924, 2854, 2731, 1694, 1601, 1577, 1509, 1467, 1428, 1393, 1311, 1258, 1215, 1159, 1109, 1016, 832, 721 and 651. GC-MS (MW = 262.19): 262.70 (M+1).

Synthesis of 4-butoxybenzaldehyde (4d): ¹H-NMR (CDCl₃, 400 MHz) δ: 9.87 ppm (s, 1H, Ar-CHO), 7.83 ppm (d, 2H, Ar-H), 6.98 ppm (d, 2H, Ar-H), 4.04 ppm (t, 2H, Ar-OCH₂), 1.80 ppm (m, 2H, Ar-OCH₂CH₂), 1.51 ppm (m, 2H, Ar-OCH₂CH₂CH₂), and 0.98 ppm (t, 3H, -CH₃). ¹³C-NMR (CDCl₃, 100 MHz) δ: 190.8 (-CHO), 164.2, 131.9, 129.7, 114.7 (Ar-C), 68.1 (-OCH₂), 31.0, 19.1 and 13.8 (aliphatic). FT-IR (KBr, cm⁻¹): 2931, 2850, 1421, 1311, 1258, 1215, 1100, 1016, 856, 832, 721 and 651. GC-MS (MW = 178.23): 179.90 (M+1).

Synthesis of 4-(pentyloxy)benzaldehyde (4e): $^1\text{H-NMR}$ (CDCl_3 , 400 MHz) δ : 9.83 ppm (s, 1H, Ar-CHO), 7.79 ppm (d, 2H, Ar-H), 6.95 ppm (d, 2H, Ar-H), 3.99 ppm (t, 2H, Ar-OCH₂), 1.78 ppm (m, 2H, Ar-OCH₂CH₂), 1.51 ppm (m, 4H, aliphatic), and 0.90 ppm (t, 3H, -CH₃). $^{13}\text{C-NMR}$ (CDCl_3 , 100 MHz) δ : 190.7 (-CHO), 164.2, 131.9, 129.6, 114.6 (Ar-C), 68.3 (-OCH₂), 28.6, 28.0, 22.3 and 13.9 (aliphatic). FT-IR (KBr, cm^{-1}): 2930, 2850, 1422, 1393, 1311, 1258, 1215, 1100, 1016, 856, 832, 721 and 651. GC-MS (MW = 192.25): 193.05 (M+1).

Synthesis of 4-(hexyloxy)benzaldehyde (4f): $^1\text{H-NMR}$ (CDCl_3 , 400 MHz) δ : 9.87 ppm (s, 1H, Ar-CHO), 7.82 ppm (d, 2H, Ar-H), 6.97 ppm (d, 2H, Ar-H), 4.03 ppm (t, 2H, Ar-OCH₂), 1.81 ppm (m, 2H, Ar-OCH₂CH₂), 1.36-1.31 ppm (m, 6H, aliphatic), and 0.91 ppm (t, 3H, -CH₃). $^{13}\text{C-NMR}$ (CDCl_3 , 100 MHz) δ : 190.8 (-CHO), 164.2, 131.9, 129.6, 114.8, and 114.6 (Ar-C), 68.5 (-OCH₂), 31.4, 30.1, 25.5, 22.4 and 13.9 (aliphatic). FT-IR (KBr, cm^{-1}): 2932, 2852, 2730, 1422, 1393, 1258, 1215, 1100, 1016, 856, 832, 721 and 650. GC-MS (MW = 206.28): 207.01 (M+1).

Synthesis of 4-(heptyloxy)benzaldehyde (4g): $^1\text{H-NMR}$ (CDCl_3 , 400 MHz) δ : 9.87 ppm (s, 1H, Ar-CHO), 7.82 ppm (d, 2H, Ar-H), 6.97 ppm (d, 2H, Ar-H), 4.03 ppm (t, 2H, Ar-OCH₂), 1.80 ppm (m, 2H, Ar-OCH₂CH₂), 1.48-1.42 ppm (m, 8H, aliphatic) and 0.86 ppm (t, 3H, -CH₃). $^{13}\text{C-NMR}$ (CDCl_3 , 100 MHz) δ : 190.7 (-CHO), 164.2, 131.9, 129.6, 114.6 (Ar-C), 68.3 (-OCH₂), 31.7, 28.9, 28.9, 25.8 and 14.0 (aliphatic). FT-IR (KBr, cm^{-1}): 2932, 2853, 2731, 1423, 1393, 1311, 1258, 1215, 1159, 1100, 1016, 856, 721 and 651. GC-MS (MW = 220.31): 221.11 (M+1).

Synthesis of 4-(octyloxy)benzaldehyde (4h): $^1\text{H-NMR}$ (CDCl_3 , 400 MHz) δ : 9.87 ppm (s, 1H, Ar-CHO), 7.82 ppm (d, 2H, Ar-H), 6.99 ppm (d, 2H, Ar-H), 4.03 ppm (t, 2H, Ar-OCH₂), 1.79 ppm (m, 2H, Ar-OCH₂CH₂), 1.30-1.36 ppm (m, 10H, aliphatic) and 0.86 ppm (t, 3H, -CH₃). $^{13}\text{C-NMR}$ (CDCl_3 , 100 MHz) δ : 190.8 (-CHO), 164.2, 131.9, 129.7, and 114.6 (Ar-C), 68.4 (-OCH₂), 31.7, 31.5, 29.1, 29.0, and 25.9 and 14.0 (aliphatic). FT-IR (KBr, cm^{-1}): 2930, 2855, 2733, 1572, 1423, 1393, 1016, 856, 832, 721 and 651. GC-MS (MW = 234.33): 235.10 (M+1).

Synthesis of 4-(nonyloxy)benzaldehyde (4i): $^1\text{H-NMR}$ (CDCl_3 , 400 MHz) δ : 9.87 ppm (s, 1H, Ar-CHO), 7.82 ppm (d, 2H, Ar-H), 6.99 ppm (d, 2H, Ar-H), 4.03 ppm (t, 2H, Ar-OCH₂), 1.81 ppm (m, 2H, Ar-OCH₂CH₂), 1.28-1.48 ppm (m, 12H, aliphatic) and 0.88 ppm (t, 3H, -CH₃). $^{13}\text{C-NMR}$ (CDCl_3 , 100 MHz) δ : 190.8 (-CHO), 164.2, 131.9, 129.6, and 114.6 (Ar-C), 68.4 (-OCH₂), 31.8, 31.5, 29.4, 29.3, 29.2, 29.0, 25.9 and 14.0 (aliphatic). FT-IR (KBr, cm^{-1}): 2930, 2850, 2731, 1600, 1573, 1428, 1393, 1311, 1258, 1215, 1159, 1100, 1016, 856, 832, 721 and 651. GC-MS (MW = 248.36): 249.19 (M+1).

Synthesis of 4-(undecyloxy)benzaldehyde (4k): $^1\text{H-NMR}$ (CDCl_3 , 400 MHz) δ : 9.87 ppm (s, 1H, Ar-CHO), 7.82 ppm (d, 2H, Ar-H), 6.99 ppm (d, 2H, Ar-H); 4.03 ppm (t, 2H, Ar-OCH₂), 1.81 ppm (m, 2H, Ar-OCH₂CH₂), 1.26-1.48 ppm (m, 16H, aliphatic) and 0.88 ppm (t, 3H, -CH₃). $^{13}\text{C-NMR}$ (CDCl_3 , 100 MHz) δ : 190.8 (-CHO), 164.2, 131.9, 129.6, and 114.7 (Ar-C), 68.4 (-OCH₂), 31.8, 29.5, 29.4, 29.3, 29.2, 29.0, 25.9, 22.6 and 14.0 (aliphatic). FT-IR (KBr, cm^{-1}): 2921, 2849, 2731, 1600, 1573, 1509, 1463, 1428, 1393, 1311, 1258, 1215, 1159, 1100, 1016, 856, 832, 721 and 652. GC-MS (MW = 276.41): 277.20 (M+1).

Synthesis of 4-(dodecyloxy)benzaldehyde (4l): $^1\text{H-NMR}$ (CDCl_3 , 400 MHz) δ : 9.85 ppm (s, 1H, Ar-CHO), 7.81 ppm (d, 2H, Ar-H), 6.95 ppm (d, 2H, Ar-H); 4.01 ppm (t, 2H, Ar-OCH₂), 1.79 ppm (m, 2H, Ar-OCH₂CH₂), 1.24-1.48 ppm (m, 18H, aliphatic) and 0.88 ppm (t, 3H, -CH₃). $^{13}\text{C-NMR}$ (CDCl_3 , 100 MHz) δ : 190.8 (-CHO), 164.2, 131.9, 129.6, and 114.7 (Ar-C), 68.3 (-OCH₂), 33.5, 31.8, 30.4, 29.4, 29.3, 29.2, 29.0, 25.9, 22.6 and 14.1 (aliphatic). FT-IR (KBr, cm^{-1}): 2922, 2849, 2731, 1694, 1600, 1573, 1509, 1467, 1428, 1393, 1311, 1258, 1215, 1159, 1100, 1016, 856, 832, 721 and 650. GC-MS (MW = 290.44): 291.30 (M+1).

Synthesis of 4-tridecyloxybenzaldehyde (4m): $^1\text{H-NMR}$ (CDCl_3 , 400 MHz) δ : 9.86 ppm (s, 1H, Ar-CHO), 7.81 ppm (d, 2H, Ar-H), 6.97 ppm (d, 2H, Ar-H), 4.02 ppm (t, 2H, Ar-OCH₂), 1.79 ppm (m, 2H, Ar-OCH₂CH₂), 1.44 ppm (m, 2H, Ar-OCH₂CH₂CH₂), 1.31-1.25 ppm (18H, aliphatic) and 0.86 ppm (t, 3H, -CH₃). $^{13}\text{C-NMR}$ (CDCl_3 , 100 MHz) δ : 190.8 (-CHO), 164.2, 131.9, 129.6, 114.7 (Ar-C), 68.4 (-OCH₂), 31.8, 29.5, 29.3, 28.9, 25.9, 22.6 and 14.1 (aliphatic). FT-IR (KBr, cm^{-1}): 2924, 2854, 2731, 1694, 1601, 1577, 1509, 1467, 1428, 1393, 1311, 1258, 1215, 1159, 1109, 1016, 856, 832, 721 and 651. GC-MS (MW = 304.47): 305.15 (M+1).

Synthesis of 4-(tetradecyloxy)benzaldehyde (4n): $^1\text{H-NMR}$ (CDCl_3 , 400 MHz) δ : 9.86 ppm (s, 1H, Ar-CHO); 7.81 ppm (d, 2H, Ar-H); 6.97 ppm (d, 2H, Ar-H); 4.02 ppm (t, 2H, Ar-OCH₂); 1.79 ppm (m, 2H, Ar-OCH₂CH₂); 1.43 ppm (m, 2H, Ar-OCH₂CH₂CH₂); 1.31-1.25 ppm (20H, aliphatic) and 0.86 ppm (t, 3H, -CH₃). $^{13}\text{C-NMR}$ (CDCl_3 , 100 MHz) δ : 190.9 (-CHO), 164.3, 132.1, 129.8, 114.8 (Ar-C), 68.5 (-OCH₂), 32.01, 29.1, 26.0, 22.7 and 14.2 (aliphatic). FT-IR (KBr, cm^{-1}): 2930, 2857, 2731, 1690, 1601, 1560, 1507, 1460, 1428, 1393, 1311, 1258, 1217, 1158, 1109, 1012, 856, 831, 717 and 649. GC-MS (MW = 318.49): 319.15 (M+1).

Synthesis of 4-(pentadecyloxy)benzaldehyde (4o): $^1\text{H-NMR}$ (CDCl_3 , 400 MHz) δ : 9.86 ppm (s, 1H, Ar-CHO); 7.81 ppm (d, 2H, Ar-H); 6.97 ppm (d, 2H, Ar-H); 4.02 ppm (t, 2H, Ar-OCH₂); 1.79 ppm (m, 2H, Ar-OCH₂CH₂); 1.43 ppm (m, 2H, Ar-

OCH₂CH₂ CH₂); 1.31-1.25 ppm (22H, aliphatic H) and 0.86 ppm (t, 3H, -CH₃). ¹³C-NMR (CDCl₃, 100 MHz) δ: 190.9 (-CHO), 164.3, 132.0, 129.8, 114.8 (Ar-C), 68.5 (-OCH₂), 32.0, 29.8, 29.4, 29.1, 26.04, 22.8 and 14.2 (aliphatic). FT-IR (KBr, cm⁻¹): 2940, 2850, 2734, 1697, 1608, 1560, 1507, 1460, 1428, 1393, 1312, 1258, 1217, 1158, 1109, 1012, 856, 831, 721 and 660. GC-MS (MW = 332.52): 333.16 (M+1).

Synthesis of 4-(hexadecyloxy)benzaldehyde (4p): ¹H-NMR (CDCl₃, 400 MHz) δ: 9.86 ppm (s, 1H, Ar-CHO), 7.81 ppm (d, 2H, Ar-H), 6.97 ppm (d, 2H, Ar-H), 4.02 ppm (t, 2H, Ar-OCH₂), 1.79 ppm (m, 2H, Ar-OCH₂CH₂), 1.43 ppm (m, 2H, Ar-OCH₂CH₂ CH₂), 1.31-1.25 ppm (24H, aliphatic) and 0.86 ppm (t, 3H, -CH₃). ¹³C-NMR (CDCl₃, 100 MHz) δ: 190.8 (-CHO), 164.3, 132.0, 129.8, 114.8 (Ar-C), 68.5 (-OCH₂), 33.6, 32.0, 29.8, 29.4, 29.1, 26.03, 22.8 and 14.2 (aliphatic). FT-IR (KBr, cm⁻¹): 2923, 2854, 2790, 2733, 1689, 1601, 1577, 1509, 1467, 1428, 1258, 1215, 1157, 1109, 1016, 856, 830, 721 and 651. GC-MS (MW = 346.29): 346.91 (M+1).

Synthesis of oligo-phenylenevinylenes (OPV) s:

Synthesis of OPV-0: Compound **3a** and benzaldehyde (0.4 g, 3.9 mmol) were taken in dry THF (30 mL) and kept under ice cold condition. Potassium tert- butoxide (9.6 mL, 1M THF solution) was added dropwise to the reaction mixture under nitrogen atmosphere. It was stirred at 30 °C for 24 h. The resultant yellow solution was concentrated and poured into large amount of methanol. The yellow green precipitate was filtered, washed with large amount of methanol until the filtrate become colorless. It was purified by passing through silica gel column using 1 % ethyl acetate in hexane as eluent. Yield = (78 %). ¹H-NMR (CDCl₃, 400MHz) δ: 7.53-6.97 ppm (m, 16H, Ar-H and vinylic H), 3.80-3.67 ppm (m, 4H, Ar-OCH₂), 2.41-0.98 ppm (m, 30H, cyclic-H). ¹³C-NMR (CDCl₃, 100 MHz) δ: 151.3, 138.1, 129.1, 128.7, 127.7, 126.8, 126.5, 123.8, 111.3 (Ar-C), 73.7 (Ar-OCH₂-TCD) 45.7, 45.3, 44.1, 41.4, 34.8, 32.0, 29.7, 29.5, 29.4, 29.1, 28.1 and 26.6 ppm. FT-IR (KBr, cm⁻¹): 2930, 2862, 1493, 1420, 1258, 1188, 1095, 804 and 688. MALDI-TOF-TOF-MS (MW=610.349): m/z = 610.380.

Synthesis of OPV-1: Compound **3a** (0.47 g, 66.0 mmol) and **4a** (0.18 g, 132 mmol) were reacted as described for OPV-0. The product was purified by passing through silica gel column using 1 % ethyl acetate in hexane as eluent. Yield = (67 %). ¹H-NMR (CDCl₃, 400MHz) δ: 7.46 ppm (d, 4H, Ar-H), 7.27 ppm (d, 2H, CH=CH), 7.14 ppm (d, 2H, CH=CH), 7.05 ppm (s, 2H, Ar-H), 6.90 ppm (d, 4H, Ar-H), 3.99 ppm (s, 6H, Ar-OCH₃), 3.82-3.75 ppm (m, 4H, Ar-OCH₂-TCD), 2.50-0.88 ppm (m, 30H,

cyclic-H). $^{13}\text{C-NMR}(\text{CDCl}_3, 100 \text{ MHz}) \delta$: 159.1, 151.1, 130.8, 128.3, 127.7, 126.6, 121.6, 114.1, 111.0 (Ar-C), 73.6 (Ar-OCH₃), 55.3(Ar-OCH₂-TCD) 45.6, 45.2, 43.9, 41.2, 34.7, 29.1, 27.9, 27.0 and 26.5 ppm. FT-IR (KBr, cm⁻¹): 2924, 2862, 1605, 1510, 1493, 1420, 1188, 1095, 971, 849, and 816. MALDI-TOF-TOF-MS (MW=670.92): m/z = 670.380.

Synthesis of OPV-2: Compound **3a** (0.47 g, 66.0 mmol) and **4b** (0.20 g, 132 mmol) were reacted as described for OPV-0. The product was purified by passing through silica gel column using 1 % ethyl acetate in hexane as eluent. Yield = (62 %). $^1\text{H-NMR}(\text{CDCl}_3, 400\text{MHz}) \delta$: 7.45 ppm (d, 4H, Ar-H), 7.29 ppm (d, 2H, CH=CH), 7.13 ppm (d, 2H, CH=CH), 7.05 ppm (s, 2H, Ar-H), 6.89 ppm (d, 4H, Ar-H), 4.06 ppm (t, 4H, Ar-OCH₂-alkyl), 3.82-3.75 ppm (m, 4H, Ar-OCH₂-TCD), 2.5-0.88 ppm (m, 36H, cyclic-H and aliphatic-H). $^{13}\text{C-NMR}(\text{CDCl}_3, 100 \text{ MHz}) \delta$: 158.5, 151.2, 130.8, 128.5, 127.7, 126.8, 121.7, 114.8, 111.1 (Ar-C), 73.7 (Ar-OCH₂-alkyl), 68.2 (Ar-OCH₂-TCD) 45.8, 45.3, 44.1, 41.4, 34.8, 29.2, 28.1, 27.1, 26.6, and 14.9 ppm. FT-IR (KBr, cm⁻¹): 2994, 2867, 1604, 1510, 1493, 1420, 1188, 1095, 971, 849, and 816. MALDI-TOF-TOF-MS (MW=698.97): m/z = 698.400.

Synthesis of OPV-3: Compound **3a** (0.47 g, 66.0 mmol) and **4c** (0.22 g, 132 mmol) were reacted as described for OPV-0. The product was purified by passing through silica gel column using 1 % ethyl acetate in hexane as eluent. Yield = (67%). $^1\text{H-NMR}(\text{CDCl}_3, 400\text{MHz}) \delta$: 7.44 ppm (d, 4H, Ar-H), 7.27 ppm (d, 2H, CH=CH), 7.13 ppm (d, 2H, CH=CH), 7.04 ppm (s, 2H, Ar-H), 6.88 ppm (d, 4H, Ar-H), 3.94 ppm (t, 4H, Ar-OCH₂-alkyl), 3.81-3.74 ppm (m, 4H, Ar-OCH₂-TCD), 2.5-0.88 ppm (m, 40H, cyclic-H and aliphatic-H). $^{13}\text{C-NMR}(\text{CDCl}_3, 100 \text{ MHz}) \delta$: 158.7, 151.2, 130.8, 128.5, 127.7, 126.8, 121.6, 114.8, 111.1 (Ar-C), 73.7 (Ar-OCH₂-alkyl), 68.6 (Ar-OCH₂-TCD) 45.8, 45.3, 44.1, 40.4, 34.8, 29.1, 28.1, 27.1, 26.6, 22.7 and 10.6. FT-IR (KBr, cm⁻¹): 2924, 2862, 1605, 1510, 1493, 1420, 1188, 1095, 971, 849 and 816. MALDI-TOF-TOF-MS (MW=727.02): m/z = 726.490.

Synthesis of OPV-4: Compound **3a** (0.47 g, 66.0 mmol) and **4d** (0.24 g, 132 mmol) were reacted as described for OPV-0. The product was purified by passing through silica gel column using 1 % ethyl acetate in hexane as eluent. Yield = (60 %). $^1\text{H-NMR}(\text{CDCl}_3, 400\text{MHz}) \delta$: 7.45 ppm (d, 4H, Ar-H), 7.29 ppm (d, 2H, CH=CH), 7.14 ppm (d, 2H, CH=CH), 7.05 ppm (s, 2H, Ar-H), 6.89 ppm (d, 4H, Ar-H), 3.99 ppm (t, 4H, Ar-OCH₂-alkyl), 3.82-3.75 ppm (m, 4H, Ar-OCH₂-TCD), 2.5-0.88 ppm (m, 44H, cyclic-H and aliphatic-H). $^{13}\text{C-NMR}(\text{CDCl}_3, 100 \text{ MHz}) \delta$: 158.6, 151.0, 130.8, 128.5, 127.7, 126.7, 121.4, 114.6, 110.9 (Ar-C), 73.6 (Ar-OCH₂-alkyl), 68.2 (Ar-OCH₂-TCD), 45.8, 45.4, 44.1, 34.8, 32.0, 29.7, 29.5, 29.4, 29.2, 28.1, 26.6, 26.1,

22.4 and 14.1 ppm. FT-IR (KBr, cm^{-1}): 2944, 2867, 1604, 1510, 1493, 1420, 1188, 1095, 971, 849, and 816. MALDI-TOF-TOF-MS (MW = 755.08): $m/z = 754.470$.

Synthesis of OPV-5: Compound **3a** (0.47 g, 66.0 mmol) and **4e** (0.25 g, 132 mmol) were reacted as described for OPV-0. The product was purified by passing through silica gel column using 1 % ethyl acetate in hexane as eluent. Yield = (67 %). $^1\text{H-NMR}$ (CDCl_3 , 400MHz) δ : 7.37 ppm (d, 4H, Ar-H), 7.22 ppm (d, 2H, CH=CH), 7.07 ppm (d, 2H, CH=CH), 6.98 ppm (s, 2H, Ar-H), 6.82 ppm (d, 4H, Ar-H), 3.90 ppm (t, 4H, Ar-OCH₂-alkyl), 3.68-3.75 ppm (m, 4H, Ar-OCH₂-TCD), 2.5-0.88 ppm (m, 48H, cyclic-H and aliphatic-H). $^{13}\text{C-NMR}$ (CDCl_3 , 100 MHz) δ : 158.6, 151.0, 130.8, 128.3, 127.5, 126.6, 121.4, 114.6, 110.9 (Ar-C), 73.6 (Ar-OCH₂-alkyl), 67.7 (Ar-OCH₂-TCD) 45.6, 45.2, 43.9, 41.3, 40.3, 34.7, 32.0, 29.7, 29.1, 27.9, 27.1, 26.5, 19.2 and 13.8 ppm. FT-IR (KBr, cm^{-1}): 2935, 2863, 2363, 1605, 1510, 1467, 1384, 1245, 1174, 1021, 971, 847 and 809. MALDI-TOF-TOF-MS (MW= 783.13): $m/z = 782.520$.

Synthesis of OPV-6: Compound **3a** (0.47 g, 66.0 mmol) and **4f** (0.27 g, 132 mmol) were reacted as described for OPV-0. The product was purified by passing through silica gel column using 1 % ethyl acetate in hexane as eluent. Yield = (63 %). $^1\text{H-NMR}$ (CDCl_3 , 400MHz) δ : 7.45 ppm (d, 4H, Ar-H), 7.28 ppm (d, 2H, CH=CH), 7.14 ppm (d, 2H, CH=CH), 7.05 ppm (s, 2H, Ar-H), 6.89 ppm (d, 4H, Ar-H), 3.98 ppm (t, 4H, Ar-OCH₂-alkyl), 3.82-3.75 ppm (m, 4H, Ar-OCH₂-TCD), 2.5-0.88 ppm (m, 52H, cyclic-H and aliphatic-H). $^{13}\text{C-NMR}$ (CDCl_3 , 100MHz) δ : 158.6, 151.0, 130.8, 128.4, 127.6, 126.6, 121.4, 114.6, 110.9 (Ar-C), 73.6 (Ar-OCH₂-alkyl), 68.2 (Ar-OCH₂-TCD) 45.6, 45.3, 43.9, 41.3, 34.8, 31.6, 29.2, 29.1, 27.9, 27.1, 26.5, 25.7, 22.6 and 14.1 ppm. FT-IR (KBr, cm^{-1}): 2943, 2864, 2363, 1604, 1511, 1467, 1384, 1246, 1174, 1026, 971, 847 and 809. MALDI-TOF-TOF-MS (MW=811.18): $m/z = 810.550$.

Synthesis of OPV-7: Compound **3a** (0.47 g, 66.0 mmol) and **4g** (0.29 g, 132 mmol) were reacted as described for OPV-0. Yield = (66%). $^1\text{H-NMR}$ (CDCl_3 , 400MHz) δ : 7.45 ppm (d, 4H, Ar-H), 7.29 ppm (d, 2H, CH=CH), 7.13 ppm (d, 2H, CH=CH), 7.05 ppm (s, 2H, Ar-H), 6.89 ppm (d, 4H, Ar-H), 3.98 ppm (t, 4H, Ar-OCH₂-alkyl), 3.82-3.75 ppm (m, 4H, Ar-OCH₂-TCD), 2.5-0.88 ppm (m, 56H, cyclic-H and aliphatic-H). $^{13}\text{C-NMR}$ (CDCl_3 , 100 MHz) δ : 158.6, 151.0, 130.6, 128.3, 127.5, 126.6, 121.4, 114.6, 110.9 (Ar-C), 73.6 (Ar-OCH₂-alkyl), 68.2 (Ar-OCH₂-TCD), 45.6, 45.2, 43.9, 34.2, 31.6, 29.2, 29.5, 27.8, 27.1, 26.5, 25.7, 22.6 and 14.1 ppm. FT-IR (KBr, cm^{-1}): 2930, 2859, 2363, 1604, 1510, 1467, 1384, 1244, 1174, 1026, 971, 847, and 809. MALDI-TOF-TOF-MS (MW=839.24): $m/z = 838.578$.

Synthesis of OPV-8: Compound **3a** (0.47 g, 66.0 mmol) and **4h** (0.31 g, 132 mmol) were reacted as described for OPV-0. Yield = (58 %). ¹H-NMR (CDCl₃, 400MHz) δ : 7.45 ppm (d, 4H, Ar-H), 7.26 ppm (d, 2H, CH=CH), 7.13 ppm (d, 2H, CH=CH), 7.05 ppm (s, 2H, Ar-H), 6.89 ppm (d, 4H, Ar-H), 3.97 ppm (t, 4H, Ar-OCH₂-alkyl), 3.82-3.75 ppm (m, 4H, Ar-OCH₂-TCD), 2.5-0.88 ppm (m, 60H, cyclic-H and aliphatic-H). ¹³C-NMR (CDCl₃, 100 MHz) δ : 158.6, 151.0, 130.8, 128.4, 127.6, 126.6, 121.4, 114.6, 110.9 (Ar-C), 73.6 (Ar-OCH₂-alkyl), 68.2 (Ar-OCH₂-TCD), 45.6, 45.2, 43.9, 41.3, 31.8, 29.3, 29.2, 29.1, 27.9, 27.1, 26.3, 22.6 and 14.1 ppm. FT-IR (KBr, cm⁻¹): 2926, 2857, 2360, 1604, 1510, 1467, 1422, 1384, 1246, 1174, 1026, 971, 847 and 809. MALDI-TOF-TOF-MS (MW=867.29): m/z = 866.640.

Synthesis of OPV-9: Compound **3a** (0.47 g, 66.0 mmol) and **4i** (0.33 g, 132 mmol) were reacted as described for OPV-0. Yield = (77 %). ¹H-NMR (CDCl₃, 400MHz) δ : 7.44 ppm (d, 4H, Ar-H), 7.30 ppm (d, 2H, CH=CH), 7.14 ppm (d, 2H, CH=CH), 7.05 ppm (s, 2H, Ar-H), 6.88 ppm (d, 4H, Ar-H), 3.97 ppm (t, 4H, Ar-OCH₂-alkyl), 3.82-3.75 ppm (m, 4H, Ar-OCH₂-TCD), 2.5-0.88 ppm (m, 64H, cyclic-H and aliphatic-H). ¹³C-NMR(CDCl₃, 100 MHz) δ : 158.6, 151.0, 130.8, 128.4, 127.6, 126.6, 121.4, 114.6, 110.9 (Ar-C), 73.6 (Ar-OCH₂-alkyl), 68.2 (Ar-OCH₂-TCD), 45.7, 44.1, 41.4, 34.9, 31.9, 29.7, 29.5, 29.3, 29.1, 26.6, 26.1, 22.8 and 14.2 ppm. FT-IR (KBr, cm⁻¹): 2925, 2856, 2363, 1604, 1510, 1467, 1384, 1245, 1174, 1026, 971, 847, and 809. MALDI-TOF-TOF-MS (MW=895.34): m/z = 894.630.

Synthesis of OPV-10: Compound **3a** (0.47 g, 66.0 mmol) and **4j** (0.35 g, 132 mmol) were reacted as described for OPV-0. Yield = (36 %). ¹H-NMR (CDCl₃, 400MHz) δ : 7.45 ppm (d, 4H, Ar-H), 7.30 ppm (d, 2H, CH=CH), 7.11 ppm (d, 2H, CH=CH), 7.05 ppm (s, 2H, Ar-H), 6.89 ppm (d, 4H, Ar-H), 3.99 ppm (t, 4H, Ar-OCH₂-alkyl), 3.82-3.75 ppm (m, 4H, Ar-OCH₂-TCD), 2.5-0.88 ppm (m, 68H, cyclic-H and aliphatic-H). ¹³C-NMR(CDCl₃, 100 MHz) δ : 158.8, 151.2, 130.8, 128.5, 127.7, 126.8, 121.6, 114.8, 111.1 (Ar-C), 73.7 (Ar-OCH₂-D), 68.2 (Ar-OCH₂-TCD) 45.8, 45.4, 44.1, 34.8, 32, 29.7, 29.5, 29.4, 29.17, 28.1, 26.6, 26.1, 22.8, and 14.2. FT-IR (KBr, cm⁻¹): 2924, 2855, 1605, 1510, 1469, 1245, 1178, 1018, 971, 849 and 816 ppm. MALDI-TOF-TOF-MS (MW=923.40): m/z = 922.677.

Synthesis of OPV-11: Compound **3a** (0.47 g, 66.0 mmol) and **4k** (0.36 g, 132 mmol) were reacted as described for OPV-0. Yield = (69 %). ¹H-NMR (CDCl₃, 400MHz) δ : 7.45 ppm (d, 4H, Ar-H), 7.30 ppm (d, 2H, CH=CH), 7.14 ppm (d, 2H, CH=CH), 7.05 ppm (s, 2H, Ar-H), 6.89 ppm (d, 4H, Ar-H), 3.98 ppm (t, 4H, Ar-OCH₂-alkyl), 3.82-3.75 ppm (m, 4H, Ar-OCH₂-TCD), 2.5-0.88 ppm (m, 72H, cyclic-H and

aliphatic-H). $^{13}\text{C-NMR}(\text{CDCl}_3, 100 \text{ MHz}) \delta$: 158.8, 151.0, 130.8, 128.4, 127.6, 126.6, 121.4, 114.6, 110.9 (Ar-C), 73.6 (Ar-OCH₂-alkyl), 68.2 (Ar-OCH₂-TCD), 45.7, 45.3, 34.9, 32.0, 29.7, 29.5, 29.4, 29.1, 28.1, 27.1, 26.1, 22.8 and 14.2. FT-IR (KBr, cm⁻¹): 2922, 2853, 2360, 1605, 1510, 1468, 1384, 1246, 1174, 1026, 971, 847 and 808. MALDI-TOF-TOF-MS (MW=951.45): $m/z = 950.708$.

Synthesis of OPV-12: Compound **3a** (0.53 g, 75.0 mmol) and **4l** (0.55 g, 190 mmol) were reacted as described for OPV-0. Yield = (90 %). $^1\text{H-NMR}(\text{CDCl}_3, 400\text{MHz}) \delta$: 7.45 ppm (d, 4H, Ar-H), 7.22 ppm (d, 2H, CH=CH), 7.14 ppm (d, 2H, CH=CH), 7.05 ppm (s, 2H, Ar-H), 6.89 ppm (d, 4H, Ar-H), 3.97 ppm (t, 4H, Ar-OCH₂-alkyl), 3.82-3.75 ppm (m, 4H, Ar-OCH₂-TCD), 2.5-0.88 ppm (m, 76H, cyclic-H and aliphatic-H). $^{13}\text{C-NMR}(\text{CDCl}_3, 100 \text{ MHz}) \delta$: 158.6, 151.0, 128.5, 127.8, 121.6, 114.6, 110.9 (Ar-C), 73.7 (Ar-OCH₂-alkyl), 68.1 (Ar-OCH₂-TCD), 45.7, 45.7, 45.3, 44.0, 41.4, 32.0, 29.9, 29.7, 29.5, 29.4, 29.1, 14.2 and 14.1. FT-IR (KBr, cm⁻¹): 2921, 2853, 2363, 1604, 1510, 1467, 1384, 1244, 1174, 1026, 971, 847 and 809. MALDI-TOF-TOF-MS (MW=979.5): $m/z = 978.717$.

Synthesis of OPV-13: Compound **3a** (0.35 g, 0.50 mmol) and **4m** (0.33 g, 1.10 mmol) were reacted as described for OPV-0. The product was purified by recrystallizing from hot saturated solution of acetone. Yield = (59 %). $^1\text{H-NMR}(\text{CDCl}_3, 400\text{MHz}) \delta$: 7.45 ppm (d, 4H, Ar-H), 7.30 ppm (d, 2H, CH=CH), 7.11 ppm (d, 2H, CH=CH), 7.05 ppm (s, 2H, Ar-H), 6.89 ppm (d, 4H, Ar-H), 3.97 ppm (t, 4H, Ar-OCH₂-alkyl), 3.82-3.75 ppm (m, 4H, Ar-OCH₂-TCD), 2.5-0.88 (m, 80H, cyclic-H and aliphatic-H). $^{13}\text{C-NMR}(\text{CDCl}_3, 100\text{MHz}) \delta$: 158.8, 151.1, 130.7, 128.5, 127.7, 126.7, 121.6, 114.8, 111.1, 73.7, 68.1, 45.8, 45.4, 44.1, 41.4, 40.4, 34.9, 32.03, 29.5, 29.1, 28.1, 23.1, 22.8 and 14.2 ppm. FT-IR (KBr, cm⁻¹): 2921, 2850, 2363, 1601, 1510, 1467, 1384, 1244, 1174, 1026, 971, 847 and 800. MALDI-TOF-TOF-MS (MW = 1006.68): $m/z = 1007.560$.

Synthesis of OPV-14: Compound **3a** (0.35 g, 0.50 mmol) and **4n** (0.35 g, 1.10 mmol) were reacted as described for OPV-0. The product was purified by recrystallizing from hot acetone. Yield = (58 %). $^1\text{H-NMR}(\text{CDCl}_3, 400\text{MHz}) \delta$: 7.45 ppm (d, 4H, Ar-H), 7.30 ppm (d, 2H, CH=CH), 7.11 ppm (d, 2H, CH=CH), 7.05 ppm (s, 2H, Ar-H), 6.89 ppm (d, 4H, Ar-H), 3.97 ppm (t, 4H, Ar-OCH₂-alkyl), 3.82-3.75 ppm (m, 4H, Ar-OCH₂-TCD), 2.5-0.88 ppm (m, 84H, cyclic-H and aliphatic-H). $^{13}\text{C-NMR}(\text{CDCl}_3, 100\text{MHz}) \delta$: 158.8, 151.1, 130.7, 128.5, 127.7, 126.7, 121.6, 114.8, 111.1, 73.7, 68.1, 45.8, 45.4, 44.1, 41.4, 40.4, 34.9, 32.0, 29.5, 29.1, 28.1, 23.1, 22.8 and 14.2 ppm. FT-IR (KBr, cm⁻¹): 2916, 2851, 1605, 1508, 1240, 1179, 1015, 961, 802, 718, 589 and 528. MALDI-TOF-TOF-MS (MW = 1035.61): $m/z = 1034.720$.

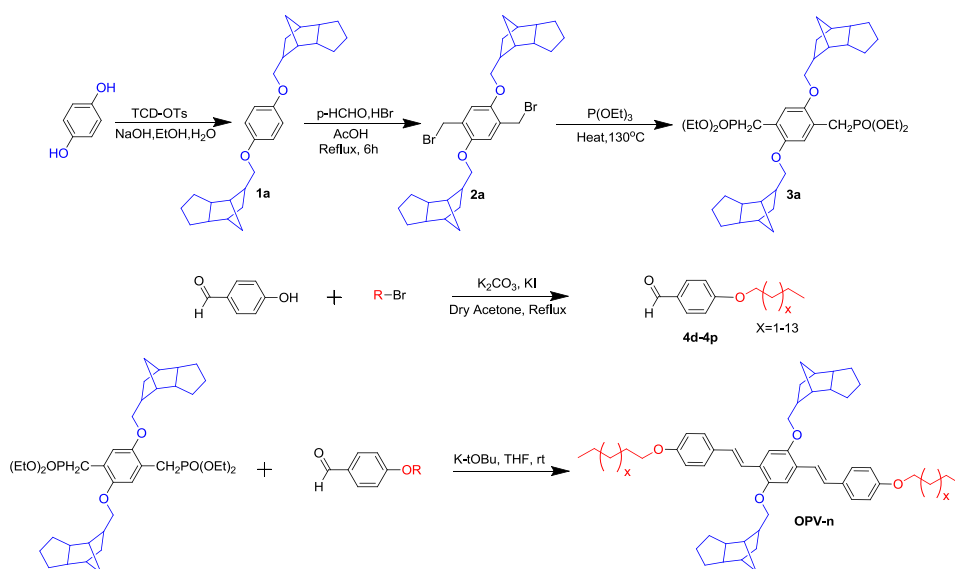
Synthesis of OPV-15: Compound **3a** (0.35 g, 0.50 mmol) and **4o** (0.36 g, 1.10 mmol) were reacted as described for OPV-0. The product was purified by recrystallizing from hot acetone. Yield = (43 %). $^1\text{H-NMR}$ (CDCl_3 , 400MHz) δ : 7.45 ppm (d, 4H, Ar-H), 7.30 ppm (d, 2H, CH=CH), 7.11 ppm (d, 2H, CH=CH), 7.05 ppm (s, 2H, Ar-H), 6.89 ppm (d, 4H, Ar-H), 3.97 ppm (t, 4H, Ar-OCH₂-alkyl), 3.82-3.75 ppm (m, 4H, Ar-OCH₂-TCD), 2.5-0.88 ppm (m, 88H, cyclic-H and aliphatic-H). $^{13}\text{C-NMR}$ (CDCl_3 , 100MHz) δ : 158.7, 151.2, 130.8, 128.5, 127.7, 126.7, 121.5, 114.7, 111.1, 73.4, 68.1, 45.7, 45.4, 44.1, 41.4, 40.4, 34.9, 32.1, 29.8, 29.1, 26.1, 22.8 and 14.2 ppm. FT-IR (KBr, cm^{-1}): 2916, 2851, 1605, 1508, 1240, 1179, 1015, 961, 802, 718, 589, 528. MALDI-TOF-TOF-MS (MW = 1062.84): m/z = 1063.660.

Synthesis of OPV-16: Compound **3a** (0.47 g, 66.0 μmol) and **4p** (0.36 g, 132 μmol) were reacted as described for OPV-0. The product was purified by recrystallizing from hot acetone. Yield = (68 %). $^1\text{H-NMR}$ (CDCl_3 , 400MHz) δ : 7.45 ppm (d, 4H, Ar-H), 7.3 ppm (d, 2H, CH=CH), 7.11 ppm (d, 2H, CH=CH), 7.05 ppm (s, 2H, Ar-H), 6.89 (d, 4H, Ar-H), 3.99 ppm (t, 4H, Ar-OCH₂-alkyl), 3.82-3.75 ppm (m, 4H, Ar-OCH₂-TCD), 2.5-0.88 ppm (m, 92H, cyclic-H and aliphatic-H). $^{13}\text{C-NMR}$ (CDCl_3 , 100MHz) δ : 158.6, 151.2, 130.8, 128.7, 127.7, 126.0, 121.5, 114.7, 111.1, 73.4, 68.1, 45.7, 45.4, 44.1, 41.4, 40.0, 34.9, 32.1, 29.8, 29.1, 26.1, 22.8 and 14.1 ppm. FT-IR (KBr, cm^{-1}): 2919.4, 2851.7, 2363.9, 1604.8, 1511.1, 1467.8, 1384.1, 1244.7, 1174.8, 1026.1, 971.8, 847.6, and 800. MALDI-TOF-TOF-MS (MW=1091.72): m/z = 1090.997.

2.3. Results and Discussion

2.3.1. Synthesis and characterization of OPVs

A homologous series of tricyclodecanemethanol (TCD) based oligophenylenevinylenes with identical aromatic core but different number of carbon atoms in the longitudinal alkyl chains was synthesized as shown in the scheme 2.1. The synthesis started from hydroquinone which was reacted with TCD-OTs in the presence of base to give 1, 4-bis(1, 8-tricyclodecanemethyleneoxy) benzene (**1a**). Compound **1a** was further reacted with paraformaldehyde and HBr in acetic acid to give corresponding bis-bromomethylated derivative (**2a**). Compound **2a** was further converted to its corresponding 1, 4-bis[(alkyloxy)]-2,5-xylenediphosphonate (**3a**) by reacting with triethylphosphite. 4-alkoxybenzaldehydes (**4d-4p**) were synthesised by reacting 4-hydroxybenzaldehyde with appropriate alkyl bromides in the presence of potassium carbonate and potassium iodide in dry acetone. Compound **3a** reacts under Wittig-Horner conditions with 4-alkoxybenzaldehydes (**4a to 4p**) leading to OPVs. The OPVs have been labelled as **OPV-n**, where n is the number of carbon atoms present in the longitudinal alkyl chains.



Scheme 2.1. Synthesis of oligophenylenevinylenes (OPV)s with various alkyl chains.

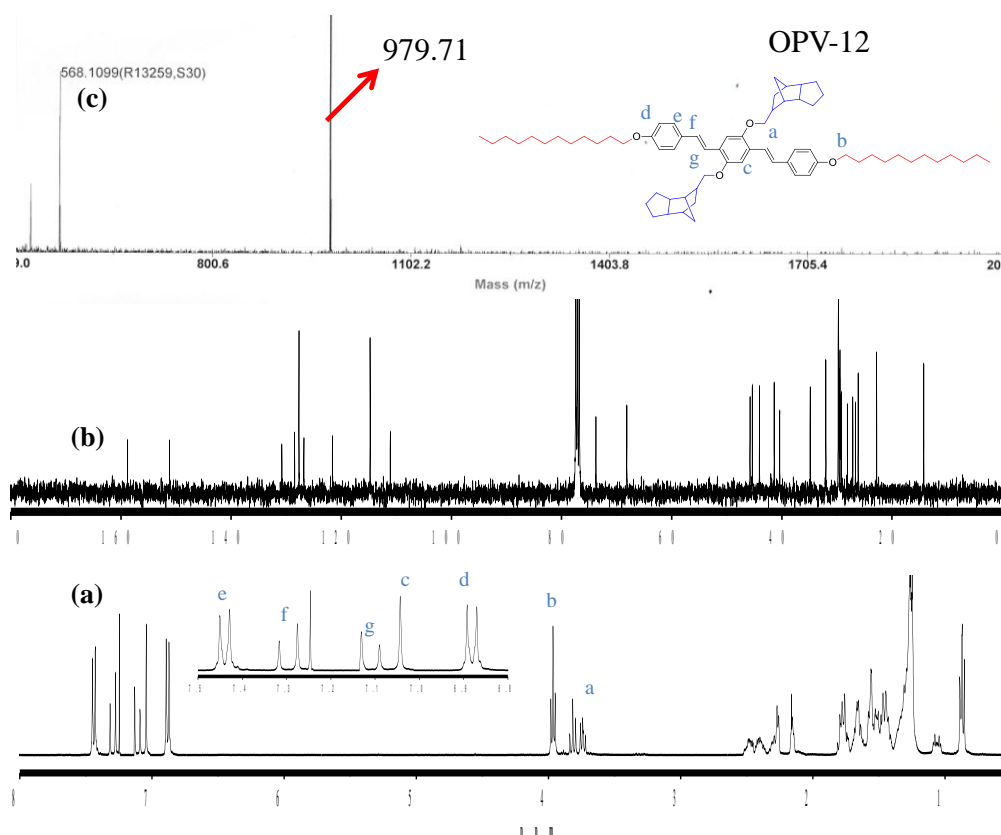


Figure 2.4: (a) $^1\text{H-NMR}$ spectrum (b) $^{13}\text{C-NMR}$ spectrum (c) MALDI-TOF-TOF spectrum of OPV-12.

The structures of all the OPVs were confirmed by $^1\text{H NMR}$, $^{13}\text{C NMR}$, FT-IR and MALDI-TOF-TOF mass spectrometers. Figure 2.4. shows the $^1\text{H-NMR}$, $^{13}\text{C NMR}$ and MALDI-TOF-TOF spectra of a representative OPV-12 sample. The inset shows the expanded proton spectrum of the aromatic region. The peaks at 7.45 ppm and 6.89 ppm corresponded to aromatic phenylene protons. The doublets at 7.30 ppm and 7.11 ppm belonged to vinylene protons. The protons in the middle aromatic ring appeared as a singlet at 7.11 ppm. The triplet at 3.99 ppm and the multiplets in the range of 3.82-3.75 ppm belonged to Ar-OCH₂-alkyl and Ar-OCH₂-TCD protons, respectively. The peaks for all other protons appeared below 3.75 ppm. The peak for terminal methyl protons belonging to alkyl side chains appeared as a triplet at 0.88 ppm. Similarly, $^{13}\text{C-NMR}$ spectrum of the OPV-12 exhibited the presence of

aromatic peaks at 158.6, 151.0, 128.5, 127.8, 121.6, 114.6 and 110.9 ppm, respectively. Ar-OCH₂-TCD and Ar-OCH₂-alkyl peaks appeared around 73 ppm and 68 ppm, respectively. All the other aliphatic carbons belonging to cyclic TCD unit and the linear alkyl chains appeared below 50 ppm. MALDI-TOF-TOF spectrum of the OPV-12 confirmed the presence of molecular ion peak (M⁺) corresponding to MALDI-TOF-TOF-MS (MW = 979.5): m/z = 978.717. All the other OPVs were similarly characterised and the detailed analysis has been given earlier in the experimental section.

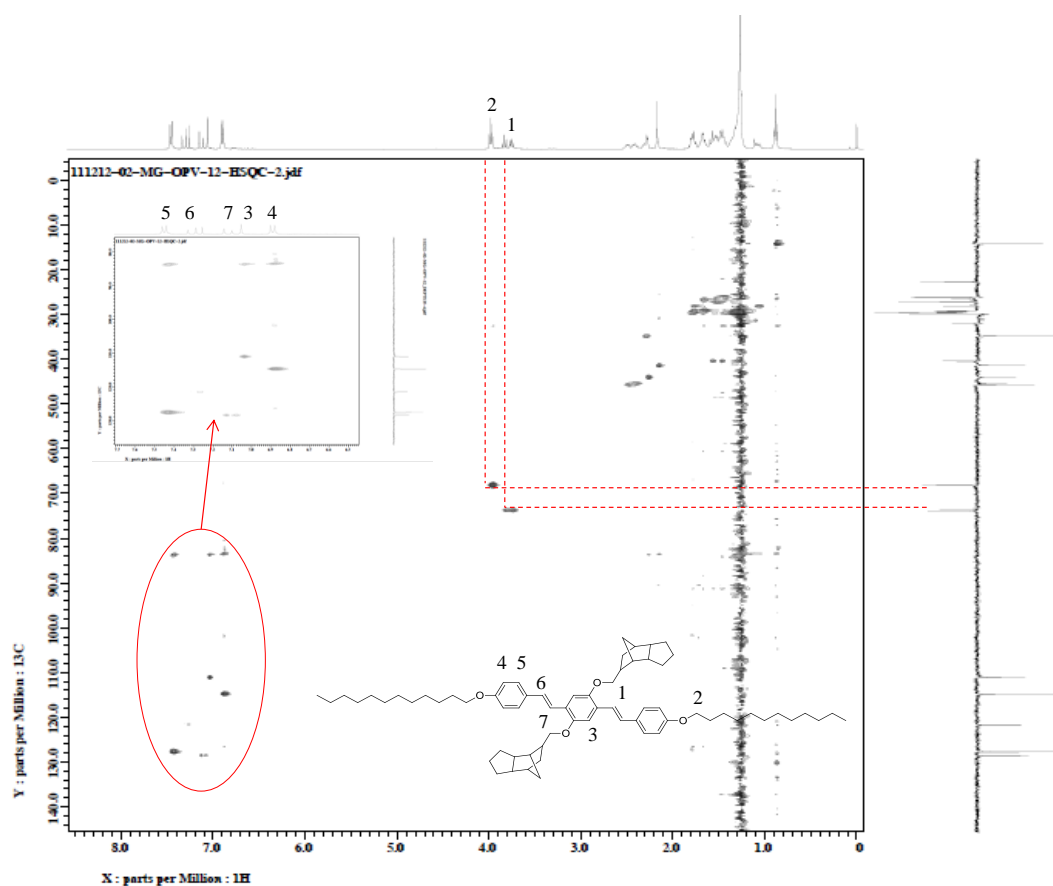


Figure 2.5. 2D-NMR (HSQC-DEPT-135) spectrum of OPV-12.

To further assign the structure of OPV-12, ¹H-¹³C coupled 2D NMR (HSQC-DEPT-135 technique) was done and shown in the figure 2.5. The ¹³C-NMR on the right hand side of the spectrum possessed feature of DEPT-135 for the carbon atoms.

The aromatic region was expanded and all the aromatic carbon appeared positive. In the aliphatic region, the carbon atoms with an odd number of aliphatic protons appeared negative to those carbons, that have an even number of attached protons. The carbon atoms belonging to Ar-OCH₂-alkyl (the triplet at 3.99 ppm) and the Ar-OCH₂-TCD (multiplets in the range of 3.82-3.75 ppm) appeared negative. These carbons have been numbered as 1 and 2 as shown in the figure 2.5. The positive carbons belonged to the -CH₃ in the terminal chains and -CH, units found in the TCD groups attached on both side of the aromatic core.

The GPC chromatograms of all the OPVs having even number of carbon atoms in the alkyl tails have been shown in figure 2.6. All the chromatograms were recorded by dissolving the OPV samples in tetrahydrofuran. Figure 2.6 shows that all the chromatograms appeared as a single peak confirming high purity of these samples. In GPC, higher molecular weight OPVs eluted faster than lower molecular weight OPVs and this is beautifully reflected in the above chromatogram showing highest molecular weight OPV-16 to extreme left and lowest molecular weight OPV-0 to the extreme right. All other OPVs fell in between these two extremes and followed a similar trend.

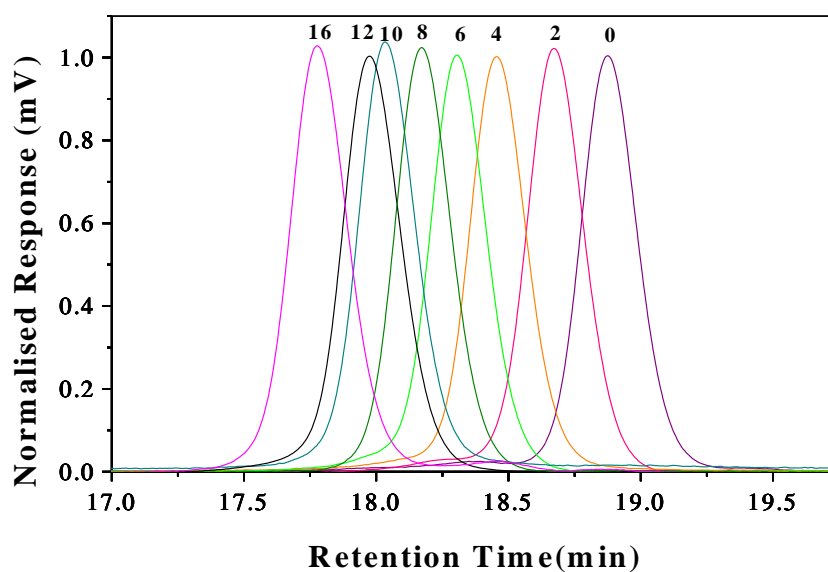


Figure 2.6. GPC Chromatograms of OPVs in tetrahydrofuran at 25 °C.

2.3.2. Thermal Properties

To study the thermal behavior of OPV molecules, powdered samples were subjected to differential scanning calorimetry (DSC) analysis at 10 °C/min heating and cooling rates. The first heating cycle data were discarded since they possessed prehistory of the sample. DSC thermograms of OPV- n with $n = 1, 8, 9, 11, 12, 13, 14, 15$ and 16 have been shown in the figure 2.7.

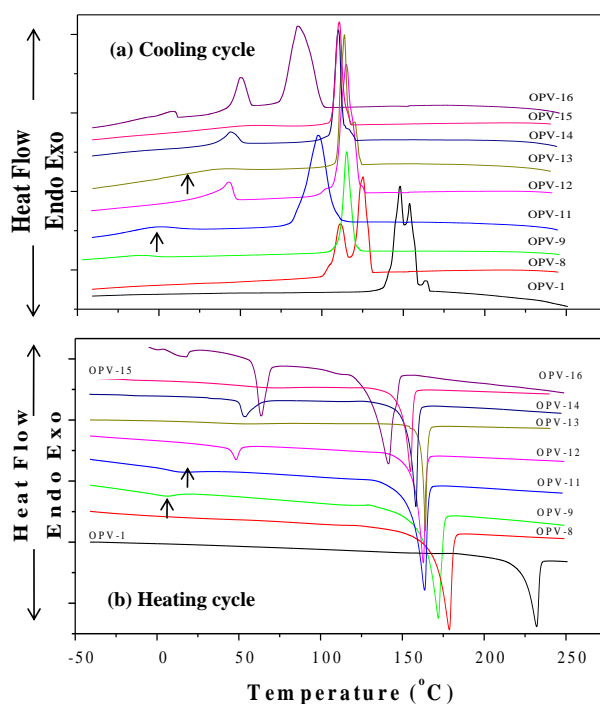


Figure 2.7. DSC thermograms of OPVs in the cooling (a) and heating cycle (b).

OPV-1, OPV-8, OPV-9, OPV-11, 12, 13, 14 and OPV-15 showed two crystallization peaks when cooled from the melt (see figure 2.7a). This represents the typical nature of thermal transitions for thermotropic liquid crystalline materials. For example, in OPV-12, the first peak at 115 °C and the second peak at 43 °C were assigned to isotropic-to-LC and LC-to-crystalline transitions, respectively. OPV-13, OPV-14 and OPV-15, showed similar two transitions as shown by OPV-12, but the LC window (the temperature range at which the molecules show LC behavior) decreased with increasing spacer length. OPV-16 showed three peaks corresponding to isotropic-to-LC (at 88 °C), LC-crystalline (at 52 °C), and at very low temperature

crystalline-to-crystalline (at 2 °C) transition. In the heating cycle (second heating), OPV-9, OPV-11, and OPV-12 showed two melting transitions and OPV-16 showed three melting transitions (Figure 2.7b). These melting transitions were assigned to their reverse phase changes; for example, in OPV-11, crystalline-to-LC (at 15 °C) and LC-to-isotropic (at 162 °C) transitions.

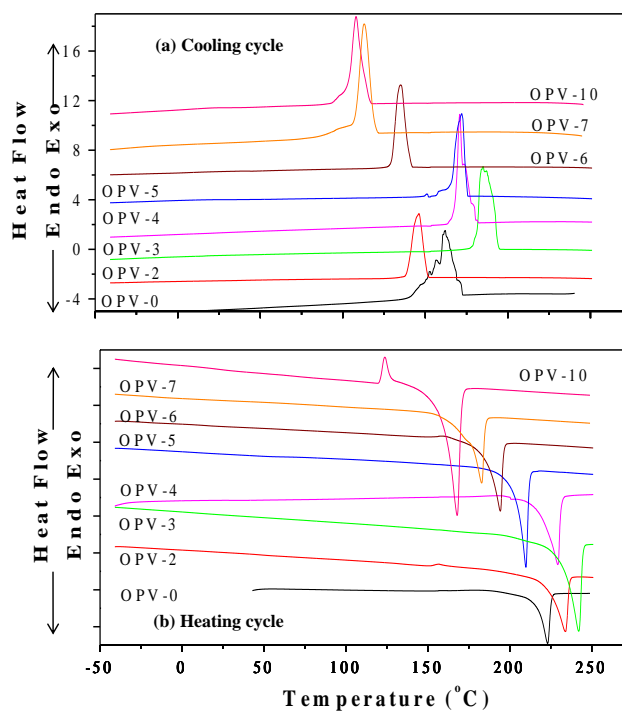


Figure 2.8. DSC thermograms of OPVs in the cooling (a) and heating cycle (b).

The samples OPV-0, OPV-1, and OPV-8 showed two thermal transitions in the cooling cycle, but only one melting transition in the heating cycle, indicating their monotropic liquid crystalline nature.³⁸⁻⁴⁰ DSC thermograms of OPV-0, 2, 3, 4, 5, 6, 7 and OPV-10 have been shown in the Figure 2.8. All the OPVs showed a single transition in the heating cycle and a single transition in the cooling cycle. OPV-10 showed two peaks at 108 °C and 24 °C which were assigned to LC and crystalline phase changes. Similar trend was seen in OPV-0, but the LC window was too narrow to effectively resolve the two peaks. Figure 2.8b shows the DSC profiles of OPVs in the heating cycles and the peaks corresponded to the temperatures at

which OPVs underwent melting transitions. The melting temperatures continuously increased from OPV-7 to OPV-3 but started to decrease in case of OPV-2 and OPV-0. Two important trends could be observed from the DSC analysis (i) the liquid crystalline active window (temperature range of isotropic-LC to LC-crystalline in the cooling cycle) increased from 5 to 15 °C (in OPV-1 to OPV-8) to a very wide 80 to 125 °C (in OPV-9 to OPV-12) after which the LC window became very narrow. (ii) with increase in the number of methylene units in alkoxy side chains, the tendency for OPVs to become liquid crystalline also increased. The LC active window for OPV-16 was significantly small, which suggested that beyond an optimum chain length the tendency for liquid crystallinity in OPVs decreased.

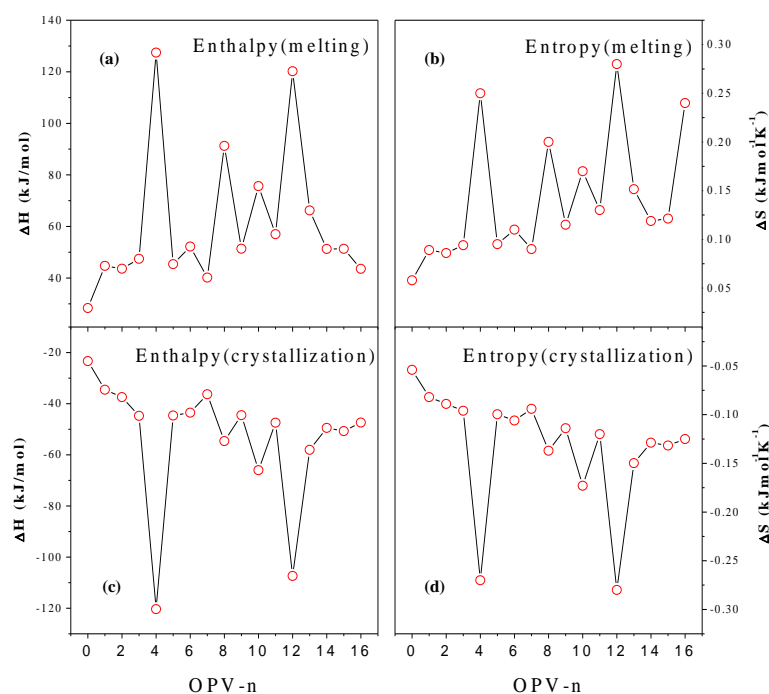


Figure 2.9. Odd-even oscillation of OPVs in the enthalpies and entropies of melting and crystallization transitions.

The enthalpies of the melting and crystallization transitions are summarized in Table 2.2. The entropies of the transitions,⁴¹ were calculated using the following thermodynamic expression: i.e.,

$$\Delta S = \Delta H/T,$$

where, ΔH is the enthalpy of the transition at the temperature T (in Kelvin scale). The thermal data have been provided in table 2.2. The enthalpies and entropies of the melting and crystallization transitions were plotted against the number of methylene units as shown in figure 2.9. It is interesting to note that the OPVs followed odd-even oscillation in their enthalpy and entropy plots. Both enthalpy and entropy of the melting transition were found to be very high for OPVs with even number of carbon atoms in the spacer compared to their odd-numbered counterparts.

Table 2.2. DSC thermal data of OPVs at 10°/min heating/cooling rate.

OPV-n	T_m^a (°C)	ΔH_m^b (kJmol ⁻¹)	$T_{ic/lc}^c$ (°C)	$\Delta H_{i-c/l.c}^d$ (kJmol ⁻¹)	ΔS_m^e (kJmol ⁻¹ K ⁻¹)	$\Delta S_{i-c/l.c}^f$ (kJmol ⁻¹ K ⁻¹)
OPV-0	216.6	28.4	161.9	-23.3	0.058	-0.054
OPV-1	231.9	44.8	147.9	-34.5	0.089	-0.082
OPV-2	233.8	43.6	145.9	-37.4	0.086	-0.089
OPV-3	232.3	47.5	193.5	-44.8	0.094	-0.096
OPV-4	229.9	127.4	173.5	-120.3	0.250	-0.270
OPV-5	205.6	45.4	174.8	-44.6	0.095	-0.099
OPV-6	194.1	52.2	134.8	-43.5	0.110	-0.106
OPV-7	174.4	40.2	112.8	-36.3	0.090	-0.094
OPV-8	178.6	91.3	125.2	-54.7	0.200	-0.137
OPV-9	171.8	51.4	115.2	-44.5	0.115	-0.114
OPV-10	167.8	75.6	107.9	-66	0.170	-0.173
OPV-11	163.7	57.0	107.2	-47.4	0.130	-0.120
OPV-12	162.4	120.2	114.8	-107.4	0.280	-0.280
OPV-13	164.0	66.2	38.2	-58.0	0.151	-0.149
OPV-14	158.3	51.2	43.9	-49.5	0.118	-0.128
OPV-15	149.7	51.3	56.1	-50.7	0.121	-0.131
OPV-16	151.4	43.5	53.7	-47.4	0.240	-0.125

(a) T_m is transition temperature for crystal/LC to isotropic phase change in °C. (b) ΔH_m is the total enthalpy change from crystal to isotropic phase change in kJ/mol. (c) T_c is transition temperature from isotropic to crystal/LC phase change in °C (d) ΔH_c is the total enthalpy change from isotropic to crystal phase change. (e) ΔS_m is the total entropy change from crystal to isotropic phase change in kJ mol⁻¹ K⁻¹. (f) ΔS_c is the total entropy change from isotropic to crystal phase change.

The highly packed structures required more energy for melting (endothermic) and similarly released more energy (exothermic) while crystallizing compared to

weakly packed molecules. This suggested that the supramolecular liquid crystalline π -conjugate packing of the OPV chromophores enhanced with even carbon chains. Further, OPVs with spacers $n = 4, 8, 12,$ and 16 showed significantly higher energy terms as compared to other even ($n = 2, 6,$ and 10) and odd- OPVs. Hence, OPVs with $n = 4, 8, 12,$ and 16 possessed higher packing in solid state and these numbers turned to be the magic numbers for solid state packing of OPV chromophores. Odd-even oscillation is typically observed in LC materials having molecular twins in which azobenzene,^{42, 43} biphenyl chromophores,⁴⁴ dimeric salicylaldiamine,⁴⁵ and LC polyesters⁴⁶ connected via methylene spacers. Here, odd-even oscillation has been observed in the LC properties of π -conjugated materials.

2.3.3. Polarized Light Microscopic studies

The PLM textures of OPVs ($n=1-9$) have been shown in the figure 2.10. OPV-0 to OPV-4 belonged to simple crystalline solids. OPV-1 started to develop some type of LC textures, but immediately crystallized out to produce fanlike textures.³⁸ OPV molecules with shorter alkoxy chains ($n = 0-4$) did not produce prominent LC textures. OPV-5 to OPV-9 exhibited spherical focal conics. The fanlike textures with focal conics observed for OPV-5 to OPV-9 resembled the typical textures observed for cholesteric LC samples.³⁸

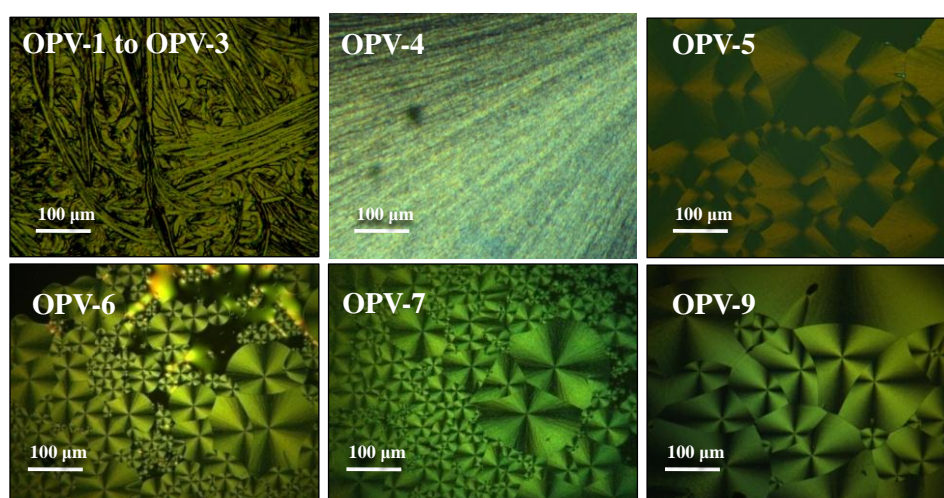


Figure 2.10. Polarized light microscope images of OPV-1 to OPV-9.

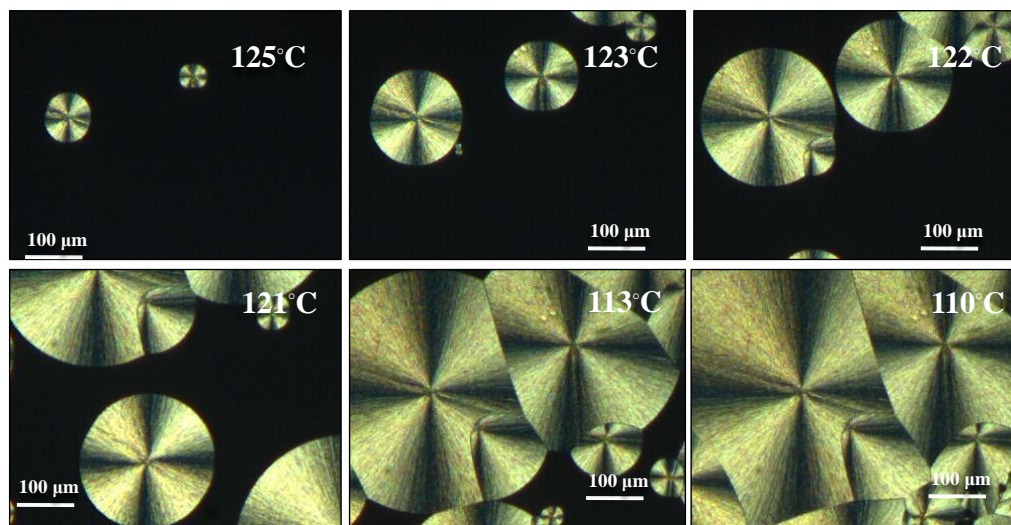


Figure 2.11. Temperature dependent PLM Images for OPV-8.

The temperature dependent PLM profile of OPV-8 belonging to short pitch cholesterics (OPV-5 to OPV-9) has been shown in the figure 2.11. OPV-8 exhibited spherical focal conics as nucleating sites (images at 125 °C and at 123 °C). These focal conics quickly impinged in to one another (at 122 °C and 121 °C) to give rise to fan shaped focal conic textures as shown in images at 113 °C and at 110 °C.

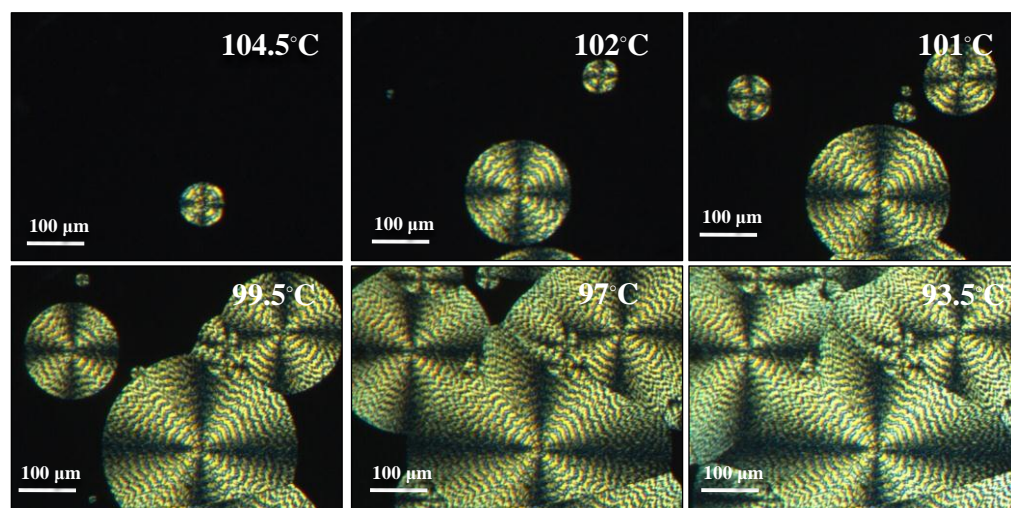


Figure 2.12. Cholesteric Liquid crystalline textures of OPV-12 under polarized light microscope.

The detailed temperature dependent PLM profile of OPV-12 belonging to ring banded textures has been shown in figure 2.12. The nucleation appeared in the form of concentric dark and bright rings (see images at 104.5 °C and at 102 °C). As the temperature decreased, these ring banded spherulites grew outwards to give rise to ring banded textures. (See images from 101°C and at 93.5°C). Closer observation of these textures revealed that rings were not concentric but originated from a common center and continued to grow vertically outwards in a left-handed helical fashion.

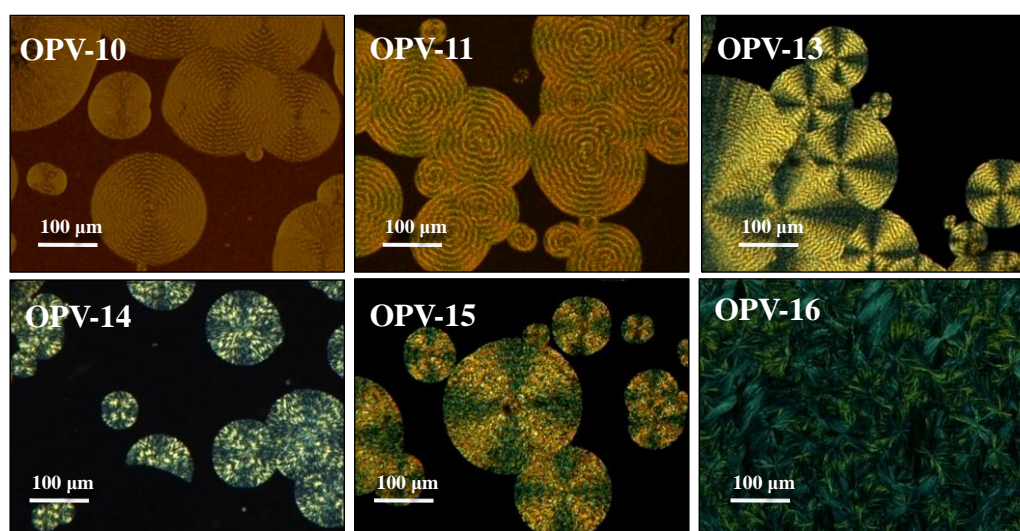


Figure 2.13. Cholesteric liquid crystalline textures of OPVs.

The PLM images for OPV-10 to OPV-15 have been shown in the figure 2.13. OPV-10 to OPV-15 produced beautiful birefringence patterns consisting of concentric dark and bright rings. The mesophase textures for OPV-10 to OPV-15 showed Grandjean lines whereas at large chain lengths (in OPV-16), the mesophase morphology was lost. The pitch lengths of helical rings gradually increased with increasing number of carbon atoms in the tail up to $n = 15$.

From the above PLM studies, it was understood that OPVs exhibited systematic transition in the mesophases from crystalline to cholesteric to ring-banded textures with an increase in methylene units in the alkyl chains. The transformation in the LC morphology was obtained in OPVs having identical aromatic π -cores, and,

therefore, the role of the van der Waals interactions among the alkyl chain in the OPV chromophores are expected to play a crucial role in determining the molecular self-organization during the crystallization process.

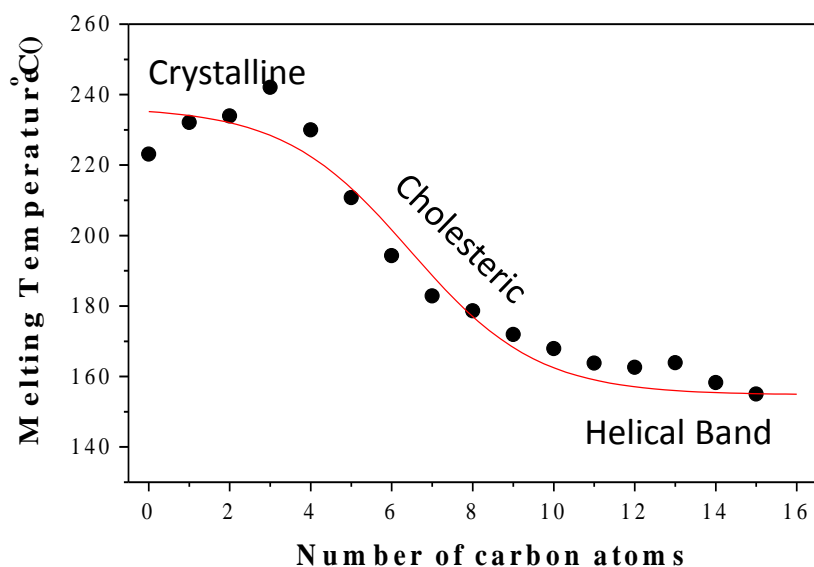


Figure 2.14. Sigmoidal self-assembly of OPVs.

To further understand the nature of the molecular self-organization, the melting transition temperatures of the OPVs were plotted against the number of carbon atoms in alkyl chains and shown in figure 2.14. The melting transitions showed a sigmoidal relationship with the spacer length. There are two flat regions in the plot: (i) crystalline OPVs of shorter alkyl chains (OPV-0 to OPV-4) and (ii) ring-banded OPVs with alkyl chains $10 \leq n$. The melting temperatures showed a sharp decrease from OPV-5 to OPV-9 where the molecules exist in the form of cholesteric LC phases. The combination of PLM textures and the sigmoidal curve indicated that the methylene chains attached in the longitudinal axis played a key role in self-organizing OPVs, which transformed from crystalline solid to ring-banded supramolecules via cholesteric intermediates. To further understand the sigmoidal transitions for the OPVs in the melt crystallization process, the LC temperatures were also plotted against the spacer length. The crystallization temperature versus spacer length was also fitted into a sigmoidal function; however, the data were found

to be more scattered. Sigmoidal transformation is usually observed in the biological systems, for example, in the denaturation of proteins in the presence of appropriate denaturant moiety.⁴⁷ However, sigmoidal self-organization is very rare in synthetic macromolecules due to the lack of cooperativity between secondary interactions unlike biological systems. Interestingly, here, OPVs have followed typical sigmoidal self-organization indicating very good cooperativity among the non-covalent interactions present in the chromophores.

2.3.4. Ring Banded Structures

Ring banded spherulitic structures have been reported in commercial semi crystalline polymers during their crystallization from the melt.^{48, 49} Keith et al. and few others had carried out detailed studies on the mechanism of formation of these ring banded structures using theoretical, microscopic studies and computational simulations.⁵⁰⁻⁵⁵ The origin of the ring banded structure as generally accepted is due to the periodic twisting of lamellar crystals along the radial growth direction of the spherulites.⁵⁶⁻⁵⁸ The lamellar twisting phenomenon was correlated to surface stress,⁵⁹ chain folding direction of the crystal growth,⁶⁰ periodic change of concentration gradient,⁶¹ and also the segregation of amorphous polymer chains from the crystal fronts of polymer binary blends.^{48,62-65} Though the twisting of the lamellar crystal mechanism was widely accepted in all of these cases, there seems to be no correlation between the structure of the materials (polymers or small molecules) for the appearance of ring banded patterns. Ring banded structures have also been observed in liquid crystalline materials. For example, few cholesteric samples were found to show dark lines and bright lines when helical structure changed its twist by angle (π). These dark lines were called Grandjean lines.³⁸ Ring-banded spherulitic structures are not common in crystalline solids; however, recently it was observed in a few commercial polymers like polyethylene, polylactides, and poly(arylether ketones), etc.⁶³ Here, the ring-banded textures are obtained from small liquid crystalline OPV molecules unlike earlier observed examples of semicrystalline commercial polymers.⁶⁴ It is also important to note that different types of mechanisms were proposed for various materials. Thus, there is no common

explanation for the formation of banded spherulites with respect to their chemical structures.

Interestingly, in the present case, these ring banded textures have been observed in a small molecular system in the LC temperature window and hence a direct correlation between ring banded textures and molecular structures can be made. Thus, to further confirm that the textures observed are not an artifact, the LC frozen samples of OPV-8 and OPV-12 were subjected to scanning electron microscope (SEM) analysis (figure 2.15). The crystalline vectors corresponding to the cholesteric phases in OPV-8 showed uniform long rectangular planks with thickness (600 nm). The rectangular planks were straight (length more than $10\ \mu\text{M}$) and loosely packed; however, all of them projected upwards in one direction. The SEM image of OPV-12 showed the formation of thin twisted sheets. The sheets were

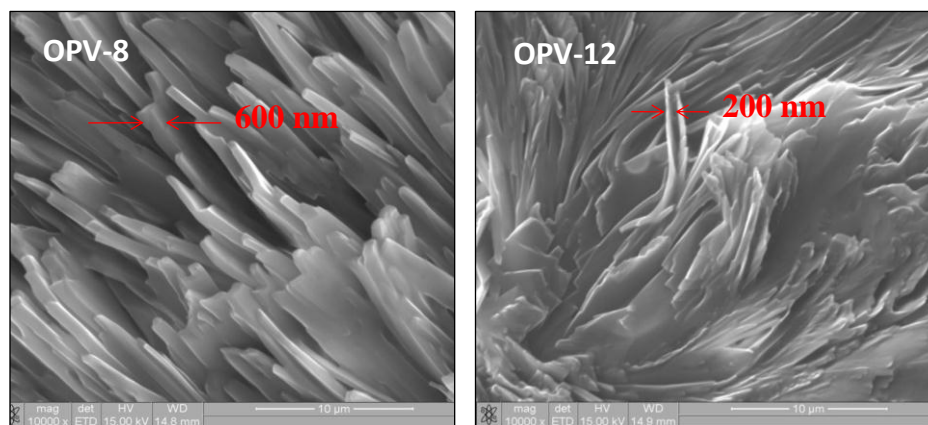


Figure 2.15. Scanning electron microscope images of OPV-8 and OPV-12 samples frozen in their LC phases.

twisted within, tightly packed and also twisted together along the same direction. The crystalline vectors are typically composed of a large number of lamellae, which could be in thousands, and these subnanometer size species pack in the solid state to produce the images shown in figure 2.15. The straight planks in OPV-8 and twisted sheets in OPV-12 revealed that the orientation of the lamellae were obviously different in both the cases. SEM analysis strongly supported the existence of twisted lamellae in OPV-12. The twisted lamellae produced ring-banded textures whereas the normal packing produced cholesteric textures.

2.3.5. Single Crystal XRD Analysis of OPV molecules

To trace the mechanism of self-organization and the non-covalent forces behind the diverse LC mesophase organization in OPVs at the molecular level, detailed single crystal X-ray analysis was done. OPVs belonging to each category of the mesophases were successfully obtained: OPV-4 (belonging to crystalline solids), OPV-8 (belonging to short pitch cholesterics) and OPV-12 (belonging to helical bands) were resolved. The crystal structures of the OPV molecules have been shown in the figure 2.16.

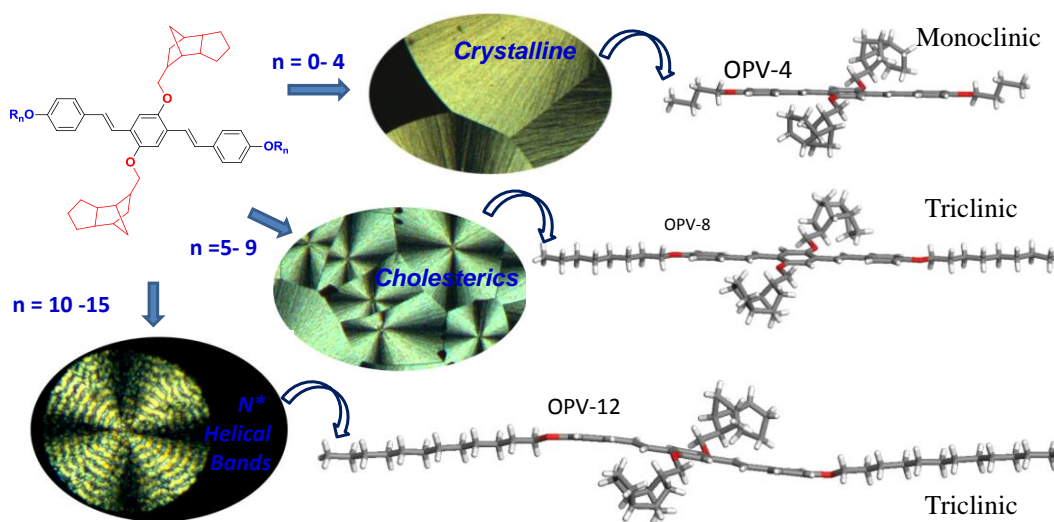


Figure 2.16. Single crystal structures of OPV-4, OPV-8 and OPV-12.

All three benzene rings in the aromatic core of the OPVs were found in the same plane and constituted the molecular axis. OPV-4 had symmetric structure and crystallized in monoclinic space group $P2_1/n$. On the other hand, OPV-8 and OPV-12 crystallized in non-centro-symmetric triclinic crystal systems. The Tricyclodecane (TCD) units attached at the center of aromatic core occupied either side of the plane perpendicular to the aromatic backbone. The butyloxy tail in OPV-4 had one cis-conformation, whereas the octyloxy tails in OPV-8 and the dodecyl chains in OPV-12 were aligned in all-trans conformations.

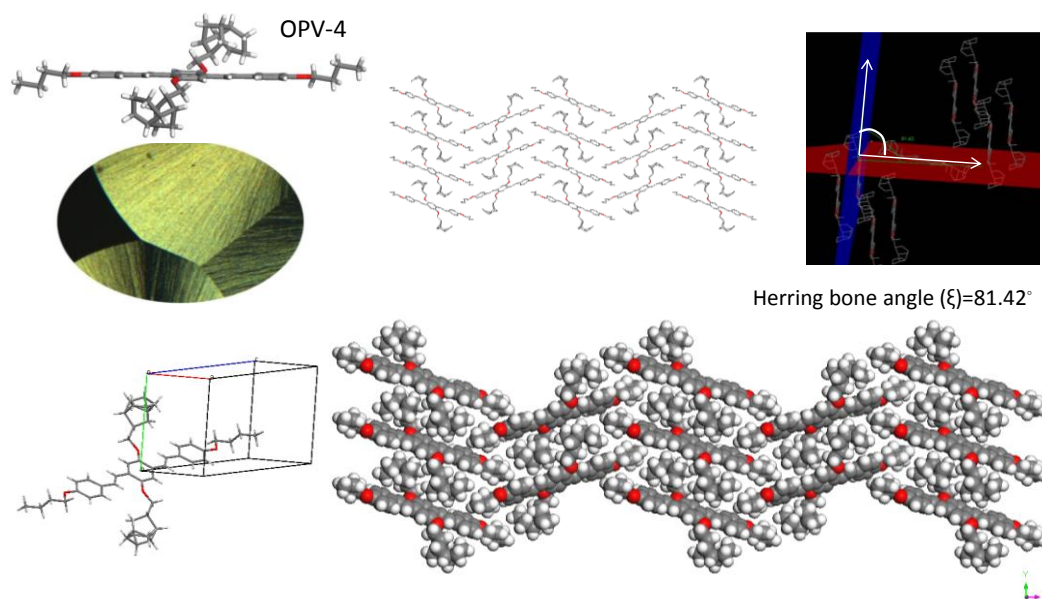


Figure 2.17. Single crystal analysis and three dimensional packing of OPV-4.

The three dimensional packing for OPV-4 molecule is shown in figure 2.17. The bulky TCD units protruded the π -cores along the direction perpendicular to the molecular axis. The butyloxy tail in OPV-4 had one cis-conformation. The rigid planar aromatic core and the absence of long lateral side chains lead the OPV-4 to arrange in “Herringbone” type packing. The herringbone arrangement is one of the most stable packing for molecules in the solid state when adjacent stacks of molecules arranged in opposite directions in the unit cell.⁶⁶ The molecular planes in the adjacent stacks are inclined with respect to each other and the inclination is known as the herring bone angle (ξ).⁶⁷ HB angle (ξ) is measured between molecules in adjacent stacks which are diagonally oriented to each other. The HB angle (ξ) for OPV-4 was measured as 81.40° which is very close to a perfect alignment of herringbone perpendicular sheets ($\xi = 90^\circ$). Herringbone type packing has so far been observed in π -conjugated molecules having no substituent in the central aromatic core which was considered to be an important structural parameter for the existence of these patterns. Interestingly, OPV-4 is a unique example in the π -conjugated

systems where herringbone pattern is observed despite having large bulky TCD substitution at the central aromatic core.

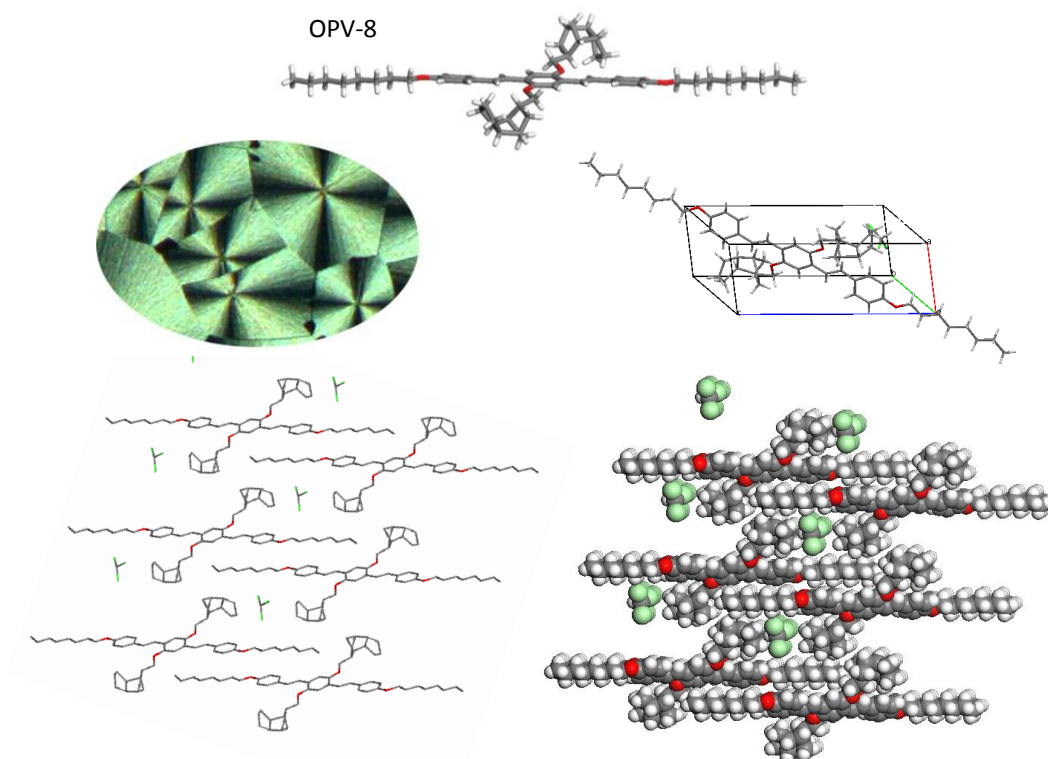


Figure 2.18. Single crystal analysis and three dimensional packing of OPV-8.

The three dimensional packing for OPV-8 has been shown in the figure 2.18. The unit cell for OPV-8 shows that the molecule crystallized in non-centrosymmetric triclinic crystal system. The TCD units attached at the center occupied either side of the plane perpendicular to the aromatic backbone and the two alkyl tails present in the terminal aryl rings were on the same plane constituted by the aromatic rings. OPV-8 crystal consisted of one solvent molecule per structure; however, the solvent molecules did not involve in any type of secondary interactions. The octyl tails were aligned in all-trans conformation in OPV-8. The torsion angles from the central aromatic ring to either side were obtained as 10.9° and 11.9° in which confirmed that the OPV backbone was indeed planar. The increase in the tail

length from four in OPV-4 to eight in OPV-8 facilitated the inter-digitations of tails along the molecular axis: as a result, the molecules in OPV-8 were closely packed as bundles.

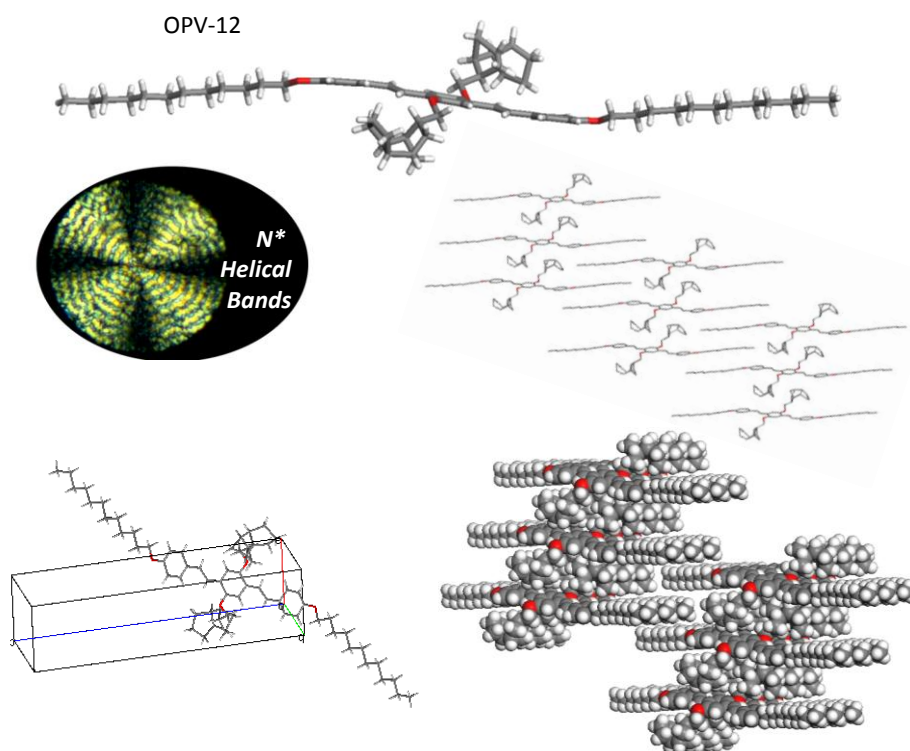


Figure 2.19. Single crystal analysis and three dimensional packing of OPV-12.

The three dimensional packing for OPV-12 has been shown in the figure 2.19. The unit cell for OPV-12 showed that the molecule crystallized in non-centrosymmetric triclinic crystal system. The two long dodecyl chains present in the terminal aryl rings were aligned in all-trans conformation in the same plane constituted by the aromatic rings. The torsion angles from the central aromatic ring to either side were obtained as 9.93° and 6.29° in OPV-12 confirming the planarity of the OPV backbone. In spite of being planar, there was a large difference in the way each of these three molecules packed with respect to the number of carbon atoms present in the alkyl tails. The long dodecyloxy tails in OPV-12 produced higher ordered structures in which the molecules were packed as columns along the

b-axis and was pushed apart in *c*-axis direction. The large difference in the packing of OPVs revealed that the custom designed OPV-TCD skeletons were very unique in producing diverse self-assembled structures in the solid state.

2.3.6. Roll and Pitch Inclinations

The packing of the planar organic molecules in the solid state could be described in terms of two different angles, termed as “pitch” and “roll” inclinations as reported by Curtis et al.⁶⁶ A schematic diagram for the pitch and roll angle displacements have been shown in figure 2.20.

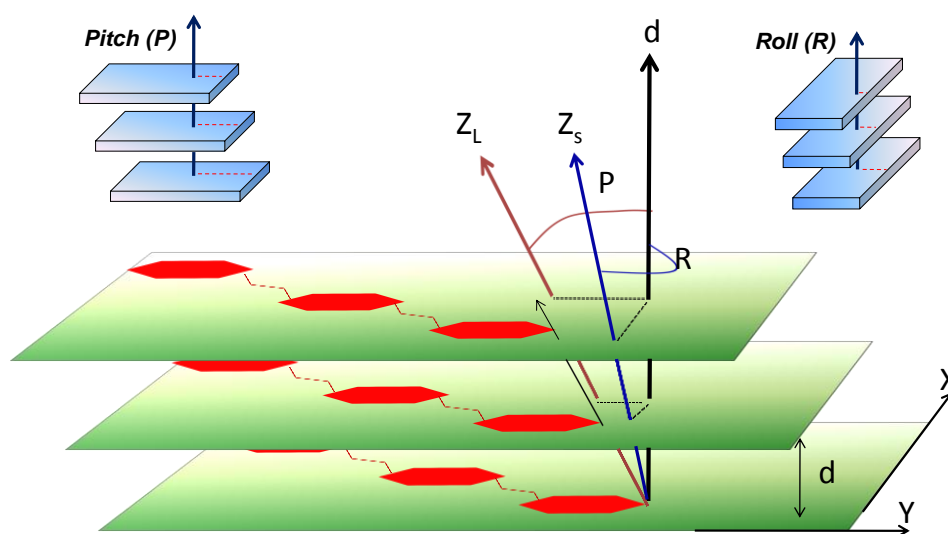


Figure 2.20. Schematic model of pitch and roll displacements.

The planar aromatic core constituted the *x*-*y* molecular plane. The axes *x* and *y* are perpendicular to each other and represented the short and long axes of the molecule, respectively (see figure 2.20). The shortest distance between two adjacent molecules is defined by a vector, *d*, and their stacking direction along the molecular packing is defined as a vector, *z*. The pitch angle (*P*) and its distance (d_p) are corresponding to the molecular slipping along Z_L direction and the vector, *d*. The roll angle (*R*) and its distance (d_r) are represented between the projection of molecules in the short molecular axis Z_s and *d* vector. The total slip distance, $d_{tot} = (d_p^2 + d_r^2)^{1/2}$ and

the crystallographic repeat distance, $z = (d_p^2 + d_r^2 + d^2)^{1/2}$ were obtained from the pitch and roll parameters.⁶⁶

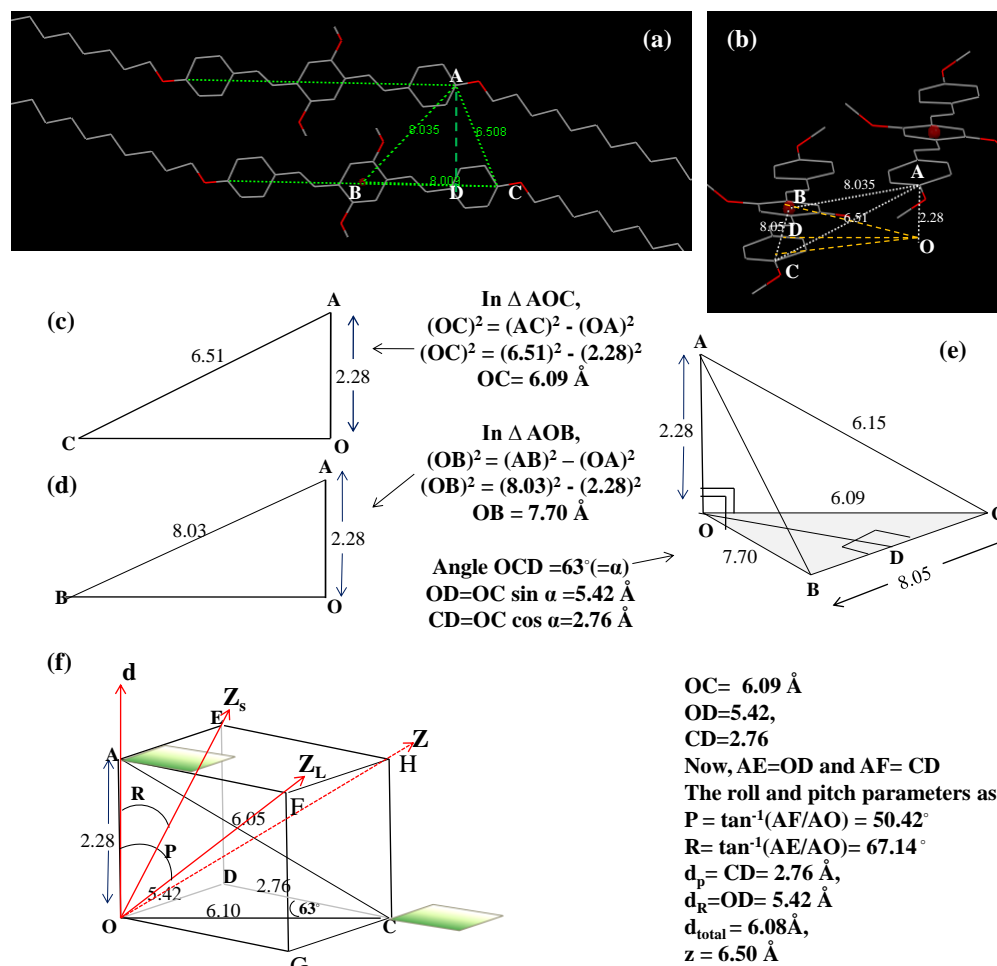


Figure 2.21. Determination of Roll and Pitch displacements for OPV-12.

The detailed procedure for the determination of d_p , d_r , P , R , d_{tot} and z for OPV-12 have been explained in figure 2.21. In figure 2.21a; a line segment AC was drawn which connects the identical parts of the two adjacent molecules. Another line segment AB connected A to B (centroid of the middle aromatic ring of the neighbouring molecule). In figure 2.21b, AO is the perpendicular distance from A to the molecular plane of the adjacent molecule. O was now joined to B and C to define a new triangle OBC. OC was determined to be 6.09 Å. Similarly, in the right angle

Δ , AOB, (in figure 2.21d), OB was determined to be 7.70 Å. Then, with the compass width equal to the line segment OC and the compass point on C, an arc was drawn near the future vertex O. Now, with the compass width equal to the line segment OB, and compass point on B, an arc crossing the first arc was drawn. The intersection point is the vertex O of the Δ OBC. Now, the angle $\text{OCD} = \text{OCB} = 63^\circ$ (α) was measured. In the Cuboid AOGFHEDC, (Figure 2.21f) A and C constituted the two diagonally opposite corners of a rectangular cuboid. The height of the cuboid constituted the interplanar distance d ($=$ AO). A similar procedure was followed to calculate roll and pitch distortions in OPV-8 and OPV-4. The detailed calculations for the determination of roll and pitch parameters for OPV-8 and OPV-4 has been pictorially summarized in figure 2.22.

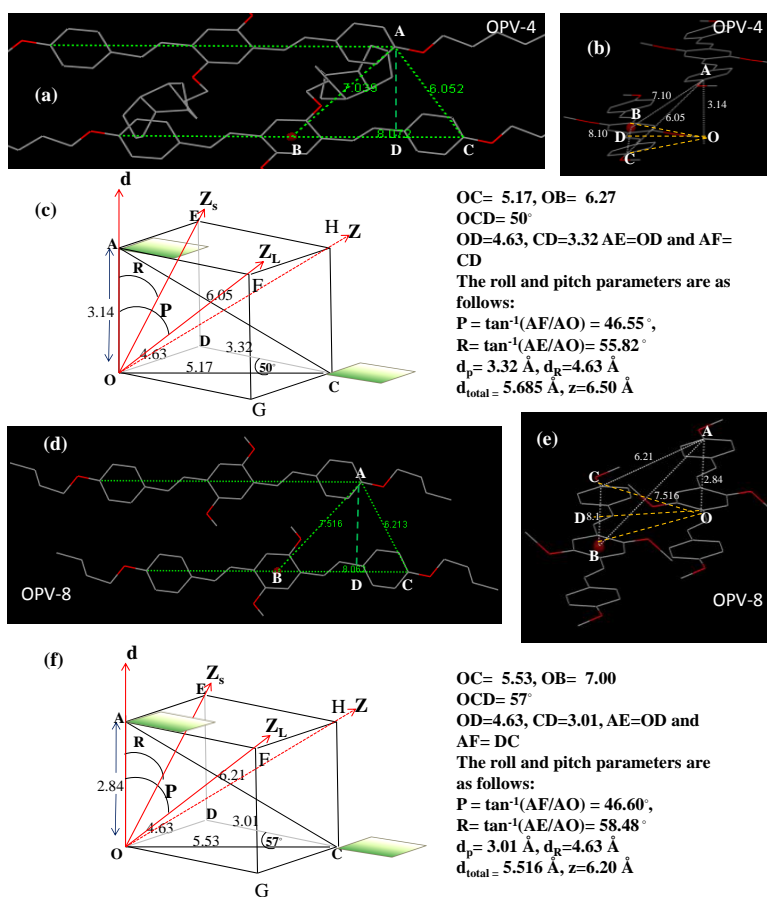


Figure 2.22. Determination of Roll and Pitch angles for OPV-4(a, b and c) and OPV-8. (d, e and f).

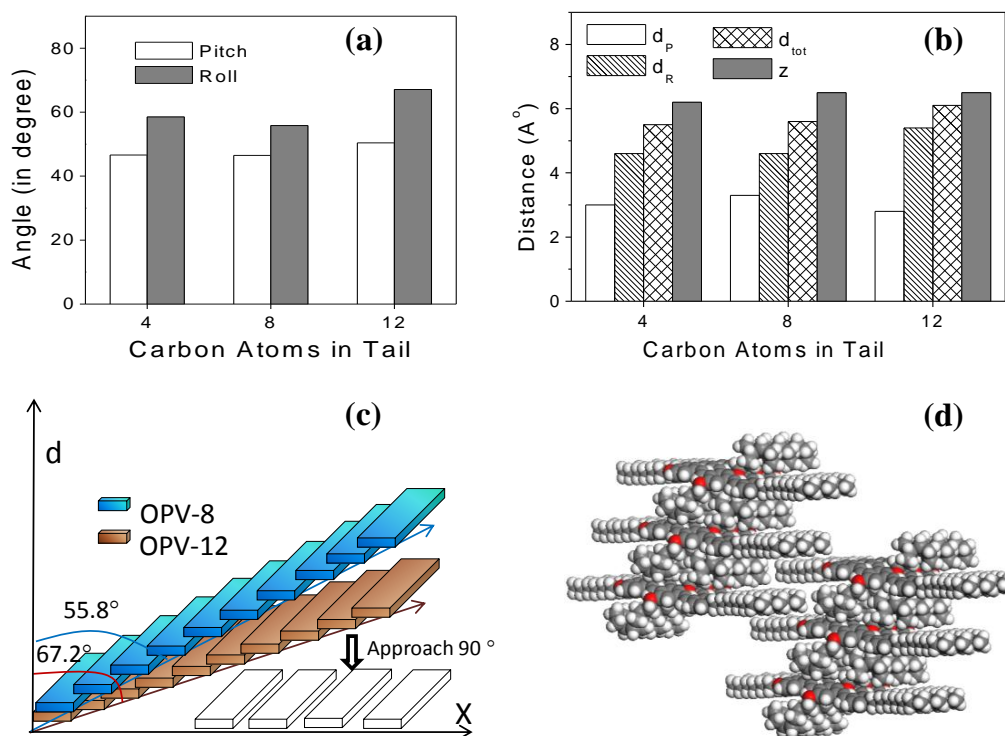


Figure 2.23. Pitch and Roll angles of OPVs (a) and Pitch and Roll distances (b) versus number of carbon atoms in the tail. Schematic representation of roll inclination in OPV-8 and OPV-12 (c) and single crystal packing of OPV-12 (d).

The plot of the pitch and roll angles versus the number of carbon atoms in OPV molecules has been shown in the figure 2.23. The data revealed that the molecules underwent a pitch angle distortion of 46.6° to 50.4° with increase in the number of C-atoms in the tail. On the other hand, the roll angle distortion was found to be much stronger and varied from 55.8 to 67.2° (~12°). In figure 2.23b, the shift distances are plotted against the variation in the C-atoms in the tail. Among the three molecules, the pitch distance varied only by 0.56 Å, however, the variation in the roll distance, $d_R = 0.90$ Å which was almost twice as compared to the pitch distances. This suggested that the effect of roll inclinations in the OPV molecules were much stronger compared to that of their displacement in the pitch direction. The increase in the tail length increased the roll angle; as a result, the OPV-12 molecules inclined more towards the x -axis to attain layer like self-assembly. This suggested that OPV-

12 molecules had more tendency for packing the chromophores in a parallel layers. This was further evident from the OPV-12 molecular arrangements in the crystal lattices (see figure 2.23d) where each stack of molecules appeared as isolated pillars along the z -axis (direction towards \mathbf{d} vector in figure 2.23d). In figure 2.23b, the total slip distance (d_{tot}) and crystallographic repeat distance (z) increased with the increase in the carbon atoms in the tail. The values of d_{tot} and ' z ' in all the cases were found to be more than 5.50 Å, which was much higher than that of the typical aromatic π -stacking distances (<3.50 Å) observed in graphite.⁶⁸ A schematic model depicting the roll inclinations has been shown in the figure 2.23.c. It was observed that the large increase in roll inclinations in the OPV molecules with increase in tail length from OPV-8 to OPV-12 led the molecules to incline more towards the x -axis to attain layer like self-assembly. Thus, it may be concluded that these OPV molecules did not possess any aromatic π -stack interaction in the solid state. Therefore, the diversity in the self-assembly of OPV chromophores in the solid state was driven by secondary forces other than aromatic π -stacking interactions.

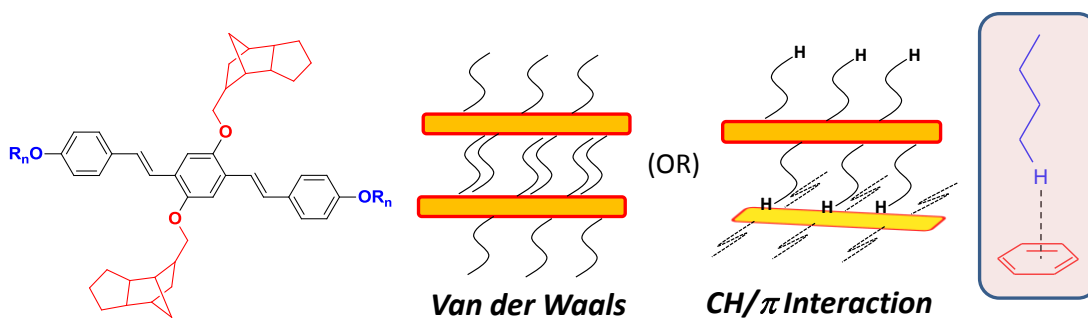


Figure 2.24. Cartoon diagrams of van der Waals and CH/ π interactions.

Large roll and pitch displacements completely destroyed π - π stacking interactions among the OPV molecules. The other possibilities for self-assembly can be either the van der Waals interaction present in the tails or weak CH/ π interactions between alkyl hydrogens and aryl rings as shown in the figure 2.24. Therefore, single crystal X-ray structure analysis was used to trace the presence of CH/ π interactions in these OPV molecules.

2.3.7. CH/ π Hydrogen Bonds

CH/ π hydrogen-bond interactions constitute an important class of weak non-covalent forces in producing well-defined secondary or tertiary structures⁶⁹ in biomacromolecules like proteins. The interactions between C-H bonds and π systems with the C-H group as hydrogen donor and π ring acting as are known as CH/ π interactions.⁷⁰ The energy associated with CH/ π interactions are much smaller (0.8 kcal mol⁻¹) relative to that of typical strong hydrogen-bonding interactions between OH \cdots H or NH \cdots H (7.8 to 3.5 kcal mol⁻¹).⁷¹ The CH/ π interactions have been projected as one of the main driving force in the complex formation of proteins with cofactors and stabilization of water molecules in the hydrophobic cavity, for example, for photosynthesis.⁷² The CH/ π interactions were also observed in chemical research⁷³ in organic molecules and inorganic crystals.⁷⁴ π -conjugated oligomers (or polymers) are one of the most promising chemical motifs for studying CH/ π interactions in the self-assembly approach because molecules possessed 1) rigid aromatic π -conjugated backbones (or extended π systems) which can serve as H-bond acceptors and 2) flexible alkyl chains anchored on the periphery for solubility purposes, which can behave as H-bond donors (CH groups).

To trace the inter-molecular interactions accountable for the self-assembly in the OPVs, the close-contact between the adjacent molecules were established. The close contact interactions in OPV-12 molecule are shown in figure 2.25.a. Each OPV-12 molecule had close contact with four neighboring molecules. Two of the molecules (green color) lay on the same plane along the *a*-axis at a distance of 6.51 Å and other two (orange color) lay above and below the plane of the central molecule along *b*-axis at 13.23 Å. Total eight CH/ π interactions per molecule (2 x 4 different types) were observed between the alkyl C-H of TCD units to the aryl rings or vinylene C=C bonds. Each pair of these interactions corresponded to C-H_{55A} to terminal aryl ring, C-H_{62A} and C-H_{51A} to central aryl ring (above and below) and C-H_{64A} to vinyl C=C bond. These multiple CH/ π interactions extended along the *b*-axis throughout the crystal lattices.

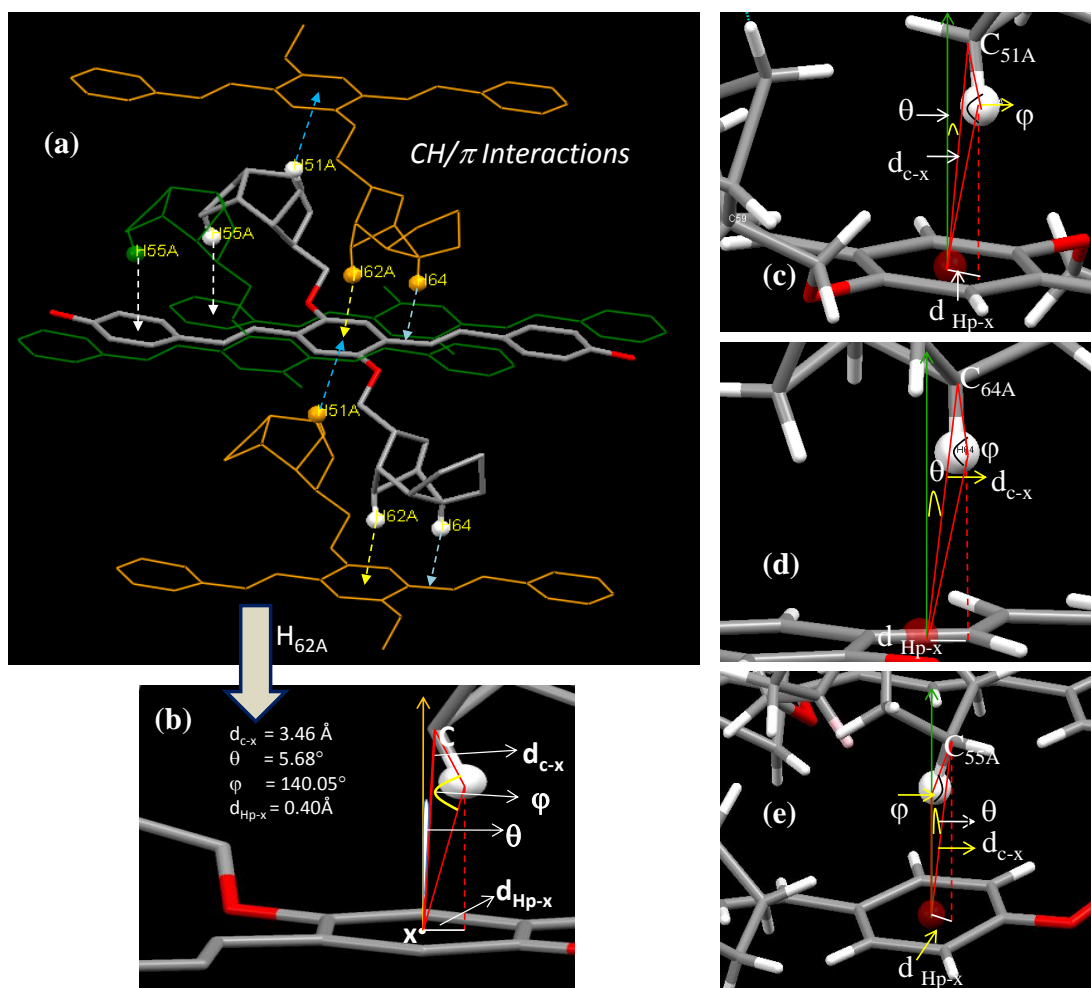


Figure 2.25. *CH/π interactions in OPV-12 along three dimensional crystal lattice. (In the orange and green molecules part of one of the TCD was omitted for clarity), Determination of CH/π interactions in OPV-12 for C_{62A} (b), C_{51A} (c), C_{64A} (d), C_{55A} (e).*

Four important crystallographic parameters determined the CH/π interactions: d_{c-x} , θ , φ and d_{H_p-x} ; where d_{c-x} is the distance between the donor carbon atom to the center of the acceptor π -ring, θ is the angle between the ring normal and a vector connecting the donor carbon atom to the center of the aryl ring, φ is the angle between C–H with the vector connecting H to ring center, and d_{H_p-x} is the projection of the C–H on the π -ring.^{69a} The determination of these C–H/π crystallographic parameters have been explained in the figure 2.25b, c ,d, and e. The CH/π parameters

were in accordance with the literature reports^{69a} and confirmed the existence of multiple arm strong CH/ π interaction in the OPV-12 molecules.

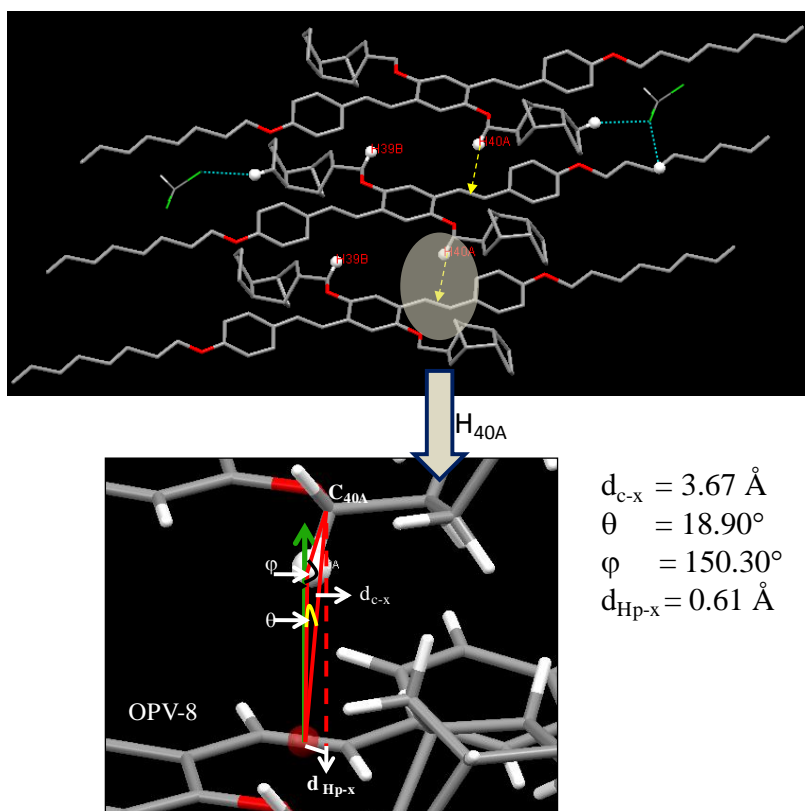


Figure 2.26. Calculation of CH- π interactions for OPV-8.

The close contacts and the determination of CH/ π interactions in OPV-8 have been shown in the figure 2.26. OPV-8 showed two identical CH/ π interactions per molecule between C-H_{40A} to C=C bond. The CH/ π interactions observed in OPV-8 were completely different from that of OPV-12: (i) the H-acceptor i.e., vinyl C=C bond in OPV-8 was relatively weak^{69a} compared to that of the strong aryl ring acceptor in OPV-12 and (ii) the existence of multiple arm CH/ π interaction locked the 3D movement of central aromatic core in OPV-12 which was completely absent in OPV-8. As a result, though OPV-8 has CH/ π interactions, it did not have strong inter molecular locking (as seen in OPV-12) and turned out to be simple liquid crystalline material. OPV- 4 did not show any CH/ π interactions validating required

crystallographic geometric parameters. In the absence of CH/ π interactions, OPV-4 packed in the herringbone motif. The detailed CH/ π parameters have been summarized in the table 2.3.

Table 2.3. Table of CH/ π parameters for OPVs.

Sample	C-H	π	d_{c-x} (Å)	θ (°)	ϕ (°)	d_{Hp-x} (Å)
OPV-12	C-H _{55A}	Aryl	3.73	15.46°	161.9	0.50
	C-H _{51A}	Aryl	3.61	15.06°	138.1	0.84
	C-H _{62A}	Aryl	3.46	4.83°	140.0	0.27
	C-H _{64A}	C ₂₀ =C ₂₁	3.64	12.57°	160.0	0.33
OPV-8	H _{40A}	C ₁₅ -C ₁₆	3.67	18.90°	150.30	0.61

Single crystal XRD analysis clearly revealed the presence and role of CH/ π interaction in the three dimensional packing of TCD- OPVs. The long terminal alkyl chains did not show any type of interactions among themselves or with aryl units (or with TCD units). But, van der Waals interactions which are difficult to measure may still play an important role in determining packing properties and molecular self-organization.

2.3.8. PLM images in Single crystal and Powder Samples

Liquid crystalline mesophases were obtained via molecular self-assembly under solvent-free crystallization process. On the other hand, single crystals were grown slowly using solvent assisted processes. Therefore, it is very important to confirm that the LC morphologies obtained during PLM analysis are independent of crystallization technique. And hence, the PLM images obtained from single crystal and powder samples should be identical. Further, to establish the existence of CH/ π interactions in the LC mesophase morphology, similar to the single-crystal structures, a direct correlation between the simulated X-ray patterns from single crystals and X-ray patterns obtained from powdered samples should be made.

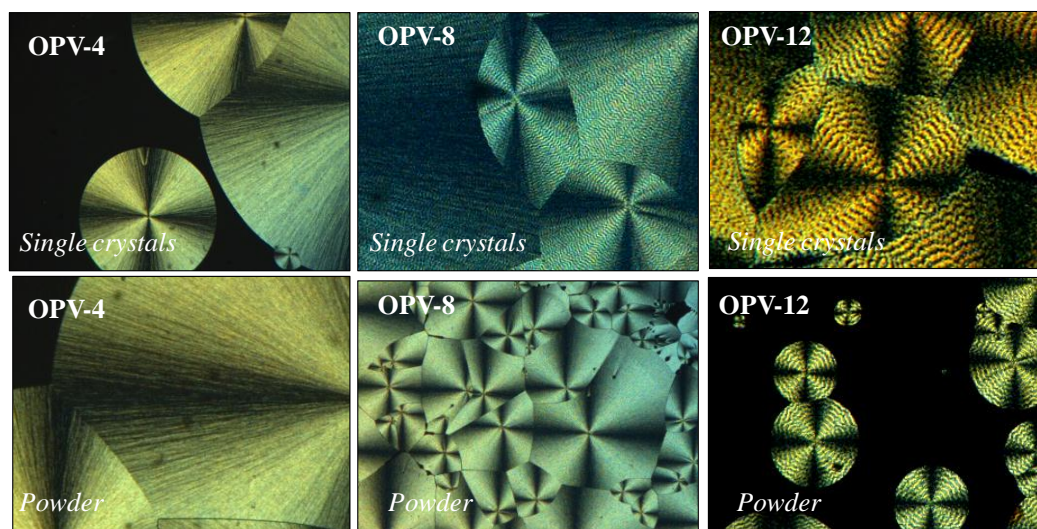


Figure 2.27. LC textures of OPV-4, OPV-8 and OPV-12 grown from single crystal and powder samples.

To confirm the similarity of LC textures, the mesophase morphology of the samples was independently analyzed using polarizing light microscope (PLM) and shown in figure 2.27. Single crystals of OPV-4 and OPV-8 exhibited patterns with respect to crystalline and cholesteric mesophases, respectively. OPV-12 exhibited birefringence pattern consisting of concentric dark and bright rings as shown in figure 2.27. This analysis suggested that the mesophase morphologies were identical irrespective of their sample source like single crystals or powder samples.

The existence of CH/ π interactions in the LC mesophase morphology, similar to the single-crystal structures, was confirmed by variable-temperature powder X-ray diffraction studies. The variable temperature XRD patterns for OPV-12 while cooling from isotropic melt has been shown in the figure 2.28a. The temperature range for the experiment was chosen based on the molecule's LC transitions in DSC traces. Simulated powder pattern obtained from single crystal data has been shown in the figure 2.28b. The sample completely melted to isotropic phase at 170 °C. Upon cooling from isotropic melt, in the LC active temperature range (at 110 °C), the sample showed very broad signals which confirmed their liquid crystalline nature.

On further cooling to room temperature, intense crystalline peaks appeared in the wide-angle region corresponding to transition to crystalline solid.

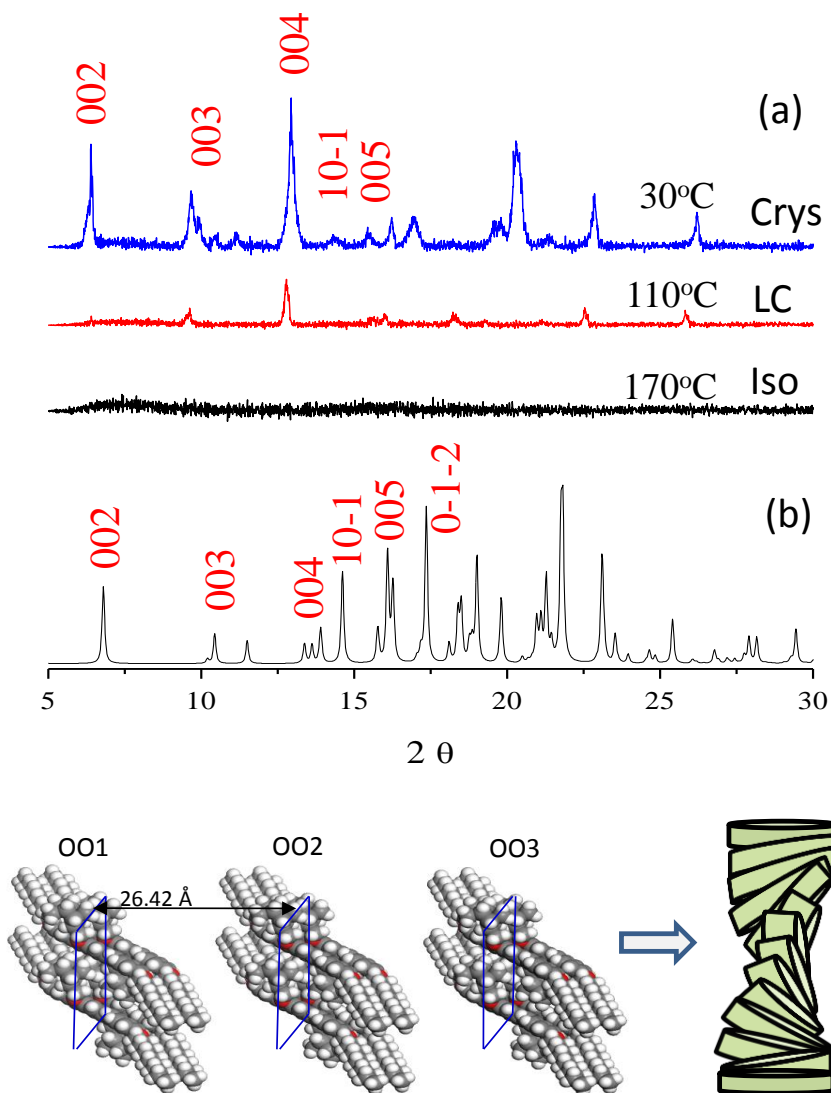


Figure 2.28. (a) Variable temperature XRD pattern (b) Single crystal powder pattern, and a molecular model depicting the formation of equidistant lamellae in OPV-12.

A comparison of experimental XRD patterns with the simulated powder X-ray diffraction patterns^{75, 76} based on the single crystal structure revealed that the miller index values for each peak in the simulated XRD plot matched very well with that of the variable temperature experimental plots. This confirmed that the

crystalline lattices in the single crystal were identical to that present in the LC phases. The perfect matching of single crystal structural data with the powder XRD confirmed the formation of crystal lattices in the LC-phases via CH/ π interactions. Similarly, the variable temperature XRD pattern and simulated single crystal pattern for OPV-8 and OPV-4 showed that the miller index values for each peak in the simulated XRD plot matched very well with that of the variable temperature experimental plots. From the above analysis, it can be concluded that packing of chromophores in LC state is almost identical to that observed in their single crystal state and can be extended to explain the molecular arrangements and mesophase morphologies in the LC state.

2.3.9. Mechanism of Helical rings- *The Grandjean Lines*

The concentric dark and bright rings in OPV-12 are simply the Grandjean lines that are typically observed in chiral nematic N* liquid-crystalline mesophase.³⁸ The appearance of dark and bright lines under plane-polarized light is schematically illustrated in figure 2.29.³⁸

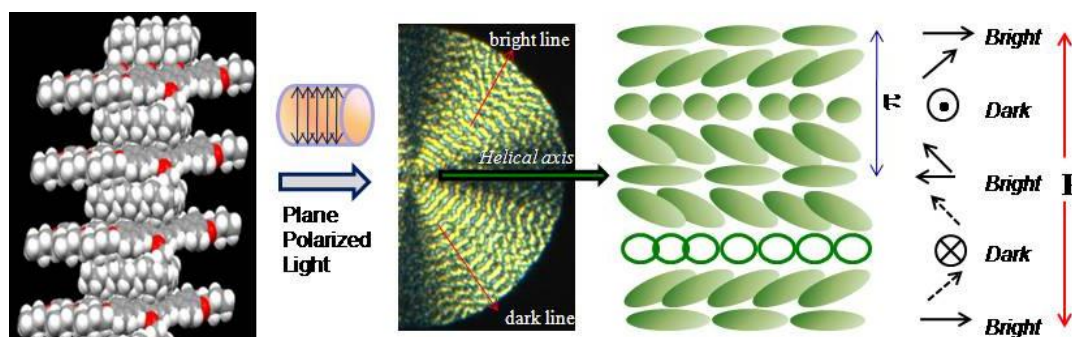


Figure 2.29. Formations of helical assemblies in OPV-12.

The dark lines were observed when the helical twist changes by p . From the distance l between the two lines, the pitch length p of the helix could be calculated as $l = p/2$. The bright lines are observed when plane polarized light passes parallel to the molecular axis and the dark lines are observed when the molecules fall perpendicular to the direction of light.

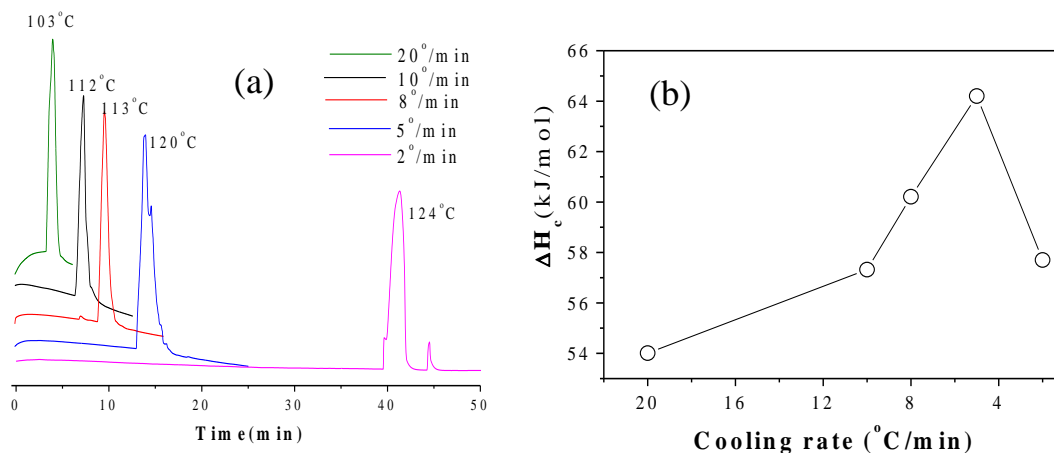


Figure 2.30. A plot of number of carbon atoms versus pitch length (a) pitch length of the Grandjean lines versus cooling rates (b) and time need for the formation /per ring versus cooling rates (c).

Experimental conditions such as the rate of cooling play an important role in determining transition temperatures, enthalpy of transitions and subsequent formation of the Grandjean lines. A plot of $T_{\text{iso-LC}}$ versus cooling rate has been shown in the figure 2.30a. It was observed that the temperature corresponding to isotropic to LC phase change gradually increased with decrease in the cooling rate from 103 °C at 20°/min to 124 °C at 2°/min. Similarly, a plot of enthalpy of crystallization versus the cooling rate (figure 2.30 b) exhibited that the enthalpies gradually increased with decrease in the cooling rates until a dramatically low value was observed at 2°/min.

To study the influence of cooling rate on the formation of Grandjean lines, PLM analysis was done by cooling OPV-12 at variable cooling rates. The PLM textures with respect to different cooling rates have been shown in the figure 2.31. It was observed that the textures were independent of cooling rate and similar Grandjean lines were produced irrespective of the cooling rate. This confirmed that ring banded textures was indeed a molecular property for this class of molecules.

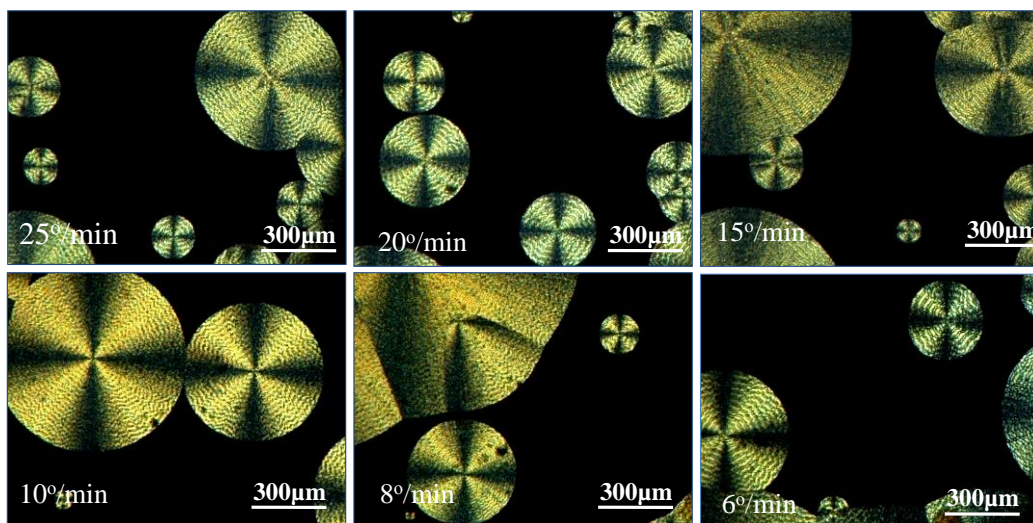


Figure 2.31. LC mesophase textures for OPV-12 at different cooling rates.

The PLM images of OPV-12 captured as a function of time by keeping the cooling rate constant at 10 °/ min has been shown in the figure 2.32. The ring banded spherulites grew radially and vertically outwards with time.

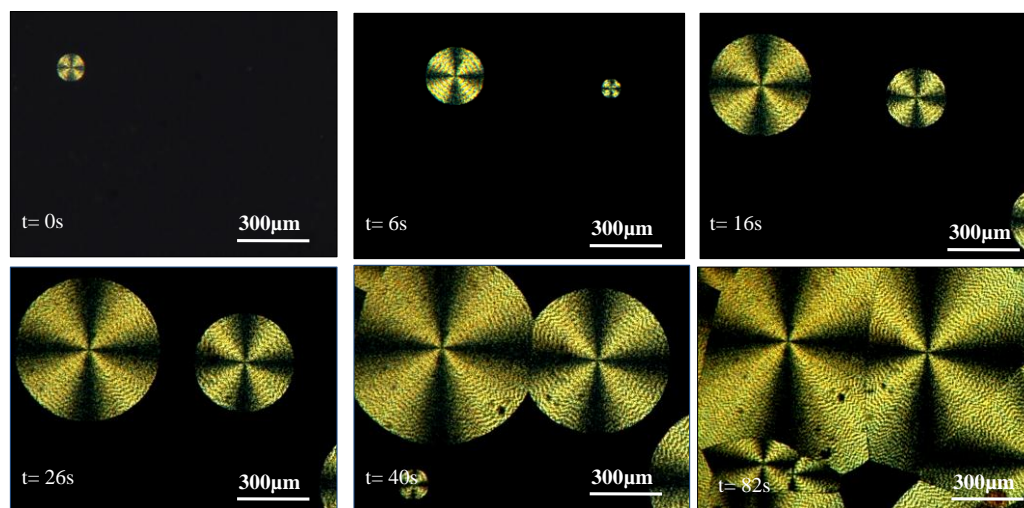


Figure 2.32. PLM images for tracing formation of Grandjean lines with capturing time.

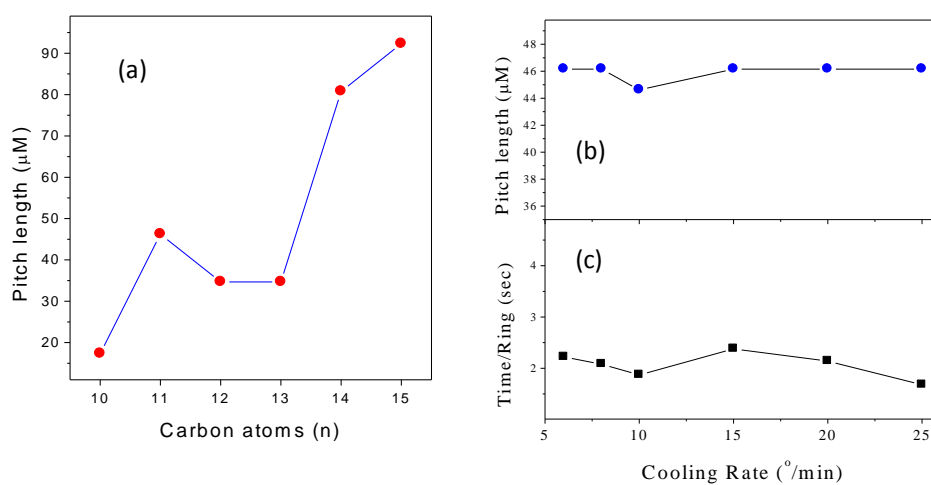


Figure 2.33. A plot of number of carbon atoms versus pitch length (a) pitch length of the Grandjean lines versus cooling rates (b) and time need for the formation /per ring versus cooling rates (c).

To summarize the effect of experimental conditions on ring band formation a plot of pitch length versus number of carbon atoms in the alkyl side chains has been plotted in the figure 2.33a. The pitch lengths of helical rings gradually increased with increasing number of carbon atoms in the tail up to $n = 5$ and lost this tendency at $n = 16$ in OPV-16. The pitch length in OPV-12 was determined to be $44.7 \pm 2.9 \mu\text{m}$. The pitch length is typically constituted by hundreds and thousands of molecules in lamellae which subsequently twist to give helical superstructure.³⁸ The pitch length can vary from as small as 100 nm to many micrometers. Similarly, a plot of pitch length of the Grandjean lines versus cooling rates (see figure 2.33b) and time needed for the formation /per ring versus cooling rates (figure 2.33c) revealed that both the pitch lengths as well as time/per ring versus cooling rates followed a straight line with almost zero slopes. This confirmed that the variation in the experimental conditions did not affect the nature of the morphology and pitch length of the Grandjean lines. Formation of the helical assembly was not affected by cooling from the isotropic state under either non isothermal or isothermal conditions. Hence, the ring-banded self-assemblies in the TCD-OPVs are a molecular property which is driven by both the number of carbon atoms in the alkyl chain and CH/π interactions.

2.3.10. Circular Dichroism Analysis

Circular dichroism (CD) spectra of the OPVs were recorded to gain more insight into their LC mesophase helical morphology. The CD spectra of OPV samples were recorded in toluene and in the solid state (fine powder) have been shown in the figure 2.34a and 2.34b.

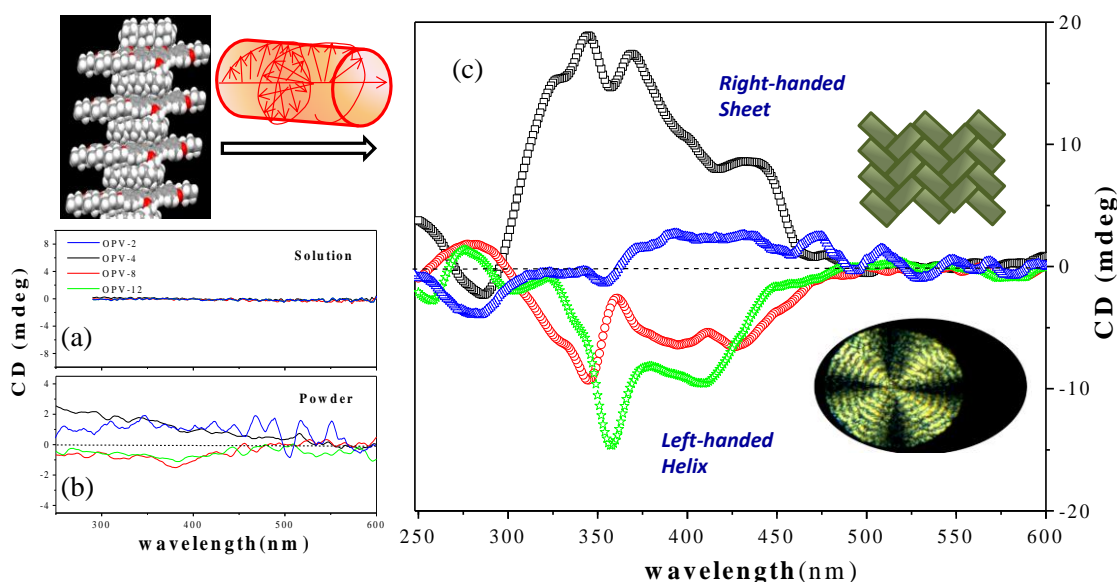


Figure 2.34. CD spectra of OPV-2, OPV-4, OPV-8 and OPV-12 in toluene (a) and in powder states (b) Solid state CD spectra of aligned OPV samples in their LC state (c).

The absence of CD signals in solution state confirmed that no helical self-organization existed in the solution state (see figure 2.34a). Therefore, the presence of weak chiral center in the TCD units (at the bridging carbon atom $\text{ArOCH}_2\text{C}^*\text{H}$) did not provide any additional advantages for molecular self-assembly in solution. In the powder state (see figure 2.34b), the samples showed very weak CD signals. The samples showed only weak positive cotton effect in the case of OPV-2 and OPV-4 and weak negative cotton effect in the case of OPV-8 and OPV-12. The CD spectra of OPVs in LC frozen state have been shown in Figure 2.34c. On aligning the molecules in the thin layer (OPV-4) or LC mesophase (OPV-8 and OPV-12; samples

were made as per the method described for PLM studies), self-organization became predominant and strong CD signals emerged from OPV- 4, 8 and OPV-12. OPV-4 showed a strong positive Cotton effect with maximum at 345 nm and zero crossing at 295 nm. This indicated that the OPV-4 molecules were arranged as right-handed sheet-like structures. In contrast, OPV-8 and OPV-12 showed intense negative CD signals corresponding to absorption of left circularly polarized light (negative Cotton effect). The CD spectrum of OPV-12 showed two strong negative bands at 357 and 408 nm and a weak positive band at 275 nm (OPV-8 also showed a similar trend). The features of these negative signals in OPV-12 (and also in OPV-8 and OPV-11) confirmed that the molecules were arranged in the left-handed helical assembly. An important observation was that OPV-2, which is a simple crystalline solid, did not give any strong CD signal even in LC aligned state. Hence, the helical lines observed under the plane-polarized illumination in OPV-12 molecules (see Figure 2.34) are nothing but helical self-assemblies of the lamella in the solid state. This further confirmed that CD signals observed in the case of OPV-4, OPV-8 and OPV-12 are a direct consequence of self-organization in the LC state. Thus, a perfect correlation between the LC helical mesophase (observed under PLM) with the helical supramolecular structures (in CD signals) was established in solid-state self-assembly.

Based on the above analysis a schematic model depicting the change in self-assembly with respect to the number of carbon atoms in the terminal alkyl chains have been proposed in the figure 2.35.

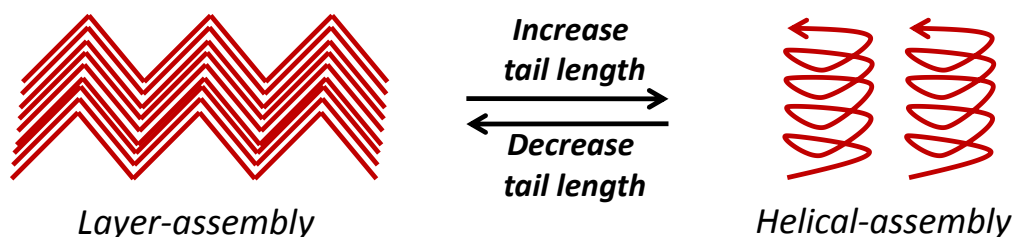


Figure 2.35. Representation of chain length driven self-assembly in OPVs.

Diverse self-assembly was achieved by only varying the number of carbon atoms in the tails. Increasing the number of carbon atoms in the tails transformed the chromophore packing from herringbone to left-handed helical twist in the chiral nematic mesophase. On the other hand, on decreasing the tail length, the chromophores organized in highly packed herringbone patterns. For longer alkyl chains ($n > 14$), the packing of the chromophore were no longer controlled by the tails and the molecular self-assemblies were lost.

2.3.11. Photophysical Analysis

The OPV building block is a highly luminescent π -conjugated unit, and therefore, photophysical characterization such as absorption, excitation, emission, and time resolved fluorescence decay measurements were employed to trace molecular self-organization in the liquid crystalline phase.⁷⁷ The absorption and the emission spectra in solution and solid state have been shown in the figure 2.36.

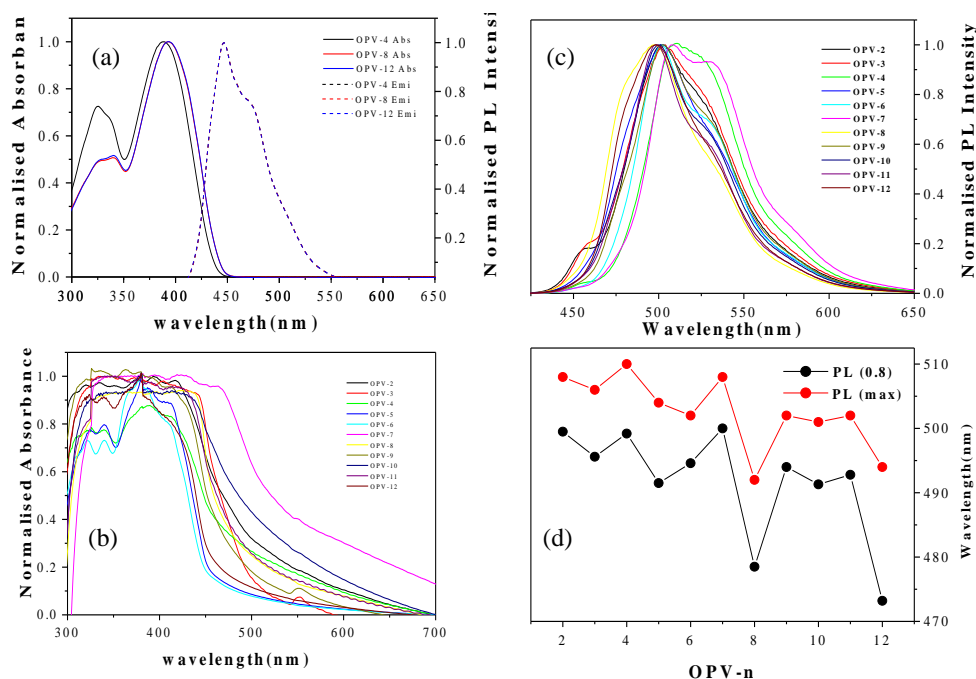


Figure 2.36. Absorption and emission spectra of OPVs in toluene (a), Absorption (c) Emission spectra in the LC frozen films(d) (excitation= 380 nm). Plot of emission wavelengths versus number of carbon atoms in the alkyl chain. The emission spectra in solution state for all the samples were exactly overlying on each other.

Figure 2.36a showed that the absorption and the emission spectra of all the OPVs were identical in solution state. This suggested that the molecules were in molecularly dissolved state and there was no difference in the photophysical properties. In the solid state, the photophysical properties were studied up to OPV-12 because the transition from herringbone to helical self-assembly was observed up to the chain length twelve, beyond which the self-organization was lost. Thin films of OPVs were prepared on a glass substrate, as described earlier in PLM studies. Figure 2.36b shows the emission spectra of OPVs in solid state. OPV-0 and OPV-1 were omitted for the photophysical studies due to the following reasons: (i) OPV-0 did not have alkoxy units in the peripheral phenyl ring and (ii) the Ar-OCH₃ inductive effect causes π -electronic structure of OPV-1 to be different from that of other OPVs. The emission spectra of OPVs were very broad and therefore, to quantify the extent of the red or blue shift among the OPV samples, emission wavelengths (in nm) at PL intensities of 0.8 and 1.0 were compared in their normalized spectra.

The plots of the emission wavelengths at PL intensities 0.8 and 1.0 have been given in figure 2.36d. Two important observations could be made from the emission spectra of OPV-*n* films: (a) both the plots in figure 2.36d showed odd-even oscillation in the emission wavelength with respect to the number of carbon atoms in the alkyl chains and (b) OPV-8 and OPV-12 were distinctly blue-shifted compared to all other OPVs. Interestingly, the odd-even oscillation in the emission spectra was not restricted to any particular type of LC texture. It was observed across the entire series in crystalline solids (OPV-2 to OPV-4), cholesteric LCs (OPV-5 to OPV-9), and ring-banded LCs (OPV-10 to OPV-12). The comparison of the odd-even oscillation behavior in the enthalpy plots and emission spectra (in Figure 2.36d) revealed that the highly crystalline and packed samples showed more blue shift compared to that of less crystalline counterparts. The extent of the blue shift was observed to be very large in OPV-8 and OPV-12, which possessed highly packed structures with higher energy terms. The highly packed structures were expected to possess strong π -overlap among the OPV- chromophores, which led to a blue shift in their emission spectra (OPV-8 and OPV-12) compared to the spectra of the weakly

packed samples (OPV-9 and OPV-11). A large number of PL experiments were carried out to verify the reproducibility of the odd-even oscillation behavior in the emission spectra. More than four sets of newly prepared LC films for each OPV samples were subjected to photoluminescence studies. Since the absorption spectra of the OPVs were very broad from 320 to 420 nm, the emission spectra were also collected by exciting the samples at 320, 340, 360, 380, 400, 420, and 440 nm. Though there is a slight deviation in the wavelength of the emission spectra, all these control experiments showed perfect reproducibility in the odd-even oscillation in their emission spectra. Therefore, the odd-even oscillation in the PL spectra was not an artifact; it is a molecular property that arose via the differences in the molecular packing among the OPV chromophores. The highly packed even numbered OPV-*n* molecules showed a blue shift compared to that of less or weakly packed odd number counterparts. The extent of the packing and blue shift was found to be predominant for alkyl chain lengths *n* = 8 and *n* = 12.

Table 2.4. Photophysical measurements of OPV samples in solid films and toluene.

Sample	Absorbance ^a $\lambda_{\max}(\text{nm})$	Emission ^b $\lambda_{\max}(\text{nm})$	τ_1 (ns)	τ_2 (ns)	χ^2
OPV- 2	392	500	0.30	1.19	1.003
OPV- 3	389	495	0.26	1.26	1.010
OPV- 4	388	499	1.19	2.34	1.001
OPV- 5	387	492	0.39	1.36	1.140
OPV- 6	390	494	0.40	1.48	1.001
OPV- 7	391	513	0.27	1.21	1.001
OPV- 8	390	478	0.41	1.95	1.001
OPV- 9	392	494	0.39	1.60	1.056
OPV- 10	389	491	0.33	1.47	1.005
OPV- 11	390	493	0.40	1.62	1.054
OPV- 12	387	473	0.36	1.77	1.020

(a and b) Measured in the LC frozen film at 25 °C.

Time dependent fluorescence decay measurements were carried out by the TCSPC technique using 370 nm nano-LED light sources. The thin films of samples employed for the PL studies were used for the fluorescence decay measurements. At least two sets of samples were subjected for each OPV to confirm the reproducibility

of the decay profiles. The decay profiles for few representative OPV molecules are shown in figure 2.37.

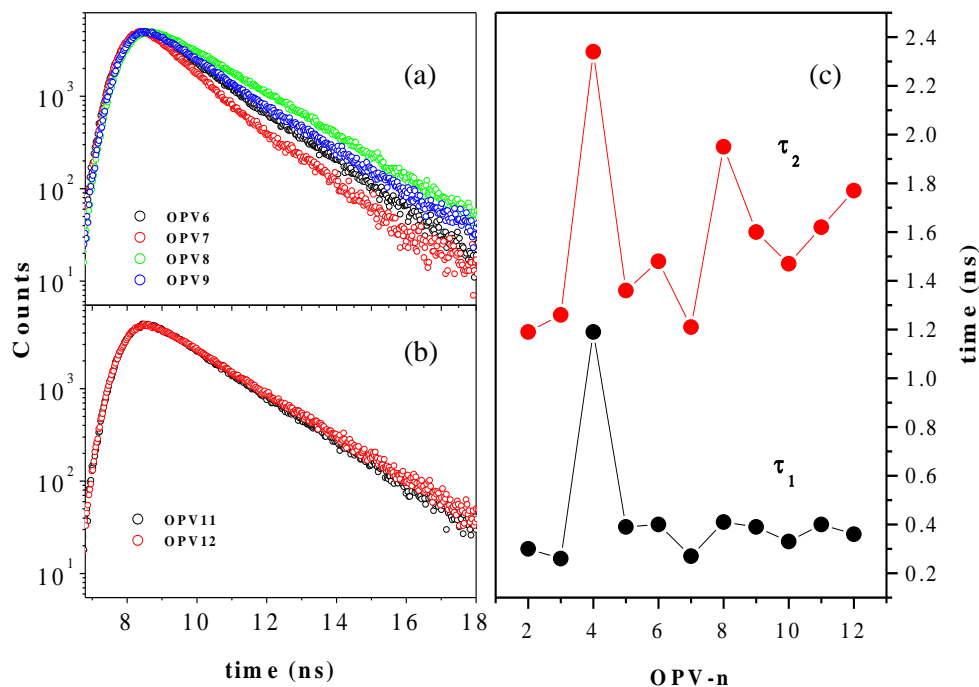


Figure 2.37. Fluorescence decay profiles of OPVs (a and b), plot of life times versus the number of the carbon atoms in the alkyl chains (c).

All the decay data followed a bi-exponential fit and their lifetime values are summarized in Table 2.4. All the OPV samples typically showed a fast decay with a lifetime of $\tau_1 = 0.28\text{-}0.40$ ns and slow second decay with $\tau_2 = 1.2\text{-}2.4$ ns. The τ_1 and τ_2 values matched with that of the earlier reports for OPV systems.³³ The τ_1 and τ_2 values were plotted against the number of carbon atoms in the alkyl chains and shown in Figure 2.37c. The overall trend of the lifetime values showed that the decay is faster for odd-OPVs when compared to their even-OPV counterparts. Among all the OPVs, the τ_2 values for OPV-8 (1.95 ns) and OPV-12 (1.77 ns) were found to be much higher, indicating their high luminescent characteristics. All the above analysis confirmed their strong self-organization for the existence of H-type aggregates in these two OPVs. Nevertheless, it has been proven in the present system that the

difference in the alkyl chain packing in the π -conjugated OPV backbone resulted in the difference in LC textures, molecular packing, and subsequently, their photophysical properties.

Photophysical characterization of OPV chromophores in single crystal state showed that the emission spectra of OPV-4, OPV-8 and OPV-12 in both LC phase and single crystals were almost identical with maxima at 490 nm. TCSPC technique revealed that the OPV chromophores showed relatively identical lifetime values irrespective of their occupancy either in the herringbone sheets (in OPV-4) or in the helical self-assembly (OPV-12 and OPV-8). The absence of aromatic π -stack interactions (responsible for photophysical variation) among the chromophores accounted for this similarity in PL characteristics. Thus, without altering luminescent characteristics of the π -conjugated chromophores, diverse self-assembly was achieved by only varying the number of carbon atoms in the tails.

2.4. Conclusion

In conclusion, a new series of bulky π -conjugated oligophenylenevinylenes (OPVs) based on tricyclodecanemethylene units with variable alkyl chain lengths in the longitudinal position were synthesized. DSC analysis revealed that the enthalpies and entropies of the melting and isotropic-to-LC transitions interestingly followed odd-even oscillation. OPV molecules with shorter alkoxy chains ($n=0-4$) were found to be crystalline solids. OPV-5 to OPV-9 produced fan shaped textures with focal conics and ring banded LC textures were observed for OPV-10 to OPV-15. The plot of melting temperatures against spacer length (n) showed a sigmoidal transition from crystalline to ring banded OPVs. Single crystal X-ray analysis revealed that solid state packing changed from herring bone (OPV-4) to helical self-assembly in OPV-12. Direct evidence for the CH/ π interaction was established on the basis of crystal structures of OPVs. The existence of multiple-arm CH/ π interaction was identified as the main driving force for helical self-assembly in the liquid-crystalline phase. Crystallographic parameters such as pitch and roll angles and their displacements were determined to find out the existence of π -stacking interactions. The large pitch and roll displacements completely destroyed the aromatic π -stacking interactions among the OPV chromophores. The larger roll displacements (67.28°) caused the OPV-12 molecules to incline towards the crystallographic b axis.

The existence of left-handed helicity in OPV-12 was further proved by a circular dichroism (CD) investigation in the solid state. CD studies revealed that the helical structures were produced only on aligning the chromophores in the LC mesophases, and were completely lost in solution. OPV-4 adopted a herringbone layer pattern and forms right-handed sheet-like structures. The uniqueness of the present approach is that both herringbone and helical assemblies could be simply varied by means of the number of carbon atoms in the tails. Though the approach demonstrated here is not restricted to any particular type of π -conjugated oligomers. The overall findings revealed that the CH/ π interaction is a very powerful non-covalent interaction in supramolecular chemistry.

2.5 References

1. Kraft, A.; Grimsdale, A.C.; Holmes, A. B. *Angew. Chem. Int. Ed.* **1998**, *37*, 402. (b) Zgierski, M. Z.; Fujiwara, T.; Lim, E. C. *Acc. Chem. Res.* **2010**, *43*, 506. (c) Bowden, N. B.; Weck, M.; Choi, I. S.; Whitesides, G. M. *Acc. Chem. Res.* **2001**, *34*, 231. (d) Hoeben, F. J. M.; Jonkheijm, P.; Meijer, E. W.; Schenning, A. P. H. *J. Chem. Rev.* **2005**, *105*, 1491.
2. Muller, K.; Wegner, G. *Electronic Materials: The Oligomer Approach*: Wiley-VCH: Newyork, **1998**.
3. Osterbacka, R.; An, C. P.; Jiang, X. M.; Vardeny, Z. V. *Science* **2000**, *287*, 839-842.
4. Siringhaus, H. Brown, P. J.; Friend, R. H.; Nielsen, M. M.; Bechgaard, K.; Langeveld-Voss, B. M. W.; Spiering, A. J. H.; Janssen, R. A. J.; Meijer, E. W.; Herwig, P.; de Leeuw, D. M. *Nature* **1999**, *401*, 685- 688.
5. Sokolov, A. N.; Evrenk, A. A.; Mondal, R.; Akkerman, H. B.; Carrera, R. S. S.; Focil, S. G.; Schrier, J.; Mannsfeld, S. C. B.; Zoombelt, A. P.; Bao, Z.; Guzik, A. A. *Nature Commun.* **2011**, *2*:437, 1-8.
6. (a) Schenning, A. P. H. J.; Jonkheijm, P.; Peeters, E.; Meijer, E. W.; *J. Am. Chem. Soc.* **2001**, *123*, 409-416. (b) Asha, S. K.; Schenning, A. P. H. J.; Meijer, E. W. *Chem. Eur. J.* **2001**, *8*, 3353-3360. (c) Herrikhuyzen, J. V.; Asha, S. K.; Schenning, A. P. H. J.; Meijer, E. W. *J. Am. Chem. Soc.* **2004**, *126*, 10021-10027. (d) Ajayaghosh, A.; Vijayakumara, C.; Varghese, R.; George, S. J. *Angew. Chem. Int. Ed.* **2006**, *45*, 456- 460. (e) Babu, S. S.; V. Praveen, K.; Prasanthkumar, S.; Ajayaghosh, A. *Chem. Eur. J.* **2008**, *14*, 9577 – 9584.
7. (a) Beck, J. B.; Rowan, S. J. *J. Am. Chem. Soc.* **2003**, *125*, 13922-13923. (b) Ghosh, S.; Ramakrishnan, S. *Angew. Chem. Int. Ed.* **2005**, *44*, 5441- 5447. (c) Ghosh, S.; Ramakrishnan, S. *Angew. Chem. Int. Ed.* **2004**, *43*, 3264- 3268.
8. (a) Lokey, R. S.; Iverson, B. L. *Nature*, **1995**, *375*, 3030-305. (b) Osswald, P.; Leusser, D.; Stalke, D.; Würthner, F. *Angew. Chem. Int. Ed.* **2005**, *44*, 250- 253. (c) Bhavsar, G. A.; Asha, S. K. *Chem. Eur. J.* **2012**, *17*, 12646-12658 (d)

- Prehm, M.; Liu, F.; Zeng, X.; Ungar, G.; Tschierske, C. *J. Am. Chem. Soc.* **2011**, *133*, 4906-4916.
9. (a) Jin, J.; Smith, D. W.; Glasser, S.; Perahia, D.; Fluoger, S. H.; Ballato, J.; Kang, S.W.; Kumar, S. *Macromolecules* **2006**, *39*, 4646. (b) Zheng, Q.; Jung, B. J.; Sun, J.; Katz, H. E. *J. Am. Chem. Soc.* **2010**, *132*, 5394.
10. (a) Curtis, M.; Nanos, J. I.; Moon, H.; Jahng, W. S. *J. Am. Chem. Soc.* **2007**, *129*, 15072. (b) Apperloo, J. J.; Groenendaal, B.; Verheyen, H.; Jayakannan, M.; Janssen, R. A. J.; Dkhissi, A.; Beljonne, D.; Lazzaroni, R.; Bredas, J. L. *Chem. Eur. J.* **2002**, *8*, 2384. (c) Luo, J.; Zhao, B.; Shao, J.; Lim, K. A.; Chan, H. S. O.C.; Chi, C. *J. Mater. Chem.* **2009**, *19*, 8327. (d) Mishra, A.; Ma, C. Q.; Bayerle, P. *Chem Rev.* **2009**, *109*, 1141.
11. (a) Trajkovska, A.; Kim, C.; Marshall, K. L.; Mourey, T. H.; Chen, S. H. *Macromolecules* **2006**, *39*, 6983. (b) Dudek, S. P.; Pouderoijen, M.; Abbel, R.; Schenning, A. P. H. J.; Meijer E. W. *J. Am. Chem. Soc.* **2005**, *127*, 11763. (c) Rathnayake, H. P.; Cripan, A.; Lahti, P. M.; Karasz, F. E. *Chem. Mater.* **2006**, *18*, 560.
12. (a) Wilson, J. N.; Steffen, W.; Mckenzie, T. G.; Lieser, G.; Oda, M.; Neher, D.; Bunz, U. H. F. *J. Am. Chem. Soc.* **2002**, *24*, 6380. (b) Sluch, M. I.; Godt, A.; Bunz, U. H. F.; Berg, M. A. *J. Am. Chem. Soc.* **1998**, *120*, 7973. (c) Prest, P. J.; Prince, R. B.; Moore, J. S. *J. Am. Chem. Soc.* **1999**, *121*, 5933. (d) Prince, R. B.; Saven, J. G.; Wolynes, P. G.; Moore, J. S. *J. Am. Chem. Soc.* **1999**, *121*, 3114. (e) Liu, R.; Chang, J.; Luo, W.; Li, Y.; Liu, S.; Zhu, H. *Colloids and Surfaces A: Physicochem. Eng. Aspects.* **2010**, *355*, 83.
13. (a) Abbel, R.; Grenier, C.; Pouderoijen, M. J.; Stouwdam J. W.; Leclere, P. E. L. G.; Sijbesma, R. P.; Meijer, E. W.; Schenning, A. P. H. J.; Meijer, E. W. *J. Am. Chem. Soc.* **2009**, *131*, 833. (b) Guerlin, A.; Dumur, F.; Dumas, E.; Miomandre, F.; Wantz, G.; Mayer, C. R. *Org. Lett.* **2010**, *12*, 2382. (c) Jorgensen, M.; Krebs, F. C. *J. Org. Chem.* **2004**, *69*, 6688-6696. (d) Jorgensen, M.; Krebs, F. C. *J. Org. Chem.* **2005**, *70*, 6004-6017. (e) Hegemann, O.; Jorgensen, M.; Krebs, F. C. *J. Org. Chem.* **2006**, *71*, 5546-5559. (f) Jiu, T.; Li,

- Y; Liu, H.; Ye, J.; Liu, X.; Jiang, L.; Yuan, M.; Li, C.; Wang, S.; Zhu, D. *Tetrahedron* **63**, 3168. (g) Guo, Y.; Li, Y.; Xu, J.; Liu, X.; Xu, J.; Lv, J.; Huang, C.; Zhu, M.; Cui, S.; Jiang, L.; Liu, H.; Wang, S. *J. Phys. Chem. C* **2008**, *112*, 8223.
14. (a) Gierschner, J.; Ehni, M.; Egelhaaf, H. J.; Medina, B. M.; Beljonne, D. *J. Chem. Phys.* **2005**, *123*, 144914-144914. (b) Zhao, C.; Wang, Z.; Yang, Y.; Feng, C.; Li, W.; Li, Y.; Zhang, Y.; Bao, F.; Xing, Y.; Zhang, X.; Zhang, X. *Cryst. Growth Des.* **2012**, *12*, 1227-1231. (c) Yoon, S. J.; Park, S. Y. *J. Mater. Chem.* **2011**, *21*, 8338-8346. (d) Gill, R. E.; Hutten, P. F. V.; Meetsma, A.; Hadziioannou, G. *Chem. Mater.* **1996**, *8*, 1341-1346. (e) Gill, R. E.; Meetsma, A.; Hadziioannou, G. *Adv. Mater.* **1996**, *8*, 212-214. (f) Xie, Z.; Wang, H.; Li, F.; Xie, W.; Liu, L.; Yang, B.; Ye, L.; Ma, Y. *Cryst. Growth Des.* **2007**, *12*, 2512-2516. (g) Melzer, C.; Brinkmann, M.; Krasnikov, V. V.; Hadziioannou, G. *ChemPhysChem* **2005**, *6*, 2376 – 2382.
15. Wang, C.; Dong, H.; Hu, W.; Liu, Y.; Zhu, D. *Chem. Rev.* **2012**, *112*, 2208-2267.
16. Gao, F.; Liao, Q.; Xu, Z.; Yue, Y. H.; Wang, Q.; Zhang, H. L.; Fu, H. *Angew. Chem. Int. Ed.* **2010**, *49*, 732 -735.
17. Hoag, B. P.; Gin, D. L. *Liquid Crystals* **2004**, *31*, 185.
18. Akcelrud, L. *Prog. Polym. Sci.* **2003**, *28*, 875.
19. (a) Precup-Blaga, F. S.; Schenning, A. P. H. J.; Meijer, E. W. *Macromolecules* **2003**, *36*, 565. (b) Pisula, W.; Tomovic, Z.; Wegner, M.; Graf, R.; Pouderoijen, M. J.; Meijer, E. W.; Schenning, A. P. H. J. *J. Mater. Chem.* **2008**, *18*, 2968.
20. Hulvat, J. F.; Sofos, M.; Tajima, K.; Stupp, S. I. *J. Am. Chem. Soc.* **2005**, *127*, 366.
21. Jonkheijm, P.; Schoot, V. D. P.; Schenning, A. P. H. J.; Meijer, E. W. *Science* **2006**, *313*, 80.
22. Reddy, R. A.; Dantlgraber, G.; Baumeister, U.; Tschierske, C. *Angew. Chem. Int. Ed.* **2006**, *45*, 1928.

23. Wicklein, A.; Lang, A.; Muth, M.; Thelakkat, M. *J. Am. Chem. Soc.*, **2009**, *131*, 14442.
24. Kuo, L. C.; Huang, W. T.; Yang, K. H.; Hsu, H. F.; Jin, B. Y.; Leung, M. K. *J. Phys. Chem. B*. **2010**, *114*, 2607.
25. Kimura, M.; Miki, N.; Adachi, N.; Tatewaki, Y.; Ohta, K.; Shirai, H. *J. Mater. Chem.* **2009**, *19*, 1086.
26. Hirai, Y.; Babu, S. S.; Praveen, V. K.; Yasuda, T.; Ajayaghosh, A.; Kato, T.; *Adv. Mater.* **2009**, *21*, 4029.
27. Ajayaghosh, A.; Praveen, V. K. *Acc. Chem. Res.* **2007**, *40*, 644.
28. (a) Balamurugan, A.; Reddy, M. L. P.; Jayakannan, M. *J. Polym. Sci, Part A: Polym. Chem.* **2009**, *4*, 5144. (b) Balamurugan, A.; Reddy, M. L. P.; Jayakannan, M. *J. Phys. Chem. B*. **2009**, *113*, 14128.
29. (a) Olsen, B. D.; Jang, S. Y.; Luning, J. M.; Segalman, R. A. *Macromolecules* **2006**, *36*, 4469. (b) Sun, X.; Li, M.; Liu, D.; Zhang, P.; Tian, W. *J. Appl. Polym. Sci.* **2004**, *91*, 396. (c) Hwang, D. H.; Shim, H. K. *Thin Solid Films* **2002**, *417*, 166. (d) Li, A. K.; Yang, S. S.; Jean, W. Y.; Hsu, C. S. *Chem. Mater.* **2000**, *12*, 2741. (e) Akagi, K.; Oguma, J.; Shibata, S.; Toyoshima, R.; Osaka, I.; Shirakawa, H. *Synth. Met.* **1999**, *102*, 1287. (f) Oguma, J.; Akagi, K.; Shirakawa, H. *Synth. Met.* **1999**, *101*, 86.
30. Liu, X.; Liu, H.; Zhou, W.; Zheng, H.; Yin, X.; Li, Y.; Guo, Y.; Zhu, M.; Ouyang, C.; Zhu, D.; Xia, A. *Langmuir* **2010**, *26*, 3179.
31. Yagai, S.; Kubota, S.; Iwashima, T.; Kishikawa, K.; Nakanishi, T.; Karatsu, T.; Kitamura, A. *Chem. Eur. J.* **2008**, *14*, 5246.
32. Sondergaard, R.; Strobel, S.; Bundgaard, E.; Norrman, K.; Hansen, A. G.; Albert, E.; Csaba, G.; Lugli, P.; Tornow, M.; Krebs, F. C. *J. Mater. Chem.* **2009**, *19*, 3899.
33. Amrutha, S. R.; Jayakannan, M. *J. Phys. Chem. B.* **2009**, *113*, 5083.
34. Amrutha, S. R.; Jayakannan, M. *J. Phys. Chem. B.* **2006**, *110*, 4083.
35. Amrutha, S. R.; Jayakannan, M. *Macromolecules* **2007**, *40*, 2380.
36. Amrutha, S. R.; Jayakannan, M. *J. Phys. Chem. B.* **2008**, *112*, 1119.

37. Resmi, R.; Amrutha, S. R.; Jayakannan, M. *J. Polym. Sci. Polym. Chem.* **2009**, *47*, 2631.
38. Dierking, I. *Textures of Liquid Crystals, Second Editions*, Wiley-VCH, **2003**, Verlag GmbH.
39. Chandrasekhar, S. *Liquid Crystals*, second edition, Cambridge University Press, **1972**.
40. Demus, D.; Richter, L. *Textures of Liquid Crystals*, Verlag Chemie, Weinheim. New York, **1978**. Edition. 1.
41. Atkins, P. W. *Physical Chemistry*, Edition. 6, Oxford University Press, Oxford Melbourne Tokyo, **1998**.
42. Asha, S. K.; Kavita, K.; Das, P. K.; Ramakrishnan, S. *Chem. Mater.* **1999**, *11*, 3352.
43. Kobayashi, T.; Seki, T. *Langmuir* **2003**, *19*, 9297.
44. Craig, A. A.; Imrie, C. T. *Macromolecules* **1999**, *32*, 6215.
45. Sepelj, M.; Lesac, A.; Baumeister, U.; Diele, S.; Bruce, D. W.; Hamersak, Z. *Chem. Mater.* **2006**, *18*, 2050.
46. Chang, S.; Han, C. D. *Macromolecules* **1997**, *30*, 1670.
47. Rose, G. D.; Fleming, P. J.; Banavar, J. R.; Maritan, A. *Proc. Natl. Acad. Sci.* **2006**, *103*, 16623.
48. Chen, J.; Yang, D. *Macromolecules* **2005**, *38*, 3371.
49. Hutter, J. L.; Bechhoefer, J. *J. Cryst. Growth* **2000**, *217*, 332.
50. Keith, H. D.; Padden, F. J., Jr. *J. Polym. Sci.* **1958**, *31*, 415.
51. Keith, H. D.; Padden, F. J., Jr. *J. Polym. Sci.* **1959**, *39*, 101.
52. Keith, H. D.; Padden, F. J., Jr. *J. Polym. Sci.* **1959**, *39*, 123.
53. Keith, H. D.; Padden, F. J.; Russel, T. P. *Macromolecules* **1989**, *22*, 666.
54. Keith, H. D.; Padden, F. J., Jr. *Polymer* **1984**, *25*, 28.
55. (a) Keller, A. *J. Polym. Sci.* **1955**, *17*, 351. (b) Keller, A. *J. Polym. Sci.* **1959**, *39*, 151.
56. Price, F. P. *J. Polym. Sci.* **1959**, *39*, 139.
57. Keller, A. *Nature (London)* **1952**, *31*, 913.

58. (a) Wang, B.; Li, C. Y.; Hanzlicek, J.; Cheng, S. Z. D.; Geil, P. H.; Grebowicz, J.; Ho, R. M. *Polymer* **2001**, *42*, 7171. (b) Gazzano, M.; Focarete, M. L.; Riekel, C.; Ripamonti, A.; Scandola, M. *Macromol. Chem. Phys.* **2001**, *202*, 1405.
59. Ho, R. M.; Ke, K. Z.; Chen, M. *Macromolecules* **2000**, *33*, 7529.
60. Wang, Y.; Chan, C. M.; Li, L.; Ng, K. M. *Langmuir* **2006**, *22*, 7384.
61. Wang, Z.; Hu, Z.; Chen, Y.; Gong, Y.; Huang, H.; He, T. *Macromolecules* **2007**, *40*, 4381.
62. Chen, J.; Yang, D. *J. Polym. Sci., Part B: Polym. Phys.* **2007**, *45*, 3011.
63. Okabe, Y.; Kyu, T.; Saito, H.; Inoue, T. *Macromolecules* **1998**, *31*, 5823.
64. Xu, J.; Guo, B. H.; Zhou, J. J.; Li, L.; Wu, J.; Kowalczyk, M. *Polymer* **2005**, *46*, 9176.
65. Cheung, Z. L.; Weng, L. T.; Chan, C. M.; Hou, W. M.; Li, L. *Langmuir* **2005**, *21*, 7968.
66. Curtis, M. D.; Cao, J.; Kampf, J. W. *J. Am. Chem. Soc.* **2004**, *126*, 4318-4328.
67. Varghese, S.; Das, S. *J. Phys. Chem. Lett.* **2011**, *2*, 863–873 and references are cited therein.
68. Desch. C. H. *The Chemistry of Solids* Cornell University Press **1934**, 180-181.
69. (a) Brandl, M.; Weiss, M. S.; Jabs, A.; Suhnel, J.; Hilgenfeld, R. *J. Mol. Biol.* **2001**, *307*, 357–377. (b) Chakrabarti, P.; Samanta, U. *J. Mol. Biol.*, **1999**, *251*, 9-14. (c) Nishio, M.; Hirota, M.; Umezawa, Y. *The CH- π interaction. Evidence, Nature, and Consequences*, Wiley-VCH, NewYork, **1998**.
70. (a) Desiraju, G. R. *Acc. Chem. Res.*, **1991**, *24*, 290. (b) Desiraju, G. R. *Acc. Chem. Res.*, **1996**, *29*, 441. (c) Steiner, T. *Chem. Comm.* 1997, 727. (d) Steiner, T.; Desiraju, G. R. *Chem. Comm.* **1998**, 891. (e) Chakrabarti, P.; Samanta, U. *J. Mol. Biol.*, **1999**, *251*, 9-14.
71. Desiraju, G. R.; Steiner, T. *The weak Hydrogen Bond*, Oxford Univ. Press, **1999**. (b) Nishio, M.; Hirota, M.; Umezawa, Y. *The CH- π interaction. Evidence, Nature, and Consequences*, Wiley-VCH, NewYork. **1998**.

72. (a) Bhayana, B.; Wilcox, C. S. A. *Angew Chem. Int. Ed* **2007**, *46*, 6833-6836.
(b) Sacksteder, C. A.; Bender, S. L.; Barry, B. A. *J. Am. Chem. Soc.* **2005**, *127*, 7879-7890.
73. (a) Desiraju, G. R. *Acc. Chem. Res.* **2002**, *35*, 565-573 (c) Steiner, T.; Desiraju, G. R. *Chem. Comm.* **1998**, 891-892. (d). Desiraju, G. R.; Steiner, T. *The weak Hydrogen Bond*, Oxford Univ. Press, London, **1999**.
74. (a) Kim, E.; Paliwal, S.; Wilcox, C. S. *J. Am. Chem. Soc.* **1998**, *120*, 1192-11193. (b) Dziubek, K.; Podasiadlo, M.; Katrusiak, A. *J. Am. Chem. Soc.* **2007**, *129*, 12620-12621. (c) Birchall, L. S.; Roy, S.; Jayawarna, V.; Hughes, M.; Irvine, E.; Okorogheye, G. T.; Saudi, N.; Santis, E. D.; Tuttle, T.; Edwards, A. A.; Ulijn, R. V. *Chem. Sci.* **2011**, *2*, 1349-1355. (d) Yamakawa, M.; Yamada, I.; Noyori, R. *Angew. Chem. Int. Ed.* **2001**, *40*, 2818-2821. (e) Gung, B. W.; Emenike, B. U.; Lewis, M.; Kirschbaum, K. *Chem. Eur. J.* **2010**, *16*, 12357-12362. (f) Kobayashi, K.; Ishii, K.; Sakamoto, S.; Shirasaka, T.; Yamaguchi, K. *J. Am. Chem. Soc.* **2003**, *125*, 10615-10624. (g) Tarakeshwar, P.; Choi, H. S.; Kim, K. S. *J. Am. Chem. Soc.* **2001**, *123*, 3323-3331.
75. Ghosh, S. K.; Kaneko, W.; Kiriya, D.; Ohba, M.; Kitagawa, S. *Angew. Chem.* **2008**, *47*, 8843-8847.
76. Ghosh, S. K.; Zhang, J-P.; Kitagawa, S. *Angew. Chem.* **2007**, *46*, 7965-7968.
77. (a) Chen, S. H.; Su, A. C.; Chou, H. L.; Peng, K. Y.; Chen, S. A. *Macromolecules* **2004**, *37*, 167. (b) Hsu, J. H.; Fann, W.; Tsao, P. H.; Chuang, K. R.; Chen, S. A. *J. Phys. Chem. A* **1999**, *103*, 2375.

Chapter 3

Hierarchical Assemblies of OPV Structural Isomers

Chapter 3

Hierarchical Assemblies of OPV Structural Isomers

The role of OPV backbone planarity, CH/ π hydrogen bond, and positional effect of peripheral substitution, alkyl chain lengths and its orientation were investigated on the solid state packing. A series of structural isomers with identical distyrylbenzene based aromatic core but opposite arrangement of alkyl side chains around the periphery were synthesized. Higher homologues OPVs with equal substitutions in the longitudinal and vertical directions were also synthesized. DSC analysis was done to understand the difference in packing properties with respect to horizontal, vertical and radial substitution of the alkyl chains. PLM imaging was used to study the influence of molecular structure on its liquid crystalline properties. The increase in the alkyl chain length in the horizontal position induced liquid crystallinity in the OPVs; however, the corresponding vertical structural isomers remained crystalline in nature. Radially substituted OPVs with equal alkyl chain substitutions in both x and y directions exhibited well-ordered two-dimensional lamellar textures. Single crystal XRD analysis was done to understand the role of planarity, alkyl chain length and its orientation on molecular ordering and intermolecular non-covalent interactions. Planar molecules were generally found to be devoid of strong CH/ π and π - π interactions. On the other hand, non-planar molecules exhibited presence of strong CH/ π interactions. Roll and pitch calculations were done to show that non-planar molecules were more prone to show π - π stacking interactions in this class of molecules. Further, OFET devices were constructed to study the effect of liquid crystalline self-assembly on charge carrier mobility. OPVs exhibited hundred fold increases in charge carrier mobility in LC frozen state as compared to drop cast films. This preliminary result showed that the LC self-organization of molecules may turn out to be a very useful tool for solid state packing in electronic devices.

3.1. Introduction

π -Conjugated oligomers and polymers are emerging organic materials for optoelectronic applications.¹⁻⁶ Organic field-effect transistors (OFETs) are one of the major emerging solid state electronic devices for next generation of cheap and flexible organic circuits consisting of an organic semiconducting layer along with a gate insulator layer.⁷⁻¹⁴ The mobility of the organic semiconductor is the key parameter for efficient OFETs.¹⁵ This important parameter is extremely dependent on the packing (arrangement) of the organic molecules in the solid state.¹⁶ Four different kinds of packing motifs commonly found in semiconducting organic molecules¹⁷⁻¹⁹ such as face to edge herring bone packing without π - π overlap (A), herring bone packing with π - π overlap between adjacent molecules (B), lamellar packing with one dimensional π -stacking (C), and lamellar packing with two dimensional π -stacking (D). Among all the four packing motifs, lamellar packing with two dimensional π -stacking has been found to be most efficient for charge transport.¹⁸

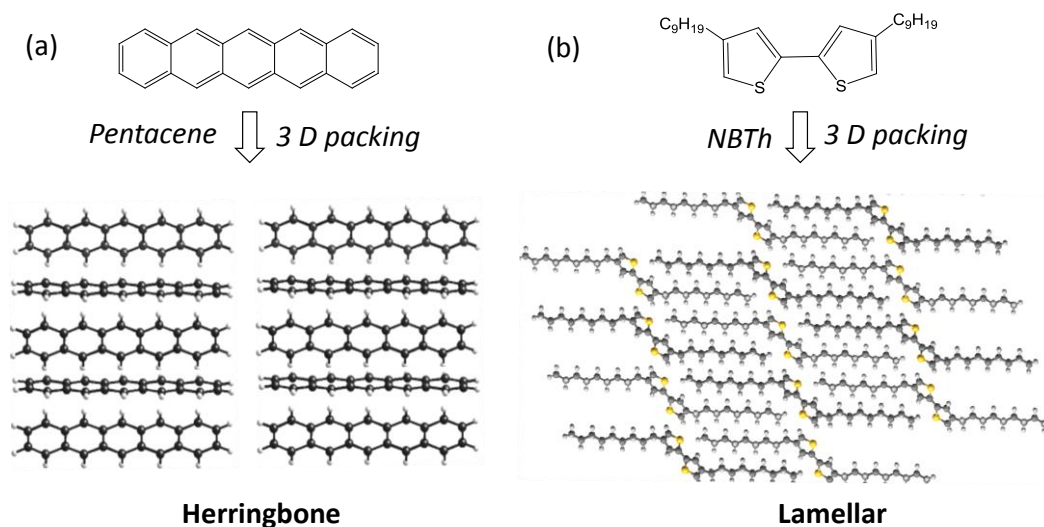


Figure 3.1. Molecular packing motifs in crystals (Crystal structure information and cif file for NBTh was taken from Curtis et al. *J. Am. Chem. Soc.* **2004**, 4318-4328).

Acenes²⁰ and fused arenes of aromatic hydrocarbons are well known to show ideal transistor behaviors when employed in OFETs. Figure 3.1 exhibits the chemical

structure of pentacene and its packing in herringbone crystalline motif. Kelly et al. reported mobilities up to $5.0 \text{ cm}^2 \text{ V}^{-1} \text{ s}^{-1}$ when polycrystalline films of pentacene were used in OFETs.²¹ One disadvantage of using these higher acenes such as pentacene was its high sensitivity to light. For example, pentacene easily formed dimers and trimers in ambient conditions and could be oxidized into 6,13-pentacenequinone (PQ). Moreover, the solubility of pentacene was also very poor in common organic solvents.²² The result is that the purification of pentacene was highly challenging (ultrapure pentacene was almost impossible to obtain due to the existence of PQ). Therefore, introduction of flexible alkyl chains in π -conjugated semiconducting molecules is a very important tool in enhancing solubility and processability. Figure 3.1b shows the structure of nonyl bithiophene with long alkyl chains along the periphery of the aromatic core. The presence of long nonyl alkyl chains promoted interdigitation and molecules packed in 2D lamellar packing motif.²³



Figure 3.2. Molecular architectures of π -conjugates and their solid state assembly.

Typically, π -conjugated systems are comprised of two chemical units: (i) a rigid aromatic conjugated backbone and (ii) flexible alkyl chains anchored for solubility purpose (see figure 3.2). Fully aromatic systems are generally planar and exhibit periodicity in their crystal lattices.²⁴⁻²⁵ Though, such systems are known to show high charge carrier mobilities, they are largely insoluble in common organic solvents restricting their processability in devices.²⁴⁻²⁵ On the other hand, the

substitution of appropriate alkyl chains in the periphery of the π -conjugated chains enhances their solubility in common organic solvents which further facilitates processing via solution casting techniques.

Another important consequence of alkyl chain alignment is planarity or non-planarity of molecular backbone. Planar molecules can pack more densely than twisted or non-planar molecules which have a direct influence on the packing of these molecules in solid state. From the above discussion, it was understood that peripheral substitution around the semi conducting aromatic core played an important role in determining planarity, solid state packing, solubility and processibility of these electronically important materials. Several examples have been reported in literature, which independently studied the role of alkyl side chains on packing of semiconducting molecules.²⁶⁻³⁷ However, the reports based on the influence of planarity, chain length; nature and orientation of peripheral alkyl side chains for the packing of a single aromatic core are limited. Therefore, the control of packing mode of the organic semiconductors in the solid state is a very important factor for better charge transport between molecules. Unfortunately, many of the so far developed OFET materials were found to be insoluble or sparingly soluble in common solvents, and therefore, they could not be processed easily.²⁴⁻²⁵ Further, these reported molecules were sluggish to crystallize; as the consequence, the molecular packing in the solid state was understood only at a premature level. This is the main limitation in the developments of π -conjugated organic materials for efficient solid state electronic applications such as OFETs. In the previous chapter, the role of van der Waals and π - π stacking interactions on self-assembly of a homologous series of oligophenylenevinylenes with tricyclodecanemethylene pendant units was studied. The length of the alkyl chain was varied for a fixed aromatic pendant group (TCD) and hence it was difficult to generalize packing parameters for OPV based π -conjugated systems.

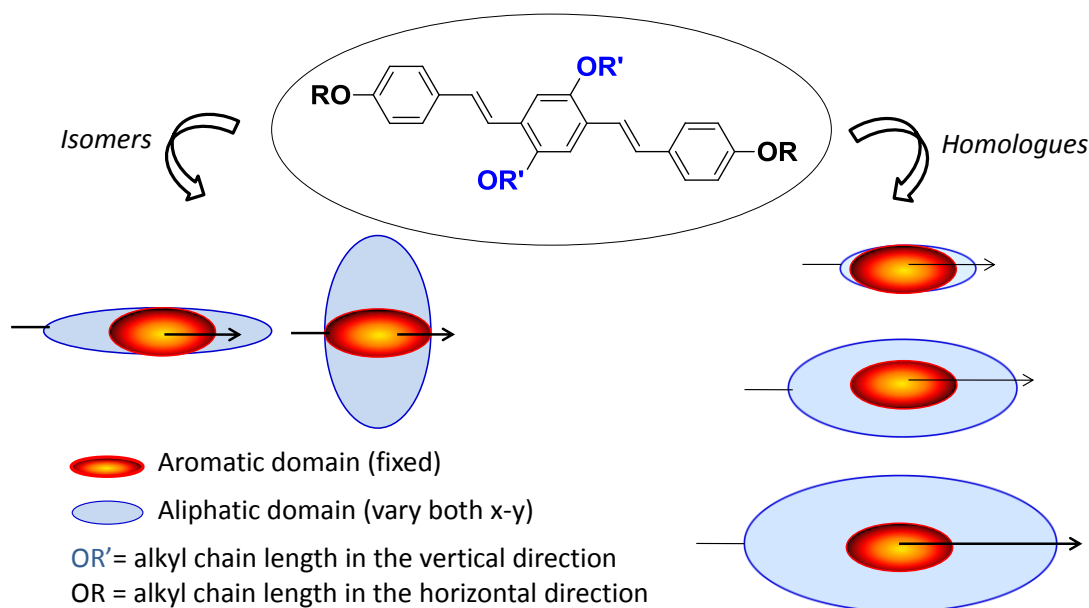


Figure 3.3. Models depicting orientation of peripheral alkyl side chains in structural isomers and higher homologues.

In this chapter, simple OPV-conjugates consisting of different hydrocarbon alkyl chains in the middle and the longitudinal position have been designed as shown in the figure 3.3. The influence of planarity, chain length and its orientation on molecular packing of a large number of oligophenylenevinylenes (OPVs) was elaborately studied using single crystal XRD analysis. A series of structural isomers with identical distyrylbenzene based aromatic core but opposite arrangement of alkyl side chains around the periphery was synthesized (see figure 3.3). Similarly, another series of higher homologues OPVs with equal substitutions in the longitudinal and vertical directions was also synthesized. DSC studies were done to understand the difference in packing properties with respect to horizontal, vertical and radial substitution of the alkyl chains. DSC analysis revealed that among the structural isomers, horizontally substituted OPVs showed higher melting and crystallization temperatures as compared to vertically substituted counterparts suggesting better packing properties. PLM imaging was used to study the influence of molecular structure on its liquid crystalline properties. The increase in the alkyl chain length in the horizontal position induced liquid crystalline properties whereas their vertical

structural isomers remained as crystalline solids. Radially substituted OPVs with equal alkyl chain substitutions in both x and y directions exhibited well-ordered two-dimensional lamellar textures. Single crystal XRD analysis was done to understand the role of planarity, alkyl chain length and its orientation on molecular ordering and intermolecular non-covalent interactions. Planar molecules were generally found to be devoid of strong CH/ π and π - π interactions. On the other hand, non-planar molecules exhibited presence of strong CH/ π interactions. Roll and pitch calculations revealed that these molecules also showed the presence of π - π stacking interactions. Among vertically substituted OPVs, as the number of carbon atoms in the vertical alkyl chain increased from (n = 1) to (n = 4 and 11), the molecular locking changed from square planar to zigzag (angular) to 1D linear fashion. The three dimensional arrangements of OPV-C1-C11 molecules were found as inseparable tightly packed bundles of π -conjugated sheets. On the other hand, OPV-C11-C11 showed layer-like packing in the x-y plane. Further, OFET was constructed to study the effect of molecular alignment on charge carrier mobility. OPV-C1-C11 exhibited hundred folds increase in charge carrier mobility in LC frozen state as compared to drop cast films. These preliminary results showed the potential of the liquid crystalline organization of organic molecules for high charge carrier mobility in OFET applications.

3.2. Experimental Methods

3.2.1. Materials: hydroquinone, 1-bromobutane, 1-bromooctane, 1-bromoundecane, triethylphosphite, potassium-t-butoxide (1M in THF), 4-hydroxybenzaldehyde, 4-methoxy benzaldehyde were purchased from Aldrich Chemicals. HBr in glacial acetic acid, paraformaldehyde, KI, K₂CO₃, dimethylsulphate and NaOH were purchased locally. Solvents were also purchased locally and were purified by standard procedures.

3.2.2. General Procedures: ¹H and ¹³C-NMR were recorded using 400 MHz JEOL NMR spectrometer. All NMR spectra were recorded in CDCl₃ containing TMS as internal standard. Infrared spectra were recorded using Bruker FT-IR (ATR mode) spectrophotometer in the range of 4000-600 cm⁻¹. The mass of all the OPVs was determined by using the Applied Biosystems 4800 PLUS MALDI TOF/TOF analyzer. The purity of all OPVs was checked by gel permeation chromatography (GPC) which was performed using Viscotek triple detector setup in THF. TGA analysis was done using Perkin Elmer STA 6000 simultaneous thermal analyzer. CHN analysis for all the oligophenylenevinylenes was done by using Elementor Vario EL cube analyzer.

Differential scanning calorimetry: Differential scanning calorimetry (DSC) measurements were performed on TA Q20 DSC. A pinch of powdered sample was placed in DSC aluminum pan and crimped. The data were recorded at a heating and cooling rate of 10 °C/min. The first heating cycle data were discarded since they possessed prehistory of the sample.

Polarized Light Microscope Analysis: To study the temperature dependent LC textures of all the OPVs, LIECA DM 2500 P polarized light microscope equipped with Linkam TMS 94 heating-freezing stage was used. A pinch of sample was placed on the glass substrate, heated to melt at 10 °C/min, and kept isothermally 20 °C above their melting temperature for 2-3 minutes. The melt was then cooled at 10 °C/min and PLM images were continuously captured using camera.

Photophysical Analysis: Absorption spectra were recorded using a Perkin Elmer Lambda 45 UV spectrophotometer. Steady state fluorescence emission and excitation spectra were recorded using a Fluorolog HORIBA JOBIN VYON fluorescence spectrophotometer in LC frozen samples.

Single Crystal X-ray Analysis: Bruker APEX duo CCD-X ray diffractometer equipped with graphite monochromator Mo K α radiation ($\lambda=0.71073$ Å) was used for single crystal X-ray analysis of all the OPVs. Good quality crystals were grown

in a mixture of DCM and methanol (2:1 v/v) for all the samples. Crystals were grown using the slow evaporation technique and subjected to data collection at 100 K. The frames were integrated with Bruker APEX software package. The structures were solved by direct methods and refined with a full matrix least squares techniques using SHELX SV97 programs. The detailed crystallographic parameters for all the OPVs have been summarized in table 3.1 and table 3.2. Crystal structures were visualized using Mercury 3.0 and Materials Studio software. The “pitch” and “roll” angles were measured using Mercury 3.0 program.

Table 3.1. Single crystal X-ray parameters for OPVs.

Compound	OPV-C11-C11	OPV-C1-C11	OPV-C8-C11
formula	C ₆₆ H ₁₀₆ O ₄	C ₄₆ H ₆₆ O ₄	C ₆₀ H ₉₄ O ₄
recrystn solv	DCM/MeOH	DCM/MeOH	DCM/MeOH
mol wt	963.55	683.01	879.39
Colour, habit	Yellow green, needle	Yellow green, needle	Yellow green, needle
temp(K)	100	100	100
system	Triclinic	Triclinic	Triclinic
space group	P-1	P-1	P-1
a, (Å)	10.368	8.51	9.177
b, (Å)	10.466	11.02	11.558
c, (Å)	16.040	11.05	12.788
α, (deg)	71.355	81.73	91.887
β, (deg)	84.295	79.66	93.410
γ, (deg)	64.438	79.72	105.928
V, Å³	1486.4	996	1300.29
d_{cacl}, g cm⁻¹	1.076	1.138	0.218
μ(mm⁻¹)	0.06	0.07	0.015
GOF	0.996	1.119	1.039
Z	2	2	2
Unique reflections	4668	3444	6881
Reflections collected	21096	7913	21.677
θ range	1.34 to 24.04	1.34 to 24.04	1.34 to 24.04
Refined parameters	318	228	292
R₁ (on F, I>2σ(I))	0.0432	0.2274	0.0448
wR₂ (on F², all data)	0.1099	0.6354	0.1120

Table 3.2. Single crystal X-ray parameters for OPVs.

Compound	OPV-C1-C1	OPV-C4-C1	OPV-C11-C1	OPV-C8-C8
formula	C ₂₆ H ₂₆ O ₄	C ₃₂ H ₃₈ O ₄	C ₄₆ H ₆₆ O ₄	C ₅₄ H ₈₂ O ₄
recrystn solv	DCM/MeOH	DCM/MeOH	DCM/MeOH	DCM/MeOH
mol wt	402.48	486.64	683.01	795.23
Colour, habit	Yellow green, needle	Yellow green, needle	Yellow green, needle	Yellow green, needle
temp(K)	100	100	100	100
system	Triclinic	Orthorhombic	Triclinic	Triclinic
space group	P-1	Pbca	P-1	P-1
a, (Å)	10.585	11.953	9.477	12.764
b, (Å)	10.707	7.692	14.859	13.807
c, (Å)	10.769	28.926	15.911	15.778
α, (deg)	113.064	90	65.093	100.392
β, (deg)	90.912	90	81.565	107.908
γ, (deg)	109.700	90	80.637	107.313
V, Å ³	1041.67	2659.53	1997.59	2410.22
d _{cacl} , g cm ⁻¹	1.283	1.215	0.568	1.096
μ(mm ⁻¹)	0.085	0.078	0.035	0.067
GOF	1.039	1.022	4.598	0.931
Z	2	8	1	2
Unique reflections	5051	3302	64.1	4579
Reflections collected	12571	37265	13224	11933
θ range	1.34 to 24.04	1.34 to 24.04	1.34 to 24.04	1.34 to 24.04
Rrefined parameters	276	166	455	528
R ₁ (on F, I>2σ(I))	0.0425	0.0380	0.1425	0.0777
wR ₂ (on F ² , all data)	0.1003	0.0957	0.2023	0.1613

Photophysical Analysis: Absorption spectra were recorded using a Perkin Elmer Lambda 45 UV spectrophotometer. Steady state fluorescence emission and excitation spectra were recorded using a Fluorolog HORIBA JOBIN VYON fluorescence spectrophotometer. For these photophysical studies, LC frozen samples were prepared by heating the samples to melt and then cooling to form thin films between two glass cover slips.

Field Effect transistor Measurements: The Field effect transistors (FETs) were fabricated by drop casting thin films of sample on prefabricated substrates. For

measurements in LC state, the samples were frozen in LC state by heating and cooling on prefabricated substrates. The FET comprised of heavily n-doped silicon as gate and 210 nm thick SiO₂ as gate oxide. The capacitance of the gate oxide was 14 nF cm⁻². The source and drain electrodes were made up of 30 nm thick gold, which was evaporated on top of a 10 nm thick ITO adhesion layer. The width and length of the channel were 10 mm and 2.5 mm, respectively. A semi probe station LA-150 with tungsten micro needles and micromanipulators was used to make contact with source, drain and gate electrodes. An Agilent 4156 C semiconductor probe analyzer was used to measure the I-V characteristics of the transistor.

3.2.3. Synthesis

Synthesis of 1, 4-dimethoxybenzene (1b): 4-methoxy phenol (24.8 g, 0.20 mol) and KOH (16.8 g, 0.30 mol) were taken in methanol (70 mL) under ice cold conditions. Dimethyl sulphate (38.5 mL, 0.40 mol) was added dropwise to this reaction mixture. This reaction mixture was stirred at room temperature for 48 h, extracted into dichloromethane, and washed with 5% NaOH solution. The organic layer was dried over anhydrous sodium sulphate and condensed to get white solid. The product was further purified by passing through silica gel column using ethyl acetate (1 % v/v) in hexane as eluent. m. p. = 56 -57 °C. Yield = (82 %). ¹H-NMR (CDCl₃, 400MHz) δ: 6.8 ppm (s, 4H, **Ar-H**) and 3.7 ppm (s, 6H, **OCH₃**). ¹³C-NMR (CDCl₃, 100MHz) δ: 153.7, 114.6 (**Ar-C**) and 55.7 (**OCH₃**). FT-IR (KBr, cm⁻¹): 3012, 2947, 2910, 2827, 1977, 1866, 1505, 1450, 1414, 1293, 1210, 1182, 1109, 1035, 804 and 582. MALDI-TOF-TOF-MS (MW = 138.16): *m/z* = 138.88 (M⁺) using TiO₂ matrix.

Synthesis of 1, 4-dibutoxybenzene (1c): Hydroquinone (11.0 g, 0.10 mol) and KOH (22.4 g, 0.40 mol) were taken in 30 mL of DMSO under ice cold conditions. 1-Bromobutane (23.7 mL, 0.22 mol) was added dropwise to this reaction mixture. This reaction mixture was then stirred at room temperature for 48 h, extracted in dichloromethane, and washed with 5% NaOH solution. The organic layer was dried over anhydrous sodium sulphate and condensed to get product. It was further purified by passing through silica gel column using ethyl acetate (1 % v/v) in hexane as eluent. Yield = (60%). ¹H-NMR (CDCl₃, 400MHz) δ: 6.8 ppm (s, 4H, **Ar-H**), 3.9 ppm (t, 4H, **OCH₂**), 1.7 ppm (m, 4H, **OCH₂CH₂**), 1.4 ppm (m, 4H, **OCH₂CH₂CH₂**), 0.9 ppm (t, 6H, **CH₃**). ¹³C-NMR (CDCl₃, 100MHz) δ: 2933, 2871, 2021, 1868, 1505, 1467, 1392, 1288, 1221, 1120, 1073, 1035, 970, 904, 153.3, 115.4 (**Ar-C**), 68.4 (**OCH₃**), 31.6, 19.4 and 13.9 ppm. FT-IR (KBr, cm⁻¹): 869 and 760. MALDI-TOF-TOF-MS (MW = 222.32): *m/z* = 245.41 (M⁺ + 23).

Synthesis of 1, 4-bis(octyloxy)benzene (1d): 1-Bromooctane (15.3 mL, 0.08 mol) was reacted with hydroquinone (4.4 g, 0.04 mol) and KOH (8.9 g, 0.16 mol) in DMSO as described for **1c**. Yield = (22 %). m. p. = 58-61 °C. ¹H-NMR (CDCl₃, 400MHz) δ: 6.8 ppm (s, 4H, **Ar-H**), 3.9 ppm (t, 4H, **OCH₂**), 1.7 ppm (m, 4H, **OCH₂CH₂**), 1.5-1.0 ppm (m, 20H, **aliphatic-H**) and 0.8 ppm (t, 6H, **CH₃**). ¹³C-NMR (CDCl₃, 100MHz) δ: 153.2, 115.4 (**Ar-C**), 68.71 (**OCH₃**), 31.9, 29.5, 29.3, 26.1, 22.7 and 14.2 ppm. FT-IR (KBr, cm⁻¹): 2921, 2856, 1504, 1466, 1369, 1287, 1223, 1116, 1026, 824, 765, 723, and 646. MALDI-TOF-TOF-MS (MW = 334.54): *m/z* = 357.24 (**M⁺ + 23**).

Synthesis of 1, 4-bis(undecyloxy)benzene (1e): 1-Bromoundecane (38.5 mL, 0.40 mol) was reacted with hydroquinone (2.2 g, 0.02 mol) and KOH (4.5 g, 0.08 mol) as described for **1c**. m. p. = 78-80 °C. Yield = (67%). ¹H-NMR (CDCl₃, 400MHz) δ: 6.8 ppm (s, 4H, **Ar-H**), 3.9 ppm (t, 4H, **OCH₂**), 1.7 ppm (m, 4H, **OCH₂CH₂**), 1.5-1.0 ppm (m, 32H, **aliphatic H**) and 0.8 ppm (t, 6H, **CH₃**). ¹³C-NMR (CDCl₃, 100MHz) δ: 153.1, 115.3 (**Ar-C**), 68.6 (**OCH₃**), 31.9, 29.6, 29.4, 29.3, 26.0, 22.7 and 14.1 ppm. FT-IR (KBr, cm⁻¹): 2952, 2932, 2916, 2847, 1512, 1472, 1463, 1395, 1288, 1238, 1160, 1111, 1092, 1051, 1030, 1017, 986, 829, 821, 769, 728, 719, 538, 509 and 505. MALDI-TOF-TOF-MS (MW = 418.71): *m/z* = 441.34 (**M⁺ + 23**).

Synthesis of 1, 4-bis (bromomethyl)-2, 5-dimethoxy benzene (2b): **1b** (2.7 g, 0.02 mol) and paraformaldehyde (2.4 g, 0.08 mol) were reacted with HBr in acetic acid (10.8 mL, 0.04 mol) following the procedure as described for **2a**. It was recrystallised from hot acetone. Yield = (64 %). ¹H-NMR (CDCl₃, 400MHz) δ: 6.8 ppm (s, 2H, **Ar-H**); 4.5 ppm (s, 2H, **CH₂Br**) and 3.8 ppm (s, 6H, **OCH₃**). ¹³C-NMR (CDCl₃, 100MHz) δ: 151.2, 127.3, 113.8 (**Ar-C**), 56.2 (**OCH₃**) and 28.6 (**CH₂Br**) ppm. FT-IR (KBr, cm⁻¹): 1505, 1460, 1427, 1401, 1317, 1225, 1204, 1177, 1147, 1038, 889, 873, 717 and 663. MALDI-TOF-TOF-MS (MW = 324.01): *m/z* = 363.12 (**M⁺ + 39**).

Synthesis of 1, 4-bis(bromomethyl)-2,5-dibutoxybenzene (2c): **1c** (4.44 g, 0.02 mol) and paraformaldehyde (2.4 g, 0.08 mol) were reacted with HBr in acetic acid (25 mL, 0.05 mol) following the procedure described for **2a**. The product was purified by recrystallizing from hot acetone. Yield = (78 %). ¹H-NMR (CDCl₃, 400MHz) δ: 6.8 ppm (s, 2H, **Ar-H**), 4.5 ppm (s, 4H, **CH₂Br**), 3.9 ppm (t, 4H, **OCH₂**), 1.8 ppm (m, 4H, **OCH₂CH₂**), 1.53 ppm (m, 4H, **OCH₂ OCH₂CH₂**), and 0.98 ppm (t, 6H, **-CH₃**). ¹³C-NMR (CDCl₃, 100 MHz) δ: 147.7, 128.1, 114.1(**Ar-C**), 69.08 (**Ar-O-CH₂**), 29.7 (**CH₂Br**), 31.8, 19.4 and 14.2 ppm. FT-IR (KBr, cm⁻¹): 2957, 2931, 2871, 1504, 1469, 1393, 1289, 1217, 1119, 1071, 1037, 1011, 971, 904,

825, 762, 528, 515, 481, 449 and 428. MALDI-TOF-TOF-MS (MW = 408.17): m/z = 447.21 ($M^+ + 39$).

Synthesis of 1, 4-bis(bromomethyl)-2,5-bis(octyloxy)benzene (2d): **1d** (2.2 g, 7.50 mmol) and paraformaldehyde (0.8 g, 26.50 mmol) were reacted with HBr in glacial acetic acid (3.6 mL, 0.01 mol) following the procedure as described for **2a**. The product was further purified by recrystallising from hot acetone. m. p. = 86 °C-88 °C. Yield = (52 %). $^1\text{H-NMR}$ (CDCl_3 , 400MHz) δ : 6.8 ppm (s, 2H, Ar-H), 4.5 ppm (s, 4H, CH_2Br), 3.9 ppm (t, 4H, OCH_2), 1.8 ppm (m, 4H, OCH_2CH_2), 1.5-1.0 ppm (m, 20H, aliphatic H) and 0.8 ppm (t, 6H, CH_3). $^{13}\text{C-NMR}$ (CDCl_3 , 100MHz) δ : 150.7, 127.6, 114.7 (Ar-C), 69.1 (Ar-O- CH_2), 31.9 (CH_2Br), 29.4, 29.3, 28.8, 26.1, 22.7 and 14.2 ppm. FT-IR (KBr, cm^{-1}): 2917, 2850, 1507, 1467, 1400, 1312, 1210, 1127, 1036, 1001, 904, 858, 723 and 685. MALDI-TOF-TOF-MS (MW = 520.38): m/z = 559.16 ($M^+ + 39$).

Synthesis of 1, 4-bis(bromomethyl)-2,5-bis(undecyloxy)benzene (2e): **1e** (2.4 g, 0.08 mol) and paraformaldehyde (2.4 g, 0.08 mol) were reacted with HBr in acetic acid (4.0 mL, 0.02 mol) following the procedure as described for **2a**. The product was purified by recrystallizing from hot acetone. m. p. = 96°C-99 °C. Yield = (46 %). $^1\text{H-NMR}$ (CDCl_3 , 400MHz) δ : 6.8 ppm (s, 2H, Ar-H), 4.5 ppm (s, 4H, CH_2Br), 3.9 ppm (t, 4H, OCH_2), 1.8 ppm (m, 4H, OCH_2CH_2), 1.5-1.0 ppm (m, 32H, aliphatic C) and 0.87 ppm (t, 6H, $-\text{CH}_3$). $^{13}\text{C-NMR}$ (CDCl_3 , 100MHz) δ : 150.7, 127.6, 114.7 (Ar-C), 69.08 (Ar-O- CH_2), 32.0 (CH_2Br), 29.7, 29.7, 29.4, 28.8, 26.1, 22.7 and 14.2 ppm. FT-IR (KBr, cm^{-1}): 2913, 2845, 1509, 1467, 1411, 1396, 1224, 1206, 1050, 1027, 860, 726, 718 and 687. MALDI-TOF-TOF-MS (MW = 718.92): m/z = 757.97 ($M^+ + 39$).

Synthesis of tetraethyl (2, 5-dimethoxy-1, 4-phenylene)bis (methylene) di phosphonate (3b): **2b** (1.5 g, 3.10 mmol) and triethyl phosphite (4.5 mL, 25.80 mmol) were reacted as described for **3a**. m. p. = 113-115 °C. Yield = (78 %). $^1\text{H-NMR}$ (CDCl_3 , 400MHz) δ : 6.8 ppm (s, 2H, aromatic), 4.0 ppm (m, 8H, POCH_2CH_3), 3.7 ppm (s, 6H, OCH_3), 3.1 ppm (d, 4H, Ar- CH_2P) and 1.2 ppm (t, 12H, POCH_2CH_3). $^{13}\text{C-NMR}$ (CDCl_3 , 100MHz) δ : 150.9, 119.3, 113.9 (Ar-C), 61.8 (POCH_2CH_3), 56.1 (OCH_3), 27.1, 25.7 and 16.3 ppm. FT-IR (KBr, cm^{-1}): 2980, 2899, 2834, 1511, 1470, 1409, 1389, 1262, 1216, 1026, 959, 877, 813, 762, 722, 697, 627 and 582. MALDI-TOF-TOF-MS (MW = 438.16): m/z = 461.20 ($M^+ + 23$).

Synthesis of tetraethyl (2, 5- dibutoxy)-1,4-phenylene)bis(methylene) diphosphonate (3c): **2c** (3.1 g, 7.50 mmol) and triethyl phosphite (3.1 g, 18.80 mmol)) were reacted as described for **3a**. Yield = (86 %). $^1\text{H-NMR}$ (CDCl_3 ,

400MHz) δ : 6.9 ppm (s, 2H, **Ar-H**), 4.0 ppm (m, 8H, **POCH₂CH₃**), 3.8 ppm (t, 4H, **OCH₂**), 3.1 ppm (d, 4H, **CH₂P**), 1.7-1.1 ppm (m, 20H, **aliphatic** and **POCH₂CH₃**) and 0.9 ppm (t, 6H, **-CH₂-CH₃**). ¹³C-NMR (CDCl₃, 100MHz) δ : 150.3, 119.4, 114.9 (**Ar-C**), 68.6 (**OCH₂**), 61.9 (**POCH₂CH₃**), 31.6, 26.9, 25.5, 19.4, 16.4, and 13.9 ppm. FT-IR (KBr, cm⁻¹): 3464, 2961, 2933, 2872, 1510, 1472, 1392, 1306, 1209, 1164, 1098, 1020, 956, 904, 827 and 782. MALDI-TOF-TOF-MS (MW = 522.55): m/z = 545.27 (M⁺ + 23) and 561.24(M⁺ + 39).

Synthesis of tetraethyl (2, 5-bis (octyloxy)-1,4-phenylene)bis(methylene) diphosphonate (3d): **2d** (1.5 g, 2.99 mmol) and triethyl phosphite (0.1 g, 5.98 mmol) were reacted as described for **3a**. m. p = 56-58 °C. Yield = (94 %). ¹H-NMR (CDCl₃, 400MHz) δ : 6.9 ppm (s, 2H, **Ar-H**), 4.0 ppm (m, 8H, **POCH₂CH₃**) , 3.9 ppm (t, 4H, **OCH₂**), 3.1 ppm (d, 4H, **CH₂P**), 1.7-1.2 ppm (m, 36 H, **aliphatic** and **POCH₂CH₃**) and 0.8 ppm (t, 6H, **-CH₂-CH₃**); ¹³C-NMR (CDCl₃, 100MHz) δ :150.4, 119.5, 114.9, 69.1 (**OCH₂**), 61.9 (**POCH₂CH₃**), 31.9, 31.0, 29.5, 29.3, 26.9, 26.2, 25.6, 22.7, 16.4 and 14.1 ppm. FT-IR (KBr, cm⁻¹): 3469, 2959, 2925, 2867, 1509, 1465, 1391, 1247, 1210, 1163, 1097, 1023, 956, 890, 782, 726, and 648. MALDI-TOF-TOF-MS (MW = 634.76): m/z = 657.47 (M⁺ + 23).

Synthesis of tetraethyl (2, 5-bis (undecyloxy)-1,4-phenylene)bis(methylene) diphosphonate (3e): **2e** (1.5 g, 2.50 mmol) and triethyl phosphite (0.9 g, 5.30 mmol) were reacted as described for **3a**. m. p. = 111-113 °C. Yield = (94 %). ¹H-NMR (CDCl₃, 400MHz) δ : 6.9 ppm (s, 2H, **Ar-H**), 4.0 ppm (m, 8H, **POCH₂CH₃**), 3.9 ppm (t, 4H, **OCH₂**), 3.1 ppm (d, 4H, **CH₂P**), 1.7-1.2 ppm (m, 48H, **aliphatic** and **POCH₂CH₃**) and 0.8 ppm (t, 6H, **-CH₂-CH₃**). ¹³C-NMR (CDCl₃, 100MHz) δ : 150.3, 119.4, 119.4, 119.4, 114.9 (**Ar-C**), 68.9 (**OCH₂**), 61.9 (**POCH₂CH₃**), 31.9, 29.6, 29.5, 29.4, 29.3, 26.9, 26.1, 22.7, 16.4, 16.3 and 14.1 ppm. FT-IR (KBr, cm⁻¹): 2916, 2849, 1516, 1471, 1392, 1241, 1223, 1053, 1032, 956, 891, 839, 788, 745, 719, and 647. MALDI-TOF-TOF-MS (MW = 718.92): m/z = 741.55 (M⁺ + 23).

The synthetic procedures for the synthesis of 4-methoxy benzaldehyde (**4a**), 4-butoxy benzaldehyde (**4d**), 4-octyloxy benzaldehyde (**4h**), 4-undecyloxy benzaldehyde (**4k**) have been described in chapter-2.

Synthesis of oligo-phenylenevinylenes (OPV)s:

Synthesis of 4,4'-(1E, 1'E)-2,2'-(2,5-dimethoxy-1,4-phenylene)bis (ethane2,1diyl) bis(undecyloxybenzene) (OPV-C1-C1): **3b** (2.4 g, 2.40 mmol) and **4a** (0.7 g, 5.50 mmol) were taken in dry THF (20 mL) and kept under ice cold condition. Potassium

tert-butoxide (16 mL, 1M THF solution) was added dropwise to the reaction mixture under nitrogen atmosphere and the stirring was continued at 30 °C for 24 h. The resultant yellow green solution was concentrated and poured into a large amount of methanol. The yellow green precipitate was filtered and washed with a large amount of methanol until the filtrate become colorless. The product was purified by recrystallizing from hot saturated solution of acetone. Yield = (31 %). ¹H NMR (CDCl₃, 400 MHz), δ: 7.49 ppm (d, 4H, **Ar-H**), 7.35 ppm (d, 2H, **CH=CH**), 7.11 ppm (s, 2H, **Ar-H**), 7.07 ppm (d, 2H, **CH=CH**), 6.90 ppm (d, 4H, **Ar-H**), 3.92 ppm (s, 6H, **OCH₃**), 3.83 ppm (s, 6H, **OCH₃**). ¹³C-NMR (CDCl₃, 100MHz) δ: 159.2, 151.4, 130.8, 128.4, 127.8, 126.5, 121.2, 114.2, 108.9, 56.5 and 55.4 ppm. FT-IR (KBr, cm⁻¹): 2918, 1595, 1497, 1453, 1402, 1334, 1205, 1159, 1026, 952, 813, 674, 629 and 535. MALDI-TOF-TOF-MS (MW = 402.48): *m/z* = 402.16. Anal. Calcd for C₂₆H₂₆ O₄: C, 77.59; H, 6.51. Found: C, 78.01; H, 6.63.

Synthesis of 4,4'-(1E, 1'E)-2,2'-(2,5-dibutoxy-1,4-phenylene)bis(ethene-2,1-diyl)bis(methoxybenzene) (OPV-C4-C1): **3c** (1.0 g, 2.00 mmol), **4a** (0.6 g, 4.40 mmol) and Potassium *tert*-butoxide (12 mL, 1M THF solution) were reacted as described for **OPV-C1-C1**. Yield = (80 %). ¹H NMR (CDCl₃, 400 MHz), δ: 7.46 ppm (d, 4H, **Ar-H**), 7.31 ppm (d, 2H, **CH = CH**), 7.09 ppm (s, 2H, **Ar-H**), 7.04 ppm (d, 2H, **CH=CH**), 6.89 ppm (d, 4H, **Ar-H**), 4.04 ppm (t, 4H, **OCH₂**), 3.82 ppm (s, 6H, **OCH₃**), 1.84 ppm (m, 4H, **OCH₂-CH₂-CH₂**), 1.55 ppm (m, 4H, **OCH₂-CH₂-CH₂**) and 1.01 ppm (t, 6H, **CH₃**). ¹³C-NMR (CDCl₃, 100MHz) δ: 159.2, 151.0, 130.9, 128.1, 127.8, 126.8, 121.4, 114.2, 110.4, 69.3, 55.4, 31.7, 19.6 and 14.1 ppm. FT-IR (KBr, cm⁻¹): 2958, 1695, 1595, 1565, 1497, 1457, 1408, 1288, 1237, 1192, 1026, 959, 845 and 812. MALDI-TOF-TOF-MS (MW = 486.64): *m/z* = 486.33. Anal. Calcd for C₃₂H₃₈ O₄: C, 78.98; H, 7.87. Found: C, 79.10; H, 8.48.

Synthesis of 4,4'-(1E, 1'E)-2,2'-(2,5-bis(octyloxy)-1,4-phenylene)bis(ethene-2,1-diyl)bis(methoxybenzene) (OPV-C8-C1): **3d** (0.2 g, 0.33 mmol), **4a** (0.1 g, 0.73 mmol) and potassium *tert*-butoxide (2 mL, 1M THF solution) were reacted as described for **OPV-C1-C1**. Yield = (24 %). ¹H NMR (CDCl₃, 400 MHz), δ: 7.45 ppm (d, 4H, **Ar-H**), 7.31 ppm (d, 2H, **CH=CH**), 7.09 ppm (s, 2H, **Ar-H**), 7.06 ppm (d, 2H, **CH=CH**), 6.89 ppm (d, 4H, **Ar-H**), 4.04 ppm (t, 4H, **OCH₂**), 3.83 ppm (s, 6H, **OCH₃**), 1.86 ppm (m, 4H, **OCH₂-CH₂-CH₂**), 1.4-1.2 ppm (m, 20H, **aliphatic-H**) and 0.87 ppm (t, 6H, **CH₃**). ¹³C-NMR (CDCl₃, 100MHz) δ: 159.2, 151.0, 130.9, 128.2, 127.7, 126.8, 121.5, 114.2, 110.5, 69.7, 55.4, 31.9, 29.6, 29.4, 26.4, 22.7 and 14.2 ppm. FT-IR (KBr, cm⁻¹): 2921, 2850, 2314, 1600, 1506, 1458, 1405, 1330, 1244, 1205, 1161, 1039, 959, 812, 724, 680 and 582. MALDI-TOF-TOF-MS (MW =

598.85): $m/z = 598.47$. Anal. Calcd for $C_{40}H_{54}O_4$: C, 80.22; H, 9.09. Found: C, 79.80; H, 8.48.

Synthesis of 4,4'-(1E, 1'E)-2,2'-(2,5-bis(undecyloxy)-1,4-phenylene)bis(ethene-2,1-diyl)bis(methoxybenzene) (OPV-C11-C1): **3e** (0.4 g, 0.50 mmol), **4a** (0.2 g, 1.10 mmol) and potassium *tert*-butoxide (3 mL, 1M THF solution) were reacted as described for **OPV-C1-C1**. Yield = (75 %). 1H NMR ($CDCl_3$, 400 MHz), δ : 7.45 (d, 4H, **Ar-H**), 7.33 (d, 2H, **CH=CH**), 7.08 (s, 2H, **Ar-H**), 7.06 (d, 2H, **CH=CH**), 6.89 (d, 4H, **Ar-H**), 4.02 (t, 4H, **OCH₂**), 3.82 (s, 4H, **OCH₃**), 1.85(m, 4H, **OCH₂-CH₂-CH₂**), 1.6-1.3 (m, 32H, **aliphatic-H**), 0.86 (t, 6H, **CH₃**). ^{13}C -NMR ($CDCl_3$,100MHz) δ : 159.1,151.0, 130.9, 128.2, 127.8, 126.9, 121.5, 114.7, 110.5, 69.7, 55.4, 32.02, 29.8, 29.5, 26.39, 22.8 and 14.2. FT-IR (KBr, cm^{-1}): 2912, 2848, 1598, 1501, 1419, 1334, 1246, 1205, 1154, 1028, 961, 847, 764, 717 and 534. MALDI-TOF-TOF-MS (MW = 683.01): $m/z = 682.55$ Anal. Calcd for $C_{46}H_{66}O_4$: C, 80.89; H, 9.74. Found: C, 81.29; H, 9.66.

Synthesis of 4,4'-(1E, 1'E)-2,2'-(2,5-bis(methoxy)-1,4-phenylene)bis(ethene-2,1-diyl)bis(butyloxy benzene) (OPV-C1-C4): **3b** (1.2 g, 2.50 mmol), **4d** (0.9 g, 5.50 mmol) and potassium *tert*-butoxide (15 mL, 1M THF solution) were reacted as described for **OPV-C1-C1**. Yield= (80 %). 1H NMR ($CDCl_3$, 400 MHz), δ : 7.46 ppm (d, 4H, **Ar-H**), 7.32 ppm (d, 2H, **CH=CH**), 7.09 ppm (s, 2H, **Ar-H**), 7.04 ppm (d, 2H, **CH=CH**), 6.87 ppm (d, 4H, **Ar-H**), 3.96 ppm (t, 4H, **OCH₂**), 3.90 ppm (s, 6H, **OCH₃**), 1.78 ppm (m, 4H, **OCH₂-CH₂-CH₂**), 1.7-1.2 ppm (m, 4H, **aliphatic-H**) and 0.88 ppm (t, 6H, **CH₃**). ^{13}C -NMR ($CDCl_3$,100MHz) δ : 158.8, 151.4, 130.6, 128.4, 127.8, 126.6, 121.0, 114.7, 108.9, 68.1, 56.4, 22.7 and 14.2 ppm. FT-IR (KBr, cm^{-1}): 2921, 2850, 2314, 1602, 1508, 1460, 1405, 1339, 1244, 1205, 959, 810, 680 and 582. MALDI-TOF-TOF-MS (MW = 486.64): $m/z = 486.42$. Anal. Calcd for $C_{32}H_{38}O_4$: C, 78.98; H, 7.87. Found: C, 79.01; H, 8.48.

Synthesis of 4,4'-(1E, 1'E)-2,2'-(2,5-bis(methoxy)-1,4-phenylene)bis(ethene-2,1-diyl)bis(octyloxy benzene) (OPV-C1-C8): **3b** (1.2 g, 2.50 mmol) and **4h** (1.3 g, 5.50 mmol) and potassium *tert*-butoxide (15 mL, 1M THF solution) were reacted as described for **OPV-C1-C1**. Yield = (83 %). 1H NMR ($CDCl_3$, 400 MHz), δ : 7.46 ppm (d, 4H, **Ar-H**), 7.32 ppm (d, 2H, **CH=CH**), 7.09 ppm (s, 2H, **Ar-H**), 7.04 ppm (d, 2H, **CH=CH**), 6.87 ppm (d, 4H, **Ar-H**), 3.96 ppm (t, 4H, **OCH₂**), 3.90 ppm (s, 6H, **OCH₃**), 1.78 ppm (m, 4H, **OCH₂-CH₂-CH₂**), 1.7-1.2 ppm (m, 20H, **aliphatic-H**) and 0.88 ppm (t, 6H, **CH₃**). ^{13}C -NMR ($CDCl_3$, 100MHz) δ : 158.8, 151.4, 130.6, 128.4, 127.8, 126.6, 121.0, 114.7, 108.9, 68.1, 56.4, 31.9, 29.4, 26.1, 22.7 and 14.2 ppm. FT-IR (KBr, cm^{-1}): 2920, 2852, 2314, 1600, 1508, 1460, 1405, 1339, 1244,

1205, 1161, 1039, 959, 812, 724, 680 and 582. MALDI-TOF-TOF-MS (MW = 598.85): m/z = 598.46. Anal. Calcd for C₄₀H₅₄ O₄: C, 80.22; H, 9.09. Found: C, 80.12; H, 8.98.

Synthesis of 4,4'-(1E, 1'E)-2,2'-(2,5-dimethoxy-1,4-phenylene)bis(ethane-2,1-diyl)bis(undecyloxy benzene) (OPV-C1-C11): 3b (0.4 g, 1.00 mmol) was reacted with 4-undecyloxybenzaldehyde (0.6 g, 2.10 mmol) were reacted as described for **OPV-C1-C1**. The product was purified by passing through a silica gel column using 1% ethyl acetate in hexane as eluent. Yield = (85 %). ¹H NMR (CDCl₃, 400 MHz), δ : 7.46 ppm (d, 4H, **Ar-H**), 7.32 ppm (d, 2H, **CH=CH**), 7.09 ppm (s, 2H, **Ar-H**), 7.05 ppm (d, 2H, **CH=CH**), 6.87 ppm (d, 4H, **Ar-H**), 3.95 ppm (t, 4H, **Ar-OCH₂-alkyl**), 3.90 ppm (s, 6H, **Ar-OCH₃**), 1.77-0.8 ppm (m, 42H, **aliphatic-H**). ¹³C-NMR (CDCl₃, 100MHz) δ : 158.7, 151.3, 130.4, 128.3, 127.7, 126.5, 120.9, 114.6, 108.8 (**Ar-C**), 68.0 (**OCH₂**), 56.3 (**OCH₃**), 31.9, 29.6, 29.5, 29.4, 29.3, 29.2, 26.0, 22.7 and 14.1 ppm. FT-IR (KBr, cm⁻¹): 2921, 2846, 1595, 1502, 1460, 1398, 1244, 1204, 1167, 1114, 1043, 1012, 959, 842, 809 and 726. MALDI-TOF-TOF-MS (MW = 683.01): m/z = 682.45. Anal. Calcd for C₄₆H₆₆ O₄: C, 80.89; H, 9.74. Found: C, 81.16; H, 9.48.

Synthesis of 4,4'-(1E, 1'E)-2,2'-(2,5-dibutoxy-1,4-phenylene)bis (ethene-2,1-diyl)bis(butoxybenzene) (OPV-C4-C4): 3c (1.0 g, 2.00 mmol), **4d** (0.8 g, 4.38 mmol) and potassium *tert*-butoxide (12 mL, 1M THF solution) were reacted as described for **OPV-C1-C1**. Yield = (79%). ¹H NMR (CDCl₃, 400 MHz), δ : 7.44 ppm (d, 4H, **Ar-H**), 7.32 ppm (d, 2H, **CH=CH**), 7.08 ppm (s, 2H, **Ar-H**), 7.04 ppm (d, 2H, **CH=CH**), 6.88 ppm (d, 4H, **Ar-H**), 4.03 ppm (t, 4H, **OCH₂**), 3.97 ppm (t, 4H, **OCH₂**), 1.84 ppm (m, 4H, **OCH₂CH₂CH₂**), 1.77 ppm (m, 4H, **OCH₂CH₂CH₂**), 1.7-1.4 ppm (m, 8H, **aliphatic H**), 0.97 ppm (m, 12H, **CH₃**). ¹³C-NMR (CDCl₃, 100MHz) δ : 158.8, 150.9, 130.7, 128.2, 127.7, 126.9, 121.3, 114.7, 110.4, 69.2, 67.8, 31.7, 31.4, 19.6 and 13.9. FT-IR (KBr, cm⁻¹): 3315, 2930, 2864, 2483, 1597, 1504, 1460, 1389, 1349, 1293, 1239, 1207, 1169, 1120, 1036, 1006, 966, 847, 800 and 746. MALDI-TOF-TOF-MS (MW = 570.80): m/z = 570.42 Anal. Calcd for C₃₈H₅₀ O₄: C, 79.96; H, 8.83. Found: C, 80.11; H, 9.33.

Synthesis of 4,4'-(1E, 1'E)-2,2'-(2,5-bis(octyloxy)-1,4-phenylene)bis (ethane-2,1diyl)bis(octyloxybenzene) (OPV-C8-C8): 3d (0.3 g, 0.50 mmol), **4h** (0.2 g, 1.10 mmol) and potassium *tert*-butoxide (3 mL, 1M THF solution) were reacted as described for **OPV-C1-C1**. Yield = (66 %). ¹H NMR (CDCl₃, 400 MHz), δ : 7.44 ppm (d, 4H, **Ar-H**), 7.32 ppm (d, 2H, **CH=CH**), 7.08 ppm (s, 2H, **Ar-H**), 7.05 ppm (d, 2H, **CH=CH**), 6.87 ppm (d, 4H, **Ar-H**), 4.02 ppm (t, 4H, **OCH₂**), 3.96 ppm (t,

4H, OCH₂), 1.86 ppm (m, 4H, OCH₂CH₂CH₂), 1.79 ppm (m, 4H, OCH₂CH₂CH₂), 1.7-1.4 ppm (m, 40H, **aliphatic-H**), 0.87 ppm (t, 12H, CH₃). ¹³C-NMR (CDCl₃, 100MHz) δ: 158.8, 151.0, 130.7, 128.2, 127.7, 126.9, 121.4, 114.7, 110.5, 69.7, 68.1, 31.9, 29.5, 26.4, 26.1, 22.7 and 14.2 ppm. FT-IR (KBr, cm⁻¹): 3040, 2916, 2851, 1599, 1504, 1459, 1415, 1293, 1201, 1023, 962, 815, 718, 589 and 527. MALDI-TOF-TOF-MS (MW = 795.23): *m/z* = 794.75. Anal. Calcd for C₅₄H₈₂O₄: C, 81.56; H, 10.39. Found: C, 82.11; H, 10.33.

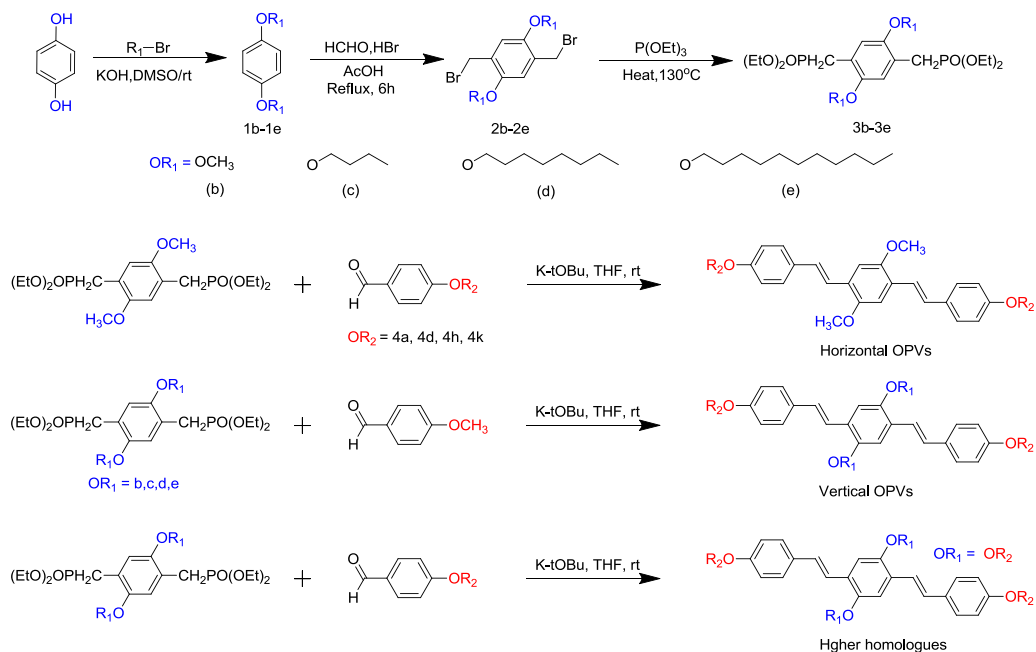
Synthesis of 4,4'-(1E, 1'E)-2,2'-(2,5-bis(undecyloxy)-1,4-phenylene)bis(ethene-2,1-diyl)bis(undecyloxy benzene) (OPV-C11-C11): 3e (0.1 g, 1.30 mmol), **4k** and potassium *tert*-butoxide (8.0 mL, 1M THF solution) were reacted as described for **OPV-C1-C1**. Yield = (31 %). ¹H NMR (CDCl₃, 400 MHz), δ: 7.45 ppm (d, 4H, **Ar-H**), 7.30 ppm (d, 2H, **CH=CH**), 7.09 ppm (s, 2H, **Ar-H**), 7.08 ppm (d, 2H, **CH=CH**), 6.88 ppm (d, 4H, **Ar-H**), 4.03 ppm (t, 4H, OCH₂), 3.97 ppm (t, 4H, OCH₂), 1.86 ppm (m, 4H, OCH₂-CH₂-CH₂), 1.79 ppm (m, 4H, OCH₂-CH₂-CH₂), 1.6-1.2 ppm (m, 64H, **aliphatic-H**) and 0.87 ppm (t, 12H, CH₃). ¹³C-NMR (CDCl₃, 100MHz) δ: 158.7, 156.5, 150.9, 130.6, 128.1, 127.6, 126.7, 121.2, 114.6, 113.8, 110.4, 69.6, 68.0, 53.2, 50.8, 31.9, 29.6, 29.6, 29.6, 29.3, 29.3, 22.6 and 14.1 ppm. FT-IR (KBr, cm⁻¹): 2919, 2851, 1604, 1573, 1509, 1467, 1423, 1391, 1296, 1244, 1202, 1173, 1110, 1017, 962, 845, 818, 800, 723 and 594. MALDI-TOF-TOF-MS (MW = 963.55): *m/z* = 962.49. Anal. Calcd for C₆₆H₁₀₆O₄: C, 82.27; H, 11.09. Found: C, 82.67; H, 11.21.

Synthesis of 4,4'-(1E, 1'E)-2,2'-(2,5-bis(octyloxy)-1,4-phenylene)bis(ethene-2,1-diyl) bis(undecyloxybenzene) (OPV-C8-C11): 3d (0.6 g, 1.00 mmol) was reacted with 4-undecyloxybenzaldehyde (0.6 g, 2.20 mmol) as described for **OPV-C1-C1**. Yield = (42 %). ¹H NMR (CDCl₃, 400 MHz), δ: 7.43 ppm (d, 4H, **Ar-H**), 7.30 ppm (d, 2H, **CH=CH**), 7.08 ppm (s, 2H, **Ar-H**), 7.05 ppm (d, 2H, **CH=CH**), 6.87 ppm (d, 4H, **Ar-H**), 4.02 ppm (t, 4H, OCH₂), 3.96 ppm (t, 4H, OCH₂), 1.86 ppm (m, 4H, OCH₂-CH₂-CH₂), 1.79 ppm (m, 4H, OCH₂-CH₂-CH₂), 1.6-1.2 ppm (m, 52H, **aliphatic-H**) and 0.87 ppm (t, 12H, CH₃). ¹³C-NMR (CDCl₃, 100MHz) δ: 158.8, 150.9, 130.7, 128.2, 127.7, 126.9, 121.3, 114.7, 110.5, 69.7, 68.1, 32, 31.04, 29.4, 26.39, 22.78 and 14.2 ppm. FT-IR (KBr, cm⁻¹): 2919, 2849, 1600, 1503, 1463, 1416, 1387, 1293, 1240, 1192, 1170, 1110, 1049, 1009, 961, 843, 815, 721, 666 and 634. MALDI-TOF-TOF-MS (MW = 879.39): *m/z* = 878.79. Anal. Calcd for C₆₀H₉₄O₄: C, 81.95; H, 10.77 Found: C, 81.57; H, 11.01.

3.3. Results and Discussion

3.3.1. Synthesis and characterisation of OPVs:

Oligophenylenevinylenes (OPV) molecules consisting of identical distyrylbenzene based aromatic core but different alkyl side chain substitutions at their periphery were synthesized by Wittig-Horner reaction as shown in scheme 3.1. The synthesis started from hydroquinone which was reacted with corresponding alkyl bromides to give 1, 4-bis(alkyloxy)benzenes (**1b-1e**). Compound **1b-e** were further reacted with paraformaldehyde and HBr in acetic acid to get their corresponding bis-bromomethylated compounds (**2b-2e**). These compounds were further converted into their corresponding 1, 4-bis[(alkyloxy)]-2,5-xylenediphosphonates (**3b-3e**) by reacting with triethyl phosphite. (**3b-3e**) reacts under Wittig-Horner condition with 4-alkoxybenzaldehydes (synthesis for these mono aldehydes has already been described in chapter 2) leading to OPVs.



Scheme 3.1. Synthesis of OPVs with different peripheral alkyl domains.

The OPVs were named as OPV-CY-CX, where Y is the number of carbon atoms present in the vertical alkyl chains and X is the number of carbon atoms

present in the horizontal alkyl chains. A series of structural isomers was synthesized by interchanging the aliphatic chains in vertical and horizontal positions. Each pair consisted of molecules that have same chemical formula, but opposite arrangement of short and long alkyl chains in the middle and the terminal aromatic rings. The horizontal isomers had longer aliphatic chains placed parallel to the aromatic core. The chemical structures of horizontal OPVs, where the number of carbon atoms in vertical direction (Y) was fixed, and the aliphatic chains increased in X-direction have been shown in the figure 3.4.

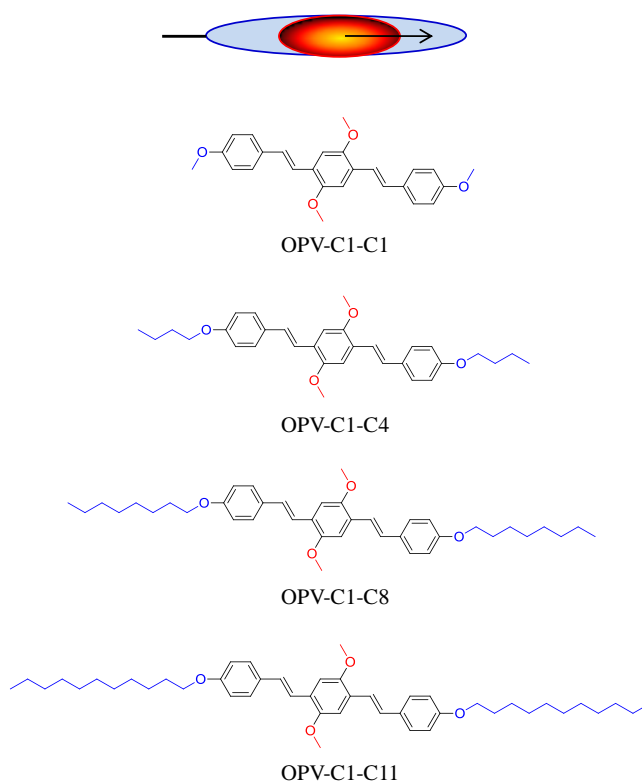


Figure 3.4. Chemical structures of horizontal OPV isomers.

Similarly, the chemical structures of the vertical isomers in which the alkyl chain length increased along the y-direction have been shown in the figure 3.5. In the vertical isomers, the longer aliphatic chains were placed perpendicular to the aromatic domain. Here, again the aromatic domain was fixed, but the aliphatic domain increased in y-direction. The (X, Y) for the pair of structural isomers are

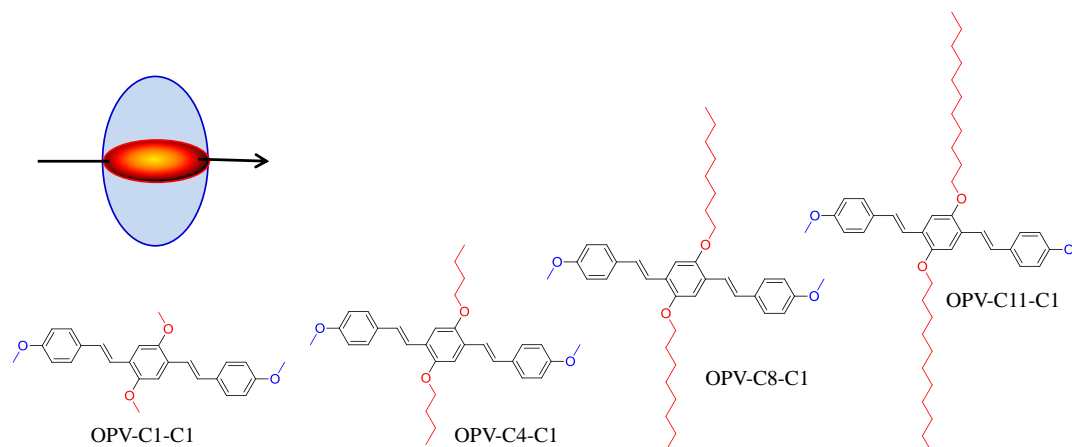


Figure 3.5. Chemical structures of vertical structural isomers.

(C1, C4) and (C4, C1) to give rise to OPV-C1-C4 and OPV-C4-C1; (C1, C8) and (C8, C1) for OPV-C1-C8 and OPV-C8-C1; and (C1, C11) and (C11, C1) for OPV-C1-C11 and OPV-C11-C1. Another series of higher homologues was also synthesized in which the number of carbon atoms in horizontal and vertical directions was kept identical. The structures of all the homologues OPVs have been shown in figure 3.6. When $X = Y$, and the series included $(X, Y) = (C1, C1), (C4, C4), (C8, C8)$ and $(C11, C11)$ to give rise to OPV-C1-C1, OPV-C4-C4, OPV-C8-C8 and OPV-C11-C11.

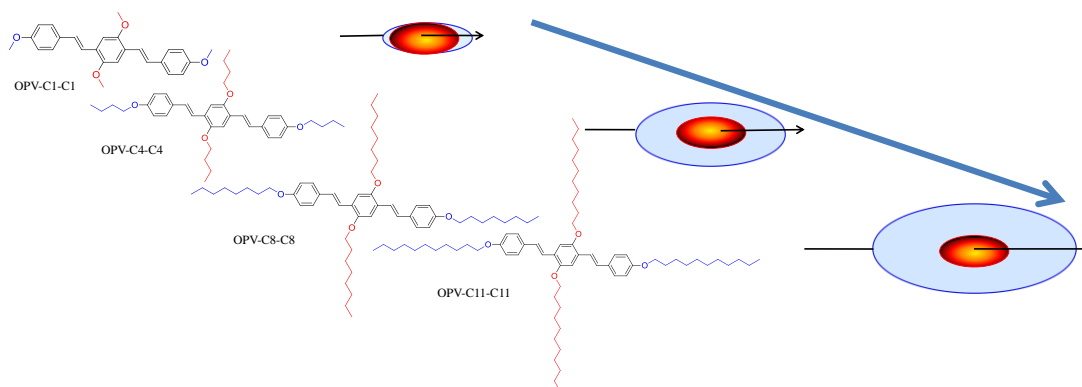


Figure 3.6. Chemical structures higher homologues OPVs.

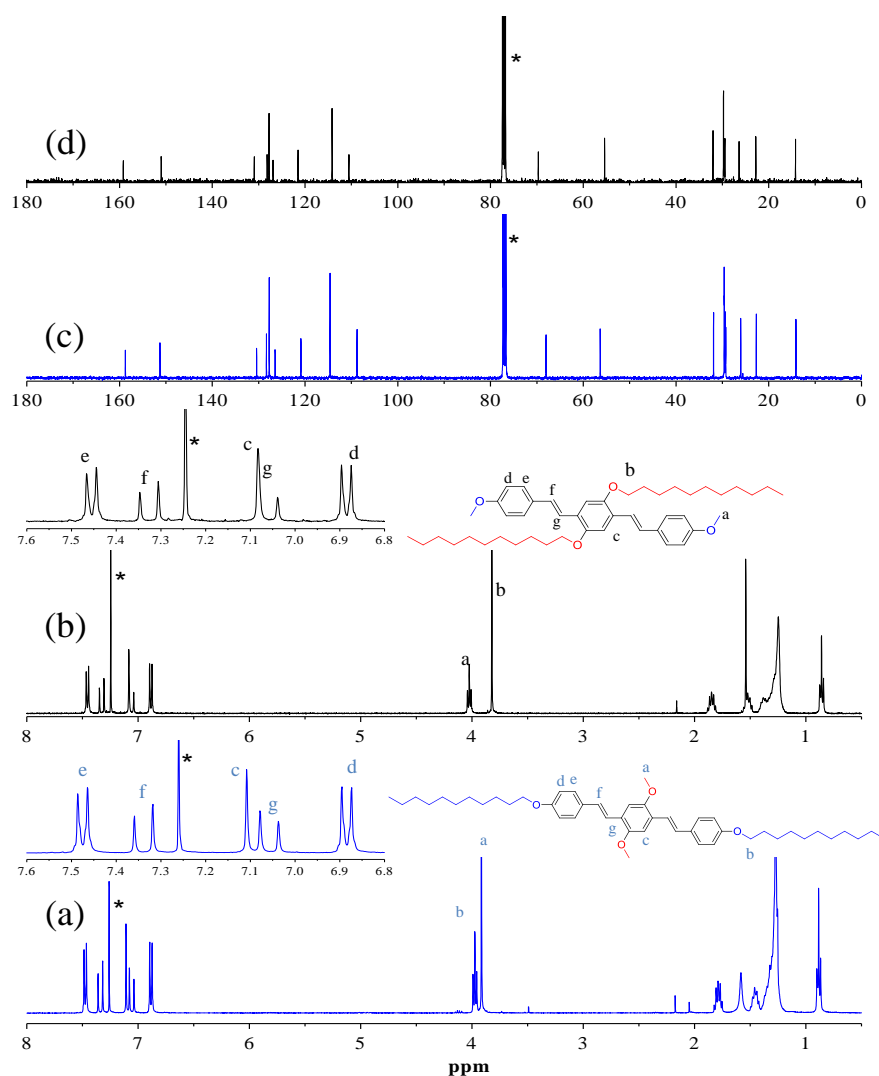


Figure 3.7. ^1H -NMR spectrum of OPV-C1-C11(a) ^1H -NMR spectrum of OPV-C11-C1 (b) ^{13}C -NMR spectrum of OPV-C1-C11(c) ^{13}C -NMR spectrum of OPV-C11-C1.

The OPVs were characterised by ^1H , and ^{13}C analysis. Figure 3.7a and 3.7b compared the ^1H NMR spectra of a representative pair of structural isomers (OPV-C1-C11 and OPV-C11-C1). The insets showed the expanded proton spectra of the aromatic regions. For OPV-C1-C11, the peaks at 7.47 ppm and 6.89 ppm corresponded to aromatic phenylene protons. The doublets at 7.35 ppm and 7.05 ppm belonged to vinylic protons. The protons in the middle aromatic ring appeared as a singlet at 7.11 ppm. A comparison of the aromatic region in OPV-C1-C11 with its structural isomer revealed that the singlet (peak c) for protons in the middle aromatic

ring was shifted downfield as compared to OPV-C11-C1. The other aromatic peaks were found to be same. A similar comparison of the alkoxy protons again reflected that the singlet for OCH₃ protons at 3.9 ppm was shifted downfield (≈ 0.1 ppm) in vertical isomer. The triplet for Ar-OCH₂-alkyl protons appeared at 4.1 ppm. The peaks for all other protons appeared below 3.75 ppm. ¹³C-NMR spectrum of the OPV-C11-C1 and OPV-C1-C11 also exhibited similar downfield shifts. Similar trend was observed for all other structural isomers, indicating that the middle aromatic ring in the horizontal isomers was slightly more electron deficient as compared to their vertical counterparts. MALDI-TOF-TOF spectrum of all the OPVs confirmed the presence of molecular ion peak (M⁺). The data for MALDI-TOF-TOF spectra and CHN analysis for all the OPVs have been given in the experimental section.

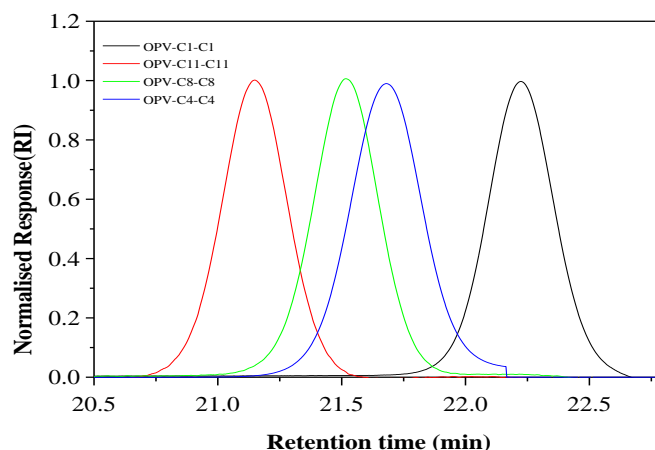


Figure 3.8. GPC chromatograms of OPVs in tetrahydrofuran at 25 °C.

The GPC chromatograms of higher homologues series have been shown in the figure 3.8. All the chromatograms were recorded by dissolving the OPV samples in tetrahydrofuran. Figure 3.8 shows that all the chromatograms appeared as a single peak confirming high purity of these samples. In GPC, higher molecular weight OPVs eluted faster than lower molecular weight OPVs and this is beautifully reflected in the above chromatogram showing highest molecular weight OPV-C11-c11 to extreme left and lowest molecular weight OPV-C1-C1 to the extreme right.

The GPC chromatogram of OPV-C8-C8 and OPV-C4-C4 followed a similar trend fell in between these two extremes.

Table 3.3. Table for characterisation parameters of OPVs.

Sample	OR ₁	OR ₂	Molecular formula	Elemental Analysis		MALDI-TOF-TOF-MS
				theoretical	found	
OPV-C1-C4	OCH ₃	OC ₄ H ₉	C ₃₂ H ₃₈ O ₄	C, 78.98 ; H, 7.87	C, 79.01 H, 8.48	(MW = 486.64): <i>m/z</i> = 486.42.
OPV-C4-C1	OC ₄ H ₉	OCH ₃	C ₃₂ H ₃₈ O ₄	C, 78.98; H, 7.87	C, 79.10; H, 8.48.	MW = 486.64): <i>m/z</i> = 486.33.
OPV-C1-C8	OCH ₃	OC ₈ H ₁₇	C ₄₀ H ₅₄ O ₄	C, 80.22 ; H, 9.09	C, 80.12; H, 8.98.	MW = 598.85): <i>m/z</i> = 598.46.
fOPV-C8-C1	OC ₈ H ₁₇	OCH ₃	C ₄₀ H ₅₄ O ₄	C, 80.22; H, 9.09	C, 79.85; H, 8.48.	(MW = 598.85): <i>m/z</i> = 598.47.
OPV-C1-C11	OCH ₃	OC ₁₁ H ₂₃	C ₄₆ H ₆₆ O ₄	C, 80.89; H,9.74	C, 81.16; H, 9.48	(MW = 683.01): <i>m/z</i> = 682.45.
OPV-C11-C1	OC ₁₁ H ₂₃	OCH ₃	C ₄₆ H ₆₆ O ₄	C, 80.89; H, 9.74.	C, 81.29; H, 9.66	(MW = 683.01): <i>m/z</i> = 682.55
OPV-C1-C1	OCH ₃	OCH ₃	C ₂₆ H ₂₆ O ₄	C, 77.59; H, 6.51	C, 78.01; H, 6.63	(MW = 402.48): <i>m/z</i> = 402.16.
OPV-C4-C4	OC ₄ H ₉	OC ₄ H ₉	C ₃₈ H ₅₀ O ₄	C, 79.96; H, 8.83	C, 80.11; H, 9.33.	(MW = 570.80): <i>m/z</i> = 570.42
OPV-C8-C8	OC ₈ H ₁₇	OC ₈ H ₁₇	C ₅₄ H ₈₂ O ₄	C, 81.56; H, 10.39.	C, 82.11; H,10.33	(MW = 795.23): <i>m/z</i> = 794.75.
OPV-C11-C11	OC ₁₁ H ₂₃	OC ₁₁ H ₂₃	C ₆₆ H ₁₀₆ O ₄	C,82.27; H,11.09	C,82.67 H,11.21	(MW = 963.55): <i>m/z</i> = 962.49.

3.3.2. Thermal Properties

The OPVs were subjected to DSC analysis at 10°/min heating and cooling cycles. The DSC thermograms of each pair of structural isomers have been shown in figure 3.9.

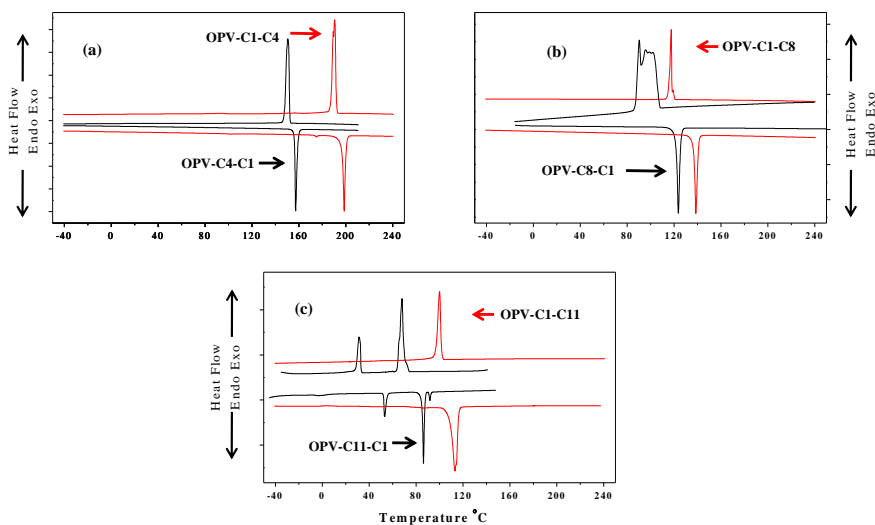


Figure 3.9. DSC profiles of structural isomers.

OPV-C1-C4 ($T_m = 199^\circ\text{C}$, $T_c = 190^\circ\text{C}$) and OPV-C4-C1 ($T_m = 159^\circ\text{C}$, $T_c = 151^\circ\text{C}$) exhibited a single endotherm and a single exotherm corresponding to melting and crystallization transitions (see figure 3.9a). Similarly, OPV-C1-C8 and OPV-C8-C1 exhibited single melting and crystallization peaks in their respective heating and cooling cycles (see figure 3.9b). As the number of carbon atoms increased to C11 (see figure 3.9c), the vertical isomer OPV-C11-C1 started exhibiting two transitions in the heating at 86.3°C and 91.8°C , which was completely reversible in the cooling cycle.

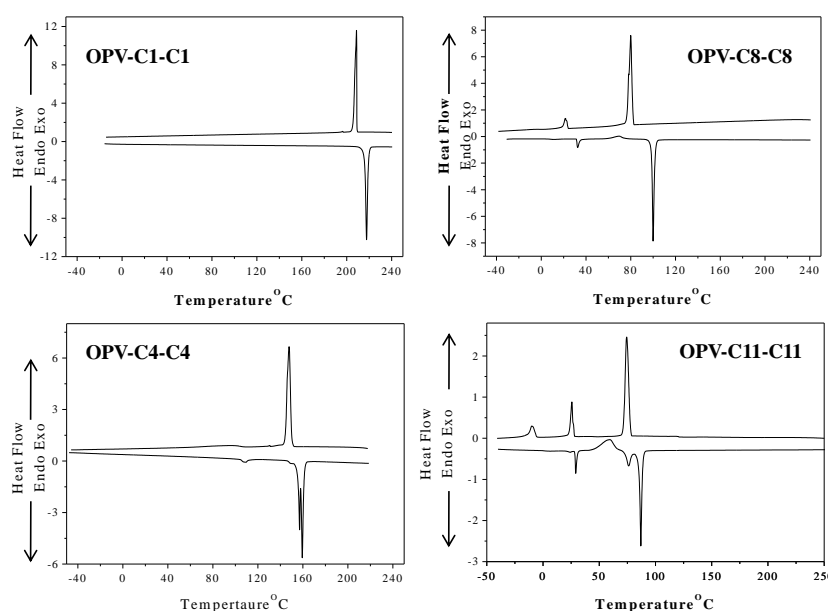


Figure 3.10. DSC profiles of higher homologues OPVs.

The DSC profiles of higher homologues have been shown in figure 3.10, the transition temperatures decreased gradually with increase in the number of the carbon atoms in both x and y-direction. OPV-C1-C1 exhibited single melting transition ($T_m = 217.6^\circ\text{C}$, $\Delta H_{m1} = 48.9 \text{ kJmol}^{-1}$) in the heating cycle and a single crystallization transition ($T_{c1} = 208.1^\circ\text{C}$, $\Delta H_{c1} = 45.2 \text{ kJmol}^{-1}$) in the cooling cycle corresponding to normal crystalline solid. As the number of carbon atoms increased to 4, 8, and 11 in both the horizontal and vertical directions equally, the transition temperatures were found to decrease and the enthalpies of transition increased.

Further, with increase in the alkyl domain, multiple transitions corresponding to several phase transformations are observed during heating and cooling cycles. The thermal data for all the OPVs in respective heating and cooling cycle have been summarized in the table 3.3.

Table 3.4. DSC thermal data of OPVs at 10 %/min heating/cooling Rate.

Sample	Heating cycle				Cooling cycle			
	T _{m1}	ΔH _{m1}	T _{m2}	ΔH _{m2}	T _{c1}	ΔH _{c1}	T _{c2}	ΔH _{c2}
OPV-C1-C4	174.9	1.02	198.7	69.2	190.8	68.4	154.4 [#]	0.9 [#]
OPV-C4-C1	-	-	157.2	50.2	150.8	50.2	-	-
OPV-C1-C8	-	-	136.9	73.2	117.6	68.4	-	-
OPV-C8-C1	-	-	123.6	57.3	92.6	49.4	-	-
OPV-C1-C11	-	-	113.1	82.8	100.0	78.3	-	-
OPV-C11-C1	86.3*	41.9*	91.8	4.5	67.6	42.6	32.2	16.6
OPV-C1-C1	-	-	197.6	48.9	208.1	45.2	195.6	0.2
OPV-C4-C4	109.0	4.2	159.4	56.5	147.1	53.3	96.8	3.2
OPV-C8-C8	32.6*	5.4*	99.9	58.3	80.6	44.8	22.8 [#]	5.5 [#]
OPV-C11-C11	71.1*	16.9*	86.7	71.2	74.3	45.7	25.4 [#]	10.9 [#]

(*) These molecule showed multiple crystal to crystal transitions. The thermal data for the transition observed in the heating cycle have been summarised as follows: T₁ = 270.01 K, ΔH₁ = 2.56 kJ mol⁻¹; T₂ = 326.33K, ΔH₂=17.26 kJ mol⁻¹ for **OPV-C11-C1**. T₁ = 239.52 K, ΔH₁ = 1.14 kJ mol⁻¹; T₂ = 261.79 K, ΔH₂ = 1.17 kJ mol⁻¹ for **OPV-C8-C8**. T₁ = 302.1 K, ΔH₁ = 10.4 kJ mol⁻¹ for **OPV-C11-C11**.

(#) These molecule showed multiple crystal to crystal transitions. The thermal data for the transition observed in the cooling cycle have been summarised as follows: T₁ = 366.18 K, ΔH₁ = 1.14 kJ mol⁻¹ for **OPV-C1-C4**. T₁ = 266.6 K, ΔH₁ = 0.51 kJ mol⁻¹ for **OPV-C8-C8**. T₁ = 263.1 K, ΔH₁ = 7.2 kJ mol⁻¹ for **OPV-C11-C11**.

a) T_{m1} is temperature for crystal to LC phase change measured in °C. **(b)** T_{m2} is temperature for LC to Isotropic phase change measured in °C. **(c)** ΔH_{m1} is the enthalpy change for crystal to LC phase change in kJ/mol. **(d)** ΔH_{m2} is the enthalpy change for LC to Isotropic phase change in kJ/mol. **(e)** T_{c1} is temperature for isotropic to LC phase change measured in °C. **(f)** T_{c2} is temperature for LC to crystal phase change measured in °C. **(g)** ΔH_{c1} is the enthalpy changes for isotropic to LC phase change in kJ/mol. **(h)** ΔH_{c2} is the enthalpy change during LC to crystal phase change in kJ/mol.

The transition temperatures, enthalpy, and entropy of melting and crystallization constituted important parameters in determining packing stability. To find a general relationship on how these thermodynamic properties changed with variation in peripheral side chains, these parameters were plotted against the number of carbon atoms in both the directions as shown in the figure 3.11.

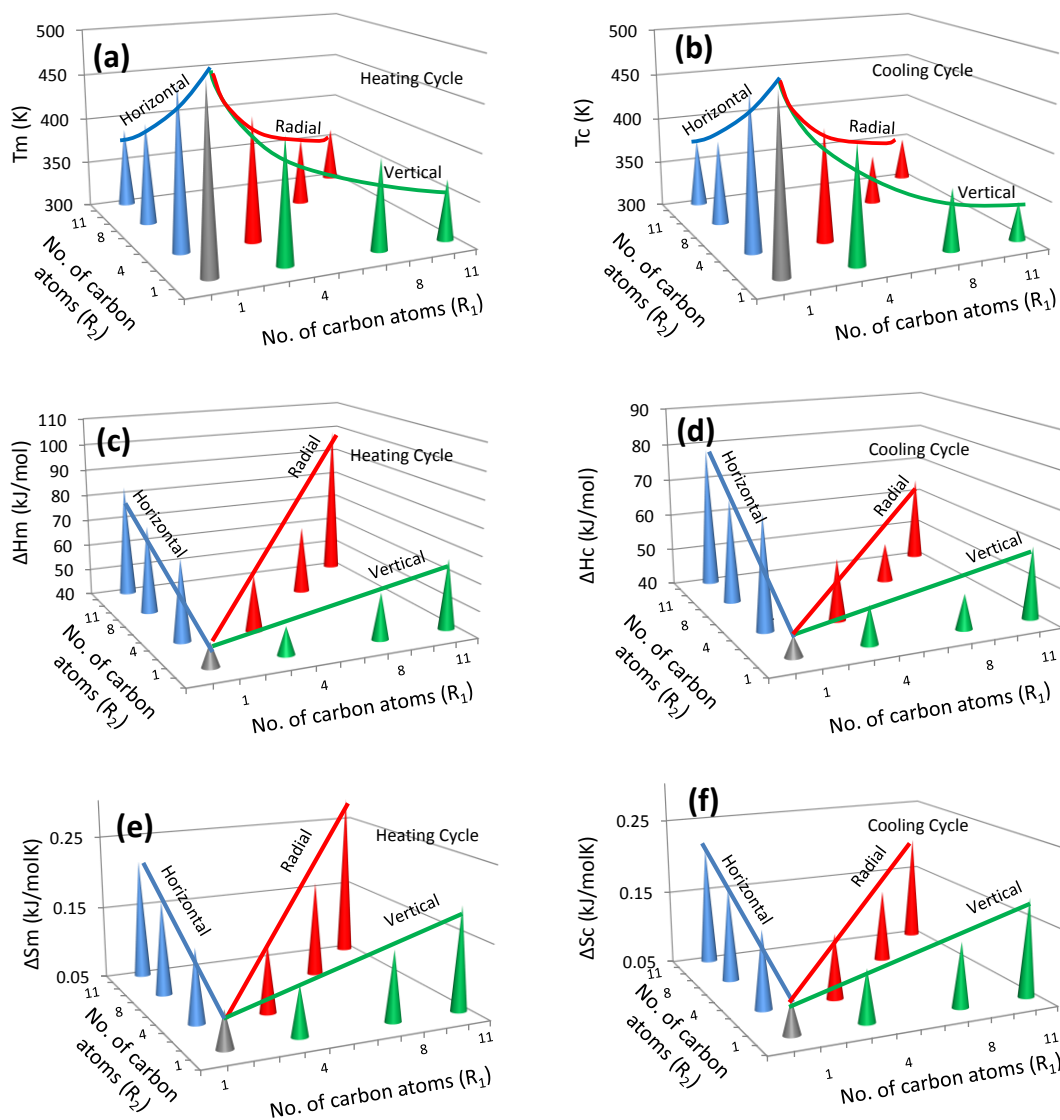


Figure 3.11. 3D plots comparing the transition temperatures (a and b), enthalpy (c and d) and entropy (e and f) in respective melting and crystallization cycles.

The variation in the thermodynamic property (in z-direction) was plotted as a function of x (the no. of carbon atoms in the horizontal alkyl chains) and y (the number of carbon atoms in the vertical alkyl chains). Figure 3.11a compared the melting points of OPVs against the number of carbon atoms in vertical and horizontal alkyl chains. The melting points of OPVs gradually decreased in horizontal, vertical and radial direction as indicated by the curved lines in blue, green and red respectively. This observation was attributed to increasing flexibility with increased alkyl chain length. Figure 3.11b showed that the trend remained same for crystallization temperatures in the cooling cycle.

Another important thermodynamic property such as the enthalpy increased in all the three directions as the number of carbon atoms increased. Among the structural isomers, OPVs having longer alkyl chains substituted along the horizontal direction of the aromatic core showed higher melting and crystallization enthalpies as compared to vertically substituted counterparts. (See figure 3.11c. and figure 3.11d). The enthalpies of melting were 15-16 kJ/mol higher for horizontal isomers as compared to vertical isomers. The effect was even more pronounced in enthalpies of crystallization as seen in the figure 3.11d. A plot of change in entropies in heating and cooling cycles (see figure 3.11e and figure 3.11f) revealed that entropies increased gradually with increasing carbon chain lengths in horizontal, vertical and radial directions.

The above thermal analysis suggested that substitution of longer alkyl chains along the horizontal direction of the aromatic core tended to increase packing among this class of OPV chromophores. In contrast, introduction of long alkyl chains in the vertical direction (or along the short molecular axis) destabilized molecular packing resulting in lower transition temperatures and lower enthalpies of transitions. Horizontal isomers underwent more compact packing than vertical molecules. Highly packed structures needed more energy for melting as well as expelled larger amount of heat during crystallization. This trend could be attributed to the fact that longer alkyl tails tend to crystallize among themselves leading to better stability and packing properties.

3.3.3. Polarised Light Microscope Analysis

To study the temperature dependent LC textures, the OPVs were subjected to polarized light microscopic analysis with a programmable hot stage. The sample was placed on the glass substrate, heated to melt at 10 °C/min and kept isothermally at 20 °C above their melting temperature for 2-3 minutes. The melt was subsequently cooled at 10 °C/min to capture the images using high resolution camera. The detailed temperature dependent LC textures for OPV-C1-C11 have been shown in figure 3.12. OPV-C1-C11 exhibited spherical droplets as nucleating sites (see images at 105.5 °C at 105 °C). These droplets quickly impinged on neighboring droplets (at 104.5 °C) to give rise to schlieren nematic liquid crystalline textures³⁸ observed at 104 °C and 103.5 °C. The LC temperature window was 2.5 ° and as the temperature decreased to 103°C, crystalline phases started to appear. These nematic LC phases were observed only at high temperatures and therefore these materials are high temperature LC materials. At room temperature, the textures resembled those of normal crystalline solids.

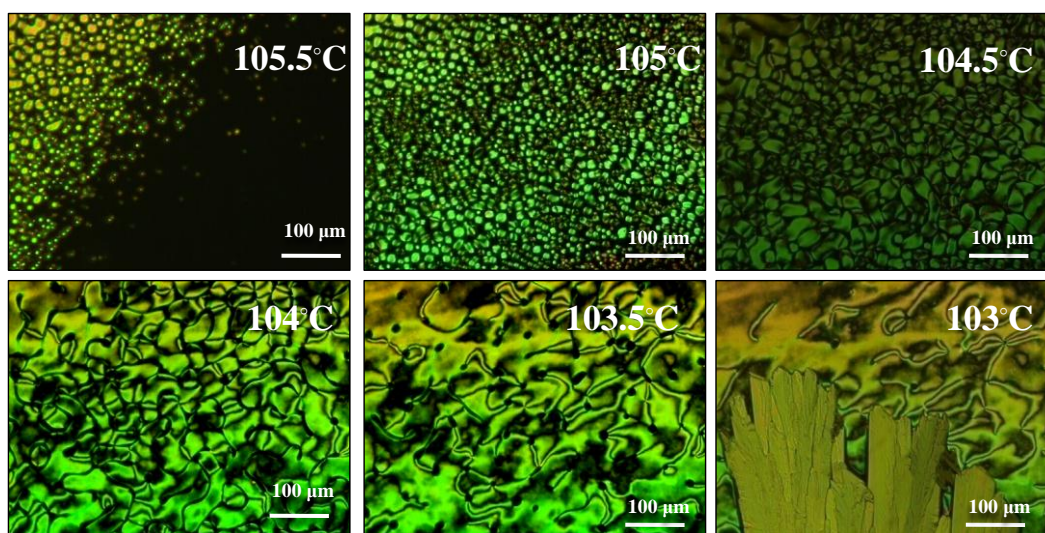


Figure 3.12. Temperature dependent PLM profile of OPV-C1-C11 in cooling cycle.

The nucleation and subsequent growth patterns of all horizontal isomers have been shown in the figure 3.13. OPV-C1-C1 exhibited sharp needle like nucleation at 212°C, the rapid growth of crystalline vectors resulted in the formation of typical crystalline images at room temperature (see image at 211° C and at 40° C). OPV-C1-C4 exhibited nucleation at 145°C. The growth patterns at 140.5° C indicated that the sample has some tendency toward liquid crystallinity, but as the temperature decreased sharp crystalline vectors were observed. As the alkyl chain length increased further to C8, the molecule became liquid crystalline in nature and Schlieren nematic liquid crystalline textures were observed at 117.5°C. The liquid crystalline window was small (around 4°C) and further decreased in temperature resulted in growth of crystalline mesophases.

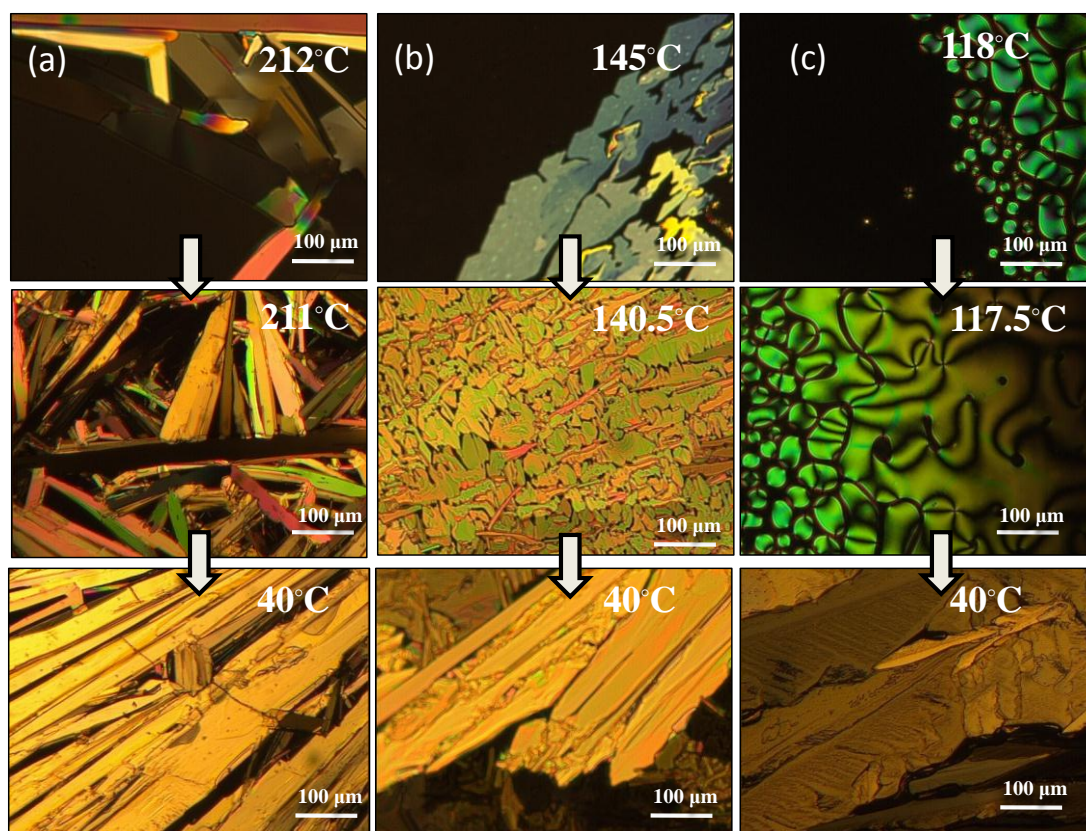


Figure 3.13. Temperature dependent PLM profiles of OPV-C1-C1(a), OPV-C1-C4 (b) and OPV-C1-C11(c) in the cooling cycle.

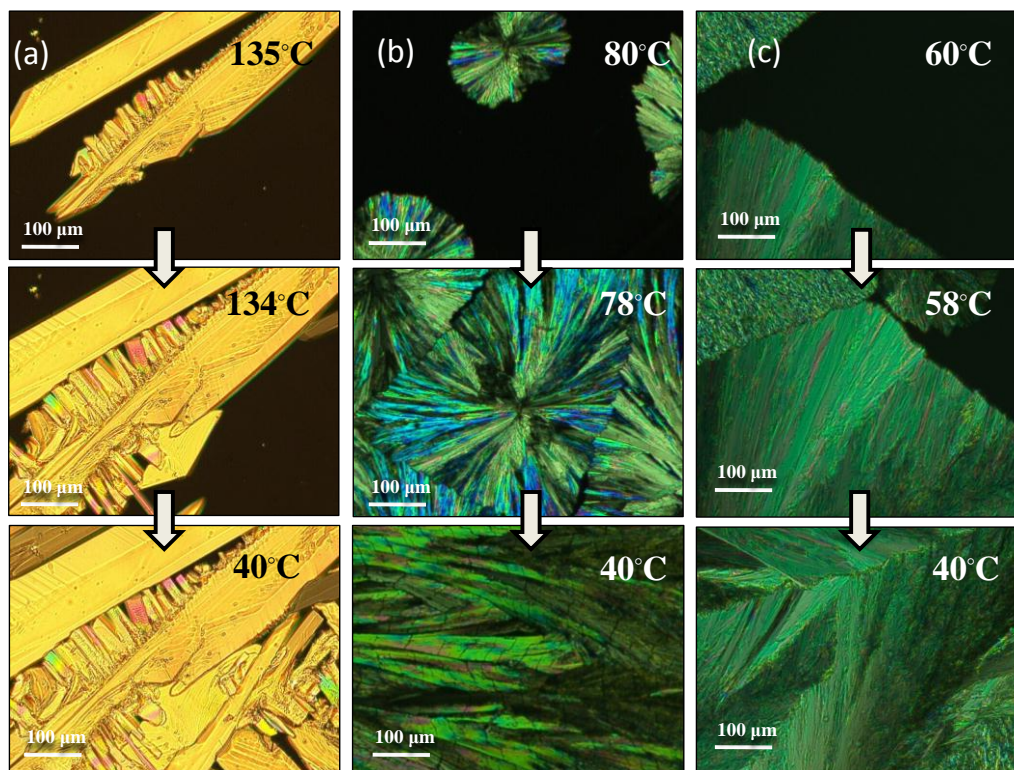


Figure 3.14. Temperature dependent PLM profiles of OPV-C4-C1(a), OPV-C8-C1 (b) and OPV-C11-C1(c) in the cooling cycle.

The PLM images for nucleation and subsequent growth patterns for the vertical isomers (with increase in alkyl chain length in the vertical direction) have been shown in the figure 3.14. The nucleation was sharp needle like in the case of OPV-C4-C1. The growth pattern at 134 °C and the PLM images at room temperature confirmed crystalline behaviour for OPV-C4-C1. OPV-C8-C1 exhibited spherulitic nucleation, these nuclei quickly grew to give crystalline images as seen in the images at 78°C and 40°C. As the number of carbon atoms increased further in the vertical direction (OPV-C11-C1), similar crystalline behaviour was observed as seen for the lower vertical counterparts. The PLM Analysis for radially substituted OPVs, when the chain length grows equally in both the directions has been shown in the figure 3.15. OPV-C4-C4 exhibited sharp layer like nucleation at 135°C, on further cooling, the sample started exhibiting lamellar like textures. These textures were completely

destroyed as the sample cooled to room temperature. On increasing the chain length to C8 in both the directions, the tendency to form lamellae increased as shown in the image at 60°C. However, the lamellae were not stable at room temperature. OPV-C11-C11, exhibited oval shaped nucleation resulting in the formation of leaf like LC textures at 70 to 65° C. On subsequent cooling below 60 °C in the LC active temperature window, these leaf like textures transformed into well ordered two-dimensional lamellar textures (see image at 42 °C).

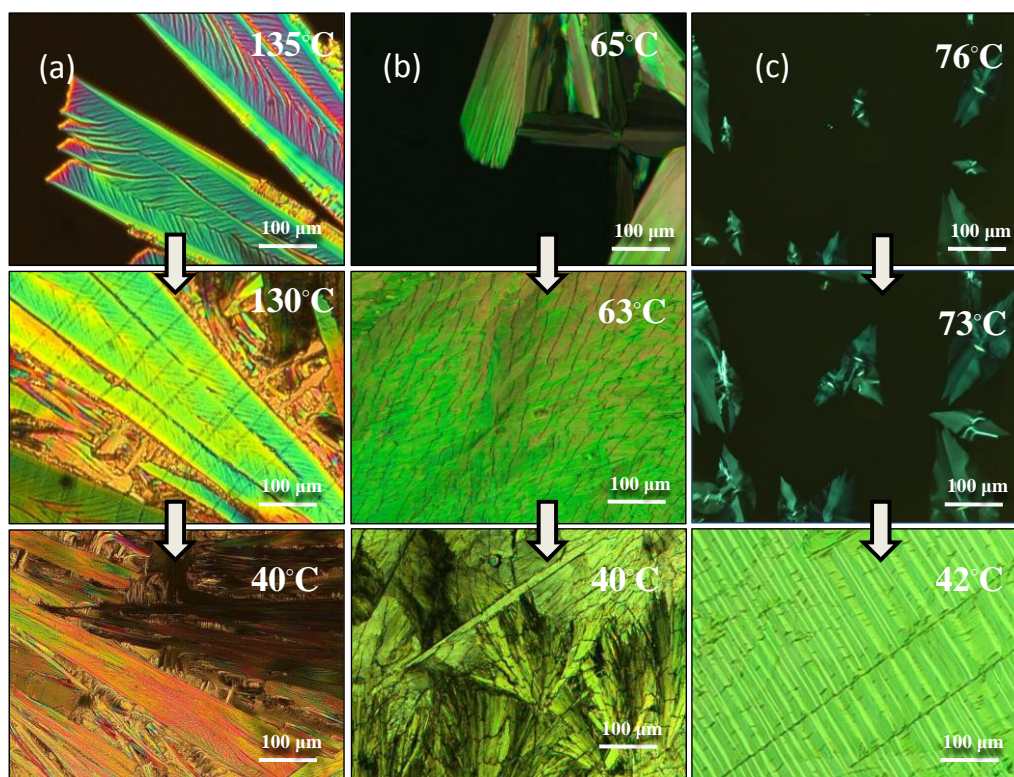


Figure 3.15. Temperature dependent PLM profiles of of OPV-C4-C4(a), OPV-C8-C8 (b) and OPV-C11-C11(c) in the cooling cycle.

Based on the above DSC and PLM analysis, a schematic model summarizing the effect of different chain length and its orientation on mesoscopic ordering of OPVs has been shown in the figure 3.16. Horizontal isomers exhibited higher melting

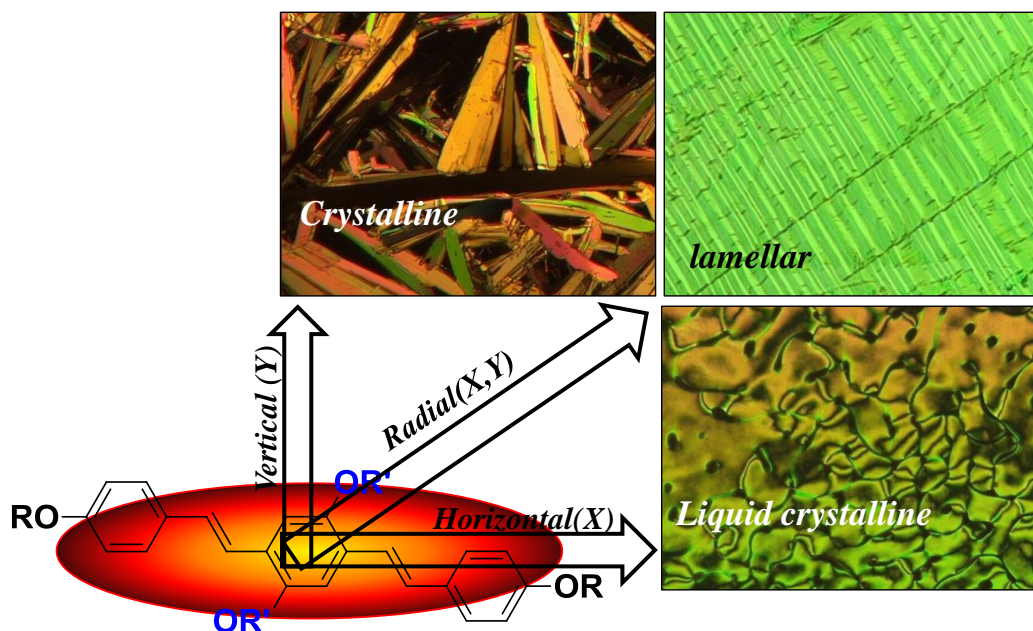


Figure 3.16. Summary of mesoscopic ordering as a function of X and Y .

and crystallization temperatures as compared to vertical isomers. Increasing alkyl chain length along the horizontal (x) direction induced LC properties. Vertical isomers were found to be crystalline in nature. This difference in mesoscopic ordering could be attributed to the difference in the position of long alkyl chains. Horizontal OPVs were I shaped and could rapidly spin around their long molecular axis.³⁹ This spinning movement is important for the generation of stable LC phases as spinning suppressed crystallization at lower temperatures. However, introduction of large alkyl chain interactions in the direction perpendicular to the aromatic core suppressed the molecular spinning leading to destabilisation of LC phase and direct transition to crystalline phase. Radially substituted OPVs showed gradual increase in enthalpies with increase in carbon chain lengths. The PLM analysis revealed that equal substitution in both x and y directions resulted in well ordered two-dimensional lamellar textures. Therefore, it is not just the alkyl chain length but orientation in which the chain length is put that is very crucial in inducing liquid crystallinity and solid state packing.

3.3.4. Single crystal XRD Analysis of OPVs

From the detailed PLM and DSC analysis, it was understood that position of peripheral alkyl side chains played a key role in determining packing properties of the molecules. To understand the effect of longitudinal, vertical and radial alignment of alkyl chains on the intermolecular packing of the molecules, detailed single crystal X-ray analysis of a large number of OPV chromophores was done. Figure 3.17 is a schematic diagram that classified all the OPV structures broadly in to two types. This classification depended on the angle subtended by two terminal rings ψ_A and ψ_B (see figure 3.17a) on the central aromatic ring.

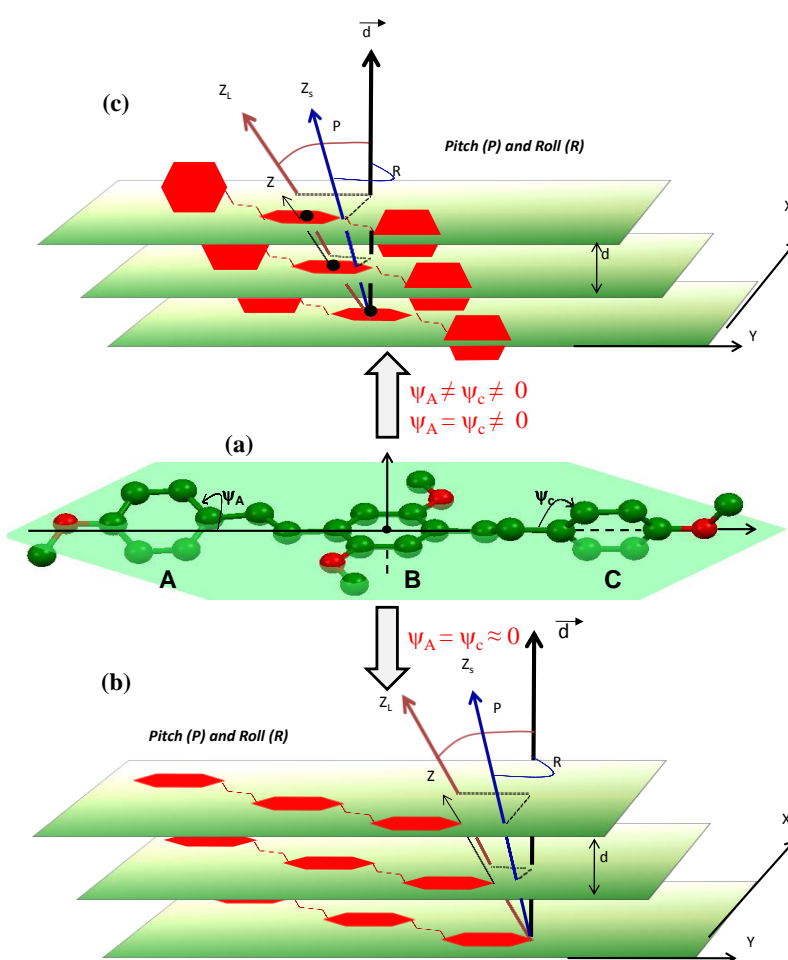


Figure 3.17. Models explaining roll and pitch calculations for non-planar (c) and planar molecules (b).

The three phenyl rings have been labelled as A, B, and C in the order of increasing carbon atom number for unsymmetrical structures. For symmetric structures, the rings were labelled as A, B, A. When $\psi_A \approx \psi_C \approx 0$, the molecules were planar, in such cases, the roll and pitch inclinations could be directly calculated using the roll and pitch model²³ shown in the figure 3.17b. But, when, $\psi_A \neq \psi_C \neq 0$ or $\psi_A \approx \psi_C \neq 0$, the molecular backbone became non-planar. In these cases, roll and pitch inclinations have been calculated with respect to the centroid of the central neighbouring aromatic rings that are parallel to each other. This model has been diagrammatically shown in the figure 3.17c.

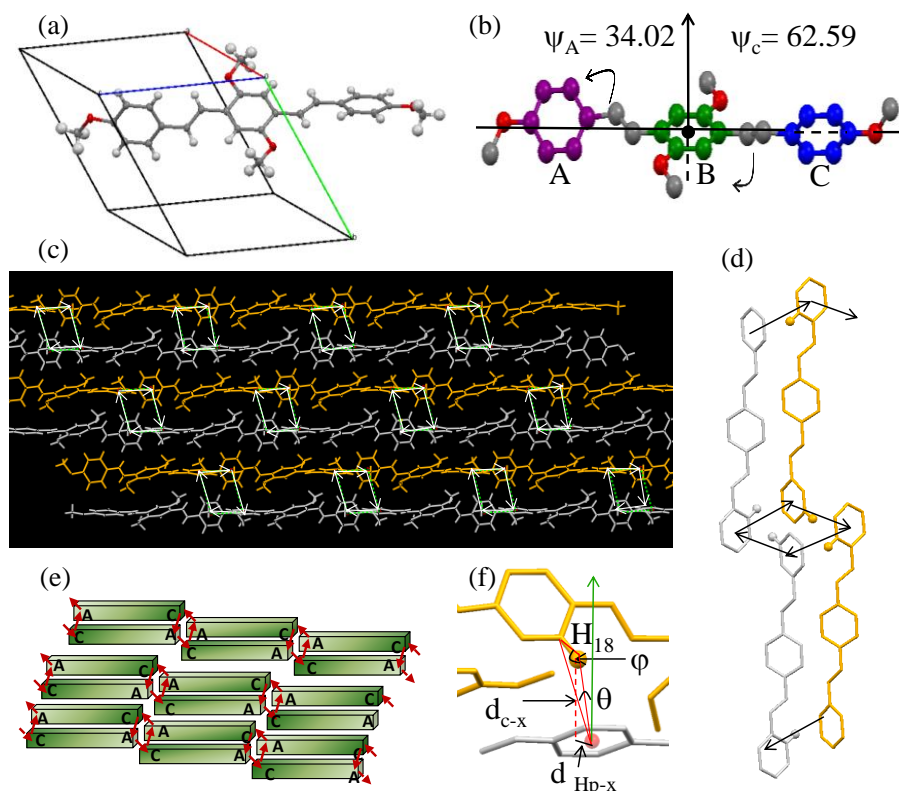


Figure 3.18. X-ray crystal structure and 3-D packing of OPV-C1-C1.

The single crystal XRD analysis for OPV-C1-C1 has been shown in figure 3.18. The crystal system is triclinic and the space group is P-1. The two terminal aromatic rings of the OPV chromophore moved out of the plane of the middle

aromatic ring in opposite directions giving rise to a non-planar molecule. The torsional angles of the central aromatic ring with the terminal aromatic rings were measured to be 34.02° (ψ_A) and 62.59° (ψ_B), respectively, (see figure 3.18b). Intermolecular close contacts in the single crystal structure revealed a total of four CH- π interactions present between four adjacent neighboring molecules. The CH/ π interactions involved donors and phenyl rings as π -acceptors in an almost perpendicular (83.47°) edge to face arrangement.^{40a} The three dimensional packing of the molecules (see figure 3.18c) reflected head to tail arrangement of the molecules, interlocked through four strong CH/ π interactions in a square planar fashion (shown in white lines in figure 3.18c). The expanded image showed the square plane formed by four such CH/ π interactions (see figure 3.18d). The molecules were continuously interlocked in a linear fashion to form long one dimensional molecular pipe, however, no strong CH/ π interactions were found between adjacent molecular pipes. The pictorial model in figure 3.18e showed that molecules arranged in head to tail fashion with A to C interlocking of the rings.

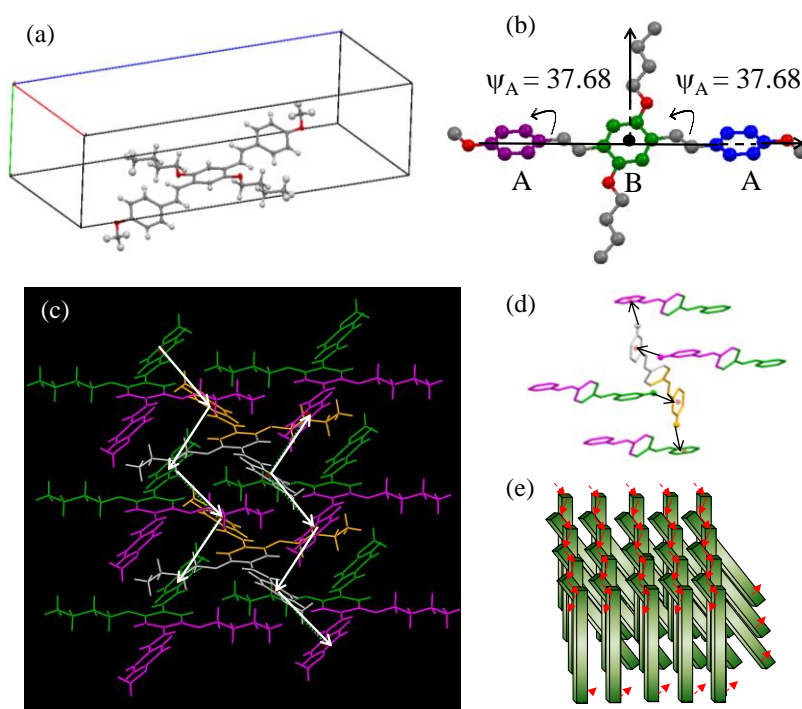


Figure 3.19. X-ray crystal structure and 3-D packing of OPV-C4-C1.

On increasing the number of carbon atoms in the vertical direction from C1 to C4, in the case of OPV-C4-C1, the crystal system became orthorhombic and the molecule belonged to centrosymmetric space group Pbca. The unit cell for OPV-C4-C1 has been shown in figure 3.19a. In contrast to OPV-C1-C1, the two terminal aromatic rings in OPV-C4-C1 moved out of the plane of the middle aromatic ring in the same direction giving rise to a symmetric non-planar molecule. The angles subtended by terminal aromatic rings on the central aromatic ring were equal and measured to be 37.68° (see figure 3.19b). The three dimensional packing of a large number of molecules revealed that an extensive network of CH/ π interactions resulted in the formation of zig-zag chains of OPV molecules (see figure 3.19c). The CH/ π interactions were directed in an angular fashion subtending an angle of 104.8° relative to each other. A detailed analysis of these interactions revealed that the molecules were locked through four identical CH/ π interactions involving Ar-C-H₆ as donor and the terminal phenyl ring as π -acceptor system. A pictorial model in figure 3.19d exhibits that each central OPV molecule was locked by four surrounding neighboring molecules through four strong CH/ π interactions. These four neighboring molecules were oriented in an opposite direction to that of the central OPV molecule. The CH/ π geometric parameters d_{c-x} , θ , φ and d_{Hp-x} involving H₆ donor atom have been calculated as $d_{c-x} = 3.64$, $\theta = 4.65^\circ$, $\varphi = 135.46^\circ$ and $d_{Hp-x} = 0.75\text{\AA}$, respectively.

As the chain length increased further in OPV-C11-C1, a drastic change in molecular packing was observed. Figure 3.20a shows the X-ray single crystal structure and the unit cell for OPV-C11-C1. The molecules were found to exist as molecular dimers; each molecular dimer consisted of two molecules with different aromatic systems. The two terminal aromatic rings of the each molecule moved out of the plane of the middle aromatic ring equally and in the same direction giving rise to a non-planar molecule. The torsional angles were measured to be 29.50° for one such aromatic system (System1), but the terminal rings lay in the same plane. For

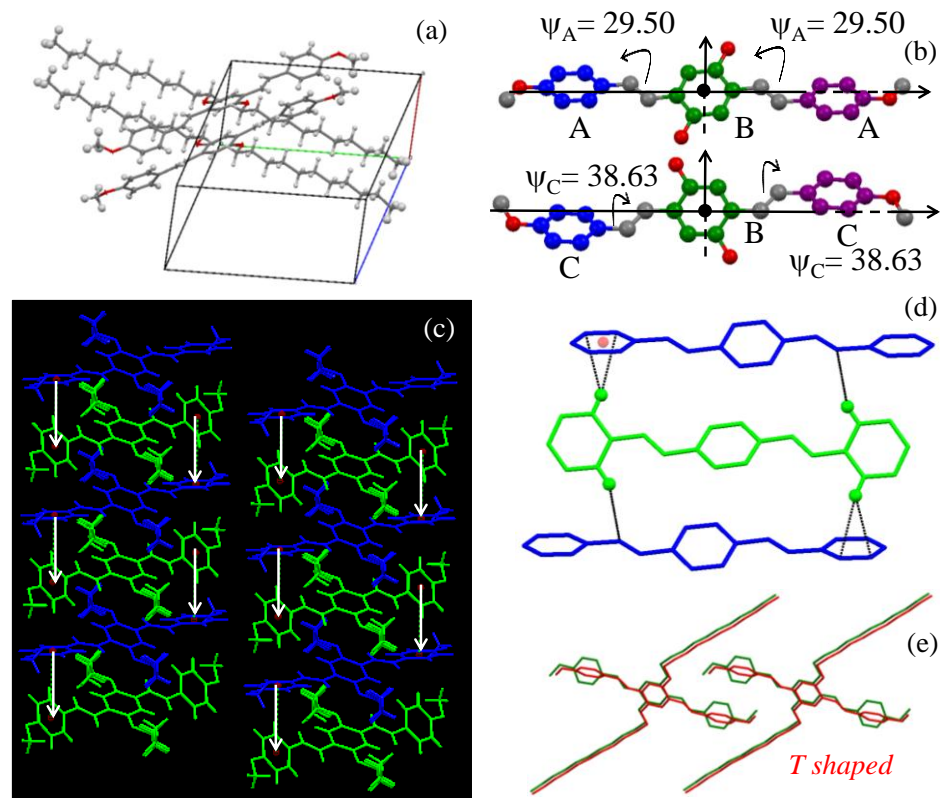


Figure 3.20. X-ray crystal structure and 3-D packing of OPV-C11-C1.

the second molecule, the torsional angles between the terminal and the central rings were measured to be 38.63 (System 2), but the two terminal rings were present in two different parallel planes separated by a distance of 1.85 Å as shown in the figure 3.20b. The undecyloxy chains present in the middle aromatic core moved out of the molecular plane and were oriented on either side of the aromatic core. The three dimensional packing revealed that molecules arranged right on the top of each other giving rise to one dimensional lamellar packing. Each green molecule presented in the one dimensional stack was locked by two blue molecules (top and bottom) from opposite side of the terminal aromatic rings. The molecular locking in each stack has been shown with white arrows. The CH/π interactions were directed in linear fashion, as against the square planar or angular fashion observed for lower counterparts. A detailed analysis of these interactions revealed that each central

molecule showed two strong Aryl-CH/ π interactions and two weak CH/ π interactions involving the double bonds. In contrast, the lower counterparts, OPV-C1-C1 and OPV-C4-C1, showed all strong Aryl CH/ π type interactions. The CH/ π interactions between Aryl-H₂₆ – terminal aromatic ring ($d_{c-x} = 3.42 \text{ \AA}$, $\theta = 8.05^\circ$, $\varphi = 137.32^\circ$ and $d_{H_p-x} = 0.34 \text{ \AA}$) and Aryl H₂₈ – C₇ = C₈ are $d_{c-x} = 3.58 \text{ \AA}$, $\theta = 20.23^\circ$, $\varphi = 135.57^\circ$ and $d_{H_p-x} = 0.819 \text{ \AA}$, respectively. The terminal rings of the neighboring molecules rotated towards each other and were oriented almost perpendicular to each other leading to edge to face π -stacking of neighboring molecules in T-shaped fashion. From the above single crystal analysis, it can be concluded that as the number of carbon atoms in the vertical alkyl chain increased from 1 to 4 to 11, the molecular locking changed from square planar to zigzag (angular) to 1D linear fashion. The lower counterparts exhibited only strong aryl-type CH- π interactions. However, in OPV-C11-C1 weaker CH/ π interactions between double bonds and aryl H-atoms were also observed.

To study the effect of horizontal substitution on molecular packing, single crystal structures of OPV-C11-C11 and OPV-C1-C11 were analyzed as shown in the figure 3.21. Both molecules crystallized in the triclinic lattice in the space group of P-1. Side views of these molecules revealed that all three benzene rings in the aromatic backbone lay in the same plane. The torsion angles from the central ring to either side were obtained as 1.39° for OPV-C11-C11 and 5.64° for OPV-C1-C11 respectively, which confirmed their co planarity. In case of OPV-C11-C11, the two undecyl chains present in the terminal aryl rings along the longitudinal position lay on the same plane of the three aromatic rings. The two other alkoxy units (undecyl or methoxy) present in the middle ring projected perpendicular on either side of the plane defined by the aromatic rings. To further understand the molecular packing, the unit cells were built in three dimensions along the crystallographic axes. The 3D arrangements of OPV-C1-C11 molecules were found as inseparable tightly packed bundles of π -conjugated sheets. On the other hand, OPV-C11-C11 showed layer-like packing in the x–y plane, which further protruded along the c axis by the long

undecyl chains in the middle aromatic ring. Each layer was separated by 16.04 Å, which was almost identical to the c-axis length in the unit cell.

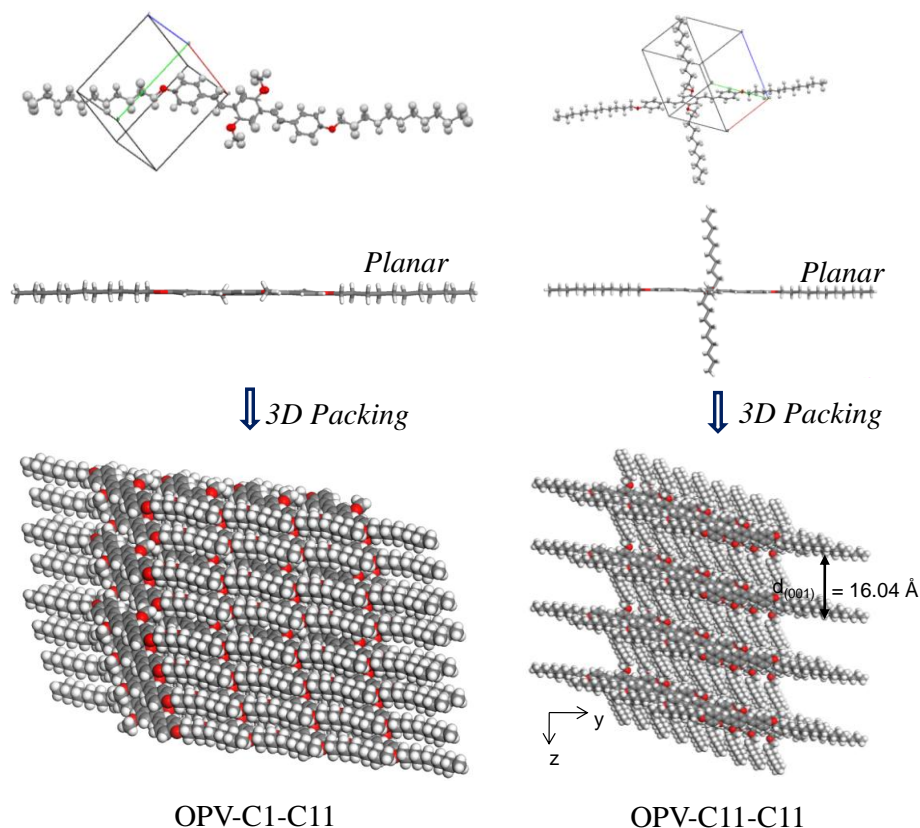


Figure 3.21. X-ray crystal structure of OPV-C1-C11 and OPV-C11-C11 and their 3D packing.

To get more insight into the layer-like formation of OPV-C11-C11 molecule, the close-contacts between the adjacent molecules were analyzed and the details are shown in figure 3.22. The central OPV molecule A showed two non-covalent interactions each with molecule B and C on either side (total of four interactions above and below the molecule A). The undecyl pendant groups in the middle benzene ring were not involved in any type of intermolecular interactions with the surroundings; as a result the molecules projected away along the c axis (see figure 3.22). The close packed structure indicated the existence of CH/ π interactions among the molecules (shown by dotted lines). Four CH/ π interactions per molecule were

found between the middle aromatic ring with hydrogen atoms H11A of the undecyl alkyl chains that lay along the molecular axis. To determine CH/ π parameters in the present case, vectors were drawn as shown in the inset of figure 3.22 and the values were calculated as: $d_{c-x}=3.79$ Å; $\theta =21.49$ °; $\Phi=150.25$ ° and $d_{Hp-x}=0.73$ Å. These values are within the range typically acceptable for CH/ π interactions (literature values are: $d_{c-x}<4$ Å; $\theta <25$ °; $\Phi >120$ ° and $d_{Hp-x}<1.20$ Å). [2, 4] This provided direct evidence for the existence of strong CH/ π interactions in the OPV-C11-C11 molecule.

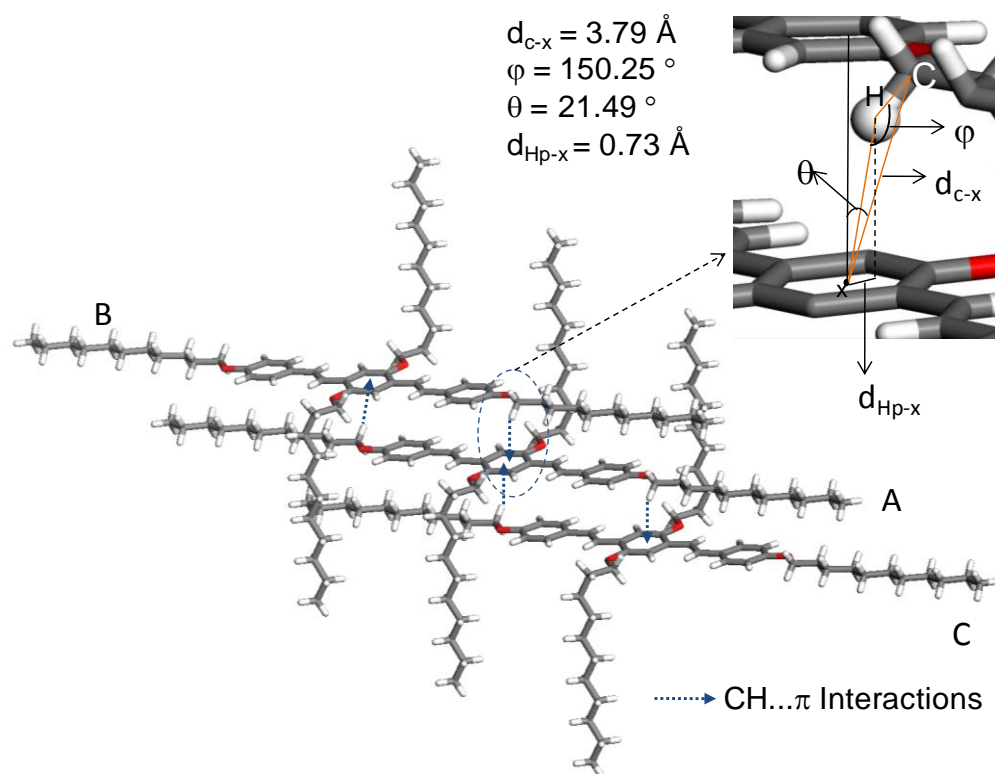


Figure 3.22. CH/ π type weak hydrogen bonding in OPV single crystal

The CH/ π interactions facilitated the alignment of the OPV chromophores in the x - y layer, which were further separated by the undecyl units that were protruded perpendicular in the c axis. A similar attempt to determine the secondary interactions in OPV-C1-C11 molecules indicated the absence of any CH/ π interactions. In OPV-C11-C11, two out of the three benzene rings overlapped with molecules on either side along the π planes in the molecular axis and the intermolecular distance was

obtained as 3.64 Å. The adjacent molecules in OPV-C1-C11 were not oriented along the plane and they were separated by 3.78 and 7.08 Å. These intermolecular distances were much larger than that of 3.41 Å that is observed for strong π - π interactions in graphite. Therefore, the existence of strong aromatic π - π interactions among the OPV molecules was not possible. It is very important to note that despite both OPV molecules being planar, the large intermolecular distance made them less favorable to self-organize by aromatic π - π interactions. The lack of the direct face-to-face π - π stacking between the aromatic planes confirmed the orientation of molecules along the *b* axis as in J-type aggregates. Hence, CH/ π interactions are the predominant secondary interactions.

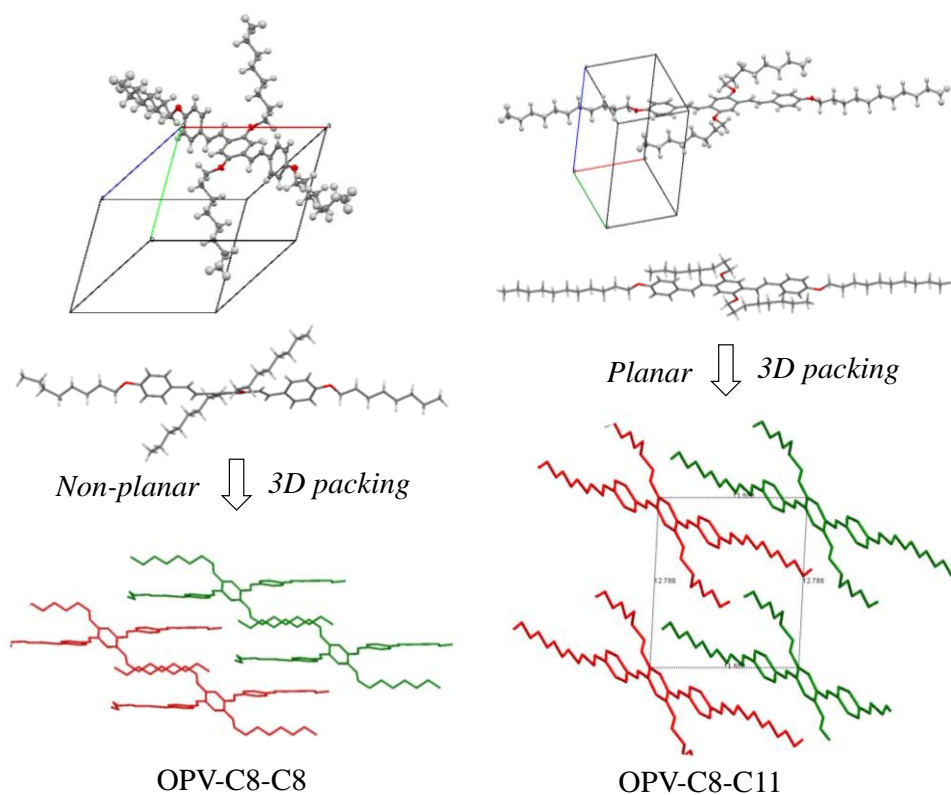


Figure 3.23. X-ray crystal structure of OPV-C8-C8 and OPV-C8-C11 and their 3D packing.

Figure 3.23 shows X-ray single crystal analysis for OPV-C8-C8 and OPV-C8-C11. The middle aromatic ring in OPV-C8-C8 moved out of plane of the

terminal rings giving rise to a non-planar OPV chromophore. The torsional angles of the central aromatic ring with the terminal aromatic rings were 45.71° and 45.71° , respectively. One of the terminal C8-alkyl tails had two carbons in gauche conformation. Octyl chains attached to the terminal rings lay along the molecular axis, but the octyl chains attached to the central aromatic rings protruded one above and one below the molecular plane. CH/ π interactions were observed between H₂₂ (donor) – Aryl (central), H₂ (Aryl) – C₁₂=C₁₅ (acceptor) and H_{35A} - C₄=C₇ (acceptor). The three dimensional packing of these molecules showed lamellar/(ladder like) packing in which the molecules were interdigitated and arranged in parallel fashion along the long molecular axis. On the other hand, in OPV-C8-C11, the three aromatic rings constituting the aromatic core lay in the same plane to give rise to a planar OPV. The 3D packing of the molecules depicted that molecules were loosely packed in layer like pattern. Based on the above single crystal analysis, the CH/ π parameters for all the OPVs have been summarized in table 3.4.

Table 3.5. CH/ π parameters for OPVs.

Sample	Donor	Acceptor	d_{c-x} (Å)	θ	ϕ	d_{Hp-x} (Å)	No.	ψ_A	ψ_B
OPV-C1-C1	H ₆ (Aryl)	Aryl (C)	3.746	16.48°	152.5°	0.82	2	34.02	62.59(-)
	H ₁₈ (Aryl)	Aryl (A)	3.592	12.60°	151.3°	0.40	2	-	-
OPV-C4-C1	H ₆ (Aryl)	Aryl (A)	3.633	4.65°	135.5°	0.75	4	37.68	37.68
	H ₆ (Aryl)	Aryl (A)	3.633	4.65°	135.5°	0.75	4	37.68	37.68
OPV-C11-C1	H ₂₆ (Aryl)	Aryl (A)	3.423	8.05°	137.3°	0.34	2	29.50	29.50
	H ₂₈ (Aryl)	C ₇ =C ₈	3.582	20.23°	135.6°	0.81	2	38.63	38.63
OPV-C8-C8	H ₂₂ (Aryl)	Aryl (B)	3.695	22.85°	140.5°	0.86	2	-	-
	H ₂ (Aryl)	C ₁₂ =C ₁₅	3.465	15.18°	138.9°	0.36	2	45.71	45.71
	H _{35A} (Alkyl)	C ₄ =C ₇	3.787	2.94°	158.8°	0.38	2	-	-

(a) d_{c-x} is the distance between the donor carbon atom to the center of the acceptor π ring (b) θ is the angle between the ring normal and a vector connecting the donor carbon atom to the centre of the ring (c) ϕ is the angle between C-H with the vector connecting H to the ring centre (d) d_{Hp-x} is the projection of the C-H on the π ring.

3.3.5. Roll and Pitch Displacements

It is understood from the detailed single crystal XRD analysis that conjugated oligomers can adopt a planar or non-planar conformation in solid state, depending on the alignment of the peripheral alkyl chains. The three dimensional packing in single crystals revealed that a direct on top or cofacial stacking of the molecules is energetically not favorable. Direct placement of molecules right one under another (cofacial stacking) places regions of like electron density on adjacent molecules in close proximity, leading to unfavorable electrostatic interactions. To minimize these electrostatic interactions molecules tend to slip from one under another and the π -stacks distort away from ideal on top stacking motif.

The slippage of molecules relative to one another can be studied in terms of pitch and roll inclinations as explained in the chapter 2. For planar molecules, the roll and the pitch parameters have been calculated by connecting two identical parts in the neighboring molecules. For non-planar OPVs, roll and pitch inclinations have been calculated with respect to the centroid of the central neighbouring aromatic rings that are parallel to each other. Figure 3.24 shows the calculation of roll and pitch parameters for one such non-planar molecule OPV-C1-C1. The middle phenyl rings of the two neighbouring molecules are parallel to each other.

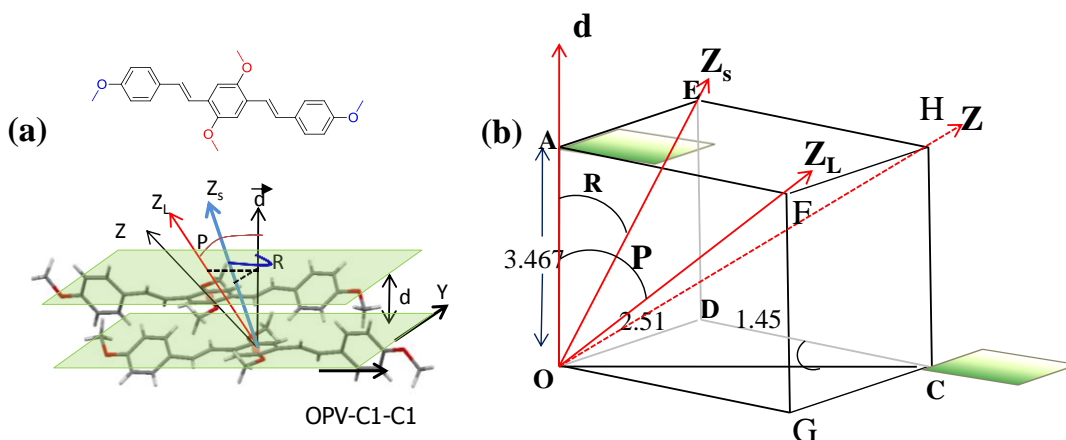


Figure 3.24. Calculation of roll and pitch parameters for OPV-C1-C1.

The distance between the two parallel planes passing through the central rings is termed and measured as d . The line connecting the two centroids constituted the z -axis. These parameters were fitted to standard cube model as shown in the figure 3.24b. and using previous mathematical expressions (explained in chapter 2), the mathematical values of P , R , d_p , d_R , d_{tot} and z were calculated. A similar method was adopted to calculate the roll and pitch parameters for all the non- planar OPVs. These pitch and roll parameters have been summarised in the table 3.5.

Table 3.6. Pitch and roll parameters for OPVs.

Sample	d_p	d_R	P	R	d_{tot}	z
OPV-C1-C1	1.45	2.51	22.69	35.90	2.90	4.52
OPV-C4-C1	1.36	5.89	18.74	55.77	6.04	7.25
OPV-C11-C1	1.44	2.83	22.49	39.13	3.17	4.70
OPV-C1-C11	9.51	6.96	83.74	81.48	11.78	5.64
OPV-C8-C8	5.74	3.32	52.80	37.27	6.62	7.93
OPV-C11-C11	9.64	1.40	68.74	20.45	9.57	10.44
OPV-C8-C11	7.77	3.46	65.75	44.67	8.51	9.20

The pitch and roll parameters were plotted as a function of longitudinal, vertical and radial growth as shown in the figure 3.25. Along the longitudinal direction, a drastic increase in roll and pitch parameters was observed from OPV-C1-C1 to OPV-C1-C11. The pitch and roll angles for OPV-C1-C1 are 22.69° and 35.9° , which is $< 45^\circ$ required for π - π stacking. The interplanar distance between the two neighbouring molecules was found to be 3.47 \AA and was very close to 3.41 \AA observed in graphite. However, as the alkyl chain length increased longitudinally to C11, large pitch and roll angles (83.74° and 81.48°) in OPV-C1-C11 resulted in large slip distance along both the long and the short molecular axis. As a consequence, the adjacent molecules in OPV-C1-C11, slid completely in x and y -directions, leaving no π - π overlap. For vertically substituted OPVs, the roll and pitch displacements remained almost constant irrespective of the alkyl chain length in the

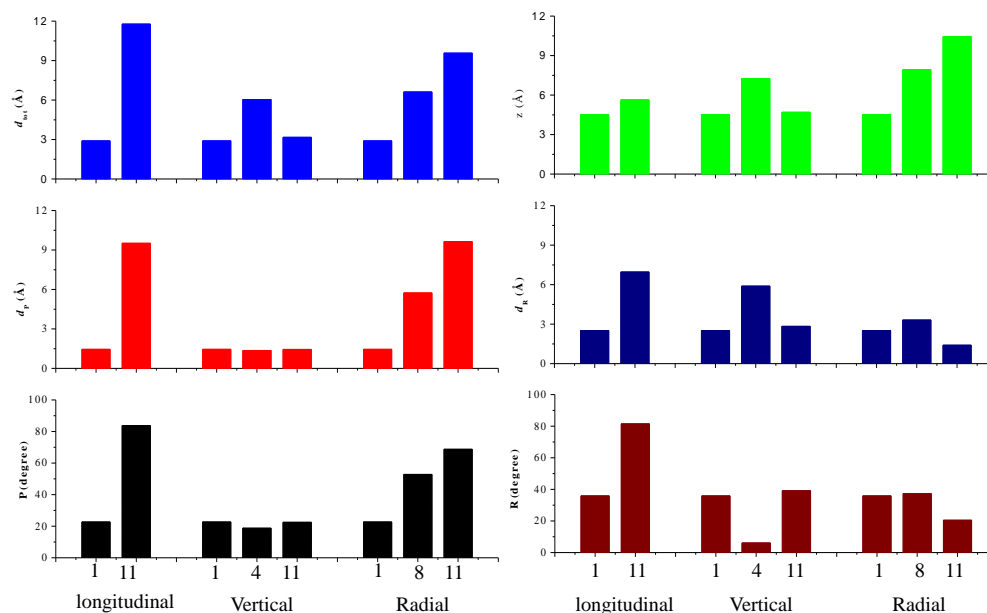


Figure 3.25. Plot of pitch and roll inclinations.

middle aromatic ring. OPV-C4-C1 showed dramatically low roll angle distortions as compared to its lower or higher analogues. The significantly low values of roll parameters in OPV-C4-C1 led to strong π - π stacking interactions. Among the radially substituted OPVs, the pitch angles increased gradually from 22.69° to 52.8° to 68.74° for OPV-C1-C1, OPV-C4-C4 and OPV-C11-C11, respectively. This indicated that as the molecular backbone tends towards planarity, molecular planes shift or distorted away from direct cofacial stacking. The roll angle distortions were less than 45° in all the three cases. The large values of d_{tot} and z , completely destroy π - π stacking interactions in OPV-C8-C8 and OPV-C11-C11.

A plot of angle subtended by two terminal rings on the central aromatic ring (ψ) for longitudinally, vertically and radially substituted OPVs has been shown in the figure 3.26. Among the vertical isomers, the two terminal aromatic rings of the OPV-C1-C1 moved out of the plane of the middle aromatic ring in opposite directions giving rise to a non-planar molecule. The torsional angle of the central aromatic ring

with the terminal aromatic rings were measured to be 34.02° (ψ_A) and 62.59° (ψ_B), respectively.

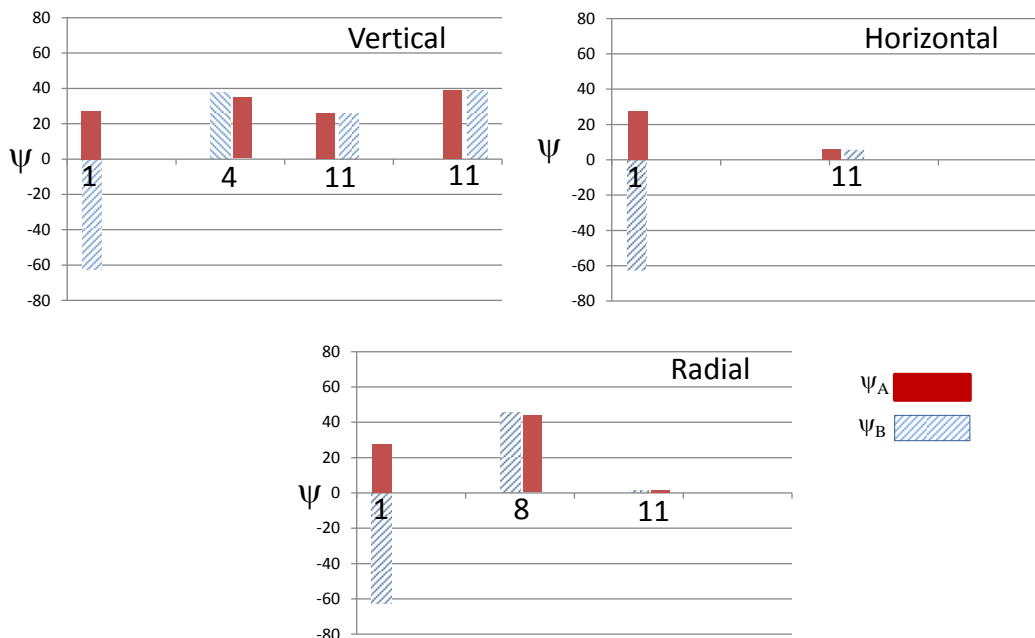


Figure 3.26. Plot of torsional angles (for ψ_A and ψ_B , refer to the figure 3.17).

In contrast to OPV-C1-C1, the two terminal aromatic rings of in OPV-C4-C1 moved out of the plane of the middle aromatic ring in the same direction giving rise to a symmetric non-planar molecule. The angles subtended by terminal aromatic rings on the central aromatic ring were equal and measured to be 37.68° . OPV-C11-C1 existed as molecular dimer with two molecules with different aromatic systems. The two terminal aromatic rings of the each molecule moves out of the plane of the middle aromatic ring equally and in the same direction giving rise to a non-planar molecule. The torsional angles were measured to be 29.50° for one such aromatic system (System1), but the terminal rings lie in the same plane. For the second molecule, the torsional angles between the terminal and the central rings was measured to be 38.63 (System2), but the two terminal rings were present in two different parallel planes separated by a distance of 1.85 \AA . As the chain length grew longitudinally, the torsional angles decreased to a large extent and the molecules

tended towards more planarity. Among the radially substituted isomers OPV-C8-C8 was found to have highest torsional twist leading to a completely twisted molecule.

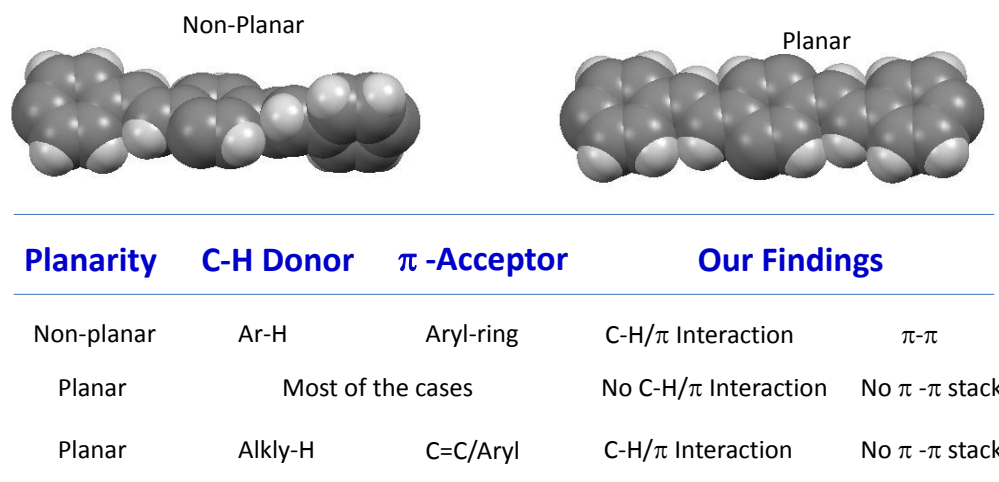


Figure 3.27. Relationships between planarity, CH/ π and π - π interactions in OPVs.

Based on the above single crystal XRD analysis, it can be concluded that planarity, alkyl chain length and the orientation in which the alkyl chains are substituted relative to the aromatic core played an important role in determining packing properties. In most of the cases, it was observed that planar molecules were devoid of strong CH/ π interactions. However, the presence of a bulky pendant group in the middle aromatic core, might give rise to some weak CH/ π H-bonding interactions in which alkyl hydrogen atoms from the pendant group served as weak H-bond donors. TCD substituted OPVs discussed in chapter 2 to belong to this category of molecules. Such systems were also found to lack π - π stacking interactions. On the other hand, non-planar molecules exhibited presence of strong CH/ π interactions. In all the cases, strong aryl-type CH/ π interactions were observed. However, in a few cases, weaker CH/ π interactions between double bonds and aryl H-atoms were also observed in addition to strong aryl-type CH/ π interactions. The roll and pitch calculations revealed that these molecules also showed the presence of π - π stacking interactions. Very few crystal structures are available for π -conjugated systems, which have identical aromatic backbone. This is for the first time such a

good correlation between solid state properties of a large number of OPVs based on single aromatic chromophore has been made.

3.3.6. Photophysical Analysis

The emission and excitation spectra of a few representative OPV structural isomers and higher homologues have been shown in the figure 3.28.

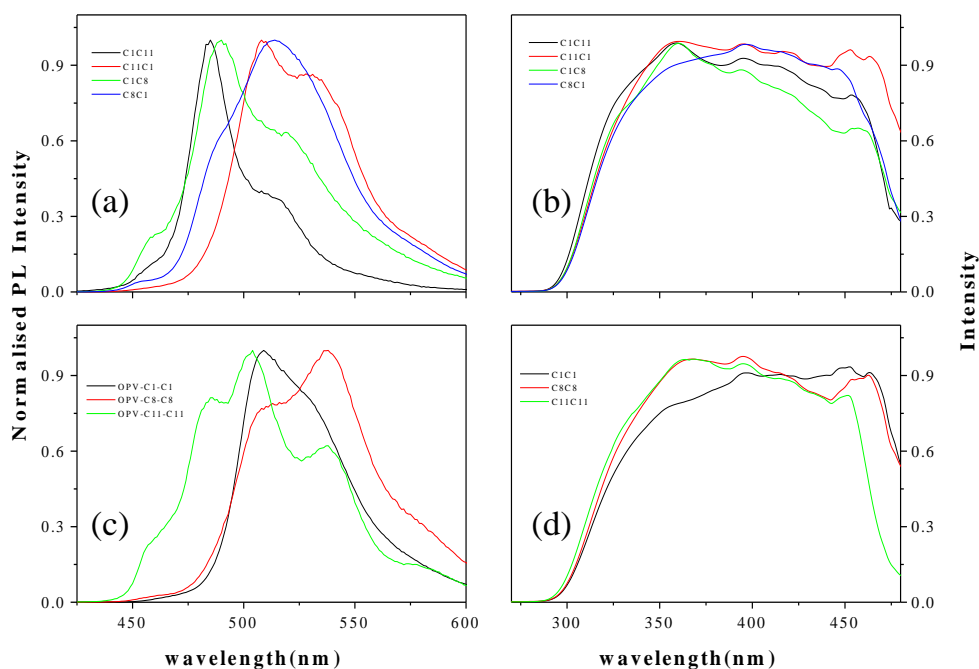


Figure 3.28. (a) Emission and (b) Excitation spectra of structural isomers. (c) Emission and (d) excitation of higher homologues in LC films.

To study the photophysical characteristics of the samples in the solid state, LC films of OPVs were cast on the glass substrates as described for PLM studies. The emission spectra of the OPV LC films were recorded by exciting at 380 nm. The emission spectra of higher homologues OPVs has been in the Figure 3.28a and emission spectra of higher homologues OPVs has been in the Figure 3.28c. OPV-C1-C1 exhibited emission maximum at 504 nm. Similarly, OPV-C8-C8 and OPV-C11-C11 exhibited emission maxima at 535 nm and 504 nm. The excitation spectra of the samples have been shown in figure 3.28b and 3.28d. The spectra were found to be very broad as similar to observed in earlier reports.^{40b-c} Following important points

can be concluded from the photophysical analysis: The photophysical properties of all the OPVs were found almost identical. The emission or the absorption properties were independent of the planarity or the non-planarity of the aromatic back bone. For example OPV-C1-C11 was planar and its structural isomer was non-planar, however, both exhibited similar emission characteristics. A similar trend was found among the pairs of structural isomers. The similarity in the photophysical properties could be attributed to weak π - π stacking interactions between the molecules which is the major non-covalent force responsible for change in absorption or emission characteristic in this class of molecules. Hence, in the present study without affecting the photophysical properties, diverse molecular self-assembly was achieved in the solid state.

3.3.7. Field Effect Transistor Measurements

As a proof of concept, preliminary studies were done and field effect transistors (FET) were fabricated by drop casting thin films of sample on prefabricated substrates. For measurements in LC state, the samples were frozen in LC state on prefabricated substrates. OFET was constructed for the OPV-C1-C11 and the device data for drop cast film and LC frozen state has been shown in the figure 3.28. The plots of drain current (I_D) vs drain voltage (V_D) for various applied gate voltage (V_G) have been shown in the figure 3.28a and 3.28b. The drain current is expressed as:⁴¹

$$I_D = \{WC_i/2L\} \times \{\mu (V_G - V_T)^2\}$$

Where, C_i is the capacitance per unit area of the dielectric layer, V_T is the threshold voltage, and μ is the field-effect mobility. From the plot of gate voltage versus square root of drain current, the field-effect mobility was calculated. The intersection point in the x-axis provides the threshold voltages of the devices. The charge carrier mobility calculated using both Linear and Saturated Regime method showed

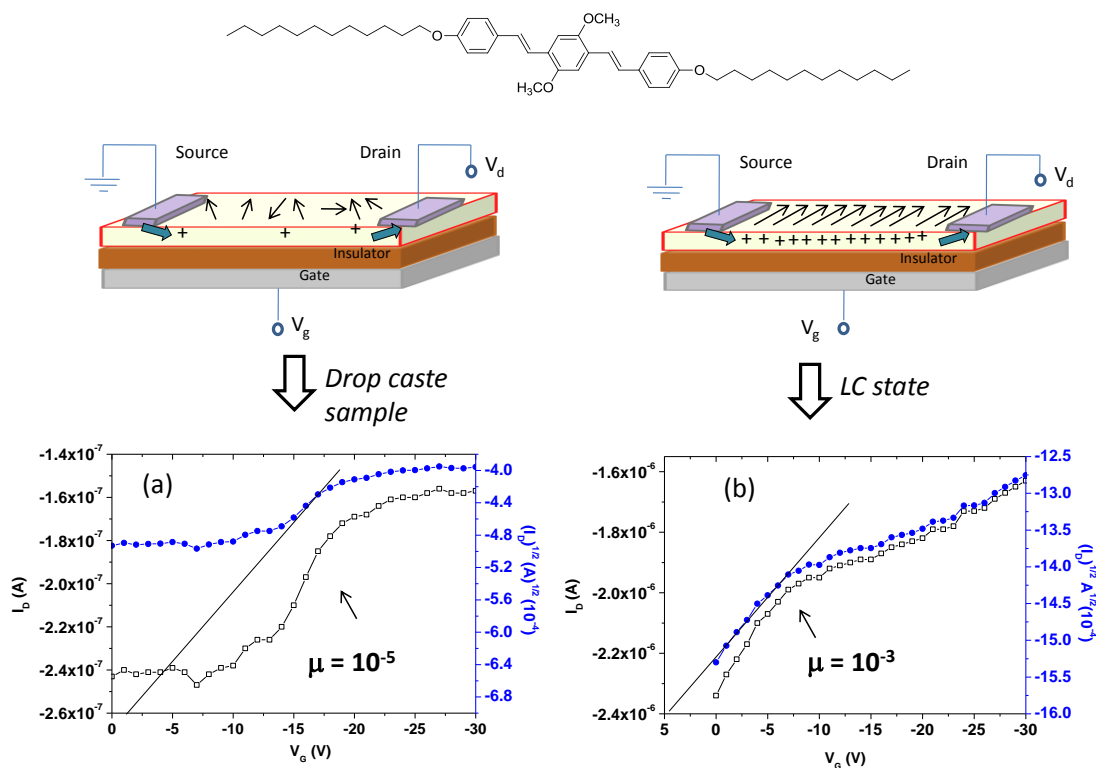


Figure 3.29. Field effect transistor measurements for OPV-C1-C11 in dropcast (a) and LC frozen film(b).

that the mobility in drop cast film of OPV-C1-C11 was of the order of 10^{-5} cm^2/Vs . As the sample was frozen in LC state as shown in the figure 3.28b, the charge carrier mobility increased to the order of 10^{-3} cm^2/Vs . Hundred folds increase in charge carrier mobility in LC frozen state was observed as compared to drop cast films in field effect transistors. The values of the mobilities were found low because the measurements were done in open air atmosphere. Nevertheless, these preliminary results showed that the potential of self-organization via LC mesophase approach can be very useful for molecular devices. And hence, the effect of alignment of chromophores was visible by hundred folds increase in the charge carrier mobility.

3.4. Conclusion

In this chapter, a detailed investigation on the role of planarity, peripheral substitution, alkyl chain lengths and its orientation on liquid crystallinity, intermolecular non covalent forces, pitch and roll displacements and solid state packing of oligophenylenevinyls (OPVs) has been done. A series of structural isomers with identical distyrylbenzene based aromatic core but opposite arrangement of alkyl side chains around the periphery was synthesized. Similarly, another series of higher homologues OPVs with equal substitutions in the longitudinal and vertical directions was also synthesized. Detailed DSC studies were done to understand the difference in packing properties with respect to horizontal, vertical and radial substitution of the alkyl chains. DSC analysis revealed among the structural isomers, horizontally substituted OPVs showed higher melting and crystallization temperatures as compared to vertically substituted counterparts suggesting better packing properties. PLM studied showed that increasing alkyl chain length in the horizontal direction induced LC properties as compared to the vertical isomers which remain crystalline in nature. Radially substituted OPVs with equal alkyl chain substitution in both x and y directions exhibited well ordered two-dimensional lamellar textures.

Single crystal XRD analysis was done to understand the role of planarity, alkyl chain length and its orientation on molecular ordering and intermolecular non-covalent interactions. Planar molecules were generally found to be devoid of strong CH/ π and π - π interactions. On the other hand, non-planar molecules exhibited presence of strong CH/ π interactions. Detailed roll and pitch calculations were done to show that in general non planar molecules were more prone to show π - π stacking interactions. Further, OFET devices were constructed to study the effect of liquid crystalline self-assembly on charge carrier mobility. OPVs exhibited hundred fold increases in charge carrier mobility in LC frozen state as compared to drop cast films. This preliminary result showed that the LC mesophase approach was indeed a good concept to explore OFET applications.

3.5. References

1. Kraft, A.; Grimsdale, A. C.; Holmes, A. B. *Angew. Chem. Int. Ed.* **1998**, *37*, 402.
2. Zgierski, M. Z.; Fujiwara, T.; Lim, E. C. *Acc. Chem. Res.* **2010**, *43*, 506.
3. Bowden, N. B.; Weck, M.; Choi, I. S.; Whitesides, G. M. *Acc. Chem. Res.* **2001**, *34*, 231.
4. Hoeben, F. J. M.; Jonkheijm, P.; Meijer, E. W.; Schenning, A. P. H. J. *Chem. Rev.* **2005**, *105*, 1491.
5. Muller, K.; Wegner, G. *Electronic Materials: The Oligomer Approach*: Wiley-VCH: Newyork, **1998**.
6. Osterbacka, R.; An, C. P.; Jiang, X. M.; Vardeny, Z. V. *Science* **2000**, *287*, 839-842.
7. Sun, Y.; Liu, Y.; Zhu, D. *J. Mater. Chem.* **2005**, *15*, 53–65.
8. Garnier, F. *Acc. Chem. Res.* **1999**, *32*, 209-215.
9. Naraso.; Nishida, J.; Kumaki, D.; Tokito, S.; Yamashita, Y. *J. Am. Chem. Soc.* **2006**, *128*, 9598-9599.
10. Ackermann, C. V.; Ackermann, J.; Brisset, H.; Kawamura, K.; Yoshimoto, N.; Raynal, P.; Kassmi, A. E.; Fages, F. *J. Am. Chem. Soc.* **2005**, *127*, 16346-16347.
11. Yasuda, T.; Saitoi, M.; Nakamurai, H.; Tsutsuij, T. *J. Appl. Phys.* **2006**, *45*, L313-L315.
12. Naraso.; Nishida, J.; Ando, S.; Yamaguchi, J.; Itaka, K.; Koinuma, H.; Tada, H. Tokito, S.; Yamashita, Y. *J. Am. Chem. Soc.* **2005**, *127*, 10142-10143.
13. Torrent, M. M.; Durkut, M.; Hadley, P.; Ribas, X.; Rovira, C. *J. Am. Chem. Soc.* **2004**, *126*, 984-985.
14. Zang L.; Che, Y.; Moore, J. S. *Acc. Chem. Res.* **2008**, *41*, 1596-1608.
15. Sirringhaus, H.; Brown, P. J.; Friend, R. H.; Nielsen, M. M.; Bechgaard, K.; Langeveld-Voss, B. M. W.; Spiering, A. J. H.; Janssen, R. A. J.; Meijer, E. W.; Herwig, P.; de Leeuw, D. M. *Nature* **1999**, *401*, 685-688.

16. (a) Wang, C.; Dong, H.; Hu, W.; Liu, Y.; Zhu, D.; *Chem. Rev.* **2012**, *112*, 2208–2267. (b) Halik, M.; Klauk, H.; Zschischang, U.; Schmid, G.; Ponomarenko, S.; Kirchmeyer, S.; Weber, W. *Adv. Mater.* **2003**, *15*, 917.
17. Wurthner, F.; Schmidt, R. *ChemPhysChem* **2006**, *7*, 793.
18. Wang, C.; Dong, H.; Li, H.; Zhao, H.; Meng, Q.; Hu, W. *Crystal Growth & Design* **2010**, *10*, 4155.
19. Dong, H.; Wang, C.; Hu, W. *Chem. Commun.* **2010**, *46*, 5211.
20. Payne, M. M.; Parkin, S. R.; Anthony, J. E.; Kuo, C.C.; Jackson, T. N. *J. Am. Chem. Soc.* **2005**, *127*, 4986-4987.
21. Jurchescu, O. D.; Baas, J.; Palstra, T. T. M. *Appl. Phys. Lett.* **2004**, *84*, 3061.
22. Ito, K.; Suzuki, T.; Sakamoto, Y.; Kubota, D.; Inoue, Y.; Sato, F.; Tokito, S. *Angew. Chem. Int. Ed.* **2003**, *42*, 1159.
23. Curtis, M. D.; Cao, J.; Kampf, J. W. *J. Am. Chem. Soc.* **2004**, *126*, 4318-4328.
24. Lin, Y. Y.; Gundlach, D. J.; Nelson, S. F.; Jackson, T. N. *IEEE Trans. Electron* **1997**, *44*, 1325-1331.
25. Meijer, E. J.; de Leeuw, D. M.; Setayesh, S.; Veenendaal, E. V.; Huisman, B. H.; Blom, P. W. M.; Hummelen, J. C.; Scherf, U.; Klapwijk, T. M. *Nature Mater.* **2003**, *2*, 678- 682.
26. Stalmach, U.; Schollmeyer, D.; Meier, H. *Chem.Mater.* **1999**, *11*, 2103-2106.
27. Velde, C. M. L. V. V.; Baeke, J. K.; Geise, H. J.; Blockhuys, F. *Acta. Cryst.* **2005**, *C6*, o284-o287.
28. Velde, C. M. L. V. V.; Chen, L. J.; Baeke, J. K.; Moens, M.; Dieltiens, P.; Geise, H. J.; Zeller, M; Hunter, A. D.; Blockhuys, F. *Crystal growth and design.* **2004**, *4*, 823-830.
29. Xie, Z.; Yang, B.; Xie, W.; Liu, L.; Shen, F.; Wang, H.; Yang, X.; Wang, Z.; Li, Y.; Hanif, M.; Yang, G.; Ye, L.; Ma, Y. *J. Phy. Chem. B* **2006**, *110*, 20993-21000.
30. Holmes, D.; Kumaraswamy, S.; Matzger, A. J.; Vollhardt, K. P. C. *Chem. Eur. J.* **1999**, *5*, 3399-3412.
31. Tschierske, C. *J. Mater. Chem.* **2001**, *11*, 2647–2671.

32. Sokolov, A. N.; Friscic, T.; MacGillivray, L. R. *J. Am. Chem. Soc.* **2006**, *128*, 2806-2807.
33. Shetty, A.S.; Liu, E. B.; Lachicotte, R. J.; Jenekhe, S. A. *Chem. Mater.* **1999**, *11*, 2292-2295.
34. Hutten, P. F. V.; Wildeman, J.; Meetsma, A.; Hadziioannou, G. *J. Am. Chem. Soc.* **1999**, *121*, 5910-5918.
35. Tour, J. M. *Chem. Rev.* **1996**, *96*, 537-553.
36. Gierschner, J.; Ehni, M.; Egelhaaf, H. J.; Medina, B. M.; Beljonne, D.; Benmansour, H.; Bazan, G. C. *J. Chem. Phys.* **2005**, *123*, 144914.
37. Feng, X.; Marcon, V.; Pisula, W.; Hansen, M. R.; Kirkpatrick, J.; Grozema, F.; Andrienko, D.; Kremer, K.; Mullen, K. *Nature Mater.* **2009**, *8*, 421-426.
38. Demus, D.; Richter, L. *Textures of Liquid Crystals*, Verlag Chemie, Weinheim. New York, **1978**. Edition. 1.
39. Kishikawa, K. *TCI Mail*, Contribution, **2009**.
40. (a) Jennings, W. B.; Farrell, B. M.; Malone, J. F. *Acc. Chem. Res.* **2001**, *34*, 885-894. (b) Amrutha, S. R.; Jayakannan, M. *J. Phys. Chem. B* **2009**, *113*, 5083-5091. (c) Amrutha, S. R.; Jayakannan, M. *Macromolecules*, **2007**, *40*, 2380-2391.
41. Wu, W.; Liu, Y.; Zhu, D. *Chem. Soc. Rev.* **2010**, *39*, 1489-1502.

Chapter 4

Fluorocarbon Versus Hydrocarbon tails on the Self-assembly of OPVs

Chapter 4

Fluorocarbon Versus Hydrocarbon tails on the Self-assembly of OPVs

The role of fluorocarbon tails on the diverse molecular self-assembly of π -conjugated oligophenylenevinylenes(OPVs) has been studied. OPVs were designed with appropriate pendants in the aromatic core with hydrocarbon or fluorocarbon tails along the long molecular axis. Thermal analysis revealed that hydrocarbon tail OPVs showed higher enthalpies of transitions as compared to their fluorocarbon counterparts suggesting better packing properties. Polarised light microscope (PLM) analysis showed that fluorocarbon tail OPVs produced identical SmC LC mesophases irrespective of the pendent groups attached in the middle aromatic core. In contrast, for hydrocarbon tailed OPVs, both pendent geometry and their length in the middle aromatic core determined the molecular self-organization. Variable temperature wide angle XRD patterns of fluorocarbon tail OPVs exhibited regular periodicity corresponding to equidistant planes formed in smectic LCs. Small angle variable temperature X-ray diffraction analysis confirmed transition from SmA to a more ordered SmC mesophase. Solid state photophysical analysis confirmed the formation of H and J aggregates in FC and HC-OPVs, respectively. Time resolved fluorescence decay measurements confirmed longer life time for H-type smectic OPVs compared to that of loosely packed one-dimensional nematic hydrocarbon tailed OPVs. In a nut shell, diverse molecular self-assembly of aromatic π -conjugated units via weak secondary forces was established.

4.1. Introduction

π -Conjugated liquid crystals (LCs) are emerging new soft materials for optoelectronic applications.¹⁻⁶ These materials combine the self organizing abilities of LCs and the semiconducting properties of π -conjugated materials.⁷⁻¹⁴ They are typically self-organised by weak non-covalent interactions such as hydrogen bonding¹⁵⁻¹⁹, metal-ion interactions²⁰⁻²⁶, aromatic π -stacking²⁷⁻²⁸ and van der Waals forces²⁹⁻³¹ etc. Fluoro-substituted liquid crystals constitute an important and exciting class of LCs, where fluoro substituents are introduced in liquid crystal structures.³² The incorporation of fluoro groups is one of the several useful tools that have been utilized to modify physical properties of LCs such as melting points, mesophase morphology, transition temperatures, dielectric anisotropy and optical anisotropy. Fluorine is the most electronegative of all the elements (3.98) which confer a high dipole moment on the C–F bond. The fluoro substituent has a low polarizability that leads to low intermolecular dispersion interactions. The van der Waals radius of fluorine atom is 1.47 Å (smallest after hydrogen); therefore, a fluoro substituent can be easily incorporated in hydrocarbons to give fluorocarbons.

Perfluoro chains are stiff and more rigid than hydrocarbon tails. There are many different positions in a liquid crystal structure where a fluoro substituent can be located, such as (i) a terminal position, (ii) within a terminal chain, as part of a semi-fluorinated or as a perfluorinated chain, (iii) as part of a linking group, (iv) or in a lateral position in the core section. A key feature of almost all the liquid crystalline materials is amphiphilicity in the molecule.³³⁻³⁴ A molecule having two chemically different molecular parts that are incompatible with each other is said to be amphiphilic. Typically, liquid crystals consist of a rigid aromatic core and flexible aliphatic side chains in which the nanosegregation between the rigid and flexible parts leads to the formation of different LC mesophases.³⁵⁻³⁸ Introduction of incompatible segments such as perfluorinated side chains or oligomeric siloxane end groups further promotes the formation of LC mesophases. Fluorine atoms are incorporated in the molecule through perfluorinated alkyl side and the fluorophobic effects³⁹⁻⁴² act as additional non-covalent interactions that drive the self assembly.



Figure 4.1. Liquid-crystalline honeycomb structures composed of cylinders having hexagonal, pentagonal, and square cross section. (Adopted from Xiaohong et al. *J. Am. Chem. Soc.* **2011**, 133, 7872–7881).

Xiaohong et al.⁴³ utilized the lateral fluorocarbon side tails to synthesize T-shaped bolaamphiphiles composed of a biphenyl rigid core, a semiperfluorinated lateral chain, two polar 1, 2-diol groups in the terminal positions and flexible alkyl spacers connecting the polar groups with the biphenyl core. The influence of spacer length and position of the spacer on the self-assembly in liquid-crystalline phases was studied as shown in figure 4.1. These LC phases represented polygonal cylinder phases where the aromatic cores together with the aliphatic spacers make up the walls of polygonal honeycombs fused at the edges by the hydrogen-bonding diol groups and enclosing cells filled by the semi perfluorinated lateral chains. A series of four different columnar phases ($Col_{hex}/p6mm$, $Col_{rec}/p2gg$, $Col_{squ}/p4gm$ and $Col_{squ}/p4mm$), representing liquid crystalline honeycomb structures composed of cylinders having hexagonal, pentagonal, and square cross section, were found on increasing the spacer length.

Perfluorinated tails have also been used to control of self-assembly of columnar mesogenic systems, stabilize mesophases, improve alignment behavior and increase phase separation. Figure 4.2 exhibits an example of a disc like molecule **1** (C₃-symmetrical 3,3'-bis(acylamino)-2,2'-bipyridine) possessing three peripheral fluorinated alkyl chains.⁴⁴

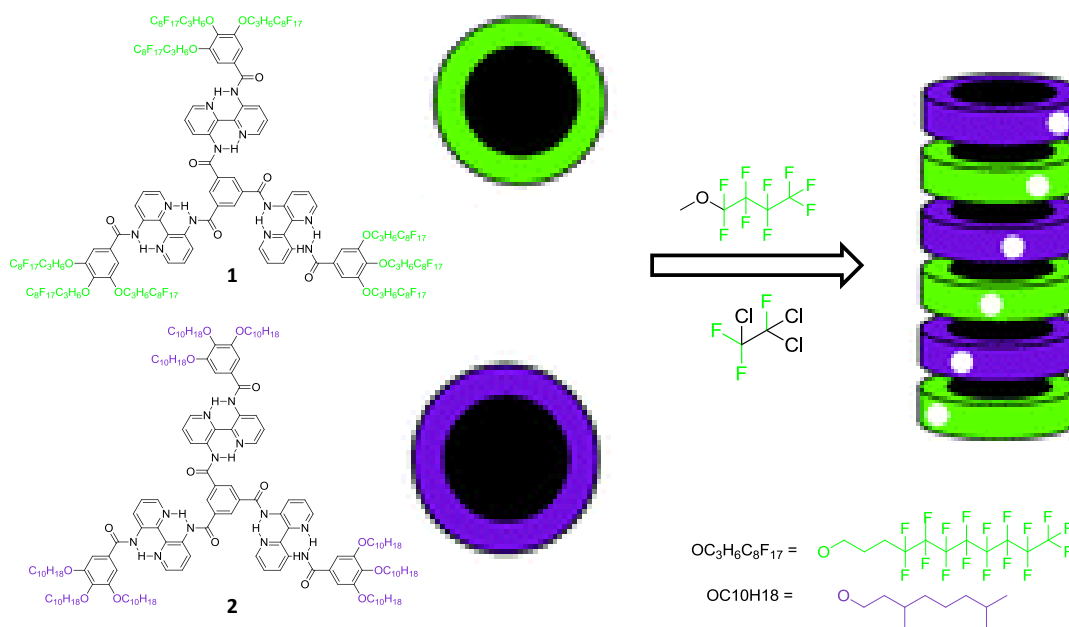


Figure 4.2. Mixed helical self-assemblies of fluorinated and hydrocarbon discotics (Adopted from Vanhoutem et al. *Org. Biomol. Chem.* **2012**, *10*, 5898 -5908).

It was found that fluorinated disc (**1**), when mixed with another hydrocarbon disc (**2**) allowed the formation of mixed helical discotic self-assemblies in fluorinated solvents (see figure 4.2). The helical assemblies of the mixed aggregates were found to be more stable compared to hydrocarbon discs alone.

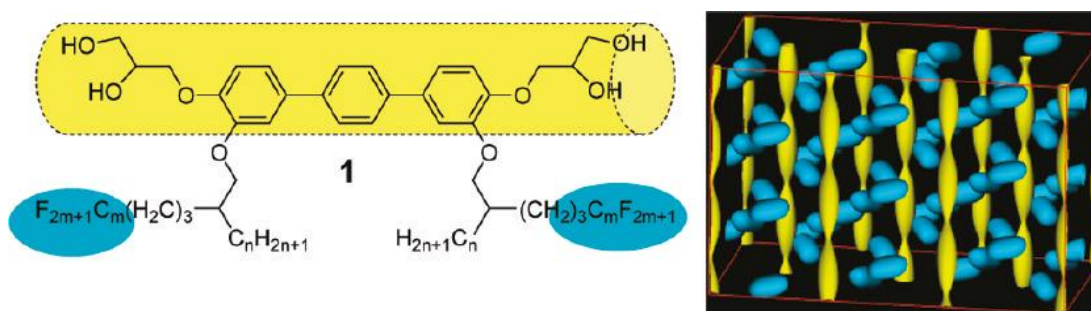


Figure 4.3. Polyphilic molecules composed of *p*-terphenyl core with semiperfluorinated sidechains exhibiting hexagonal columnar mesophases (Adopted from Prehm et al. *J. Am. Chem. Soc.* **2011**, *133*, 7872-7881).

Recently, Prehm et al.⁴⁵ reported the formation of hexagonal columnar phases composed of amphiphilic molecule based on *p*-terphenyl core as shown in figure 4.3. Two series of polyphilic molecules composed of a rigid and linear *p*-terphenyl core, terminated at both ends with polar glycerol groups and two branched fluorinated and a nonfluorinated chains were synthesized. Hexagonal columnar phases were formed by all molecules at high temperatures.

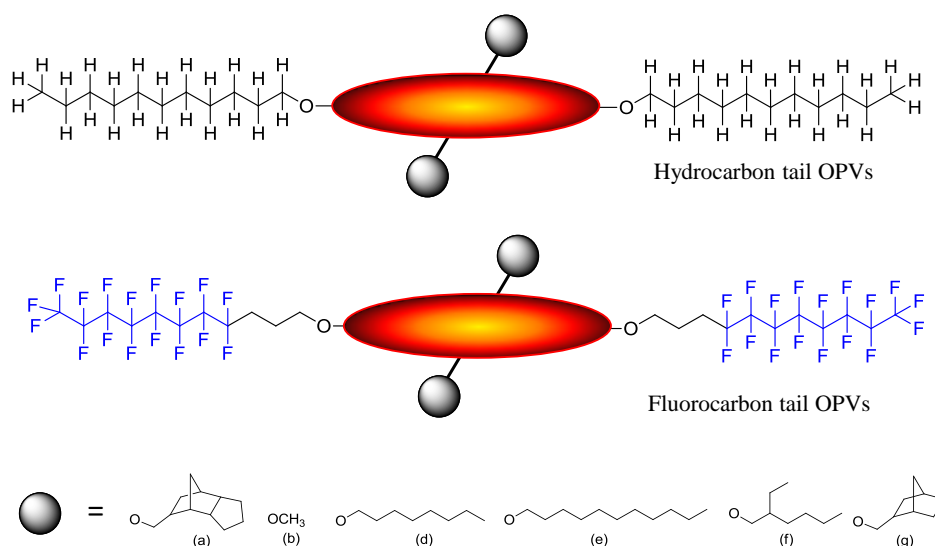


Figure 4.4. Schematic models for fluorocarbon and hydrocarbon tailed OPVs.

In this chapter, the role of fluorocarbon tails on the diverse molecular self-assembly of π -conjugated OPVs has been studied. OPVs were designed with appropriate pendants in the aromatic core with hydrocarbon or fluorocarbon tails along the long molecular axis as shown in the figure 4.4. Detailed DSC and PLM analysis was done to understand the thermal and liquid crystalline properties of OPVs. Hydrocarbon tail OPVs showed higher enthalpies (ΔH) of transitions as compared to their fluorocarbon counterparts suggesting better packing properties. PLM analysis revealed that fluorocarbon tail OPVs produced identical SmC liquid crystalline mesophases irrespective of the pendant groups attached in the middle aromatic core. In contrast, for hydrocarbon tailed OPVs, both pendant geometry and

their length in the middle aromatic core determined the molecular self-organization rather than the flexible tail in the longitudinal position (see figure 4.5).

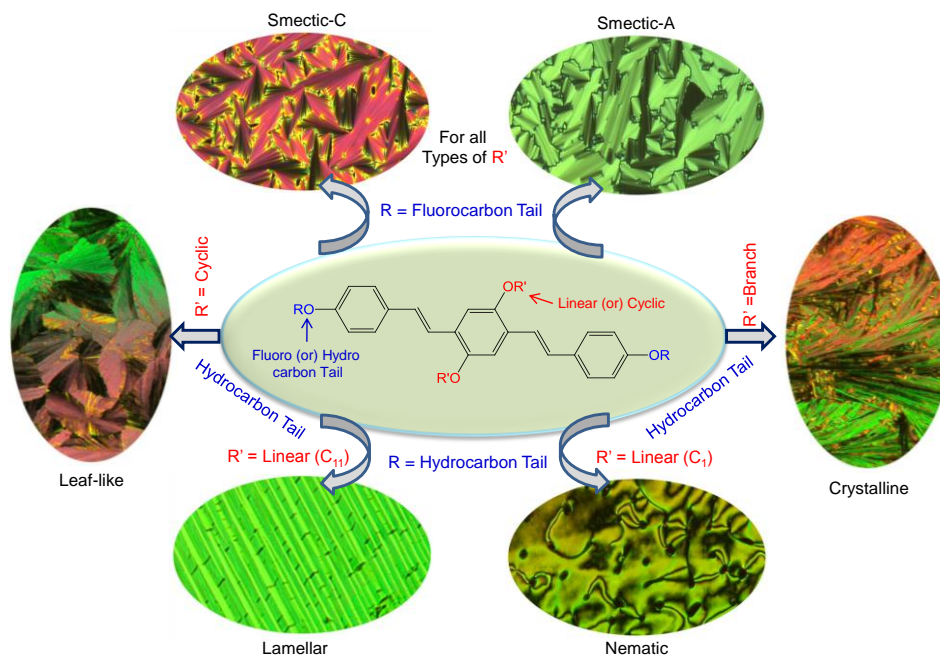


Figure 4.5. Weak-force-driven diverse self assembly in π -conjugates.

Wide angle and small angle XRD analysis was done to understand the diverse self assembly shown by the OPVs. Variable temperature wide angle XRD patterns of fluorocarbon tail OPVs exhibited regular periodicity in diffraction peaks corresponding to equidistant planes formed in smectic LCs. Small angle variable temperature X-ray diffraction analysis showed that the molecules underwent a transition from SmA to a more ordered SmC mesophase. Photophysical analysis was done to understand the difference in mesogen packing in solution and solid state. Solid state photophysical analysis confirmed the formation of H and J aggregates in FC and HC-OPVs, respectively. Time resolved fluorescence decay measurements confirmed longer life time for H-type smectic OPVs compared to that of loosely packed one-dimensional nematic hydrocarbon tailed OPVs. In a nut shell, diverse molecular self-assembly of aromatic π -conjugated units via weak secondary forces was established.

4.2. Experimental Methods

4.2.1. Materials: 2-Norbornanemethanol, p-toluenesulphonylchloride, triethylamine, hydroquinone, 1-bromooctane, 1-bromoundecane, 2-ethylhexyl bromide, triethylphosphite, potassium-t-butoxide (1M in THF), 4-(4,4,5,5,6,6, 7,7,8,8,9,9,10, 10,11,11,11-heptafluoroundecyloxy)benzaldehyde and 4-hydroxybenzaldehyde were purchased from Aldrich Chemicals. HBr in glacial acetic acid, para formaldehyde, KI, K₂CO₃, Dimethylsulphate and NaOH were purchased locally. Solvents were also purchased locally and were purified by standard procedures.

4.2.2. General Procedures: ¹H and ¹³C NMR were recorded using 400 MHz JEOL NMR spectrometer. All NMR spectra were recorded in CDCl₃ containing TMS as internal standard. Infrared spectra were recorded using Bruker FT-IR (ATR mode) spectrophotometer in the range of 4000-600 cm⁻¹. The mass of all the OPVs was determined by using the Applied Biosystems 4800 PLUS MALDI TOF/TOF analyzer. The purity of OPVs was checked by gel permeation chromatography (GPC) performed using Viscotek triple detector setup in tetrahydrofuran. TGA analysis was done using Perkin Elmer STA 6000 simultaneous thermal analyzer.

Differential scanning calorimetry (DSC): Differential scanning calorimetry (DSC) measurements were performed on TA Q20 DSC. A pinch of powdered sample was placed in DSC aluminum pan and crimped. The data were recorded at a heating and cooling rate of 10 °C/min. The first heating cycle data were discarded since they possessed prehistory of the sample.

Polarized Light Microscope (PLM) Analysis: To study the temperature dependent LC textures of all the OPVs, LIECA DM2500 P polarized light microscope equipped with Linkam TMS 94 heating-freezing stage was used. A pinch of sample was placed on the glass substrate, heated to melt at 10 °C/min, and kept isothermally at 20 °C above their melting temperature for 2-3 minutes. The melt was subsequently cooled at 10 °C/min which leads to nucleation and further growth patterns and these images were continuously captured using camera.

Wide Angle Variable Temperature XRD Analysis: Wide angle X-ray diffraction patterns were recorded using Bruker D8 Advance diffractometer with a copper target. The system consisted of a rotating anode generator with a copper target and a wide angle powder goniometer fitted with a high temperature attachment. Spectra were recorded using Cu K α radiation in the range of $2\theta = 3-50^\circ$ at a heating and cooling rate of 10°C/min.

Small Angle Variable Temperature XRD Analysis: SAXS measurements were made using a Bruker Nanostar (Cu K α radiation). The Nanostar was equipped with 18 kW rotating anode generator and a 2D multiwire detector, with a sample-detector distance of roughly 1 m. The entire X-ray flight path, including the sample chamber was evacuated to minimize air scattering. Samples were placed in capillary and were mounted on the Bruker heating stage. 2-dimensional SAXS data was azimuthally averaged, and 1-D data was presented after background subtraction.

Photophysical Analysis: Absorption spectra were recorded using a Perkin Elmer Lambda 45 UV spectrophotometer. Steady state fluorescence emission and excitation spectra were recorded using a Fluorolog HORIBA JOBIN VYON fluorescence spectrophotometer. For these photophysical studies, LC frozen samples were prepared by heating the samples to melt and then cooling to form thin films between two glass cover slips. Fluorescence intensity decays were collected by time correlated single photon counting technique (TCSPC) setup from Horiba Jobin Yvon. 375 nm diode Laser (IBH, UK, NanoLED-375L, with a $\lambda_{\text{max}} = 375$ nm) having a FWHM of 102.3 ps as a sample excitation source. The fluorescence signals were collected in magic angle using a MCP-PMT (Hamamatsu, Japan) detector and the fluorescence decays were collected at emission maxima for all the samples. The quality of fit was judged by fitting parameters such as $\gamma^2 \approx 1$, as well as the visual inspection of the residuals.

4.2.3. Synthesis

The synthesis for compounds **1a**, **2a**, **3a** and **4k** have been reported in chapter-2. The synthetic procedures for compounds **1b**, **1d**, **1e**, **2b**, **2d**, **2e**, **3b**, **3d** and **3e** have been reported in chapter-3.

Synthesis of 1, 4-bis(2-ethyl-hexyloxy)benzene (1f): 2-Ethylhexylbromide (57.9 mL, 0.30 mol) was reacted with hydroquinone (11.0 g, 0.10 mol) and KOH (22.4 g, 0.40 mol) in DMSO as described for **1c**. Yield = (11%). ¹H-NMR (CDCl₃, 400MHz) δ : 6.8 ppm (s, 4H, **Ar-H**), 3.7 ppm (m, 4H, **OCH₂**), 1.7 ppm (m, 2H, **OCH₂CH**) and 1.5 - 0.8 ppm (m, 28H, **aliphatic-H**) ppm. ¹³C-NMR (CDCl₃, 100MHz) δ : 153.3, 115.3(Ar-C), 71.09 (**OCH₂**), 40.9, 39.4, 39.1, 31.8, 30.5, 29.1, 28.8, 26.9, 25.1, 23.8, 23.0, 22.8, 14.1, 14.0, 11.1 and 10.9 ppm. FT-IR (KBr, cm⁻¹): 2957, 2924, 2864, 1506, 1465, 1382, 1285, 1221, 1109, 1037, 928, 822, and 779. MALDI-TOF-TOF-MS (MW = 334.54): $m/z = 357.25$ (M⁺ + 23).

Synthesis of (1S, 4R)-bicyclo[2.2.1]heptane-2-ylmethyl benzene sulphonate (NB-OTs) : 2-Norbornanemethanol (15.1 g, 0.12 mol) and *p*-toluene sulfonyl chloride (22.9 g, 0.12 mol) were taken in 80 mL of dichloromethane. Triethylamine (24.2 g, 0.24 mol) was added drop wise under ice cold conditions. This reaction mixture was then stirred at room temperature, poured in 100 mL of water and extracted in dichloromethane. The organic layer was then dried over anhydrous sodium sulphate and condensed to get product. It was further purified by passing through silica gel column using ethyl acetate (1 % v/v) in hexane as eluent. Yield = (59%). ¹H-NMR (CDCl₃, 400MHz) δ: 7.7 ppm (d, 2H, **Ar-H**), 7.3 ppm (d, 2H, **Ar-H**), 3.5-4.2 ppm (m, 2H, **-OCH₂**), 2.5 ppm -0.5 ppm (m, 14H, **cyclic-H and CH₃**). ¹³C-NMR (CDCl₃, 100MHz) δ: 144.7, 133.3, 129.8, 127.9 (**Ar-C**), 73.5, 72.5 (**-OCH₂**), 41.0, 39.6, 38.1, 36.6, 35.1, 33.3, 29.8, 29.5, 22.4 and 21.7 ppm. FT-IR (KBr, cm⁻¹): 2952, 2924, 2872, 1598, 1455, 1356, 1302, 1174, 1098, 1020, 943, 813, and 662. MALDI-TOF-TOF-MS (MW = 280.38): *m/z* = 319.07 (M⁺ + 39).

Synthesis of (1S, 4R)-bicyclo[2.2.1]heptane-2-ylmethoxy-4-(bicyclo[2.2.1]heptane-2-ylmethoxy)benzene (1g): Hydroquinone (3.3 g, 0.03 mol), NaOH (2.6 g, 0.07 mol) and NB-OTs (17.6 g, 0.06 mol) were dissolved in ethanol (45 mL) and water (5 mL). The mixture was refluxed for 36 h at 80 °C. It was extracted in DCM. The organic layer was dried over anhydrous sodium sulphate and the product was further purified by passing through silica gel column using ethyl acetate (1 % v/v) in hexane as eluent. Yield = (17 %). m. p. = 95-97 °C. ¹H-NMR (CDCl₃, 400MHz) δ: 6.8 ppm (m, 4H, **Ar-H**), 3.9-3.4 ppm (m, 4H, **-OCH₂**), 2.5 ppm -0.5 ppm (m, 22H, **cyclic-H**). ¹³C-NMR (CDCl₃, 100MHz) δ: 153.4, 144.7, 133.3, 129.9, 127.9, 115.8 (**Ar-C**), 72.5, 70.9(**-OCH₂**), 41.7, 41.1, 39.8, 39.4, 38.4, 36.8, 36.3, 35.3, 34.3, 33.9, 33.3, 29.8, 28.9, 22.8, 22.4 and 21.8 ppm. FT-IR (KBr, cm⁻¹): 2945, 2908, 2866, 1501, 1457, 1388, 1285, 1214, 1111, 1026, 954, 816, 775 and 668. MALDI-TOF-TOF-MS (MW = 326.47): *m/z* = 349.12 (M⁺ + 23)

Synthesis of 1, 4-bis(bromomethyl)-2,5-bis(2-ethylhexyloxy)benzene (2f): 1f (0.8 g, 0.03 mol) and paraformaldehyde (0.8 g, 26.50 mmol) were reacted with HBr in acetic acid (5.4 mL, 0.02 mol) following the procedure as **described for 2a**. The product was further purified by recrystallising from hot saturated solution of acetone. Yield = (34%). ¹H-NMR (CDCl₃, 400MHz) δ: 6.8 ppm (s, 2H, **Ar-H**), 4.5 ppm (s, 4H, **CH₂Br**), 3.6-3.4 ppm (dd, 4H, **OCH₂**), 1.75 ppm (m, 2H, **OCH₂CH**), 1.5 - 0.88 ppm (m, 22H, **aliphatic**), and 0.87 ppm (t, 6H, **CH₃**). ¹³C-NMR (CDCl₃, 100MHz) δ: 150.7, 127.3, 114.1 (**Ar-C**), 70.8(**Ar-O-CH₂**), 40.9, 39.5, 39.1, 31.8, 30.6, 29.1, 28.8, 25.1, 24.0, 23.05, 22.8, 14.1, 14.06, 11.2 and 10.8 ppm. FT-IR (KBr, cm⁻¹):

2956, 2923, 2866, 1505, 1459, 1405, 1313, 1264, 1220, 1115, 1033, 1 904, 871, 770, 731 and 686. MALDI-TOF-TOF-MS (MW = 520.38): m/z = 559.10 (M^+ + 39).

Synthesis of 2-((4-((1S,4R)-bicyclo[2.2.1]heptane-2-ylmethoxy)-4-(bicyclo[2.2.1]heptane-2,5-bis(bromomethyl)phenoxy)methylbicyclo[2.2.1] heptanes(2g): **1g** (1.1 g, 3.30 mmol) and paraformaldehyde (0.4 g, 13.2 mmol) were reacted with HBr in acetic acid (4.9 mL, 9.90 mmol) following the procedure as **described for 2a**. The product was recrystallised from a saturated solution of acetone. Yield = (17%). m. p. = 159-161 °C. $^1\text{H-NMR}$ (CDCl_3 , 400MHz) δ : 6.85- 6.82 ppm (m, 2H, **Ar-H**), 4.5 ppm (m, 4H, **CH₂Br**), 4.0 -2.3 ppm (m, 4H, **OCH₂**), 2.5 ppm -0.5 ppm (m, 22H, **cyclic-H**). $^{13}\text{C-NMR}$ (CDCl_3 , 100MHz) δ : 150.8, 127.6, 114.7 (**Ar-C**), 72.7, 70.9 (**OCH₂**), 41.8, 38.7, 36.3, 35.5, 29.9, 28.9 and 22.8 ppm. FT-IR (KBr, cm^{-1}): 2944, 2865, 2308, 2006, 1738, 1505, 1471, 1444, 1405, 1308, 1221, 1196, 1018, 913, 859 and 683. MALDI-TOF-TOF-MS (MW = 512.32): m/z = 535.04 (M^+ + 23)

Synthesis of tetraethyl (2, 5-bis (2-ethylhexyloxy)-1,4-phenylene)bis(methylene) diphosphonate (3f) : **2f** (1.5 g, 2.87 mmol) and triethyl phosphite (0.1 g, 5.75 mmol) were reacted **as described for 3a**. Yield: (54 %). $^1\text{H-NMR}$ (CDCl_3 , 400MHz) δ : 6.8 ppm (s, 2H, **Ar-H**), 3.9 ppm (m, 8H, **POCH₂CH₃**) ; 3.7 ppm (t, 4H, **OCH₂**), 3.1 ppm (d, 4H, **CH₂P**), 1.7-1.2 ppm (m, 36 H, **aliphatic** and **POCH₂CH₃**) and 0.8 ppm (t, 6H, **-CH₂-CH₃**). $^{13}\text{C-NMR}$ (CDCl_3 , 100MHz) δ :150.5, 119.4, 114.8, 71.2 (**OCH₂**), 61.9 (**POCH₂CH₃**), 39.7, 30.7, 29.2, 26.9, 25.5, 23.9, 23.1, 16.4, 14.2 and 11.2 ppm. FT-IR (KBr, cm^{-1}): 3469, 2959, 2925, 2867, 1509, 1465, 1391, 1247, 1210, 1163, 1097, 1023, 956, 890, 782, 726, and 648. MALDI-TOF-TOF-MS (MW = 634.76): m/z = 657.47 (M^+ + 23)

Synthesis of tetra ethyl(2-((1S,4R)-bicyclo[2.2.1.]heptanes-2-ylmethoxy)-5-(bicycle[2.2.1]heptan-2-ylmethoxy)-1,4-phenylene)bis(methylene)diphosphonate (3g): **2g** (0.3 g, 0.50 mmol) and triethyl phosphite (0.2 mL, 1.09 mmol) were reacted **as described for 3a**. Yield = (95 %). $^1\text{H-NMR}$ (CDCl_3 , 400MHz) δ : 6.91-6.87 ppm (m, 2H, **Ar-H**), 4.1 ppm (m, 8H, **POCH₂CH₃**), 3.9-3.5 ppm (m, 4H, **OCH₂**), 3.2 ppm (d, 4H, **CH₂P**) and 2.5-0.5 ppm (m, 22H, **Cyclic H**). $^{13}\text{C-NMR}$ (CDCl_3 , 100MHz) δ : 150.4, 119.4, 115.1, 72.8, 63.7, 62.2, 61.6, 58.5, 41.9, 39.6, 38.6, 36.2, 35.4, 34.3, 33.8, 29.9, 28.9, 25.6, 22.8, 18.4 and 16.2 ppm. FT-IR (KBr, cm^{-1}): 2950, 2869, 1509, 1466, 1393, 1210, 1021, 964, 820, 729, 645. MALDI-TOF-TOF-MS (MW = 626.31): m/z = 649.38 (M^+ + 23).

Synthesis of oligo-phenylenevinylenes: The synthetic procedures for OPV-C1-C11 (renamed here as **OPV-HC-C₁**), OPV-C8-C11 (renamed here as **OPV-HC-C₈**) and OPV-C11-C11 (renamed here as **OPV-HC-C₁₁**) have been provided in the

chapter 3. Similarly, detailed synthetic procedure for OPV-11 (renamed here as **OPV-HC-TCD**) in chapter 2.

Synthesis of 4,4'-(1E, 1'E)-2,2'-(2,5-bis(2-ethylhexyloxy)-1,4-phenylene)bis(ethene-2,1-diyl)bis(undecyloxy benzene) (OPV-HC-EH): 3f (1.3 g, 2.00 mmol) was reacted with **4k** (1.2 g, 2.20 mmol) as described for **OPV-C1-C1**. Yield = (59 %). ¹H NMR (CDCl₃, 400 MHz), δ: 7.42 ppm (d, 4H, **Ar-H**), 7.30 ppm (d, 2H, **CH=CH**), 7.07 ppm (s, 2H, **Ar-H**), 7.07 ppm (d, 2H, **CH=CH**), 6.86 ppm (d, 4H, **Ar-H**), 3.95 ppm (t, 4H, **OCH₂-CH₂**), 3.90 ppm (d, 4H, **OCH₂-CH**), and 1.9 - 0.86 ppm (m, 72H, **aliphatic-H**). ¹³C-NMR (CDCl₃, 100MHz) δ: 158.7, 150.9, 130.7, 128.01, 127.5, 126.6, 121.2, 114.6, 110.0, 68.04, 39.7, 31.9, 29.6, 29.4, 29.3, 29.2, 22.6, 14.1 and 11.3 ppm. FT-IR (KBr, cm⁻¹): 2920, 2850, 1600, 1571, 1507, 1463, 1418, 1388, 1292, 1239, 1193, 1170, 1111, 960, 845, 816, 788, 725 and 590. MALDI-TOF-TOF-MS (MW = 879.39): *m/z* = 878.71. Anal. Calcd for C₆₀H₉₄O₄: C, 81.95; H, 11.09. Found: C, 81.81; H, 10.94.

Synthesis of 2-((4((1S,4R)-bicyclo[2.2.1]heptane-2-yl)methoxy)-2,5-bis(4-undecyloxy) styryl)phenoxy)methyl)bicyclo[2.2.1]heptane (OPV-HC-NB): 3g (0.2 g, 0.32 mmol) was reacted with **4k** (0.2 g, 0.70 mmol) as described for **OPV-C1-C1**. Yield = (42 %). ¹H NMR (CDCl₃, 400 MHz), δ: 7.43 ppm (d, 4H, **Ar-H**), 7.30 ppm (d, 2H, **CH=CH**), 7.05 ppm (s, 2H, **Ar-H**), 7.07 ppm (d, 2H, **CH=CH**), 6.88 ppm (d, 4H, **Ar-H**), 4.03 ppm and 3.89 - 3.72 ppm (m, 4H, **OCH₂-NB**), 3.96 ppm (t, 4H, **OCH₂**), 0.8- 2.5 ppm (m, 64H, **aliphatic and cyclic-H**). ¹³C-NMR (CDCl₃, 100MHz) δ: 158.7, 151.2, 130.7, 127.7, 126.9, 121.5, 114.7, 110.9, 110.7, 73.6, 71.6, 68.2, 41.9, 39.5, 38.8, 36.3, 34.5, 32.0, 29.9, 29.4, 26.1, 22.8 and 14 ppm. FT-IR (KBr, cm⁻¹): 2922, 2855, 1603, 1509, 1467, 1420, 1390, 1294, 1246, 1201, 1173, 1111, 1025, 962, 925, 845, 816 and 722. MALDI-TOF-TOF-MS (MW = 879.39): *m/z* = 878.71. MALDI-TOF-TOF-MS (MW = 871.35): *m/z* = 870.79. Anal. Calcd for C₆₀H₈₆O₄: C, 82.71; H, 9.95. Found: C, 82.68; H, 10.05.

Synthesis of 4,4'-(1E,1'E)-2,2'-(2,5-bis(undecyloxy-1,4-phenylene)bis(ethane-2,1-diyl)bis((4,4,5,5,6,6,7,7,8,8,9,9,10,10,11,11-heptadecaundecyloxybenzene): (OPV-FC-C₁₁): 3e (0.2 g, 0.33 mmol) was reacted with 4-(4,4,5,5,6,6,7,7,8,8,9,9,10,10,11,11,11-heptadecafluoroundecyloxy)benzaldehyde (0.4 g, 0.69 mmol) as described for **OPV-C1-C1**. Yield = (47 %). ¹H NMR (CDCl₃, 400 MHz), δ: 7.46 ppm (d, 4H, **Ar-H**), 7.34 ppm (d, 2H, **CH=CH**), 7.09 ppm (s, 2H, **Ar-H**), 7.08 ppm (d, 2H, **CH=CH**), 6.88 ppm (d, 4H, **Ar-H**), 4.05 ppm (m, 8H, **OCH₂**), 2.4 - 1.0 ppm (m, 44H, **aliphatic-H**) and 0.87 ppm (t, 6H, **CH₃**). ¹³C-NMR (CDCl₃, 100MHz): 127.7, 121.4, 114.6, 69.6, 66.3, 34.8, 31.9, 29.6, 29.5, 29.4, 29.3,

26.2, 22.6, 20.6 and 14.0 ppm. ^{19}F NMR (CDCl_3) : -80.6 (3F), -114.2 (2F), -121.6 (2F), -121.8 (4F), -122.6 (2F), -123.3 (2F) and -125.9 ppm (2F). FT-IR (KBr, cm^{-1}): 2922, 2852, 1602, 1510, 1466, 1420, 1374, 1332, 1292, 1240, 1198, 1141, 1054, 1026, 967, 850, 818 and 655. MALDI-TOF-TOF-MS (MW = 1575.22): m/z = 1573.90.

Synthesis of 4,4'-(1E, 1'E)-2,2'-(2,5-bis(octyloxy)-1,4-phenylene)bis (ethene-2,1-diyl) bis((4,4,5,5,6,6,7,7,8,8,9,9,10,10,11,11,11-heptadecafluoroundecyloxy benzene) (OPV-FC-C₈): 3d (0.3 g, 0.50 mmol) was reacted with 4-(4,4,5,5,6,6,7,7,8,8,9,9,10,10,11,11,11-heptadecafluoroundecyloxy)benzaldehyde (0.6 g, 1.05 mmol) as described for OPV-C1-C1. Yield = (53 %). ^1H NMR (CDCl_3 , 400 MHz) δ : 7.43 ppm (d, 4H, Ar-H), 7.30 ppm (d, 2H, CH=CH), 7.07 ppm (s, 2H, Ar-H), 7.03 ppm (d, 2H, CH=CH), 6.87 ppm (d, 4H, Ar-H), 4.02 ppm (t, 4H, OCH₂), 3.95 ppm (t, 4H, OCH₂), 2.0-1.2 ppm (m, 32H, aliphatic-H) and 0.87 ppm (t, 6H, CH₃). ^{19}F NMR (CDCl_3) : -80.6 (3F), -114.28 (2F), -121.63 (2F), -121.84 (4F), -122.64 (2F), -123.35 (2F) and -126.02 ppm (2F). FT-IR (KBr, cm^{-1}): 2925, 2857, 1603, 1509, 1463, 1420, 1379, 1333, 1293, 1240, 1142, 1027, 968, 851, 819, 706 and 657. MALDI-TOF-TOF-MS (MW = 1491.06): m/z = 1490.46.

Synthesis of 4,4'-(1E,1'E)-2,2'-(2,5-bis(2-ethylhexyloxy)-1,4-phenylene)bis (ethane-2,1-diyl)bis((4,4,5,5,6,6,7,7,8,8,9,9,10,10,11,11-heptadeca undecyloxy) benzene)(OPV-FC-EH): 3f (0.2 g, 0.33 mmol) was reacted with 4-(4,4,5,5,6,6,7,7,8,8,9,9,10,10,11,11,11-heptadecafluoroundecyloxy) benzaldehyde (0.4 g, 0.69 mmol) as described for OPV-C1-C1. Yield = (40 %). ^1H NMR (CDCl_3 , 400 MHz), δ : 7.44 ppm (d, 4H, Ar-H), 7.35 ppm (d, 2H, CH=CH), 7.09 ppm (s, 2H, Ar-H), 7.08 ppm (d, 2H, CH=CH), 6.88 ppm (d, 4H, Ar-H), 4.02 ppm (t, 4H, OCH₂CH₂), 3.92 ppm (d, 4H, OCH₂CH) 2.2-0.8 ppm (m, 32H, aliphatic-H) and 0.89 ppm (t, 6H, CH₃). ^{13}C -NMR (CDCl_3 , 100MHz): 150.8, 150.9, 131.2, 127.9, 127.6, 126.7, 121.6, 114.6, 110.0, 71.7, 66.3, 39.7, 30.9, 29.2, 28.0, 24.2, 23.1, 20.5, 14.1 and 11.3 ppm. ^{19}F NMR (CDCl_3): -80.6 (3F), -114.2 (2F), -121.6 (2F), -121.8 (4F), -122.6 (2F), -123.2 (2F) and -125.9 ppm (2F). FT-IR (KBr, cm^{-1}): 2959, 2929, 2866, 1603, 1511, 1462, 1422, 1377, 1333, 1238, 1240, 1196, 1142, 1028, 966, 933, 847, 816, 774, 729, 703, 657 and 583. MALDI-TOF-TOF-MS (MW = 1491.06): m/z = 1490.32.

Synthesis of (1S,4R)- 2-((4-(2-bicyclo[2.2.1]heptane-2-yl)ethyl)-2,5-bis(4-(4,4,5,5,6,6,7,7,8,8,9,9,10,10,11,11,11-heptadecafluoroundecyloxy styryl) phenoxy)methyl) bicyclo[2.2.1]heptane (OPV-FC-NB): 3g (0.2 g, 0.32 mmol) was reacted with 4-(4,4,5,5,6,6,7,7,8,8,9,9,10,10,11,11,11-heptadecafluoroundecyloxy)

benzaldehyde (0.4 g, 0.70 mmol) **as described for OPV-C1-C1**. Yield = (5 %). ^1H NMR (CDCl_3 , 400 MHz), δ : 7.45 ppm (d, 4H, **Ar-H**), 7.31 ppm (d, 2H, **CH=CH**), 7.08 ppm (d, 2H, **CH=CH**), 7.05 ppm (s, 2H, **Ar-H**), 6.88 ppm (d, 4H, **Ar-H**), 4.06 ppm (t, 4H, OCH_2CH_2), 4.0 -3.6 ppm (m, 4H, OCH_2CH) and 2.5-0.8 ppm (m, 30H, **cyclic-H**). ^{13}C -NMR (CDCl_3 , 100MHz): 131.4, 127.8, 114.7, 101.3, 66.4, 41.9, 38.8, 35.5, 34.4, 28.9, 25.1 and 20.7 ppm. ^{19}F NMR (CDCl_3): -80.6 (3F), -114.2 (2F), -121.6 (2F), -121.8 (4F), -122.6 (2F), -123.3 (2F) and -126.1 ppm (2F). FT-IR (KBr, cm^{-1}): 2951, 1603, 1509, 1201, 1145, 1026, 970, 841 and 657. MALDI-TOF-TOF-MS (MW = 1483.00): m/z = 1482.48.

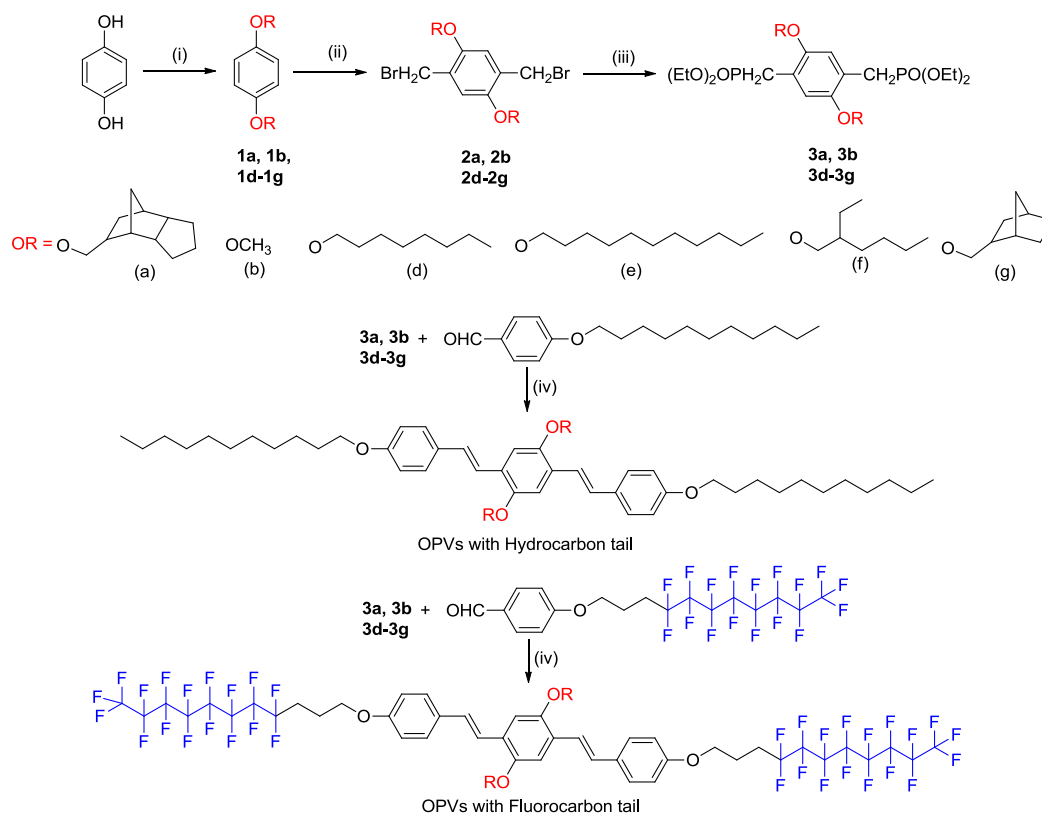
Synthesis of 4,4'-(1E,1'E)-2,2'-(2,5-dimethoxy-1,4-phenylene)bis(ethane-2,1-diyl)bis((4,4,5,5,6,6,7,7,8,8,9,9,10,10,11,11-heptadecaundecyloxy)benzene) (OPV-FC-C₁): 3b (0.4 g, 1.00 mmol) was reacted with 4-(4,4,5,5,6,6,7,7,8,8,9,9,10,10,11,11,11-heptadecafluoroundecyloxy)benzaldehyde (1.2 g, 2.20 mmol) **as described for OPV-C1-C1**. Yield = (10 %). ^1H NMR (CDCl_3 , 400 MHz), δ : 7.49 ppm (d, 4H, **Ar-H**), 7.35 ppm (d, 2H, **CH=CH**), 7.11 ppm (s, 2H, **Ar-H**), 7.08 ppm (d, 2H, **CH=CH**), 6.85 ppm (d, 4H, **Ar-H**), 4.07 ppm (t, 4H, Ar- OCH_2 -alkyl), 3.92 ppm (s, 6H, Ar- OCH_3), 2.45 ppm (m, 4H, O- CH_2 -**CH₂**) and 2.11 ppm (m, 4H, O- CH_2 -**CH₂**-**CH₂**). ^{19}F NMR (CDCl_3): -80.6 (3F), -114.2 (2F), -121.6 (2F), -121.8 (4F), -122.6 (2F), -123.3 (2F) and -126.1 ppm (2F). FT-IR (KBr, cm^{-1}): 1602, 1509, 1461, 1413, 1377, 1332, 1294, 1241, 1199, 1142, 1026, 966, 849, 818, 702, 654, and 592. MALDI-TOF-TOF-MS (MW = 1294.69): m/z = 1293.99.

Synthesis of OPV-FC-TCD: 3a (0.5 g, 0.66 mmol) was reacted with 4-(4,4,5,5,6,6,7,7,8,8,9,9,10,10,11,11,11-heptadecafluoroundecyloxy)benzaldehyde (0.8 g, 1.32 mmol) **as described for OPV-C1-C1**. The product was purified by passing through a silica gel column using 1% ethyl acetate in hexane as eluent. Yield = (25 %). ^1H NMR (CDCl_3 , 400 MHz), δ : 7.46 ppm (d, 4H, **Ar-H**), 7.31 ppm (d, 2H, **CH=CH**), 7.15 ppm (d, 2H, **CH=CH**), 7.05 (s, 2H, **Ar-H**), 6.89 ppm (d, 4H, **Ar-H**), 4.06 ppm (m, 4H, $\text{OCH}_2\text{-CH}_2$), 3.83 -3.75 ppm (m, 4H, OCH_2 -TCD) and 2.4 -1.0 ppm (m, 38H, Cyclic and aliphatic-H). ^{19}F NMR (CDCl_3): -80.6 (3F), -114.3 (2F), -121.6 (2F), -121.8 (4F), -122.6 (2F), -123.3 (2F) and -126.0 ppm (2F). FT-IR (KBr, cm^{-1}): 2948, 2869, 1605, 1510, 1480, 1455, 1383, 1371, 1331, 1289, 1224, 1199, 1173, 1115, 1057, 1028, 971, 847, 819, 803, 747, 721, 703, 655, 622, 575 and 557. MALDI-TOF-TOF-MS (MW = 1563.13): m/z = 1562.25.

4.3. Results and Discussion

4.3.1. Synthesis and structure characterisation of OPVs

Two series of OPVs consisting of hydrocarbon and fluorocarbon tails were synthesized by multi-step reactions as shown in scheme 4.1. The OPVs were referred as OPV-HC-Cx or OPV-FC-Cx, in which HC and FC stand for hydrocarbon and fluorocarbon tails, respectively. Cx = C1, C8 or C11 represented the number of carbon atoms present in the linear chains as methyl, n-octyl and n-undecyl units. 2-Ethylhexyl and norbornane methyl are referred to as EH and NB instead of Cx.



Scheme 4.1. Synthesis of hydrocarbon and fluorocarbon tailed OPVs

The structures of all the OPVs have been shown in figure 4.6. The terminal alkyl tails were kept same in all the OPVs, but the middle pendent group is varied from methoxy, linear octyloxy, undecyloxy, cyclic norbornane, tricyclodecane and

branched ethyl hexyl pendants. Similarly, in the hydrocarbon tail OPVs, the fluorine atoms in the fluorocarbon tails were replaced with hydrogen atoms to give rise to a completely hydrocarbon tail, but the OPVs differ from each other in having different middle pendant groups.

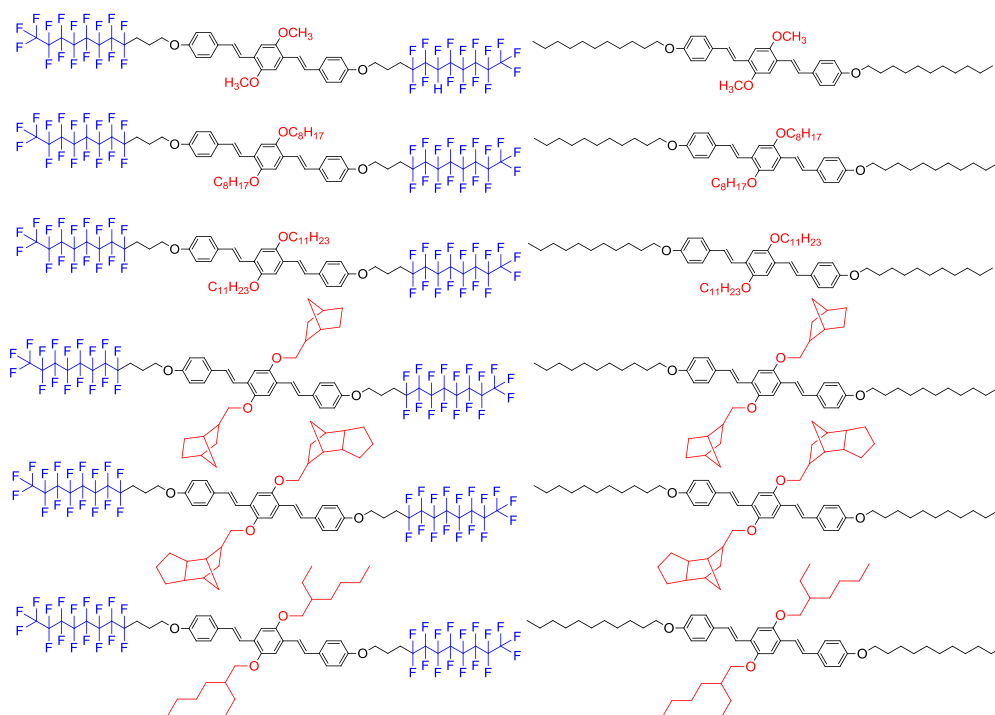


Figure 4.6. Chemical structures of fluorocarbon and hydrocarbon tailed OPVs.

The OPVs were characterised by ^1H , ^{13}C and ^{19}F NMR analysis. Figure 4.7a. and 4.7b. shows the ^1H , and ^{19}F -NMR spectra of a representative fluorocarbon tailed molecule (OPV-FC- C_{11}). Similarly, figure 4.7c. and 4.7d. shows the ^1H , and ^{13}C -NMR spectra of its corresponding hydrocarbon tailed molecule (OPV-HC- C_{11}). The insets showed the expanded proton spectra of the aromatic regions. The peaks at 7.45 ppm and 6.89 ppm corresponded to aromatic phenylene protons. The doublets at 7.30 ppm and 7.11 ppm belonged to vinylene protons. The protons in the middle aromatic ring appeared as a singlet at 7.11 ppm. The peak pattern for the aromatic region was found to be the same in case of hydrocarbon and fluorocarbon OPVs. A comparison

of alkoxy protons in HC and FC-OPVs in figure 4.7.a and 4.7.c. revealed that in the case of HC-OPVs, the alkoxy protons appeared as two well resolved triplets at 3.9 ppm and 4.1 ppm belonging to Ar-OCH₂-alkyl protons. However, in the case of FC-OPVs, the two alkoxy proton triplets merged to give rise to a multiplet. The peaks for all other protons appeared below 3.75 ppm. ¹³C-NMR spectrum of the OPV-HC-C₁₁ was used to characterise the carbon atoms in HC-OPVs, but ¹³C-NMR spectrum for FC-OPVs were poorly resolved and hence further characterisation was done using ¹⁹F-NMR spectrum. The three terminal fluorine atoms appeared at -80.6.

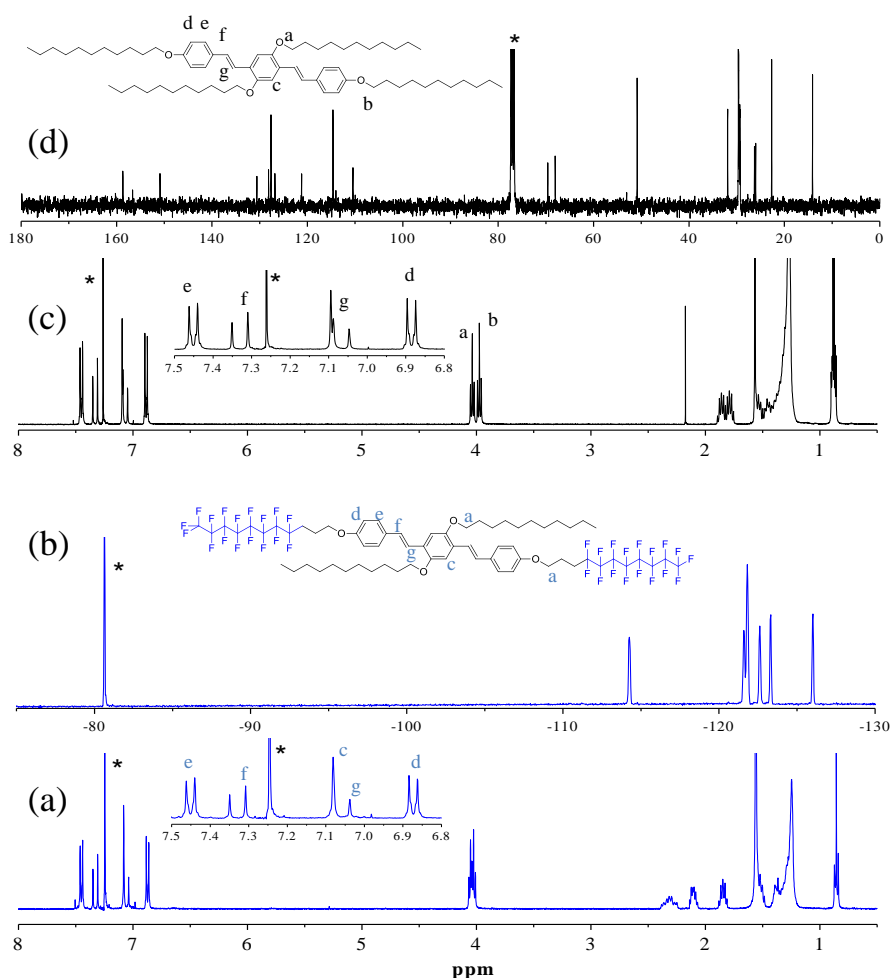


Figure 4.7. ¹H-NMR spectrum of OPV-FC-C₁₁ (a) ¹⁹F-NMR spectrum of OPV-FC-C₁₁ (b) ¹H-NMR spectrum of OPV-HC-C₁₁ (c) ¹³C-NMR spectrum of OPV-HC-C₁₁.

Similarly, all the fluorine atoms belonging to other carbon atoms appeared at -114.2 (2F), -121.6 (2F), -121.8 (4F), -122.6 (2F), -123.3 (2F) and -126.1 ppm (2F), respectively. All the other HC and FC OPVs followed the same peak patterns in their ^1H , ^{13}C and ^{19}F NMR spectra and the detailed analysis for other OPVs have been given in the experimental section.

GPC Chromatograms of hydrocarbon and fluorocarbon tail OPVs have been shown in figure 4.8. All the chromatograms showed a single peak confirming high purity of these samples. The molecular weight of fluorocarbon tail OPVs was higher than their corresponding hydrocarbon tail OPVs because of which the fluorocarbon tail OPVs eluted faster than HC-OPVs. The TGA profiles for the hydrocarbon as well as fluorocarbon OPVs have been shown in figure 4.8c and 4.8d, respectively. Thermo gravimetric analysis revealed that both fluorocarbon and hydrocarbon OPVs were stable at high temperatures up to 300 °C.

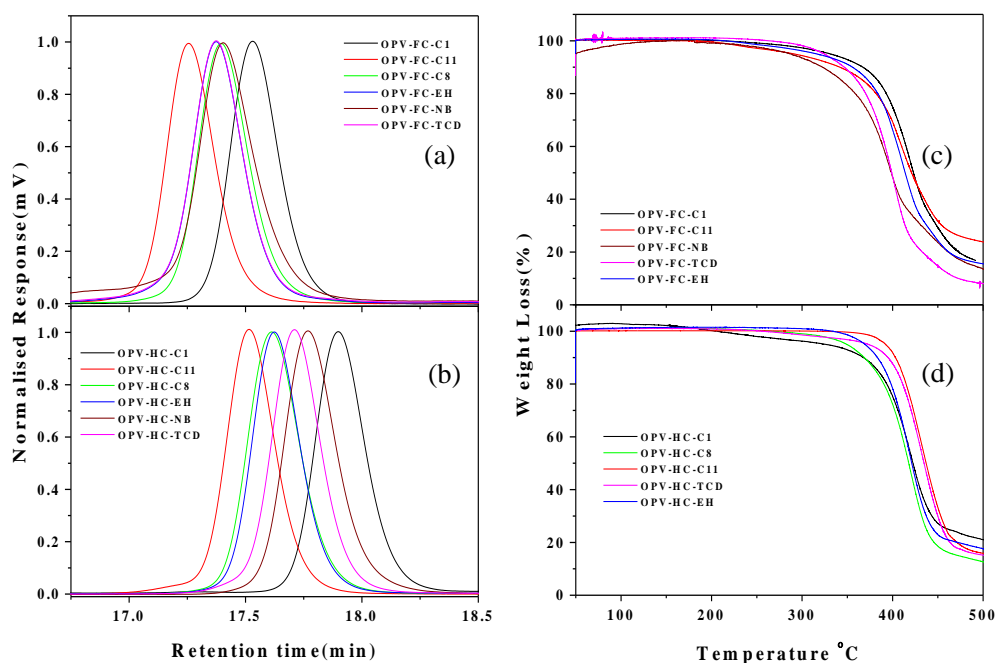


Figure 4.8. GPC chromatograms of fluorocarbon tailed OPVs (a) and of hydrocarbon tailed OPVs in tetrahydrofuran at 25 °C (b). TGA profiles of fluorocarbon tailed OPVs (c) and of hydrocarbon tailed OPVs (d).

4.3.2. Thermal Properties

Thermal transitions in OPVs were studied by differential scanning calorimetry (DSC). The DSC profiles at $10^{\circ} \text{ min}^{-1}$ heating and cooling rates have been shown in figure 4.9. OPVs with fluorocarbon tails showed two thermal transitions in heating and cooling cycles suggesting their thermotropic LC nature (see figure 4.9.a and b). OPV-FC-C₁ showed two transitions at 210.5 °C and 153.6 °C in the cooling cycle for the isotropic-to-LC and LC-to-crystalline phase transitions, respectively. In the subsequent heating cycle, these two transitions appeared at 182.4 °C and 212.0 °C with respect to crystal-to-LC and LC-to-isotropic phase changes. The change in the chain length or cyclic nature of middle alkoxy unit (from C₁ to C₁₁, C₈ or NB) decreased the LC-transition window by almost 60 to 80 °C in the case of FC-OPVs. Among the three C₈ carbon atom pendants, the OPVs having branched side chain unit ethylhexyl was found to show only a single transition in the heating and cooling cycles as similar to crystalline solids. OPV-FC-

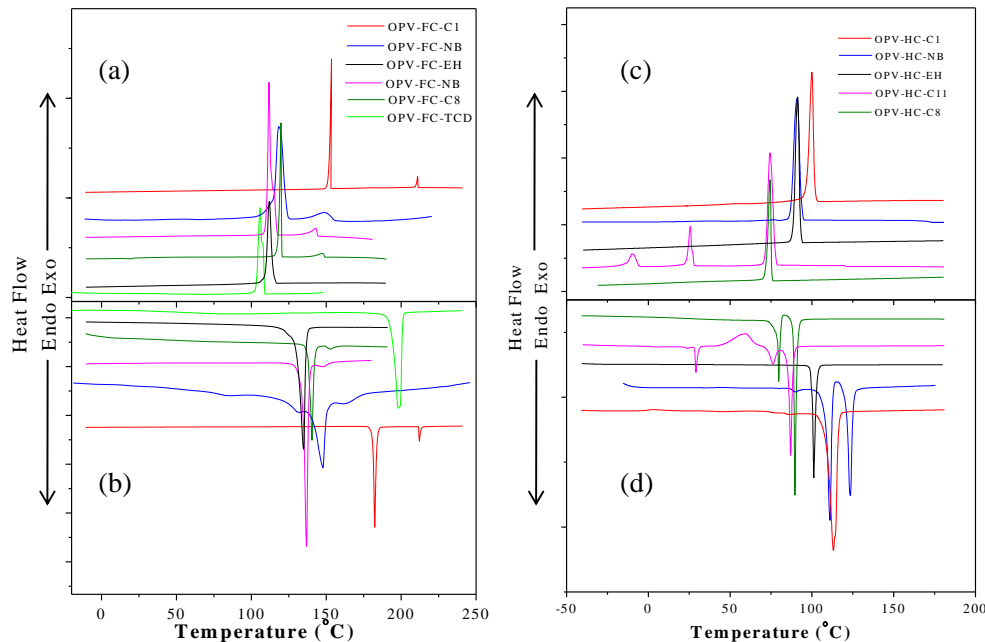


Figure 4.9. DSC thermograms of fluorocarbon OPVs in cooling cycle (a), in heating cycle (b) and of hydrocarbon OPVs in cooling cycle (c), in heating cycle (d) recorded at $10^{\circ}/\text{min}$ heating/cooling rates.

TCD did not show two transitions in the DSC profile, but its smectic LC nature was confirmed by PLM analysis and is discussed later in this chapter. The peak transition temperatures and their enthalpies for fluorocarbon OPVs in both heating and cooling cycles have been summarized in Table 4.1.

Table 4.1. DSC thermal data of FC tail OPVs at 10%/min heating/cooling Rate.

FC-OPVs	Heating Cycle				Cooling Cycle				T_d^i
	T_{m1}^a	T_{m2}^b	ΔH_{m1}^c	ΔH_{m2}^d	T_{c1}^e	T_{c2}^f	ΔH_{c1}^g	ΔH_{c2}^h	
OPV-FC-NB	147.8	163.9	9.6	0.6	151.1	118.8	1.8	17.6	363.9
OPV-FC-C ₁	182.4	211.9	59.6	5.1	210.4	153.7	5.4	56.7	350.1
OPV-FC-C ₁₁	136.7	148.3	67.6	1.2	142.1	111.6	6.6	68.7	331.4
OPV-FC-EH	-	134.9	-	78.4	111.9	-	67.1	-	368.9
OPV-FC-C ₈	144.1	152.6	84.6	3.7	146.4	121.4	7.2	63.3	349.4
OPV-FC-TCD	-	180.7	-	-	179.9	-	-	-	360.2

(a) T_{m1} is temperature for crystal to LC phase change measured in °C. (b) T_{m2} is temperature for LC to Isotropic phase change measured in °C. (c) ΔH_{m1} is the enthalpy change for crystal to LC phase change in kJ/mol. (d) ΔH_{m2} is the enthalpy change for LC to Isotropic phase change in kJ/mol. (e) T_{c1} is temperature for isotropic to LC phase change measured in °C. (f) T_{c2} is temperature for LC to crystal phase change measured in °C. (g) ΔH_{c1} is the enthalpy changes for isotropic to LC phase change in kJ/mol. (h) ΔH_{c2} is the enthalpy change during LC to crystal phase change in kJ/mol. (i) T_d is the thermal decomposition temperature measured in °C.

The DSC thermograms of the hydrocarbon OPV series showed completely different types of LC trends compared to that of the fluorocarbon tailed OPVs. Three transitions were found in OPV-HC-C₁₁ and all these transitions were completely reversible in the subsequent heating cycles. OPV-HC-NB showed two thermal transitions in heating cycle, however, the second transition (LC-to-crys) was found to be very weak in the cooling cycle. Similarly, OPV-HC-C₁ was also found to show only predominant isotropic-to-LC transition (at 100 °C) and LC-to- isotropic (at 113 °C) in the cooling and heating cycles, respectively (the LC properties of these compounds were confirmed by PLM studies). OPV-HC-EH (also OPV-HC-C₈) was a crystalline solid similar to its fluorocarbon counterpart OPV-FC-EH. DSC analysis

suggested that branched side chains (ethylhexyl unit) in OPVs hindered the packing of chromophores and restricted the formation of LC mesophases. The peak transition temperatures and their enthalpies for hydrocarbon OPVs in both heating and cooling cycles are summarized in Table 4.2. The comparison of the enthalpies of thermal

Table 4.2. DSC thermal data of HC tail OPVs at 10 %/min heating/cooling Rate

HC-OPVs	Heating Cycle				Cooling Cycle				T _d
	T _{m2} ^a	T _{m3} ^b	ΔH _{m2} ^c	ΔH _{m3} ^d	T _{c1} ^e	T _{c2} ^f	ΔH _{c1} ^g	ΔH _{c2} ^h	
OPV-HC-NB	111.2	123.4	30.3	21.1	90.8	77.6	46.0	0.17	388.5
OPV-HC-C ₁		111.9		90.9	99.8	52.8	87.0	0.75	313.9
OPV-HC- C ₁₁	71.05	86.8	10.4	71.2	74.3	25.4*	45.7	10.86 [#]	404.1
OPV-HC- EH		101.1		86.3	91.1		84.7	-	370.9
OPV-HC- C ₈	79.8	89.8	35.6	66.5	74.4		85.5	-	374.6
OPV-HC-TCD	13.5	161.0	1.3	42.2	108.6	0.5	44.2	0.17	388.1

* A small crystal to crystal transition was observed at T_{c3} = -10 °C. # A small crystal to crystal transition was observed at ΔH_{c3} = 7.2 kJ mol⁻¹.

(a) T_{m1} is temperature for crystal to crystal phase change measured in °C. (b) T_{m2} is temperature for Cry to LC phase change measured in °C. (c) T_{m3} is temperature for LC to Isotropic phase change measured in °C. (d) ΔH_{m1} is the enthalpy change for crystal to crystal phase change in kJ/mol. (e) ΔH_{m2} is the enthalpy change during crystal to LC phase change in kJ/mol. (f) ΔH_{m3} is the enthalpy change during LC to Isotropic phase change in kJ/mol. (g) T_{c1} is temperature for isotropic to LC phase change measured in °C. (h) T_{c2} is temperature for LC to crystal phase change measured in °C. (i) T_{c3} is temperature for crystal to crystal phase change measured in °C. (j) ΔH_{c1} is the enthalpy changes during isotropic to LC phase change measured in kJ/mol. (k) ΔH_{c2} is the enthalpy change during LC to crystal phase change measured in kJ/mol. (l) ΔH_{c3} is the enthalpy change during crystal to crystal phase change measured in kJ/mol

transitions (see table 4.1 ,4.2) and the peak intensities in figure 4.9 indicated that all the fluorocarbon OPVs, in general, underwent less energetic crystallization process initially (isotropic-to-LC) followed by larger crystallization during LC-to-crystalline phase. Unlike in the fluorocarbon tailed OPVs, the HC -OPV series was

characterized by a strong isotropic-to-LC phase transition followed by weak LC-to-crystalline phase. This suggested that the nature of the flexible tail attached in the longitudinal position of OPVs dictated the types of crystal packing while cooling from isotropic molten state.

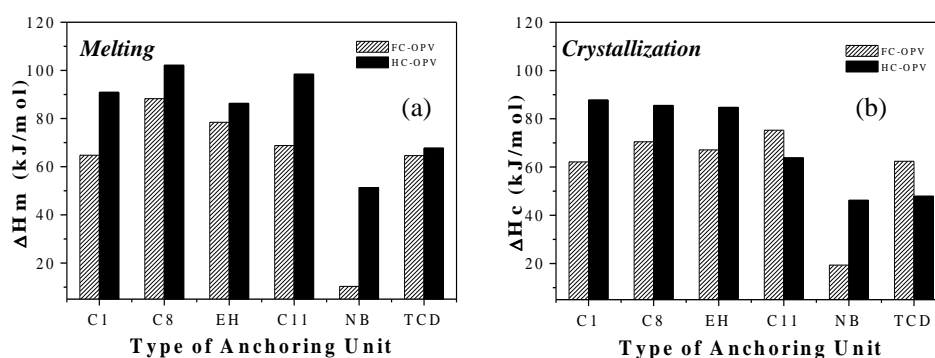


Figure 4.10. (a) Plot of enthalpy of melting against the type of pendent groups. (b) Plot of enthalpy of crystallization against the type of pendent groups.

In order to understand the role of the pendant groups on the packing of the OPV chromophores, the enthalpies of melting and crystallization transitions were plotted against the type of pendent groups (see Figure 4.10). Among the hydrocarbon OPV series, the enthalpies of melting (or crystallization) of OPVs followed the order: $NB \approx TCD < C_1 = EH < C_8 = C_{11}$. The enthalpies of the transitions in fluorocarbon tailed OPVs followed the trend: $NB < C_{11} < C_8 = C_1 = EH = TCD$, which was almost similar to that of the hydrocarbon tailed series. The enthalpies (ΔH) of the transitions were directly associated with the packing of the chromophores, and therefore based on their values in the tables (4.1 and 4.2) and figure 4.9, it may be concluded that the hydrocarbon tails produced high crystalline samples compared to that of the fluorocarbon tails. Further, the OPVs with alkyl chains substitution in the middle core (methoxy, undecyloxy, and octyloxy) have much higher enthalpy values than their cycloaliphatic systems (NB). It suggested that though the cycloaliphatic system was capable of inducing LC-mesophase in OPVs, the chromophore packing was relatively weak compared to their linear chain analogues.⁷⁻¹⁴

4.3.3. Polarised Light Microscopic Analysis

The temperature dependent LC textures of the OPVs were studied by PLM analysis with a programmable hot stage. The LC textures of OPV-FC-C₁₁ have been shown in figure 4.11. The nucleation of the OPV-FC-C₁₁ from isotropic phase appeared as smectic batonnets (at 147 °C) which subsequently grew both in lateral and longitudinal directions as smectic A (SmA) type images (at 145 °C). On further cooling (or holding at this temperature isothermally), the morphology transformed into fan-shaped smectic-C (SmC) LC mesophases (see image at 140 °C).⁴⁶

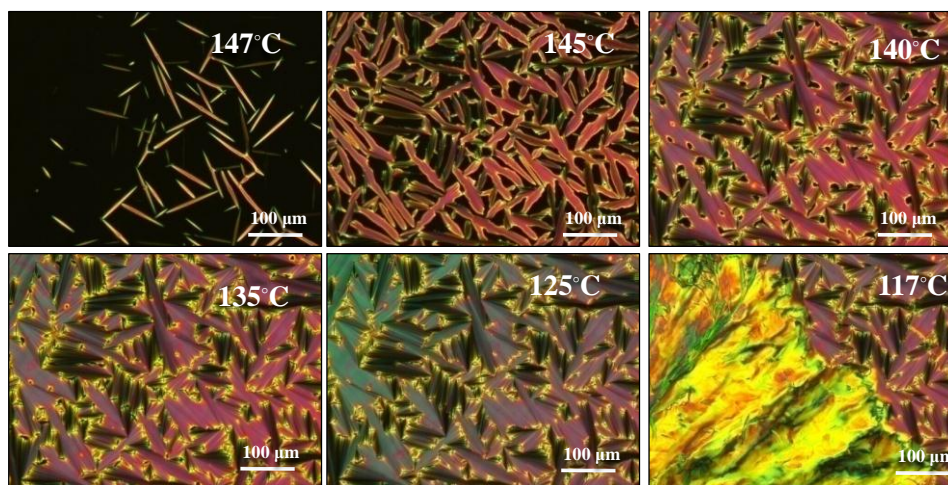


Figure 4.11. PLM images of OPV-FC-C₁₁ at 10%/min in cooling cycle.

The nucleation and subsequent growth patterns for OPV-FC-C₁, OPV-FC-C₈ and, OPV-FC-NB have been shown in the figure 4.12. All the OPVs showed similar nucleation and growth patterns as observed for OPV-FC-C₁₁. The nucleation of the OPV-FC-C₁ from isotropic phase appeared at 207 °C, and the transition to smectic phase occurred at 198 °C. Similarly, OPV-FC-C₈ and OPV-FC-NB exhibited smectic batonnets at 155 °C and 173 °C, respectively. The nucleation and crystal growth patterns of all the fluorinated molecules were found to be almost identical. The slight differences in the orientation of the crystalline vectors in the smectic phases and variation in the optical birefringence among fluorinated OPVs were attributed to

their difference in the pendant units attached in the central aromatic ring. Thus, the formations of identical SmC LC mesophases irrespective of the pendent groups attached in the middle aromatic core suggested that the molecular self-assembly was predominately directed by the fluorocarbon tail rather than pendent units.

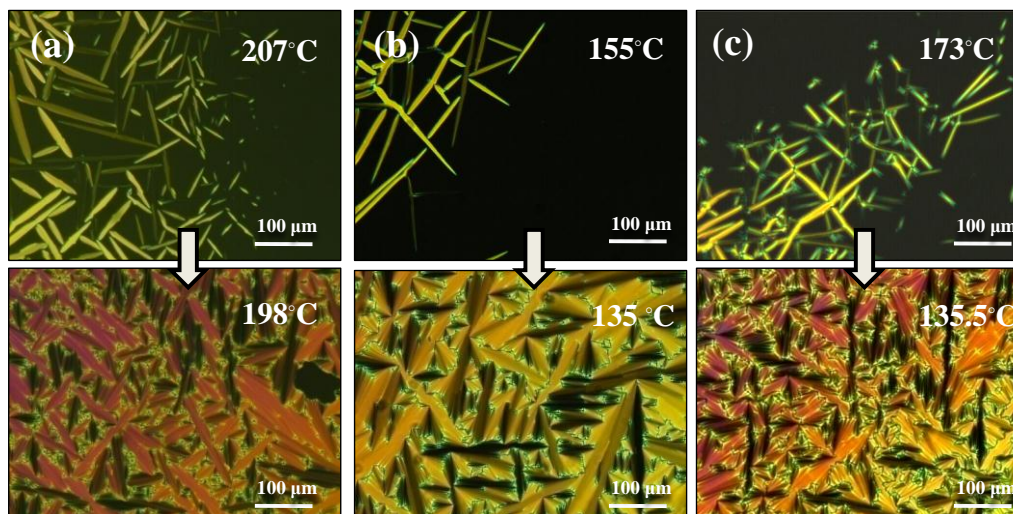


Figure 4.12. PLM images of nucleation and subsequent growth for OPV-FC-C₁ (a) OPV-FC-C₈ (b) and OPV-FC-NB(c) at 10 °/min.

In contrast, the nucleation and growth patterns of HC-OPVs were completely different from FC-OPVs. The PLM images for hydrocarbon OPVs have been shown in figure 4.13. OPV-HC-C₁ exhibited spherical droplets as nucleating sites, these droplets quickly impinged on neighboring droplets to give rise to Schlieren nematic liquid crystalline textures. The detailed temperature dependent LC textures for OPV-HC-C₁ have already been explained in the chapter-3. Figure 4.13. shows the detailed temperature dependent PLM images for OPV-HC-C₁₁. The shape and nature of the nuclei in OPV-HC-C₁₁ was very much different from oily droplets and the oval-shaped nuclei resulted in the formation of a leaf-like LC texture at 70° to 65°C. The nuclei in OPV-HC-C₁₁ had almost identical aspect ratio (length/width) = 2.3 (see image at 77 °C) and the growth of these oval shaped nuclei resulted in the formation of leaf like LC texture at 70 to 65° C. On subsequent cooling below 60 °C in the LC active temperature window, these leaf like textures transformed into well ordered

two-dimensional lamellar textures (see image at 42 °C). This lamellar texture persisted at 25 °C for more than two days. The comparison of the LC textures with DSC temperature profile (see Figure 4.9c. and 4.9d) suggested that the morphology transformation from leaf to lamellar ordering actually occurred in the LC active temperature window.

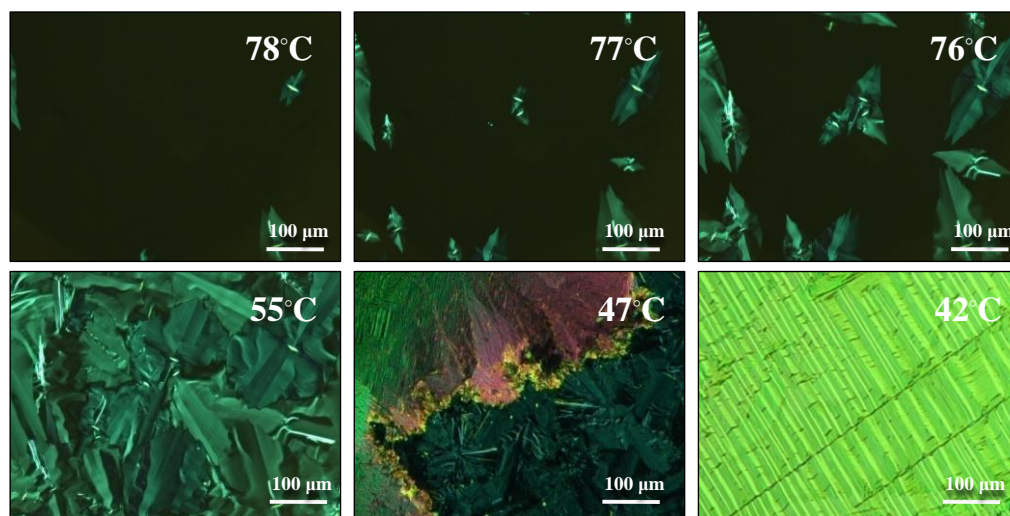


Figure 4.13. Temperature dependent PLM profile of OPV-HC-C₁₁.

The nucleation and crystal growth patterns of other HC-OPVs have been shown in figure 4.14. OPV-HC-C₁ exhibited spherical droplets as nucleating sites and gave

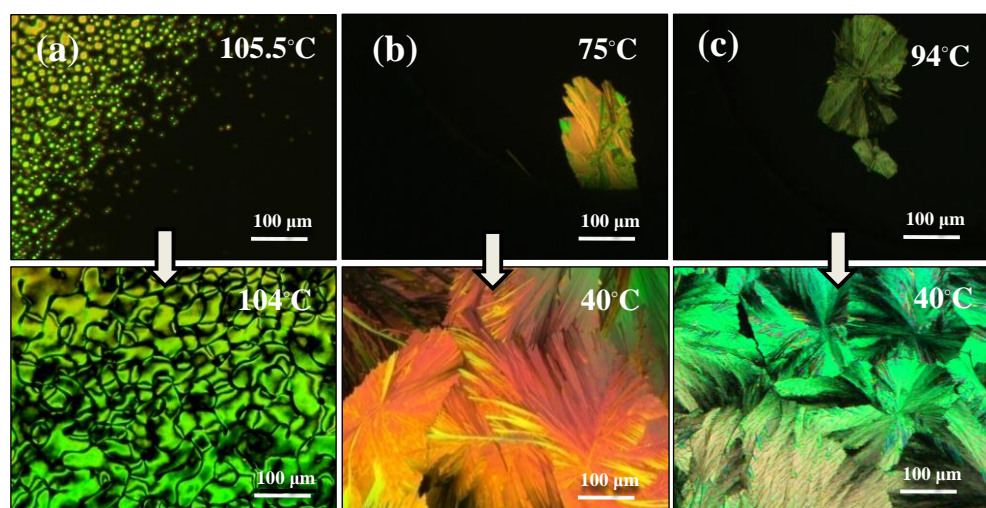


Figure 4.14. PLM images of nucleation and subsequent growth for OPV-HC-C₁ (a), OPV-HC-C₈ (b) and OPV-HC-NB (c) at 10%/min.

rise to schlieren nematic liquid crystalline textures. OPV-HC-NB and OPV-HC-C₈ showed leaf-like nucleation at 94 °C and 75 °C, which quickly grew to produce flower paddle-like textures. These textures were stable and remained unchanged until room temperature. The LC patterns for these samples at room temperature are shown in the figure 4.14. OPV-HC-EH did not show any LC characteristic textures and their images were found to be similar to crystalline solids.

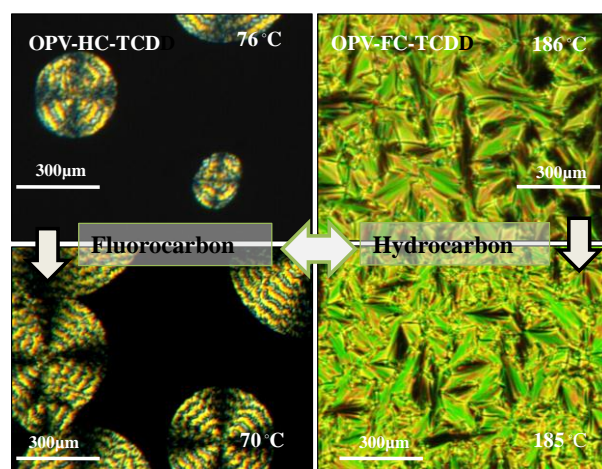


Figure 4.15. PLM images of OPV-HC-TCD and OPV-FC-TCD at 10 °/min

A comparison of nucleation and LC growth patterns of TCD substituted fluorocarbon and hydrocarbon OPV has been shown in the figure 4.15. OPV-HC-TCD exhibited ring banded nucleation and gave rise to ring banded LC mesophases. In contrast, OPV-FC-TCD appeared as smectic batonnets from isotropic phase (at 186 °C) which subsequently grew both in lateral and longitudinal directions as smectic type images (at 185 °C). The PLM images exhibited by OPV-FC-TCD were similar to its other fluorocarbon counterparts, but the LC window was found to be very small ($\approx 1-2$ °C). Two important points could be derived from the LC textures: (i) in hydrocarbon tailed OPVs, both pendent geometry and their length in the middle aromatic core determined the molecular self-organization rather than the flexible tail in the longitudinal position and (ii) in fluorocarbon tailed OPVs, the stiff and rigid nature of tail dominated the self-organization and the nature of pendants had less influence.

4.3.4. Variable temperature XRD Analysis

Fluorocarbon-tailed OPVs in smectic LC phases were subjected to variable temperature powder X-ray diffraction. The X-ray diffraction patterns of OPV-FC-C₁₁ in the respective LC temperature range are shown in Figure 4.16a. Upon cooling from isotropic melt, in the LC active temperature range (at 150 °C), the sample showed very broad signals which confirmed their liquid crystalline nature. Upon further cooling, intense crystalline peaks appeared in the wide-angle region in a regular periodic fashion corresponding to layer like packing (see Figure 4.16a). To determine smectic layer thickness and the optical tilt angle of mesophases,

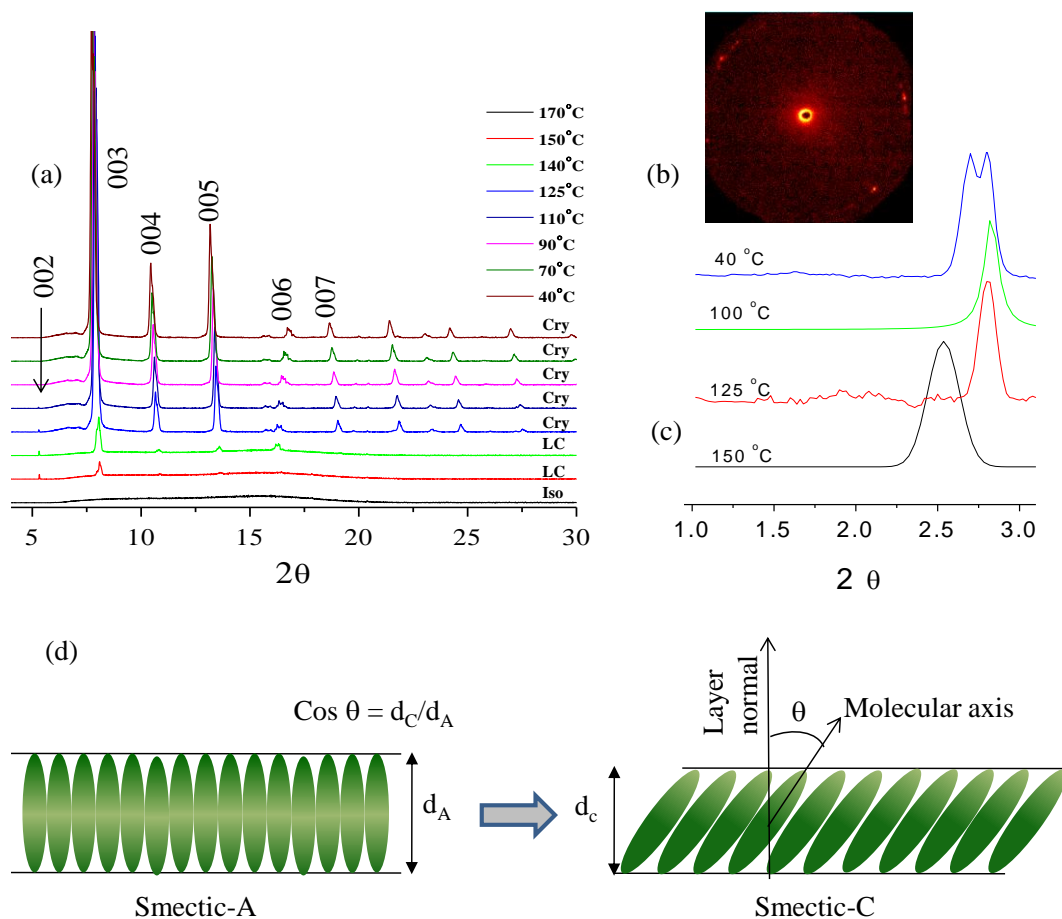


Figure 4.16. Variable-temperature wide-angle X-ray patterns (a), 2D electron-density diagram (b) and small-angle X-ray diffraction patterns (c) of OPV-FC-C₁₁. A mesogen packing model describing the SmA to SmC transformation (d).

OPV-FC-C₁₁ was further subjected to variable-temperature small-angle X-ray diffraction analysis. The two-dimensional electron density diagram at 40 °C (see figure 4.16b) and the small angle analysis at 150, 125, 100 and 40 °C are shown in figure 4.16.c. In figure 4.16c, the fundamental peak corresponding to the 001 lattice was observed at $2\theta = 2.52^\circ$ ($d_A = 35.01 \text{ \AA}$, at 150 °C). At 125°C, the peak was shifted to $2\theta = 2.80$ (d_c spacing = 31.51 Å), which indicated that the molecules underwent a transition from SmA to a more ordered SmC phase. Upon further cooling, the peak position did not change much, which confirmed the formation of stable layer-like arrangements. According to the classic rigid-rod model, the SmA-to-SmC phase transition is accompanied by a contraction of the layer spacing d that scales with the cosine of the tilt angle θ (see Figure 4.16d).^{46, 47-49} Comparing the SmC and SmA layer spacing, the tilt angle of the molecules in the SmC mesophase was calculated as $\theta = \cos^{-1}d_C/d_A$, with d_C and d_A being the layer thickness in the SmC and SmA phases. The phase transition was accompanied by 11% reduction in the interlayer shrinkage $((d_A - d_C)/d_A) \times 100$ which is typically observed in a SmA to SmC transition. The tilt angle was calculated as $\theta = 25.18^\circ$, which was in accordance to the range of θ (≈ 25 to 35°) typically reported in earlier examples.⁷⁻¹⁴ This confirmed that the peak shift in the small angle patterns is corresponding to the phase transition from SmA to SmC. Based on the 001 fundamental peak at $2\theta = 2.52$ ($d_A = 35.01 \text{ \AA}$, in small angle diffraction), the wide angle XRD patterns peaks were assigned for 002, 003...007 layers, respectively (see Figure 4.16a.).

The detailed variable temperature XRD patterns of other fluorocarbon tail OPVs exhibited similar regular periodicity in diffraction peaks corresponding to equidistant planes formed in their respective smectic LC windows. The peaks were indexed in series as 001, 002, 003, 004, 005 and 006 corresponding to smectic layer planes. The X-ray diffraction pattern for OPV-FC-C₁ could not be recorded due to experimental difficulties. Based on the above analysis, it may be summarized that all the fluorocarbon- tailed OPV mesogens arranged in two-dimensional layers (as H-type organization) leading to the formation of SmA textures, which transformed into a SmC mesophase at lower temperature.

The single-crystal X-ray analysis for OPV-HC-C₁₁ and OPV-HC-C₁ has been explained in the previous chapter. Single crystal X-ray structures were determined for the crystals (in the solid state) that were grown by using solvent-assisted processes. On the other hand, liquid-crystalline mesophases were obtained by molecular self-assembly under a solvent-free crystallization process (in the solid state). Therefore, it is very important to establish correlation between the single crystal X-ray structures with those crystal lattices generated in the LC phases. To identify the liquid crystalline crystal lattices, the OPVs were subjected to variable temperature wide-angle powder X-ray diffraction analysis. Variable-temperature wide-angle XRD patterns for OPV-HC-C₁₁ are shown in Figure 4.17a. The sample

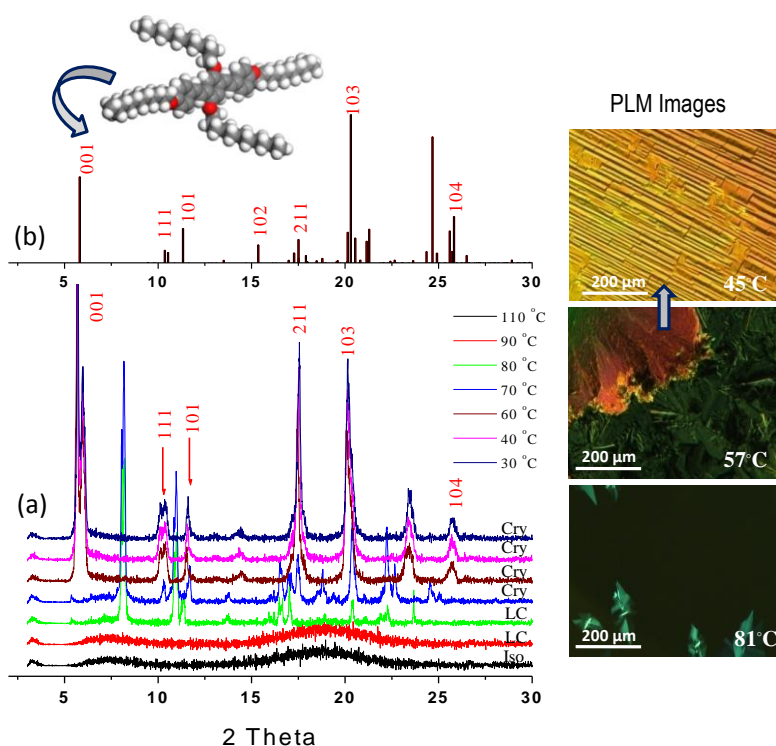


Figure 4.17. a) Variable-temperature powder X-ray diffraction patterns of OPV-HC-C₁₁ (b) Simulated X-ray diffraction pattern for OPV-HC-C₁₁ based on the single-crystal data. c) PLM images of OPV-HC-C₁₁ captured while cooling from isotropic (molten state).

was completely melted at 110 °C. Upon cooling from isotropic melt, in the LC active temperature range (at 90 °C), the sample showed very broad signals which confirmed their liquid crystalline nature. Upon further cooling crystalline peaks

started to appear at 80 °C. These peaks became sharp and intense at 70 °C. The intense peaks were found at $2\theta = 8.2$ ($d=10.76$ Å, two close peaks), 10.2, 11.6, 17.6, 20.1, 23.5 and 25.7°. At much lower temperatures 60–40 °C, the two close peaks at $2\theta = 8.2$ to 5.6° were completely shifted to the low-angle region at $2\theta = 5.6$ ($d = 16.04$ Å) and 5.98 ($d = 15.4$ Å) without affecting other peaks in the region from $2\theta = 10$ –25°. The comparison of PLM images at 81, 57 and 45 °C along with the X-ray diffraction pattern revealed that the shift in the low-angle peaks from $2\theta = 8.2$ to 5.6° were due to higher order the lamellar textures. Powder X-ray diffraction patterns were computationally simulated based on single-crystal structure (for OPV-HC-C₁₁) and plotted along with experimental XRD patterns in Figure 4.17b.⁵⁰⁻⁵¹ The miller index values for each peak in the simulated XRD plot matched very well with that of the variable temperature experimental plots. This confirmed that the crystalline lattices in the single crystal were identical to those present in the LC-phases. The comparison of the PLM images and WXRd analysis suggested that the peaks at $2\theta = 5.6$ ° were corresponding to the 001 fundamental lamellae layer in the lamellar LC textures of OPV-HC-C₁₁ (see PLM picture at 45 °C). This further proved that the formation of the 001 fundamental peak in the XRD pattern of LC texture corresponded to the layer arrangements of OPV-HC-C₁₁ as seen in figure 4.13.

Similarly, OPV-HC-C₁ was also subjected to XRD analysis. The single crystal powder pattern, variable temperature XRD pattern and corresponding PLM images showing nucleation and formation of nematic textures for OPV-HC-C₁ have been shown in figure 4.18. Upon cooling from the isotropic melt corresponding to nematic liquid crystalline window broad signal in the small angle region which confirmed the LC nature of the sample. Upon further cooling, intense crystalline peaks appeared in the wide-angle region corresponding to appearance of crystalline phases. (see Figure 4.18a). The peaks in variable temperature XRD were indexed using simulated powder pattern from its single crystal structure. The planes 001, 01-1, and 02-1 could be exactly assigned in the wide angle X-ray pattern establishing correlation between the single crystal structure and LC mesophase ordering. However, no sharp peaks in the low-angle regions were observed below $2\theta < 10$ ° for

self-organized structures. The variable temperature XRD patterns of other hydrocarbon tail OPVs (OPV-HC-NB, OPV-HC-C₁₁, OPV-HC-C₈) showed similar peak patterns in low angle and wide angle regions suggesting similar lamellar self-organization.

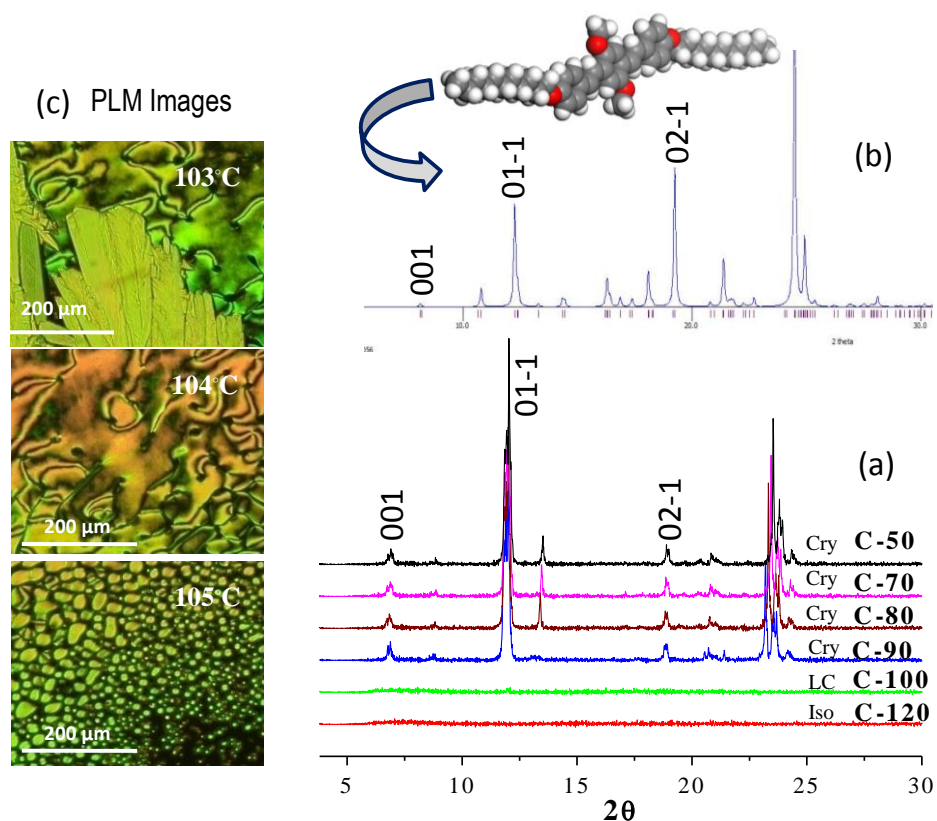


Figure 4.18. a) Variable-temperature powder X-ray diffraction patterns of OPV-HC-C₁. b) Simulated X-ray diffraction pattern for OPV-HC-C₁ based on the single crystal data. c) PLM images of OPV-HC-C₁ captured while cooling from isotropic (molten state).

The perfect matching of single-crystal structural data with the powder XRD proved that the crystal lattices in the LC phases were organized through strong CH/ π interactions while cooling from isotropic melt. Therefore, for the first time, such good correlation between the single-crystal structure and LC mesophase ordering has been established in π -conjugated skeletons. An important feature of all these LC compounds was that the LC morphologies were observed only at high temperatures and therefore these are high temperature liquid crystalline materials.

4.3.5. Photophysical Analysis

Both hydrocarbon and fluorocarbon-tailed OPVs were subjected to photophysical studies in solution (toluene) and in the LC frozen films. The absorbance, excitation and emission spectra of OPVs in solution state have been shown in figure 4.19. The absorption, emission and excitation spectra were found to be almost identical, which suggested that the chromophores did not possess any intermolecular ordering in solution state.

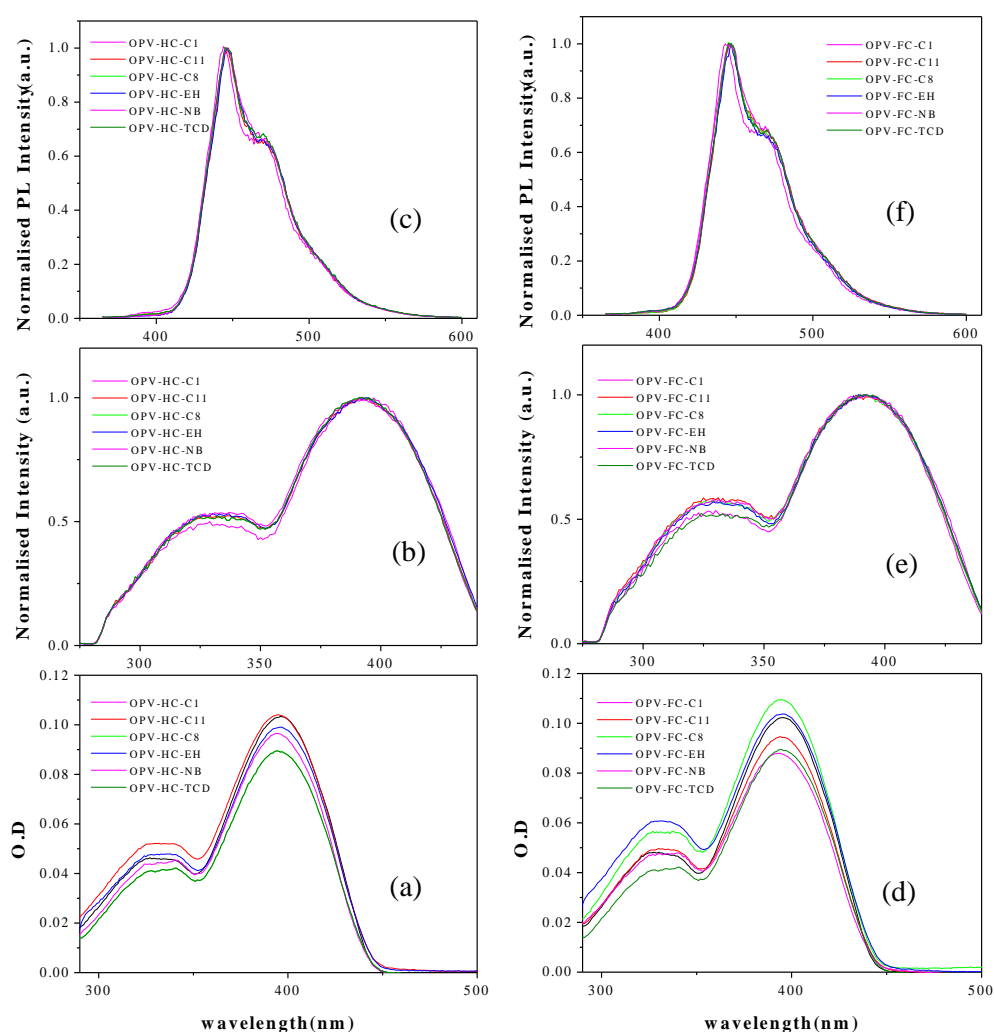


Figure 4.19. Absorption (a), excitation (b) and emission (c) spectra of hydrocarbon tailed OPVs in toluene recorded at 25°C. Absorption (d), excitation (e) and emission (f) spectra of fluorocarbon tailed OPVs in toluene recorded at 25°C.

The quantum yields of the samples were determined by using quinine sulfate as the reference. The quantum yields of the OPV samples lie in the range between 0.40–0.50 and these values matched with earlier reports.^{29-31,52} Table 4.3 summarises the absorption, steady state fluorescence and lifetime data obtained for OPV samples in toluene.

Table 4.3. Photophysical measurements of OPV samples in toluene.

Sample	Absorbance ^a $\lambda_{\max}(\text{nm})$	Emission ^b $\lambda_{\max}(\text{nm})$	Φ^c	τ_1^d	γ^2
OPV-HC-C ₁	390	445	0.41	1.24	1.09
OPV-FC-C ₁	390	443	0.52	1.28	1.04
OPV-HC-NB	395	447	0.57	1.29	1.03
OPV-FC-NB	393	445	0.46	1.31	1.04
OPV-HC- C ₁₁	402	447	0.51	1.29	1.04
OPV-FC- C ₁₁	394	446	0.45	1.31	1.02
OPV-HC- EH	396	447	0.47	1.29	1.09
OPV-FC- EH	388	447	0.45	1.31	1.08
OPV-HC- C ₈	395	446	0.41	1.29	1.09
OPV-FC- C ₈	394	446	0.54	1.31	1.09
OPV-HC- TCD	400	443	0.43	1.27	1.08
OPV-FC- TCD	396	440	0.49	1.30	1.07

(a) Measured in toluene for 0.1 O.D. solution at 25 °C. (b) Measured in toluene for 0.1 O.D. solution at 25 °C, excitation wavelength = 380 nm. (c) Quantum yield was determined using quinine sulfate as standard at 25 °C. (d) decay lifetime obtained by fitting with single exponential decay. The data were collected by exciting with 375 nm laser diode source.

To study the photophysical characteristics of the samples in the solid state, LC films of OPVs were cast on the glass substrates as described for PLM studies. The emission and excitation spectra of a few representative OPVs have been shown in the figure 4.20. The emission spectra of the OPV LC films were recorded by exciting at 380 nm. It was found that the emission spectra of the hydrocarbon tailed OPVs were 20-40 nm red shifted relative to their fluorocarbon counterparts (see figure 4.20a and figure 4.20b). The trend was uniformly observed among all the hydrocarbon tail OPVs. The excitation spectra (see figure 4.20c and figure 4.20d) were found to be very broad as similar to observed in earlier reports,²⁹⁻³¹ but the

onset of the absorbance spectra for hydrocarbon tailed OPVs were found 20-35 nm red shifted as compared to FC-OPVs. The reason for the shift in the emission color was attributed to the difference in the OPV molecular packing.

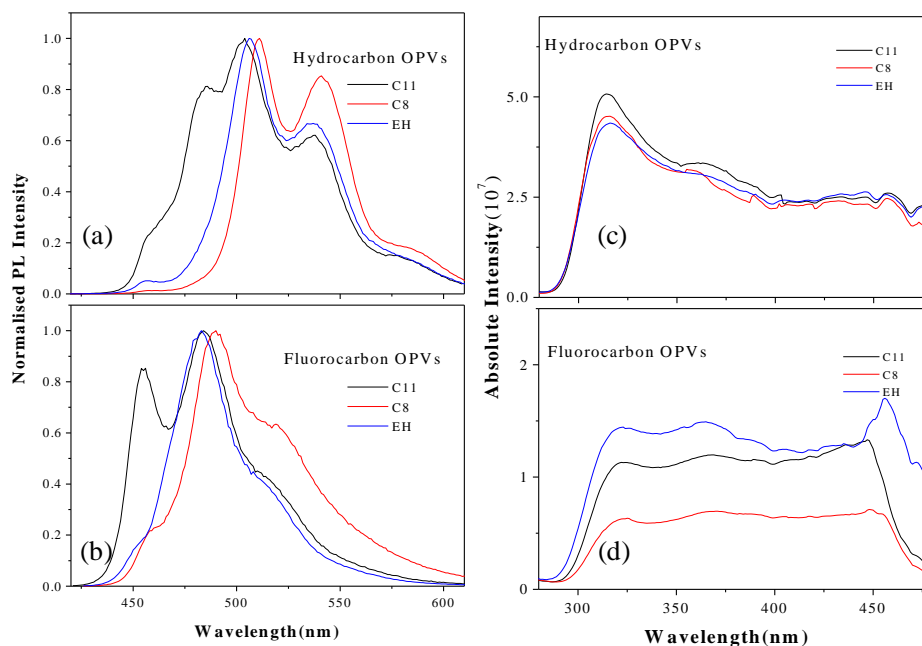


Figure 4.20. Emission of HC (a) and FC (b) OPVs. Excitation spectra of HC (c) and of FC-OPV (d) in LC films.

Based on above analysis, a general model for molecular packing in fluorocarbon and hydrocarbon tail OPVs has been proposed and shown in the figure 4.21.

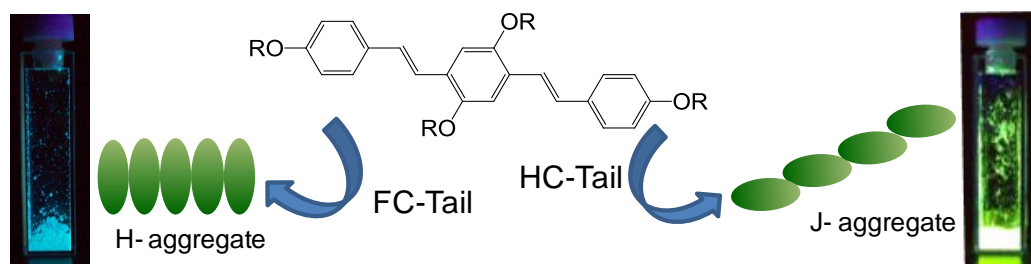


Figure 4.21. Schematic representation of H and J aggregates formed by FC and HC OPVs. (blue and green emission color obtained by exciting the samples with a hand-held UV lamp at 365 nm in FC and HC OPVs, respectively).

All fluorinated OPV molecules exhibited layer-like self-assembly in the smectic LC phase and the molecules were packed parallel as in H-type aggregates. On the other hand, the hydrocarbon-tailed OPV molecules were orientated in slip-through arrangements as in J-type aggregates. The photographs of the OPV samples in vials in figure 4.21 clearly showed the difference in emission color obtained by exciting the samples with a hand-held UV lamp at 365 nm. The blue emission from the fluorocarbon OPVs and yellowish/green from the hydrocarbon OPVs directly provided evidence of the difference in their H- and J-type aggregates in the solid state. As observed in the photophysical properties of OPVs in chapter 3 (figure 3.28), in the present case also among the HCs the variation was negligible. However, a comparison of HC versus FC- OPVs, there is significant difference in H and J aggregates.

The fluorescence intensity decays for FC and HC-OPV molecules in the LC frozen films are shown in Figure 4.22 a–d.

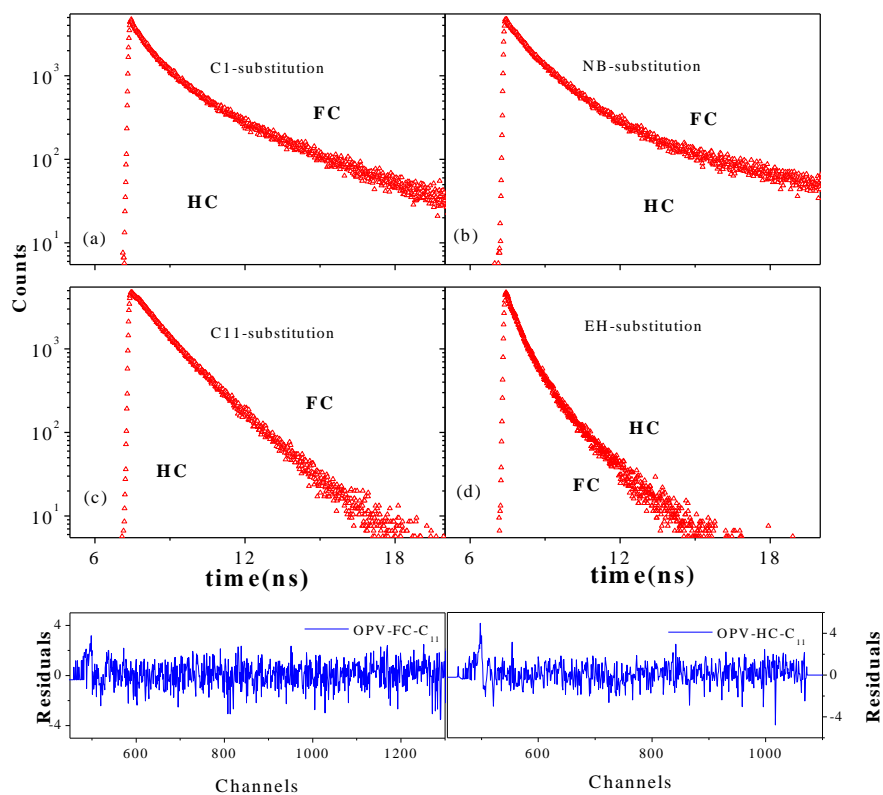


Figure 4.22. Time-resolved fluorescent decay profiles of the OPVs in solid state.

Time-dependent fluorescence decay measurements were carried out by the TCSPC technique by using a 375 nm diode laser as the excitation source and the fluorescence intensity decays were collected at emission maxima. The overall observation of the decay profiles clearly indicated that the fluorocarbon tailed OPVs had more stable emission characteristics relative to those of the hydrocarbon OPVs. The decay profiles were fit into multi-exponential decay models and all the OPVs either fitted to bi or triexponential fits. Table 4.4 summarises the absorption, steady state fluorescence and lifetime data obtained for OPV samples in LC films. The fluorescent decay profiles of OPVs in solution (monomer emission) were found to be almost identical with single exponential decay with lifetimes in the range of 1.2–1.3 ns.^{29-31,52} This further confirmed that OPV molecules do not possess any self-assembly in the solution state.⁵²

Table 4.4. Photophysical measurements of OPV samples in solid films.

Sample	Absorbance ^a λ_{\max} (nm)	Emission ^b λ_{\max} (nm)	τ_1^c	τ_2^c	τ_3^c	γ^2
OPV-HC-C₁	480	485	0.72	1.76	-	1.08
OPV-FC-C₁	460	458	1.20	0.33	4.09	0.99
OPV-HC-NB	512	506	1.13	3.48	-	1.08
OPV-FC-NB	486	470	1.58	0.414	8.87	1.11
OPV-HC-C₁₁	512	504	0.44	1.08	-	1.05
OPV-FC-C₁₁	458	484	0.83	1.68	-	1.01
OPV-HC-EH	508	506	0.44	1.07	-	1.03
OPV-FC-EH	463	483	0.41	1.38	-	1.09
OPV-HC-C₈	510	511	0.17	1.15	-	1.02
OPV-FC-C₈	470	490	0.46	1.27	-	1.08
OPV-FC-TCD	383	503	0.39	1.65	-	1.04
OPV-HC-TCD	381	498	0.40	1.62	-	1.05

(a) Measured in the LC frozen film at 25 °C. Since the spectra are very broad, a tangent is drawn on the on-set of the absorption to determine the values. (b) Measured in the LC frozen film at 25 °C, excitation wavelength = 380 nm. The emission spectra showed more than one peak and the peak maxima were taken corresponding to the first emission peak. (c) Fluorescent decay lifetime obtained by fitting with multi-exponential decay. The data were collected by exciting with 375 nm laser diode source in the LC frozen film.

In the solid state, the τ_1 , τ_2 and τ_3 values for the fluorocarbon OPVs were almost twice compared to that of hydrocarbon OPVs. The fluorocarbon tail OPVs were closely packed in H-aggregate form, and therefore, the possibility for the orientational relaxation is very less in the solid state. On the other hand, the slip through arrangements in the J-aggregates of the hydrocarbon tail possessed a high degree of freedom for molecular orientation in the excited state. As a consequence, the J-aggregated hydrocarbon-tailed OPVs showed fast decay in the time-resolved fluorescence measurements.

In summary, diverse molecular self-assembly of hydrocarbon and fluorocarbon tail OPVs through weak non-covalent forces was established. DSC analysis revealed that hydrocarbon tails OPVs packed better than fluorocarbon OPVs. Fluorocarbon tail OPVs produced identical smectic mesophases, where as, hydrocarbon tailed OPVs produced diverse LC mesophases. Photophysical analysis revealed the presence of H and J- aggregates in FC and HC-OPVs. H-type smectic OPVs showed longer life times as compared to hydrocarbon tailed OPVs.

4.4. Conclusion

This chapter investigated the non covalent forces responsible for diverse mesoscopic self-organization in hydrocarbon and fluorocarbon π -conjugated OPV building blocks. OPVs were designed with appropriate pendants in the aromatic core with hydrocarbon or fluorocarbon tails to self-organize in thermotropic liquid crystalline phases. Thermal analysis revealed that hydrocarbon tails OPVs showed higher enthalpies (ΔH) of the transitions as compared to their fluorocarbon counterparts. PLM Analysis showed that fluorocarbon tail OPVs produced identical SmC LC mesophases irrespective of the pendent groups attached in the middle aromatic core. In contrast, for hydrocarbon tailed OPVs, both pendent geometry and their length in the middle aromatic core determined the molecular self-organization rather than the flexible tail in the longitudinal position.

Variable temperature wide angle XRD patterns of fluorocarbon tail OPVs exhibited regular periodicity in diffraction peaks corresponding to equidistant planes formed in smectic LCs. Small-angle variable-temperature X-ray diffraction analysis showed that the molecules underwent a transition from SmA to a more ordered SmC mesophase. Comparing the SmC and SmA layer spacing, the tilt angle of the molecules in the SmC mesophase was calculated as $\theta = 25.18^\circ$, corresponding to 11% interlayer shrinkage. Powder X-ray diffraction patterns were computationally simulated based on single crystal structure for OPV-HC-C₁₁ and OPV-HC-C₁. When plotted along with experimental XRD patterns, the miller index values for each peak in the simulated XRD plot matched very well with that of the variable temperature experimental plots. This confirmed that the crystalline lattices in the single crystals were identical to those present in the LC mesophases. Photophysical analysis confirmed the formation of H and J aggregates in FC and HC-OPVs, respectively. Time resolved fluorescence decay measurements confirmed longer lifetime for H-type smectic OPVs compared to that of loosely packed one-dimensional nematic hydrocarbon tailed OPVs. In a nut shell, diverse molecular self-assembly of aromatic π -conjugated units via weak secondary forces was established.

4.5. References

1. Kraft, A.; Grimsdale, A.C.; Holmes, A. B. *Angew. Chem. Int. Ed.* **1998**, *37*, 402.
2. Zgierski, M. Z.; Fujiwara, T.; Lim, E. C. *Acc. Chem. Res.* **2010**, *43*, 506.
3. Hoeben, F. J. M.; Jonkheijm, P.; Meijer, E. W.; Schenning, A. P. H. J. *Chem. Rev.* **2005**, *105*, 1491.
4. Skotheim, T. A.; *Handbook of Conducting Polymers*, Marcel Dekker, New York, **1986**.
5. Nalwa, H. S. *Handbook of Advanced Electronic and Photonic Materials and Devices*, Academic Press, **2000**.
6. Akcelrud, L. *Prog. Polym. Sci.* **2003**, *28*, 875.
7. Precup-Blaga, F. S.; Schenning, A. P. H. J.; Meijer, E. W. *Macromolecules* **2003**, *36*, 565-572.
8. Pisula, W.; Tomovic, Z.; Wegner, M.; Graf, R.; Pouderoijen, M. J.; Meijer, E. W.; Schenning, A. P. H. J. *J. Mater. Chem.* **2008**, *18*, 2968-2977.
9. Hulvat, J. F.; Sofos, M.; Tajima, K.; Stupp, S. I. *J. Am. Chem. Soc.* **2005**, *127*, 366-372.
10. Jonkheijm, P.; Schoot, V. D. P.; Schenning, A. P. H. J.; Meijer, E. W. *Science* **2006**, *313*, 80-83.
11. Maddux, T.; Li, W.; Yu, L. *J. Am. Chem. Soc.* **1997**, *119*, 844-845.
12. Strehmel, B.; Sarker, A. M.; Malpert, J. H.; Strehmael, V.; Seifert, H.; Neckers, D. C. *J. Am. Chem. Soc.* **1999**, *121*, 1226-1236.
13. Olsen, B. D.; Jang, S. Y.; Luning, J. M.; Segalman, R. A. *Macromolecules* **2006**, *36*, 4469-4479.
14. Bao, Z.; Amundson, K. R.; Lovinger, A. J. *Macromolecules* **1998**, *31*, 8647-8649.
15. Janssen, P. G. A.; Meeuwenoord, N.; Marel, G. V.; Jabbari-Farouji, S.; Schoot, P. V.; Surin, M.; Tomovic, Z.; Meijer, E. W.; Schenning, A. P. H. J. *Chem. Commun.* **2010**, *46*, 109-111.
16. Schenning, A. P. H. J.; Jonkheijm, P.; Peeters, E.; Meijer, E. W. *J. Am. Chem. Soc.* **2001**, *123*, 409-416.

17. Asha, S. K.; Schenning, A. P. H. J. *Chem. Eur. J.* **2002**, *8*, 3353-3361.
18. Herrikhuyzen, J. V.; Asha, S. K.; Schenning, A. P. H. J.; Meijer, E.W. *J. Am. Chem. Soc.* **2004**, *126*, 10021-10027.
19. Babu, S. S.; Praveen, V. K.; Prasanthkumar, S.; Ajayaghosh, A. *Chem. Eur. J.* **2008**, *14*, 9577 – 9584. (b) Hirai, Y.; Babu, S. S.; Praveen, V. K.; Yasuda, T.; Ajayaghosh, A.; Kato, T. *Adv. Mater.* **2009**, *21*, 4029-4033.
20. Linton, B.; Hamilton, A. D. *Chem. Rev.* **1997**, *97*, 1669-1680.
21. Han, F. S.; Higuchi, M.; Kurth, D. G. *Adv. Mater.* **2007**, *19*, 3928-3931.
22. Stang, P. J.; Seidel, S. R. *Acc. Chem. Res.* **2002**, *35*, 972-983.
23. Knapton, D.; Rowan, S. J.; Weder, C. *Macromolecules* **2006**, *39*, 651-657.
24. Beck, J. B.; Rowan, S. J. *J. Am. Chem. Soc.* **2003**, *125*, 13922-13923.
25. Ghosh, S; Ramakrishnan, S. *Angew. Chem. Int. Ed.* **2005**, *44*, 5441- 5447.
26. Ghosh, S; Ramakrishnan, S. *Angew. Chem. Int. Ed.* **2004**, *43*, 3264- 3268.
27. Lokey, R. S.; Iverson, B. L. *Nature* **1999**, *375*, 303-305.
28. Baby, J.; Asha, S. K. *Chem. Mater.* **2008**, *20*, 169-181.
29. Goel, M.; Jayakannan M. *J. Phys. Chem. B* **2010**, *114*, 12508-12519.
30. Amrutha, S. R.; Jayakannan, M. *J. Phys. Chem. B* **2009**, *113*, 5083-5091.
31. Amrutha, S. R.; Jayakannan, M. *Macromolecules*, **2007**, *40*, 2380-2391.
32. Hird, M. *Chem. Soc. Rev.*, **2007**, *36*, 2070-2095. (b) Berger, R.; Resnati, G.; Metrangolo, P.; Weberd, E.; Hulliger, J. *Chem. Soc. Rev.*, **2011**, *40*, 3496-3508. (c) Babudri, F.; Farinola, G.M.; Naso, F.; Ragni, R. *Chem. Comm.*, **2007**, 1003-1022. (d) Percec, V.; Johansson, G.; Ungar, G.; Zhou, J. *J. Am. Chem. Soc.* **1996**, *118*, 9855-9866.
33. Yamaguchi, A.; Maeda, Y.; Yokoyama, H.; Yoshizawa, A. *Chem. Mater.* **2006**, *18*, 5704-5710.
34. Ainsa, S. H.; Marcos, M.; Barbera, J.; Serrano, J. L. *Angew. Chem. Int. Ed.* **2008**, *47*, 8843-8847.
35. Alameddine, B.; Aebischer, O. F.; Amrein, W.; Donnio, B.; Deschenaux, R.; Guillon, D.; Savary, C.; Scanu, D.; Scheidegger, O.; Jenny, T. A. *Chem. Mater.* **2005**, *17*, 4798-4807.

36. Kohlmeier, A.; Janietz, D. *Chem. Mater.* **2006**, *18*, 1483-1489.
37. Mathevet, F.; Masson, P.; Nicoud, J. F.; Skoulios, A. *J. Am. Chem. Soc.* **2005**, *127*, 9053-9061.
38. Vega, L.; Ortiz, P. D.; Hennrich, G.; Omenat, A.; Tejedor, R. M.; Barbera, J.; Go´mez-Lor, B.; Serrano, J. L. *J. Phys. Chem. B* **2010**, *114*, 4811-4815.
39. Stillinger, F. H.; Wasserman, Z. *J. Phys. Chem.* **1978**, *82*, 929-940.
40. Percec, V.; Glodde, M.; Johansson, G.; Balagurusamy, V. S. K.; Heiney, P. A. *Angew. Chem., Int. Ed.* **2003**, *42*, 4338-4342.
41. Feyter, S. D.; Schryver, F. C. D. *J. Phys. Chem. B*, **2005**, *109*, 4290-4302.
42. Smith, J. A.; DiStasio, R. A. J.; Hannah, N. A.; Winter, R. W.; Weakley, T. J. R.; Gard, G. L.; Rananavare, S. B. *J. Phys. Chem. B*, **2004**, *108*, 19940-19948.
43. Xiaohong, C.; Liu, F.; Zeng, X.; Ungar, G.; Kain, J.; Diele, S.; Prehm, M.; Tschierske, C. *J. Am. Chem. Soc.* **2011**, *133*, 7872-7881.
44. Van Houtem, M. H. C. J.; Benaskar, F.; Fitié, C. F. C.; Rapún, R. M.; Vekemans, J. A. J. M.; Meijer, E. W. *Org. Biomol. Chem.* **2012**, *10*, 5898-5908.
45. Prehm, M.; Liu, F.; Zeng, X.; Ungar, G.; Tschierske, C. *J. Am. Chem. Soc.* **2011**, *133*, 4906-4916.
46. Dierking, I. *Textures of Liquid Crystals*, 2nd ed.; Wiley-VCH Verlag GmbH: Berlin, **2003**.
47. Roberts, J. C.; Kapernaum, N.; Song, Q.; Nonnenmacher, D.; Ayub, K.; Giesselmann, F.; Lemieux, R. P. *J. Am. Chem. Soc.* **2010**, *132*, 364-370.
48. Lagerwall, J. P. F.; Giesselmann, F. *Phys. Rev. E*, **2002**, *66*, 031703/1-031703/11.
49. Krueger, M.; Giesselmann, F. *Phys. Rev. E*, **2005**, *71*, 041704/1-041704/8.
50. Ghosh, S. K.; Kaneko, W.; Kiriya, D.; Ohba, M.; Kitagawa, S. *Angew. Chem.* **2008**, *47*, 8843-8847.
51. Ghosh, S. K.; Zhang, J-P.; Kitagawa, S. *Angew. Chem.* **2007**, *46*, 7965-7968.
52. Babu, S. S.; Praveen, V. K.; Prasanthkumar, S.; Ajayaghosh, A. *Chem. Eur. J.* **2008**, *14*, 9577-9584.

Chapter 5

*Donor-acceptor Assemblies of Segmented OPV
Polymers and Perylenebisimides*

Chapter 5

Donor-acceptor Assemblies of Segmented OPV Polymers and Perylenebisimides

The effect of chemical structure and polymer chain topology on donor-acceptor self-organization of segmented OPV polymers and perylenebisimide chromophore was investigated. A series of OPV segmented polymers with identical OPV optical chromophores, but, different alkyl chain segments (Poly-n, n = 4, 8, and 12) was synthesised. Poly-0 (without any alkyl segment) was synthesised as m-PPV utilizing the 1,3 linkages by introduction of m-linkages along the polymer back bone. The design strategy was adopted in such a way so that all the polymers had almost identical energy levels but differed in their topology. Differential scanning calorimetry was done to understand the difference in thermal properties from small oligomers to polymers. OPVs exhibited strong tendency to self-assemble in to highly order crystalline domains whereas the polymers were found amorphous. Photophysical analysis was done to understand the effect of chemical structure and chain topology of polymer on its aggregation properties. Photophysical analysis revealed that segmented polymers were superior to rigid polymers and OPVs in forming strong inter-molecular aggregates in solution state. Polymers were found to form D-A arrays with electron deficient perylene bisimide based chromophore. The chemical structure and the topology of the polymer backbone determined the stability and type of self-assembly in these donor-acceptor arrays. The composition (donor to acceptor ratio), stability and association constants of D-A complexes were determined by Molar ratio method. Segmented polymer formed extended D-A arrays in which the chains folded in stacked fashion to accommodate acceptor perylene units in 3: 2 (donor: acceptor) ratio. On the other hand, the rigid polymer was found to form only weak 1:1 complexes. The stability constants revealed that the donor and the acceptor complexes formed by segmented polymer were ten times more stable than their rigid counterparts. Hence, the role of chemical structure and topology of polymer chains on donor-acceptor self-assembly was established.

5. 1. Introduction

Supramolecular ordering of donor (D) and acceptor (A) molecules into well-defined architectures was first used in the field of crystal engineering for fundamental studies at molecular level.¹ Crystal engineers were among the first to study the charge transfer in ordered D-A mixtures. Following the experimental observation of charge transfer complexes, a large number of aromatic complexes were studied for understanding the arrangement of donor and acceptor molecules in small aromatic and polymeric systems. A few very good examples of donor-acceptor systems²⁻⁹ based on small organic molecules and polymers have been shown in the figure 5.1.

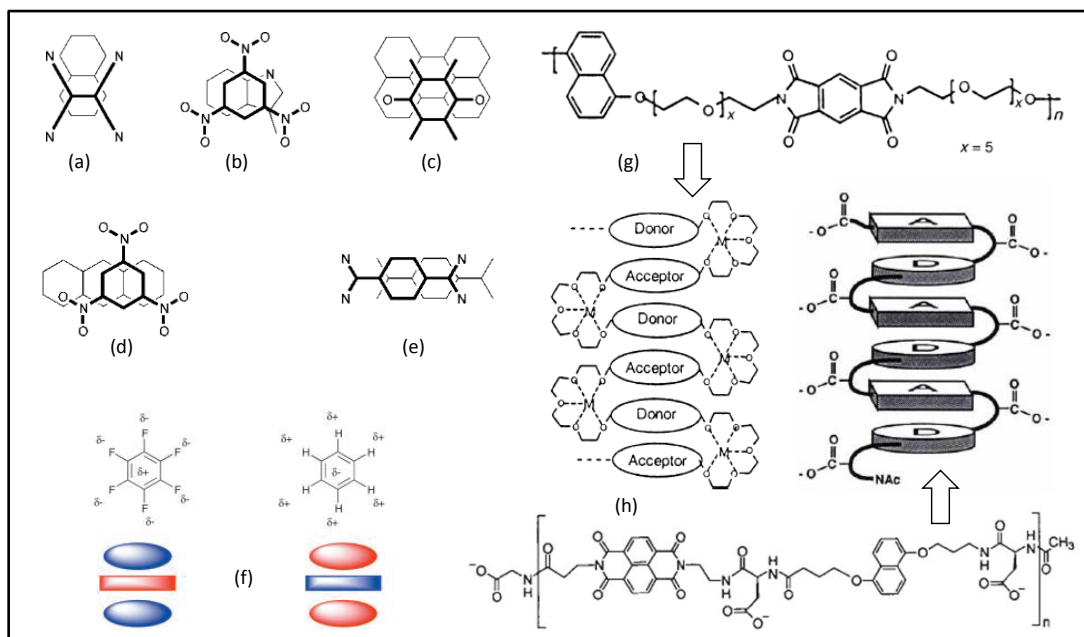


Figure 5.1: Donor-acceptor self-assembly in small organic molecules and polymers. (Adopted from Hunter et al. *J. Chem. Soc. Perkin Trans.* **2001**, 2, 651-669; Ghosh et al. *Angew. Chem. Int. Ed.* **2004**, 43, 3264-3268; Lokey et al. *Nature* **1995**, 375, 303-305).

A common feature of all the small molecule based donor-acceptor systems was that electron cloud of one molecule (donor) was approximately centred over the edges of the second molecule² (acceptor) as shown in figure 5.1a-e. Benzene (D) and

hexafluorobenzene (A)¹⁰ were found to arrange in a cofacial manner with alternating donor and acceptor units maximising electrostatic interactions (see figure 5.1f). Ghosh et al.³ designed and synthesized segmented donor-acceptor polyimides (5g) which folded via weak intrachain interactions leading to stacking of aromatic donor and acceptor segments. Iverson and co-workers demonstrated folding in **5h** by intrachain aromatic donor-acceptor charge-transfer interactions. The system consisted of electron acceptor (naphthalene-1,8 : 4,5-tetracarboxylic diimide) and electron donor (1,5-dialkoxy naphthalene) units with alternating arrangement of D-A groups.⁴

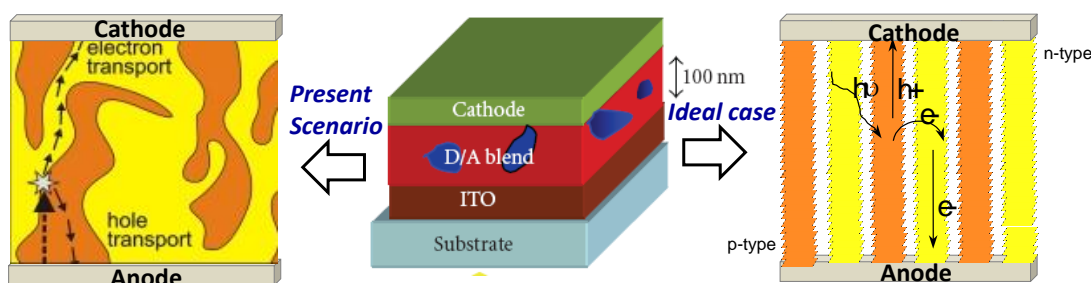


Figure 5.2: General device set up of a solar cell and arrangement of donor and acceptor layers in films.

With the introduction of π -conjugated systems in electronic devices,¹¹⁻¹⁶ π -conjugated D-A arrays have become one of the most important components in optoelectronic devices such as solar cells.¹⁷⁻²³ An organic solar cell consists of an electro donating p-type molecule and electron accepting n-type molecule. In a solar cell, light induced electron-hole generation, separation and migration of charges leads to conversion of light to electrical energy (see figure 5.2).²⁴ The devices consisting of molecular or polymeric organic compounds as active parts exhibited very low efficiencies due to random arrangement of donor and acceptor molecules. This haphazard arrangement led to recombination, before charges can reach their respective electrodes. An ideal case would require a perfectly aligned donor and acceptor layer where the charges can hop effectively leading to better charge

transport. Therefore, creating well-ordered D-A assemblies exhibiting energy and electron transfer has become extremely important for efficient organic solar cells.

Important examples of hole conducting donor-type semiconducting polymers are (i) derivatives of phenylene vinylene backbones such as poly[2-methoxy-5-(3,7-dimethyloctyloxy)-1,4-phenylenevinylene] (MDMOPPV), (ii) derivatives of thiophene chains such as poly(3-hexyl thiophene) (P3HT), and (iii) derivatives of fluorene backbones such as (poly(9,9'-dioctyl fluorene-*co*-bis-*N,N'*-(4-butylphenyl)-1,4-phenylenediamine)(PFB). In addition to semiconducting polymers, small oligomers such as phthalocyanine, pentacene, α -sexithiophene etc. have also been used successfully for solar cell devices. Buckminster fullerene (C_{60}) and its derivative PCBM (1-(3-methoxy carbonyl)propyl-1-phenyl[6,6] C_{61}) are among the most commonly used n-type semiconducting materials. Buckminster fullerene has limited solubility and, therefore, PCBM, a soluble derivative of C_{60} has been widely used.²⁵ Among the other n-type acceptors, perylene and its derivatives are becoming increasingly popular.

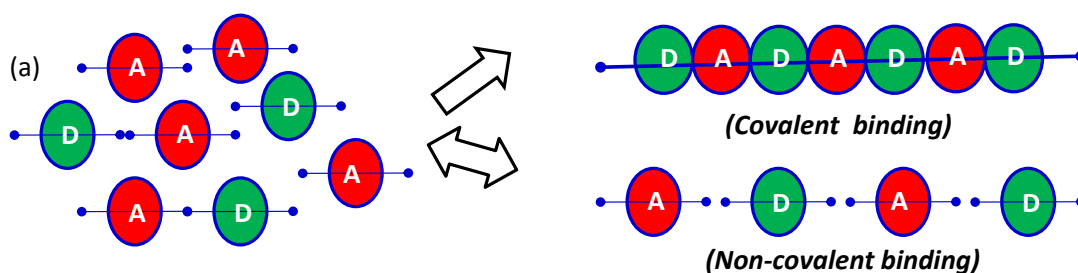


Figure 5.3. Schematic representation of covalently or non-covalently linked donor-acceptor systems.

Various methodologies have been employed to obtain functional donor-acceptor architectures in π -conjugated systems. The donor and the acceptor groups can be either connected covalently or non-covalently using weak non-covalent forces as shown in the figure 5.3. The most commonly used strategy is to covalently connect donor and acceptor units into either oligomers or polymers.²⁶⁻²⁸ For example, perylene bisimide has been included into the PPV main chain to form covalently

linked donor-acceptor co-polymer²⁹ as shown in the figure 5.4a. The resulting copolymer was characterized by highly efficient electron-transfer to the perylene moiety. Figure 5.4b shows another example of a covalently linked donor-acceptor polymer with dangling perylene units on a blend of PPV and poly-fluorene.³⁰ Covalently linked donor-acceptor systems have been known to form stable assemblies, but tedious multistep synthesis and rigorous alteration in electro-optical properties of individual donor and acceptor chromophores are some of the issues to be addressed in covalently linked systems.

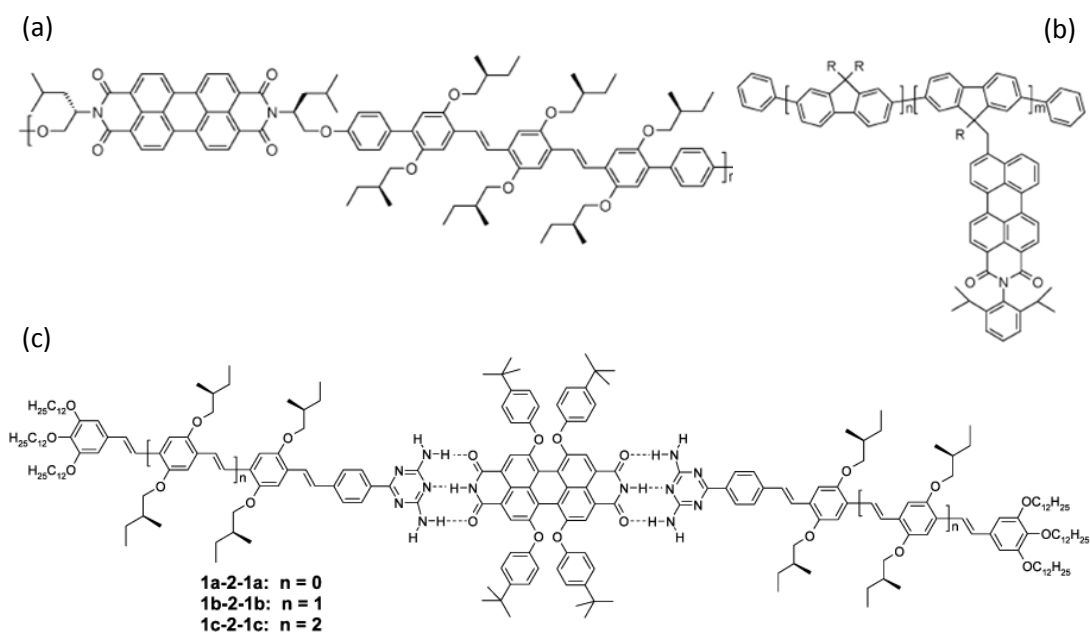


Figure 5.4: Chemical structures of covalently linked (a and b) donor-acceptor copolymers (Adopted from Hoeben et al. *Chem. Rev.* **2005**, 105, 1491-1546). Supramolecular donor-acceptor-donor array of oligo(p-phenylene vinylene) and perylene bisimide units (c) (Wurthner et al. *J. Am. Chem. Soc.* **2004**, 126, 10611-1061).

As an alternative to covalent incorporation of acceptors, physical blending of fluorescent or phosphorescent³¹ dyes into polymer films has gained a lot of importance. Doping PPV-LEDs with small amounts of porphyrin³² or boronic dyes³³ led to sensitized emission from the guest molecules as a consequence of energy

transfer with high efficiencies. Welter and coworkers³⁴ elegantly applied this principle to an electroluminescent device containing a PPV doped with dinuclear ruthenium complexes. However, phase separation in physically blended systems was known to drastically reduce energy transfer efficiency and led to a distortion of the emitted color. The use of non-covalent interactions such as H-bonding,³⁵⁻³⁷ metal coordination³⁸ and electrostatic interactions to assemble donor and acceptor moieties is another important approach for making D-A arrays. Figure 5.4c exhibits an example of a supramolecular D-A-D array consisting of an oligo(p-phenylene vinylene) donor and a perylene bisimide as acceptor. A diaminotriazine hydrogen bonding motif has been utilized for hierarchical self-assembly of donor and acceptor units into chiral fibers.

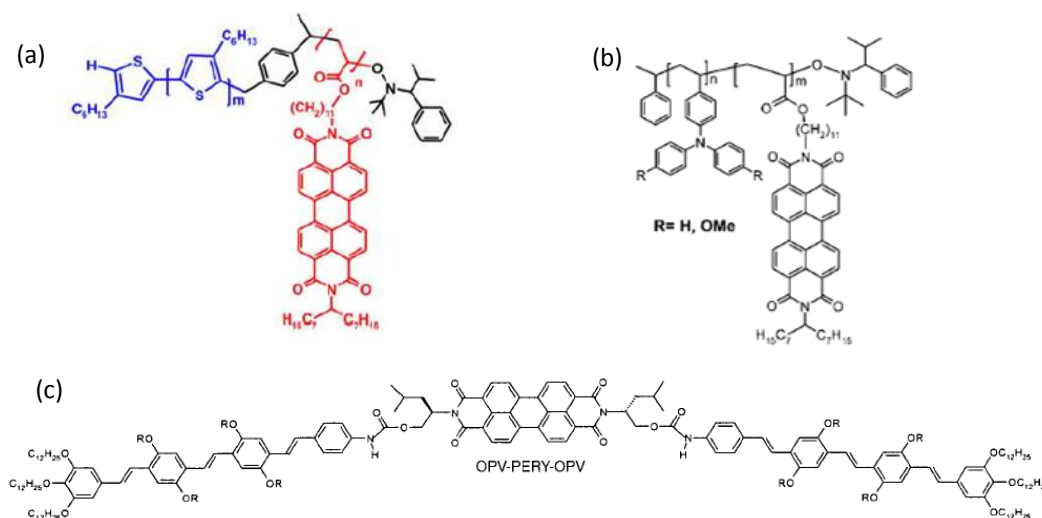


Figure 5.5. Various donor-acceptor polymers and oligomers based on perylenebisimide derivatives as n-type material. (Adopted from (a) Huettner et al. *J. Phys. Chem. B* **2012**, 116, 10070–10078; (b) Lindner et al. *Macromolecules*, **2004**, 37, 8832; (c) Asha et al. *Chem. Eur. J.* **2002**, 8, 3353-3361).

Perylene bisimide derivatives are among the best n-type semiconductors available to date.^{39, 40} Perylene bis imide derivatives exhibit excellent aggregating properties and have been extensively used for making self-assembled π -conjugated donor acceptor systems.⁴¹⁻⁴⁸ For example, figure 5.5a exhibits an example of block copolymer consisting of a poly (3-hexylthiophene) (P3HT) as donor block coupled to

a polymerized perylene bisimide acrylate (PPerAcr) acceptor.⁴⁹ Lindner et al have utilized block copolymers with poly (triphenylamine) as the donor and a highly soluble polymerisable perylene bisimide derivative to give soluble donor-acceptor block copolymers (5.5b) exhibiting all important requirements for photovoltaic applications.⁵⁰ Asha et al. synthesized a donor-acceptor-donor triad molecule (figure 5.5c) with a perylene bisimide derivative as electron acceptor, and an oligo(p-phenylene vinylene) (OPV) derivative as electron donor.⁵¹ From the above discussion it becomes clear that donor acceptor assemblies based on perylene bisimide derivatives are important constituents for molecular electronics such as organic solar cells. Despite significant advances in self-assembly of donor-acceptor systems, processibility in to thin films is a major challenge. Therefore, designing and making new processable donor-acceptor systems are important tasks to be addressed.

In this chapter, donor acceptor self-assemblies of segmented OPV polymers with perylenebisimide chromophore has been investigated. A series of OPV segmented polymers with identical OPV optical chromophores but variable alkyl chain spacers (OPVn, n = 4, 8, and 12) were synthesized. A rigid polymer (m-PPV) was also synthesised by introduction of m-linkages along the polymer back bone as shown in the figure 5.6.

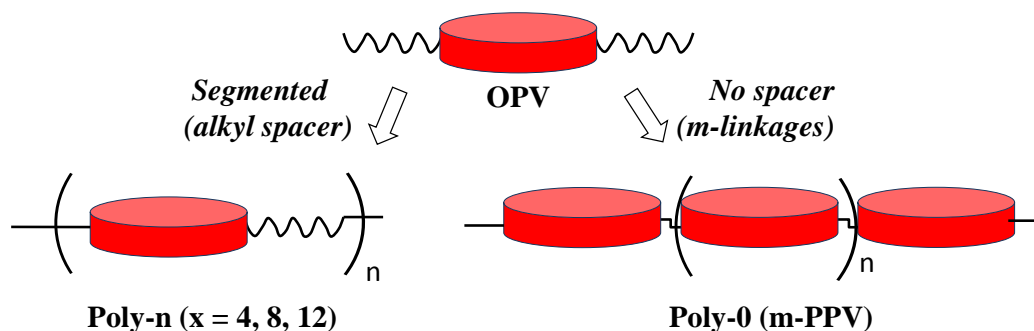


Figure 5.6: Schematic representation of segmented OPV polymers.

The design strategy was adopted in such a way so that all the polymers had almost identical energy levels but differed in their topology. This facilitated the study on effects of chemical structures and polymer chain topology on donor acceptor self-

assembly of OPV and perylenebisimide chromophores. The macroscopic properties of polymers were completely different from their oligomeric OPV analogues. OPVs exhibited strong tendency to self-assemble into highly ordered crystalline domains whereas the polymers were amorphous. Photophysical analysis was done to understand the effect of chemical structure and chain topology of polymer on its aggregation properties. Photophysical analysis revealed that segmented polymers were superior to rigid polymers and OPVs in forming strong inter-molecular aggregates in solution state. The flexible alkyl spacers facilitated segmented polymer (Poly-12) to fold in a helical fashion upon addition of bad solvent methanol. The interdigitated OPV chromophores in polymer chains arrange in J-type fashion.

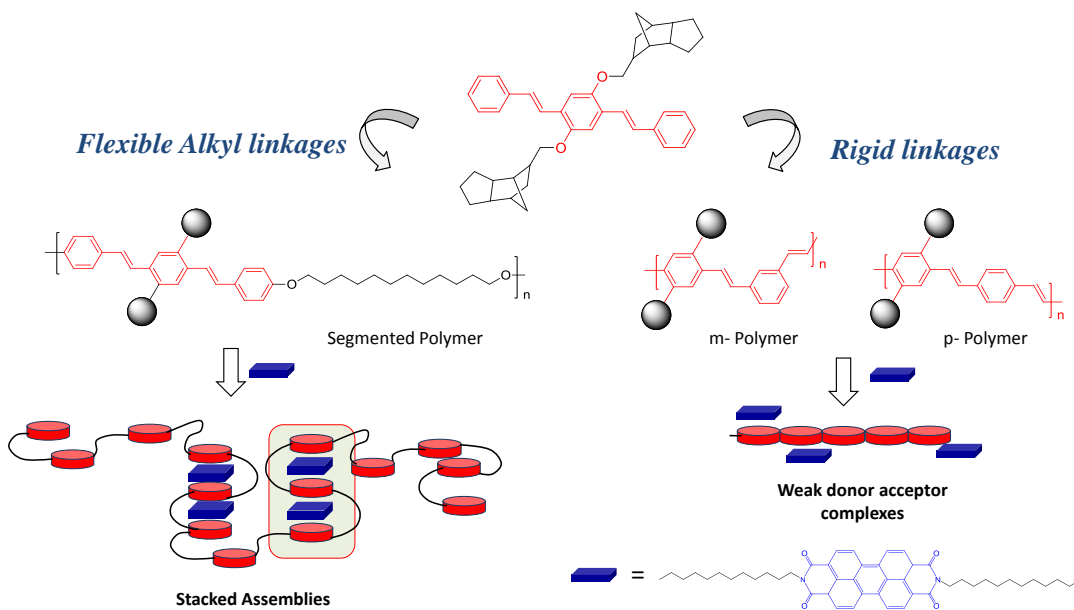


Figure 5.7: Donor-acceptor self-assembly in segmented OPV and rigid polymers.

Polymers were found to form D-A arrays with electron deficient perylene bisimide based chromophore, but the stability and type of self-assembly in these arrays was highly dependent on the chemical structure and the topology of the polymer backbone (see figure 5.7). Molar ratio method was used to determine the composition (donor to acceptor ratio) of D-A complexes and their stability or association constants. Segmented polymer formed extended D-A arrays in which the

chains folded in stacked fashion to accommodate acceptor perylene units in 3:2 (donor:acceptor) ratio. On the other hand, the rigid polymer was found to form only weak 1:1 complexes. The stability constant between the donor and the acceptor molecules in the above D-A arrays was calculated by using Scatchard equation. The stability constants revealed that the donor and the acceptor complexes formed by segmented polymer were ten times more stable than their rigid counterparts. Thus, the role of chemical structure and polymer chain topology on donor-acceptor self-assembly was established using the segmented polymer approach.

5.2. Experimental Methods

5.2.1. Materials: 1, 8-tricyclodecanemethanol was donated by Celanese Chemicals and Co. and was used without further purification. Hydroquinone, p-toulenesulphonylchloride, triethylamine, triethylphosphite, 1, 4-dibrombutane, 1, 8-dibromoctane, 1,12-dibromododecane, 4-hydroxybenzaldehyde, potassium-t-butoxide (1M in THF), isophthaldehyde and terephthaldehyde were purchased from Aldrich Chemicals. HBr in glacial acetic acid, paraformaldehyde, KI, K₂CO₃, and NaOH were purchased locally. Solvents were also purchased locally and were purified by standard procedures. Perylenebisimide molecule used for photophysical analysis was donated by Dr. Asha, S. K. group at NCL. Compound **3a** was synthesized according to our earlier procedures described in chapter-2.

5.2.2. General Procedures: ¹H and ¹³C NMR were recorded using 400 MHz JEOL NMR spectrometer. All NMR spectra were recorded in CDCl₃ containing TMS as internal standard. Infrared spectra were recorded using a Thermo-Scientific Nicolet 6700 FT-IR spectrometer in solid state in KBr in the range of 4000-600 cm⁻¹. The mass of all the precursors was determined by using the Applied Biosystems 4800 PLUS MALDI TOF/TOF analyzer. The purity and molecular weights of polymers were determined using gel permeation chromatography (GPC) which was performed using Viscotek triple detector setup in tetrahydrofuran. TGA analysis was done using Perkin Elmer STA 6000 simultaneous Thermal Analyzer. CV Analysis was done using BASI epsilon cyclic voltameter.

Differential scanning calorimetry (DSC): Differential scanning calorimetry (DSC) measurements were performed on TA Q20 DSC. A pinch of powdered sample was placed in DSC aluminum pan and crimped. The data were recorded at a heating and cooling rate of 10 °C/min. The first heating cycle data were discarded since they possessed prehistory of the sample.

Photophysical Analysis: Absorption spectra were recorded using a Perkin Elmer Lambda 45 UV spectrophotometer. Steady state fluorescence emission and excitation spectra were recorded using a Fluorolog HORIBA JOBIN VYON fluorescence spectrophotometer. For photophysical studies in solid state, homogeneous drop cast films of oligomers and polymers were prepared on quartz plate. Solvent induced photophysical analysis was done by choosing THF /Methanol combination as good and bad solvent mixture. The absorption and emission spectra of samples were recorded at different solvent compositions in THF/MeOH mixture (from 0 to 100% v/v). For concentration dependent photophysical analysis,

absorption and the emission spectra were recorded by keeping concentrations of the donor (1.0×10^{-5} mol L⁻¹) and acceptor (1.0×10^{-5} mol L⁻¹) fixed and varying the THF/MeOH mixture (from 0 to 100% v/v). Fluorescence intensity decays were collected by time correlated single photon counting technique (TCSPC) setup from Horiba Jobin Yvon. 375 nm diode Laser (IBH, UK, NanoLED-375L, with a $\lambda_{\text{max}} = 375$ nm) having a FWHM of 102.3 ps as a sample excitation source. The fluorescence signals were collected in magic angle using a MCP-PMT (Hamamatsu, Japan) detector and the fluorescence decays were collected at emission maxima for all the samples. The quality of fit was judged by fitting parameters such as $\gamma^2 \approx 1$, as well as the visual inspection of the residuals.

5.2.3. Synthesis

The synthesis for tetraethyl-1,4-bis (1,8-tricyclodecanemethyleneoxy)-2, 5-xylenediphosphonate (**3a**) and **OPV-12** has been described in detail in the chapter-2.

Synthesis of 4, 4'-(butane-1,4-diylbis(oxy))dibenzaldehyde(5a): 4-hydroxy benzaldehyde (4.8 g, 0.04 mol), anhydrous KI (6.6 g, 0.04 mol), and powdered anhydrous K₂CO₃ (11.0 g, 0.08 mol) were taken in dry acetone (60.0 mL) and refluxed for 2 h under nitrogen atmosphere. 1, 4-dibromobutane (4.3 g, 0.02 mol) was added dropwise to the above hot reaction mixture. The reaction mixture was further refluxed for 24 h under a nitrogen atmosphere. It was cooled, acetone was removed under vacuum, and the residue was poured into water (100 mL). It was extracted into dichloromethane and washed with NaOH (150 mL, 2% solution) and with brine. The organic layer was dried over anhydrous Na₂SO₄ and condensed to get a pale yellow liquid as product. It was further purified by passing through a silica gel column using ethyl acetate (8% v/v) in hexane as eluent. Yield = (60 %). ¹H NMR (CDCl₃, 400 MHz), δ : 9.90 ppm (s, 2H, **CHO**), 7.85 ppm (d, 4H, **Ar-H**), 7.00 ppm (d, 4H, **Ar-H**), 4.14 ppm (t, 4H, **OCH₂**), 2.05 ppm (m, 4H, **-CH₂CH₂-**). ¹³C-NMR (CDCl₃, 100 MHz) δ : 191.1, 164.2, 132.3, 130.2, 115.1, 68.1, 29.1. FT-IR (KBr, cm⁻¹): 2945, 1693, 1574, 1500, 1470, 1420, 1386, 1310, 1100, 1029, 990, 854, 780, 725, 649, 613 and 508. MALDI-TOF-TOF-MS (MW = 298.33): $m/z = 337.00$ (M+39).

Synthesis of 4, 4'-(octane-1, 8-diylbis(oxy))dibenzaldehyde (5b): 4-hydroxybenzaldehyde (4.8 g, 0.04 mol), anhydrous KI (6.6 g, 0.04 mol), and powdered anhydrous K₂CO₃ (11.0 g, 0.08 mol) were reacted with 1, 8-dibromooctane (5.4 g, 0.02 mol) as described for **5a**. m. p. = 84 to 85°C. Yield = (55 %). ¹H NMR (CDCl₃, 400 MHz), δ : 9.88 ppm (s, 2H, **CHO**), 7.83 ppm (d, 4H, **Ar-H**), 6.98 ppm (d, 4H, **Ar-H**), 4.04 ppm (t, 4H, **OCH₂**), 1.80 ppm (m, 4H, **OCH₂CH₂**) and 1.43 - 1.28 ppm (m, 8H, **aliphatic-H**). ¹³C-NMR (CDCl₃, 100 MHz) δ : 191.12, 164.45,

132.05, 129.79, 114.96, 68.36, 29.06, 25.95. FT-IR (KBr, cm^{-1}): 2946, 1690, 1574, 1500, 1470, 1420, 1387, 1310, 1211, 1156, 1105, 1029, 997, 854, 780, 725, 649, 614 and 510. MALDI-TOF-TOF-MS (MW = 354): m/z = 393.14 (M+39).

Synthesis of 4-4'-(dodecane-1,12-diylbis(oxy))dibenzaldehyde(5c): 4-hydroxy benzaldehyde (4.8 g, 0.04 mol), anhydrous KI (6.6 g, 0.04 mol), and powdered anhydrous K_2CO_3 (11.0 g, 0.08 mol) were reacted with 1,12-dibromododecane (6.5 g, 0.02 mol) as described for **5a**. m. p. = 75 to 76°C. Yield = (31 %). ^1H NMR (CDCl_3 , 400 MHz), δ : 9.86 ppm (s, 2H, **CHO**), 7.82 ppm (d, 4H, **Ar-H**), 6.97 ppm (d, 4H, **Ar-H**), 4.02 ppm (t, 4H, **OCH₂**), 1.79 ppm (m, 4H, **OCH₂CH₂**) and 1.43 - 1.28 ppm (m, 16H, **aliphatic-H**). ^{13}C -NMR (CDCl_3 , 100 MHz), δ : 190.8, 164.2, 131.9, 129.7, 114.7, 68.4, 29.5, 29.3, 29.0 and 25.9. FT-IR (KBr, cm^{-1}): 2943, 1697, 1574, 1509, 1469, 1427, 1392, 1317, 1212, 1161, 1108, 1029, 997, 855, 788, 725, 649, 614 and 515. MALDI-TOF-TOF-MS (MW =410): m/z = 449.217(M+39).

Synthesis of Poly-4: Compound **3a** (0.50 g, 0.71 mmol) and **5a** (0.21 g, 0.71 mmol) were taken in dry THF (30 mL) and kept under ice cold condition. Potassium *tert*-butoxide (3.96 mL, 1M THF solution) was added dropwise to the reaction mixture under nitrogen atmosphere and the stirring was continued at 30 °C for 24 h. The resultant yellow solution was concentrated and poured into a large amount of methanol. The yellow precipitate was redissolved in minimum amount of THF but some of the polymer remained undissolved. It was filtered and the soluble portion was reprecipitated in hexane. Yield = 30 mg. ^1H NMR and ^{13}C NMR could not be recorded due to insoluble nature of the sample. FT-IR (KBr, cm^{-1}): 3035, 2939, 2860, 2365, 1600, 1543, 1508, 1252, 1173, 1065, 1030, 971 and 453.

Synthesis of Poly-8: Compound **3a** (0.47 g, 0.67 mmol) and **5b** (0.24 g, 0.67 mmol) were taken in dry THF (30 mL) and kept under ice cold condition. Potassium *tert*-butoxide (3.96 mL, 1M THF solution) was added dropwise to the reaction mixture under a nitrogen atmosphere and the stirring was continued at 30 °C for 24 h. The resultant yellow solution was concentrated and poured into a large amount of methanol. The yellow precipitate redissolved in minimum amount of THF but some of the polymer remained undissolved. It was filtered and the soluble portion was reprecipitated in hexane. Yield = 24 mg. ^1H NMR (CDCl_3 , 400 MHz), δ : 7.45 ppm (d, 4H, **Ar-H**), 7.29 ppm (d, 2H, **CH=CH**), 7.13 ppm (d, 2H, **CH=CH**), 7.05 ppm (s, 2H, **Ar-H**), 6.89 ppm (d, 4H, **Ar-H**), 3.98 ppm (t, 4H, **OCH₂**), 3.84-3.72 ppm (m, 4H, **OCH₂-TCD**) and 2.3 -1.2 ppm (m, **Cyclic and aliphatic-H**). FT-IR (KBr, cm^{-1}): 3037, 2939, 2859, 2365, 1604, 1543, 1510, 1252, 1173, 1065, 1033, 967 and 461.

Synthesis of Poly-12: Compound **3a** (0.47 g, 0.67 mmol) and **5b** (0.27 g, 0.67 mmol) were taken in dry THF (30 mL) and kept under ice cold condition. Potassium *tert*-butoxide (3.96 mL, 1M THF solution) was added dropwise to the reaction mixture under a nitrogen atmosphere and the stirring was continued at 30 °C for 12 h. The resultant yellow green solution was concentrated and poured into a large amount of methanol. The yellow green precipitate was redissolved in minimum amount of THF and reprecipitated in hexane. Yield= 110 mg. ¹H NMR (CDCl₃, 400 MHz), δ : 7.45 ppm (d, 4H, **Ar-H**), 7.30 ppm (d, 2H, **CH=CH**), 7.12 ppm (d, 2H, **CH=CH**), 7.05 ppm (s, 2H, **Ar-H**), 6.89 ppm (d, 4H, **Ar-H**), 3.98 ppm (t, 4H, **OCH₂**), 3.84-3.72 ppm (m, 4H, **OCH₂.TCD**) and 2.4 -1.3 ppm (m, **Cyclic and aliphatic-H**). ¹³C-NMR (CDCl₃, 100 MHz) δ : 158.7, 150.1, 130.7, 128.4, 127.5, 126.6, 121.5, 114.6, 110.9, 68.0, 43.9, 41.3, 34.7, 30.9, 29.6, 29.4, 29.2, 29.1, 28.0, and 26.5 ppm. FT-IR (KBr, cm⁻¹): 2936, 2859, 1604, 1511, 1472, 1387, 1299, 1252, 1173, 1032, 966, 845 and 815.

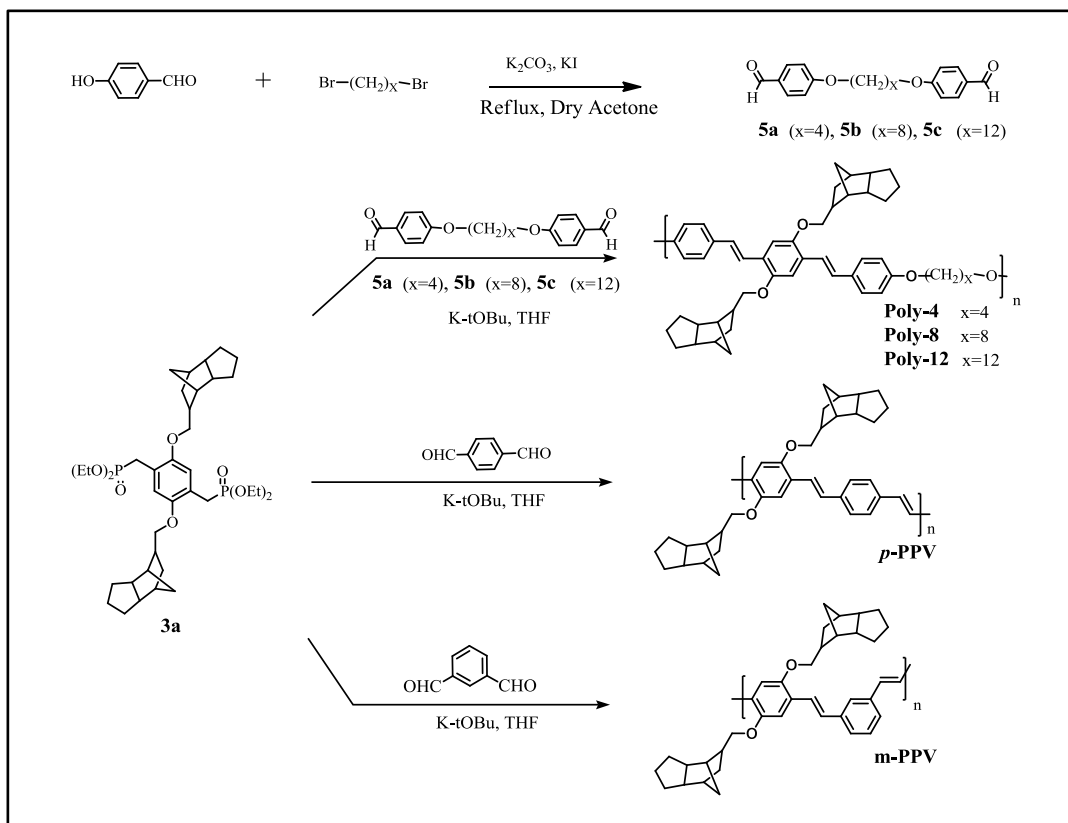
Synthesis of m-PPV: Compound **3a** (0.50 g, 0.71 mmol) and isophthalaldehyde (0.09 g, 0.71 mmol) were taken in dry THF (30 mL) and kept under ice cold condition. Potassium *tert*-butoxide (4.25 mL, 1M THF solution) was added dropwise to the reaction mixture under nitrogen atmosphere and the stirring was continued at 30 °C for 24 h. The resultant yellow green solution was concentrated and poured into a large amount of methanol. The yellow green precipitate was filtered and washed with a large amount of methanol until the filtrate become colorless. The product was redissolved in minimum amount of THF and reprecipitated in hexane. ¹H NMR (CDCl₃, 400 MHz), δ : 7.67-6.81 ppm (m, **Ar-H and vinylic H**), 3.77 ppm (t, 4H, **OCH₂.TCD**) and 2.4 -1.3 ppm (m, 30 H, **Cyclic H**). ¹³C-NMR (CDCl₃, 100 MHz) δ : 151.34, 150.30, 138.4, 129.0, 123.9, 73.5, 67.9, 45.7, 45.2, 44.0, 41.3, 40.3, 34.8, 34.7, 29.1, 27.9, 27.0 and 26.5 ppm. FT-IR (KBr, cm⁻¹): 2944, 2862, 2361, 2340, 1497, 1420, 1198, 1028 and 964.

Synthesis of p-PPV: Compound **3a** (0.50 g, 0.71 mmol) and terephthalaldehyde were taken in dry THF (30 mL) and kept under ice cold condition. Potassium *tert*-butoxide (4.25 mL, 1M THF solution) was added dropwise to the reaction mixture under nitrogen atmosphere and the stirring was continued at 30 °C for 24 h. The resultant yellow green solution was concentrated and poured into a large amount of methanol, filtered and reprecipitated in hexane. Yield = 280 mg. ¹H NMR (CDCl₃, 400 MHz), δ : 7.52-6.73 ppm (m, **Ar-H and vinylic H**), 3.75 ppm (t, 4H, **OCH₂.TCD**) and 2.4 -1.3 ppm (m, 30 H, **Cyclic H**). FT-IR (KBr, cm⁻¹): 2941, 2860, 2364, 2342, 1655, 1561, 1543, 1199, 1049, 1028 and 964.

5. 3. Results and Discussion

5.3.1. Synthesis and structure characterisation of Polymers

The reaction scheme for the synthesis of polymers is depicted in scheme 5.1. 4-hydroxybenzaldehyde was reacted with dibromoalkanes to give a series of segmented dialdehydes (**5a-c**) with different alkyl spacers such as $x = 4, 8,$ and 12 . **5a-c** were reacted with compound (**3a**) via Wittig-Horner reaction to give a series of segmented polymers named as **Poly-4** ($x = 4$), **Poly-8** ($x = 8$), and **Poly-12** ($x = 12$). The detailed synthetic procedures for synthesis of **3a** and oligomers have been explained in chapter-2. **Poly-0** (without any alkyl segment) can be synthesised either as poly-*p*-phenyleneyinylene (p-PPV) having para linkages between the OPV units or as m-PPV utilizing the 1, 3 linkages. **3a** was reacted terephthalaldehyde to give **p-PPV** and isophthalaldehyde to give **m-PPV**. Hereafter, **Poly-0** with *m*- and *p*-linkages are called **m-PPV** and **p-PPV**, respectively.



Scheme 5.1. Synthesis of polymers.

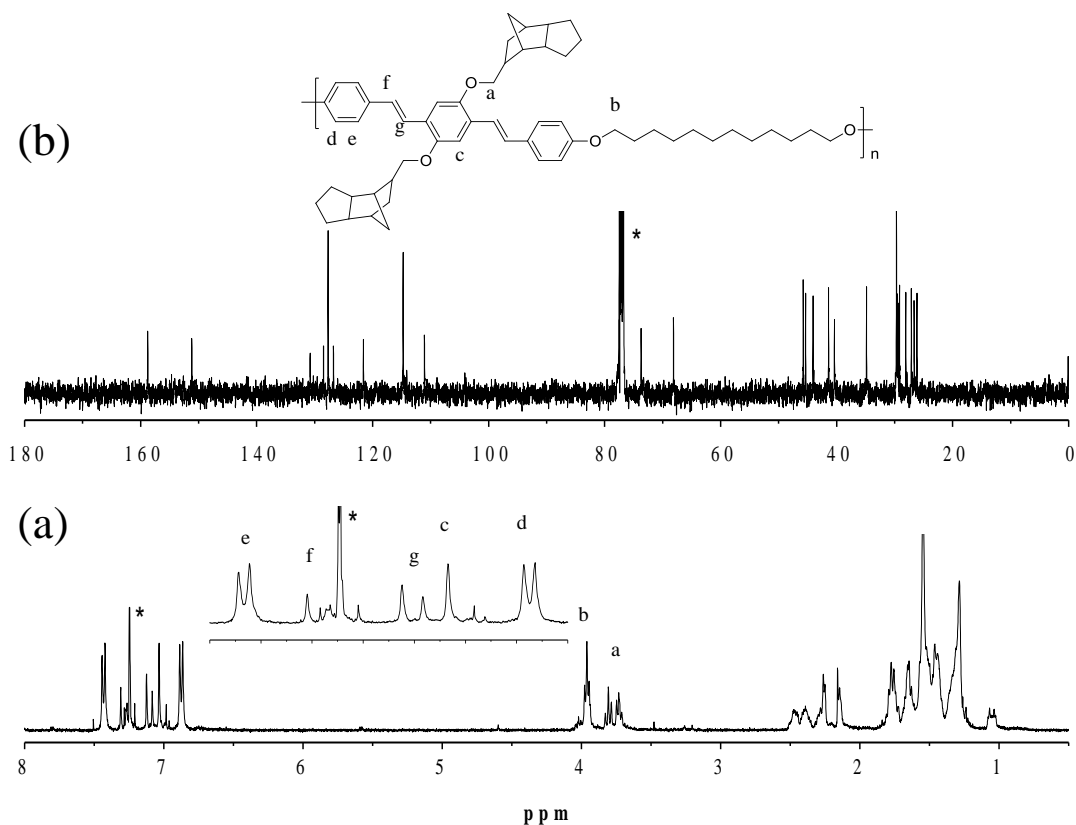


Figure 5.8. (a) $^1\text{H-NMR}$ spectrum of Poly-12 (b) $^{13}\text{C-NMR}$ spectrum of Poly-12.

Figure 5.8a shows the $^1\text{H-NMR}$ spectra of the Poly-12. The inset showed the expanded proton spectrum of the aromatic region. The peaks at 7.45 ppm and 6.89 ppm corresponded to aromatic phenylene protons. The doublets at 7.30 ppm and 7.11 ppm belonged to vinylene protons. The triplet at 3.99 ppm and the multiplets in the range of 3.82-3.75 ppm belonged to Ar-OCH₂-alkyl and Ar-OCH₂-TCD protons, respectively. The peaks for all other protons appeared below 3.75 ppm. Similarly, in figure 5.8b, $^{13}\text{C-NMR}$ spectrum of the Poly-12 exhibited the presence of aromatic peaks at 158.6, 151.0, 128.5, 127.8, 121.6, 114.6, 110.9 ppm, respectively. Ar-OCH₂-TCD and Ar-OCH₂-alkyl peaks appeared around 73 ppm and 68 ppm, respectively. All the other aliphatic carbons belonging to cyclic TCD unit and the linear alkyl chains appeared below 50 ppm. Other oligomers and polymers followed the same peak patterns in their ^1H and ^{13}C -NMR spectra and the detailed analysis have been given in the experimental section.

5.3.2. Molecular weight Determination

The molecular weights of the polymers were determined by gel permeation chromatography (GPC) in tetrahydrofuran using both RI and UV-Vis detectors and polystyrene as standards for calibration. The GPC chromatograms of the polymers have been shown in the figure 5.9. The number and weight average molecular weights (M_n and M_w), polydispersities, number average degree of polymerization (n) and thermal properties of the polymers have been summarized in table 5.1.

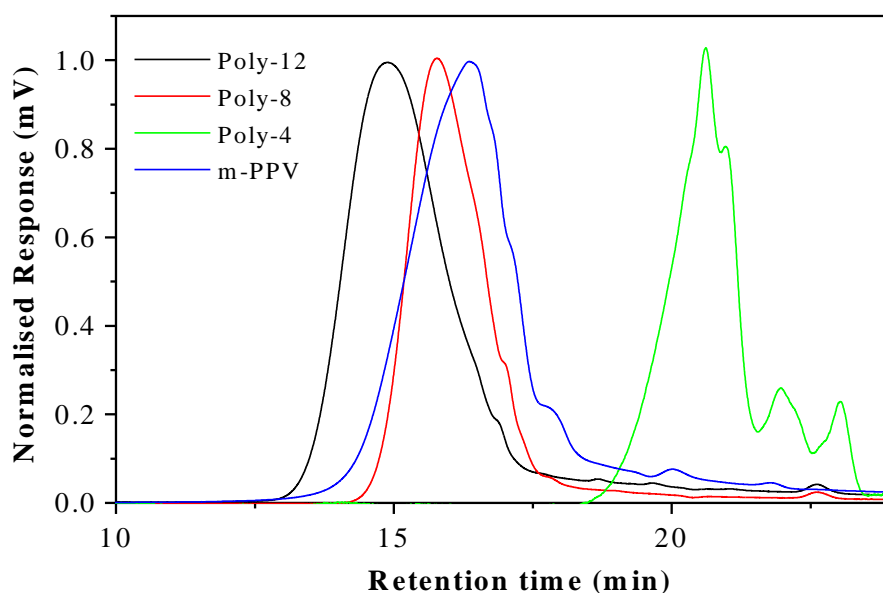


Figure 5.9. GPC Chromatograms of polymers in tetrahydrofuran at 25 °C.

The molecular weight of Poly-12 was found to be much higher ($M_w = 56,000$) compared to that of Poly-8 ($M_w = 16,400$) and m-PPV ($M_w = 15,700$). The reason for the formation of the high molecular weight for Poly-12 was attributed to the high solubility induced by the long dodecyl alkyl segment compared to shorter octyl units. Poly-8 was partially soluble and the data indicated the molecular weight obtained by dissolving the soluble fraction of the polymer. Poly-4 was completely insoluble and the GPC chromatogram exhibited the presence of monomer peaks. p-PPV was insoluble in THF and therefore its molecular weight could not be determined. The low molecular weight of m-PPV was attributed to presence of m-linkages. The incorporation of a 1,3-unit in the conjugated polymeric chains may

inherently limit the formation of high molecular weight polymers due to steric hindrance. A similar trend was earlier observed in the polycondensation of meta-linkage in π -conjugated polymers.⁵²⁻⁵⁸ The photophysical properties of the π -conjugated polymers are known to attain the maxima with 6-8 aryl units.⁵³⁻⁵⁸ In the present system, the average chain length of $n = 12$ carries almost 25 aryl units in m-PPV and Poly-8 chains which is sufficient enough for the studying their photophysical characteristics.

Table 5.1. Molecular weights and thermal properties of the polymers.

Polymer	M_n^a	M_w^a	M_n/M_w	N^b	T_D^c (°C)	T_g^d (°C)
Poly-4 ^e	2500	3900	1.5	4	360	130
Poly-8 ^f	8600	16400	1.9	12	352	126
Poly-12	20700	56000	2.7	25	349	102
m-PPV	6400	15700	2.4	12	347	166

(a) Molecular weights were determined by GPC in THF at 30 °C using polystyrene as standards. (b) Number average degree of polymerization (n) (c) Decomposition temperature at 10% weight loss. (d) Glass transition temperature from DSC analysis. (e) Poly-4 showed extremely low solubility in THF. (f) Poly-8 was only partially soluble in THF.

5.3.3. Thermal Properties

Thermal gravimetric analysis confirmed that all the polymers were stable up to 350°C. The TGA profiles of the polymers are shown in figure 5.10a. The thermal transitions were studied by using differential scanning calorimetry. DSC thermograms of the polymers at 10 °C/min heating and cooling rate have been shown in the figure 5.10b. m-PPV showed highest glass transition temperature at 166°C. A plot of glass transition temperatures against the type of polymer has been shown in the figure 5.10c. As the length of the alkyl segment increased from zero to twelve, the glass transition temperatures gradually decreased from m-PPV (Poly-0) at 166°C to 102 °C in Poly-12. Among the segmented polymers, glass transition temperatures decreased with increasing flexibility/mobility of the polymer chains, for example,

Poly-4 at 130°C, Poly-8 (126 °C) and Poly-12 at 102 °C. A comparison of the DSC thermograms of polymers with their oligomeric analogues (OPV-8 and OPV-12 reported in chapter-2) revealed that OPVs were found liquid crystalline in nature, but corresponding polymers turned out to be amorphous. All the polymers were found amorphous in nature irrespective of the nature of linkage (m-linkage or alkyl segments) between the OPV chromophores. The trend was found to be similar in the cooling cycle. The high T_g values observed for above polymers confirmed high thermal stability of all the polymers.

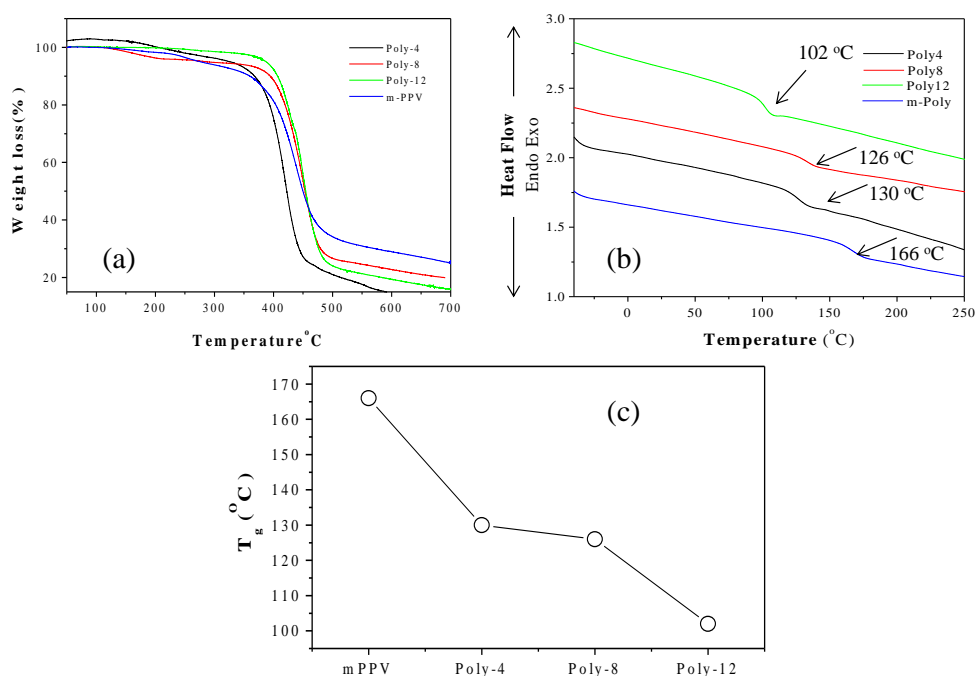


Figure 5.10. (a) TGA profiles of polymers. (b) DSC thermograms of polymers at 10 °C/min in the heating cycle. (c) Plot of T_g versus the type of polymer.

From the above thermal analysis, it can be concluded that the macroscopic properties of polymers differed significantly from their oligomeric analogues. High molecular weight, polydisperse polymer chains were sluggish to crystallize. Polymers formed amorphous films, whereas OPVs had a strong tendency to self-assemble in to highly ordered crystalline domains as evidenced from the single crystals of such systems reported in earlier chapters.

5.3.4. Photophysical Characterization

As seen in the GPC analysis, p-PPV and Poly-4 were completely insoluble and hence these polymers were not taken for further photophysical studies. The photophysical properties (absorption and emission) of the other samples were studied in solution as well as in the solid state (in film).

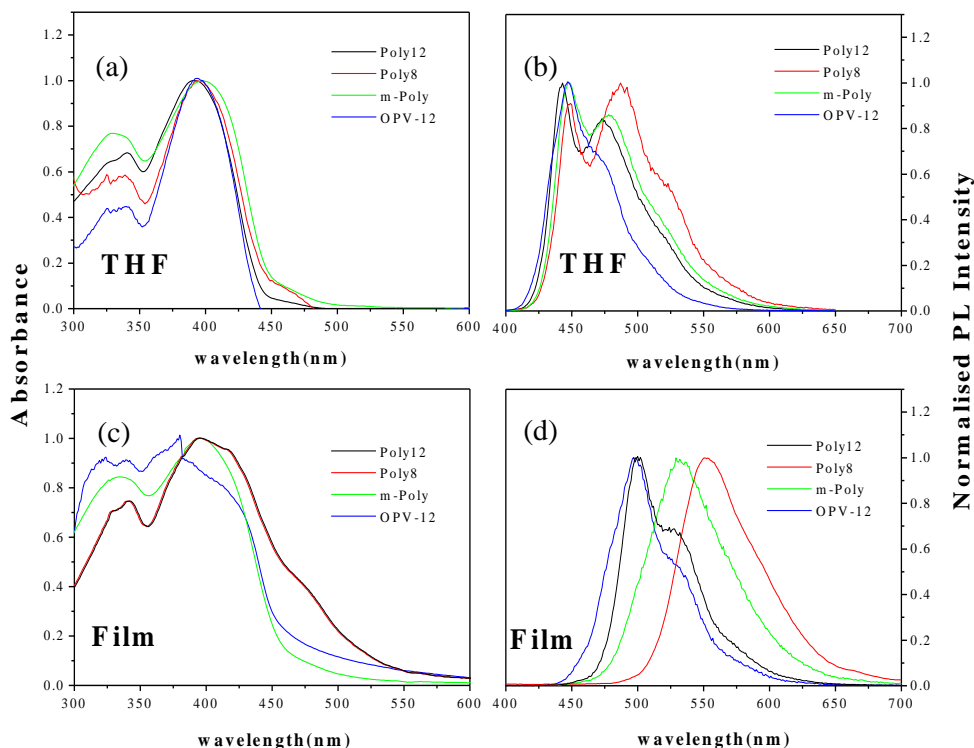


Figure 5.11. Absorption spectra (a) and emission spectra (b) of samples in THF at 25 °C. Absorption spectra (c) and emission spectra (d) of samples in solid films.

The absorption spectra of the samples in the solution and solid state are given in figure 5.11 and the data are summarized in table 5.2. Figure 5.11a exhibited that the absorption spectra for polymers and OPV-12 in solution state were similar with absorption maxima at 393 nm corresponding to OPV unit. This suggested that the chromophores did not possess any intermolecular ordering in solution. In figure 5.11b, the emission maxima (λ_{max}) for OPV-12 and Poly-12 was found at 444 nm. The emission spectrum of Poly-8 was slightly red shifted as compared to other polymers. The absorption and emission spectra of OPV-12, Poly-8, Poly-12 and m-

PPV recorded in thin solid films have been shown in figure 5.11c and 5.11d, respectively. The absorption spectra in solid state were broad as compared to solution state. A comparison of the emission spectra in solution and solid state revealed that OPV-12 and Poly-12 exhibited a strong 50 nm red shift in the emission spectra in solid films as compared to THF. Similarly, Poly-8 and m-PPV exhibited strong red shift in the emission spectra as compared to solution state. The strong red shift in the spectra was attributed to aggregation of molecular chains leading to formation of J-aggregates. An interesting observation in the above analysis revealed that the photophysical properties of the segmented Poly-12 in solution state and solid films were identical to its oligomeric counterpart OPV-12. It is clear from the above photophysical analysis that OPV-12, m-PPV and Poly-12 were completely soluble and had similar optical band gap. Therefore, these polymers were carefully selected to study the influence of topology and polymer back bone on self-assembly properties using photophysical tools.

Table 5.2. Photophysical measurements of OPV and polymer samples in THF and films.

Sample	In THF			In Film	
	$\lambda_{\max}(\text{Abs})^a$ (nm)	$\lambda_{\max}^b(\text{Em})$ (nm)	Φ^c	$\lambda_{\max}(\text{Abs})$ (nm)	$\lambda_{\max}^c(\text{Em})$ (nm)
Poly-12	393	444	0.37	393	498
Poly-8	393	487	0.33	393	550
m-PPV	398	443	0.39	393	530
OPV-12	393	444	0.42	380	498

(a) Measured in THF for 0.1 O.D. solution at 25 °C. (b) Measured in THF for 0.1 O.D. solution at 25 °C, excitation wavelength = 393 nm. (c) Quantum yield was determined using quinine sulfate as standard at 25 °C.

5.3.5. Solvent Induced Molecular Self-assembly

π -Conjugated polymers are important *p*-type materials for opto-electronic applications. The mesoscopic ordering of the polymer chains play a crucial role in

determining the electronic properties of these materials, which, in turn, depends upon the intermolecular chain-chain interactions. Therefore, understanding intermolecular interactions present between individual polymer chains has become a major challenge to understand the self-assembling properties in this class of materials. Several external stimuli such as temperature, pH, and solvent combination have been utilized to bring the polymer chains close to each other.

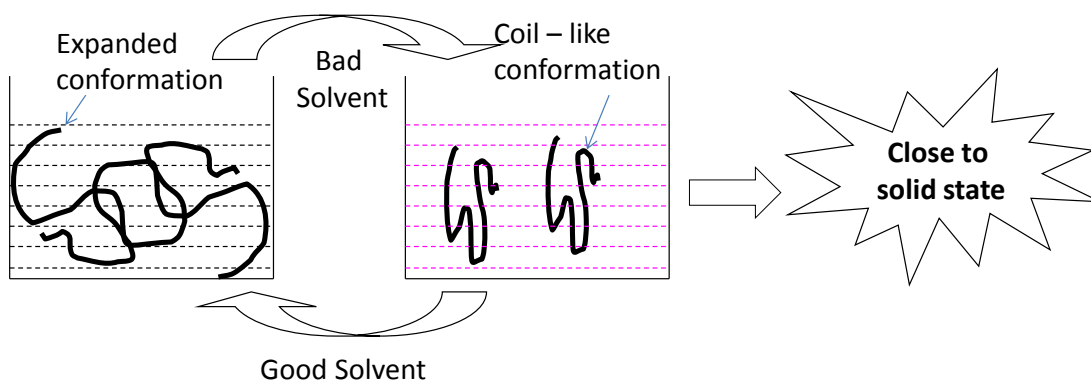


Figure 5.12. Cartoon diagram for polymer chain dynamics in good and bad solvents.

Among all the approaches, solvent induced aggregation is an important approach to study intermolecular chain-chain packing interactions. This approach provides a close estimate of polymer chain interactions that may be present in solid state. A schematic model exhibiting the effect of good and bad solvent conditions on polymer chain dynamics has been shown in the figure 5.12. In this method, isolation or aggregation of polymer chains can be controlled by choosing the appropriate combination of good and bad solvent.⁵⁹ In a good solvent, the polymer chains are molecularly dissolved and exist in open conformations. Upon addition of bad solvent molecular chromophores tend to aggregate due to solvent induced self-organization. For this purpose, THF /Methanol combination was chosen as good and bad solvent mixture and photophysical techniques were employed to study the aggregation properties by exploiting the OPV optical chromophore unit present in the polymers.

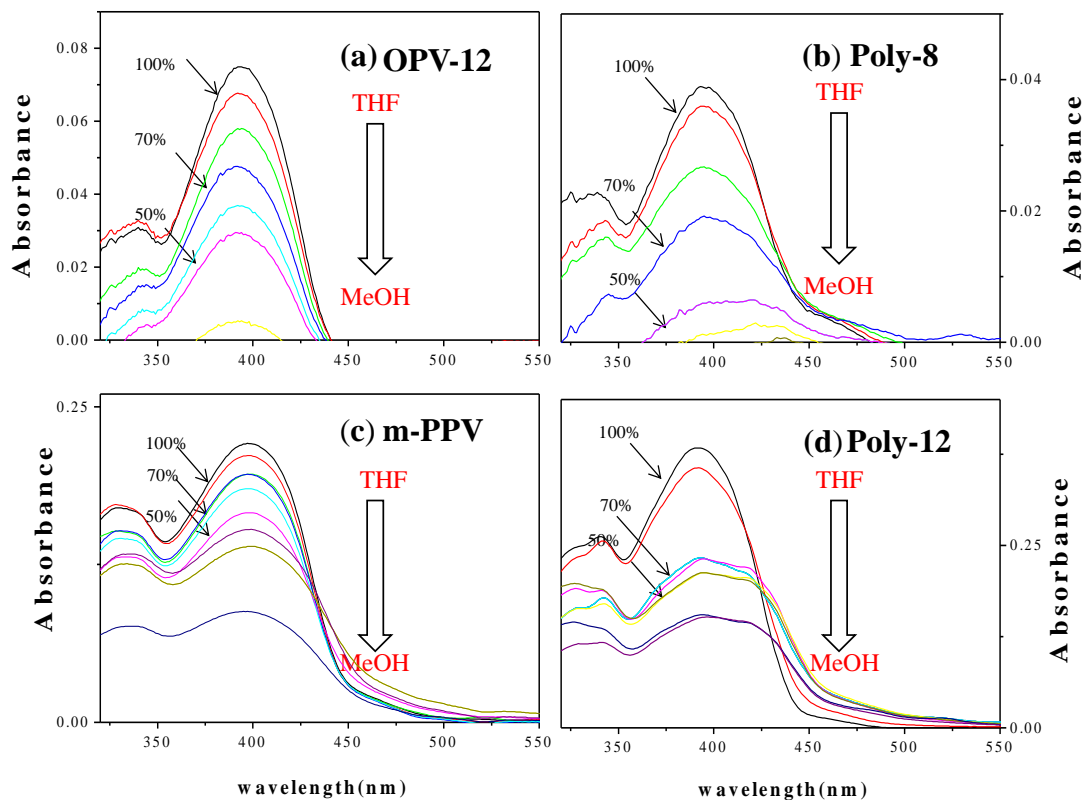


Figure 5.13. Absorption spectra of OPV-12 (a), Poly-8 (b), m-ppv (c) and Poly-12 (d) at different solvent composition in THF/MeOH mixture (from 0 to 100% v/v).

Figure 5.13 shows the absorption spectra of samples at different solvent composition in THF/MeOH mixture (from 0 to 100% v/v). In a good solvent, such as THF, the polymer chains were molecularly dissolved and the absorption maximum (λ_{\max}) of OPV unit was found at 393 nm in all the cases. (See figure 5.13a-d.). As the concentration of the poor solvent increased, the absorption spectra for OPV-12 and m-PPV remained almost unchanged (See figure 5.13a and 5.13c). Poly-8 exhibited slight spectral broadening with increase in the concentration of methanol, but a distinct isosbestic point was not observed (See figure 5.13b). In the case of Poly-12, as the concentration of methanol increased up to 20% (v/v), a red shift and broadening of absorption band occurred, with a distinct vibrational shoulder at 417

nm (see figure 5.13d). The presence of an isosbestic point at 425 nm provided evidence that two different phases (molecularly dissolved polymer chains and aggregated) existed in solution.

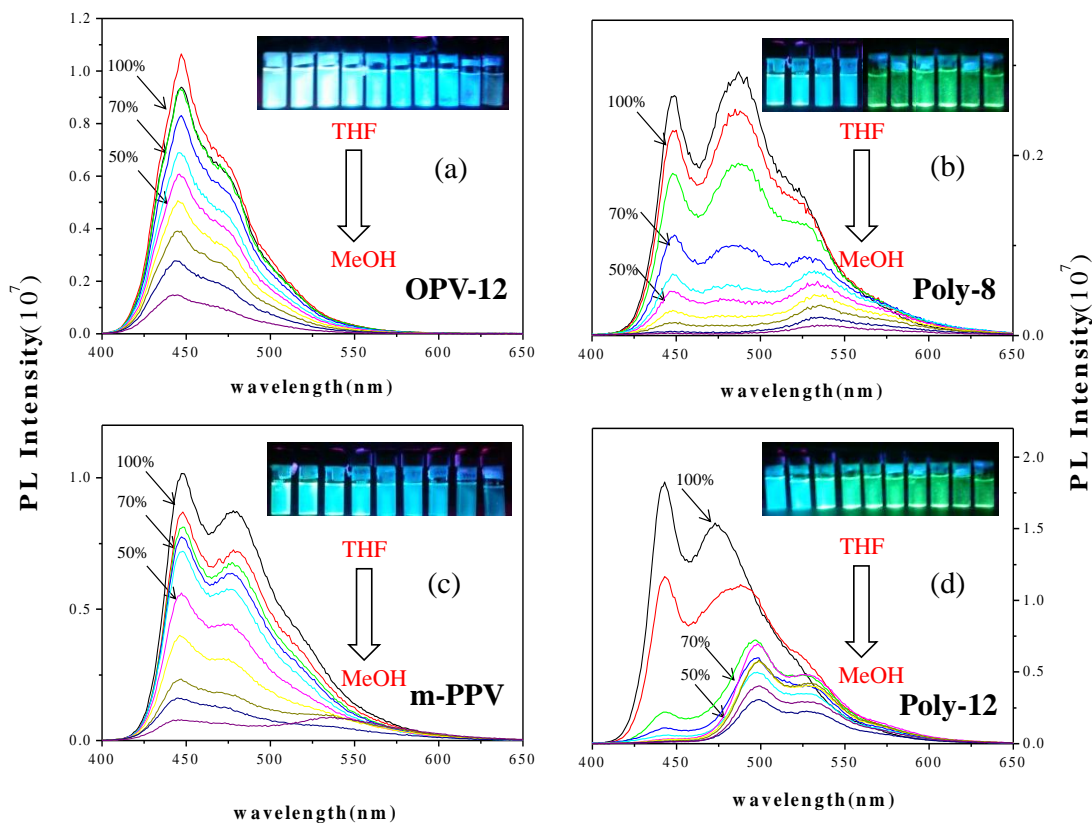


Figure 5.14. Emission spectra of OPV-12 (a) Poly-8 (b), m-ppv (c) and Poly-12 (d) at different solvent composition in THF/MeOH mixture (from 0 to 100% v/v). Photographs of polymer solutions in vials were captured under UV light.

The emission spectra of OPV-12, Poly-8, m-PPV and Poly12 at different solvent composition in THF/MeOH (from 0 to 100% v/v) have been shown in figure 5.14. The emission maximum was found at 444 nm in case of OPV-12, m-PPV and Poly-12 corresponding to λ_{\max} for the OPV chromophore in THF. As the concentration of bad solvent methanol increased, the emission spectra of OPV-12 and m-PPV remained unchanged (see 5.14a and 5.14b). The photographs of solution vials captured on UV irradiation of these samples showed that the color of the polymer solutions remained blue (irrespective of the solvent composition). In

contrast, addition of methanol drastically affected the emission spectra of Poly-8 and Poly-12. At lower concentrations of methanol (up to 10 %), Poly-12 showed emission maximum at 444 nm. The emission spectrum was similar to its corresponding oligophenylenevinylene (OPV-12) molecule suggesting presence of isolated molecular chromophores (OPV segments) in the polymer backbone. As the concentration of methanol increased to 20 %, the emission spectrum exhibited a drastic 55 nm red shift. The emission maximum shifted to 498 nm and a new peak appeared at 530 nm, indicating the presence of aggregated species. The emission maximum of aggregated polymer chains was found at 498 nm and remained unchanged once the transition point was achieved at 20/80 (MeOH/THF (v/v)). At 50 % concentration of methanol, the peak at 444 nm disappeared completely suggested that the OPV segments were fully stacked and there were no free and isolated optical chromophores. The colour of the polymer solution gradually changed from blue to green and the transition point was observed at 20 % MeOH in THF in as seen in vials shown in figure 5.14d. The decrease in PL intensity with increasing concentration of methanol was attributed to increase in quenching due to bad solvent effect. Poly-8 exhibited aggregation similar to Poly-12, but the polymer solution contained both aggregated chains and isolated molecular chains as depicted by mixed emission from aggregated and isolated species at different compositions.

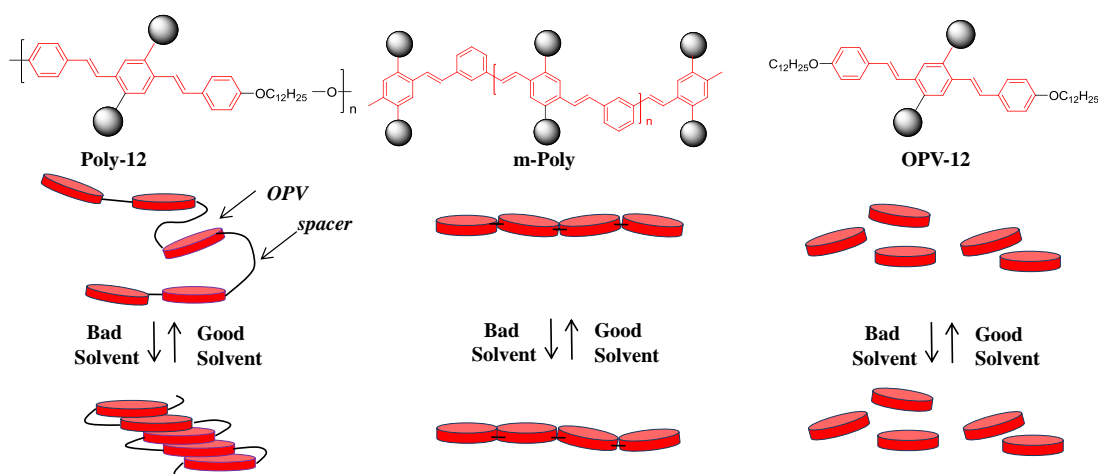


Figure 5.15. Models displaying aggregation properties for Poly-12, m-PPV and OPV-12 in good and bad solvent conditions.

Three important trends can be observed from the above photo physical analysis- (1) the segmented polymers were superior to rigid polymers or their oligomeric counterparts in forming aggregates in solution. (2) The photophysical properties were similar in aggregated and solid state, therefore, by studying the solution state properties, a close idea about the photophysical properties in solid state can be obtained which are important for device applications. (3) The photophysical properties of the segmented Poly-12 in solution state aggregates and solid films were identical to its oligomer (OPV-12). Based on above analysis, a model depicting the self-assembly of OPV-12, m-PPV and Poly-12 has been proposed in the figure 5.15. The flexible alkyl spacers facilitated segmented polymer (Poly-12) to fold in a helical fashion upon addition of bad solvent methanol. The interdigitated OPV chromophores in polymer chains arranged in J-type fashion. This J-type arrangement was also seen in the X-ray single crystal structure of OPV-12. As Poly-12 and its oligomer OPV-12 had identical photophysical properties in aggregated and solid state, X-ray single crystal structure of OPV-12 can be used to predict chain packing in Poly-12. On the other hand, the rigid m-PPV and OPV-12 failed to aggregate even at high concentrations of methanol and existed as isolated chains or chromophores.

5.3.6. Donor- Acceptor Self-assembly

Polymers consisting of OPV chromophores are electron rich p-type molecules and are widely used for constructing donor acceptor arrays with electron deficient molecules.^{41,42} Perylene bisimides are among some of the best n-type semiconductors.³⁹⁻⁴⁰ Polymers containing oligo(*p*-phenylene vinylene) units are electron rich in nature and can form D-A arrays with electron deficient perylene bis imide based chromophores. For this purpose, a custom designed perylenebisimide based chromophore (PERY), was used for D-A self-assembly. The PERY molecule was synthesized using perylenetetracarboxylic acid dianhydride with dodecylamine in the presence of catalytic amounts of imidazole at 110 °C as reported in earlier procedures (free sample was donated from Dr. Asha Syamakumari's group from NCL-Pune).⁴¹

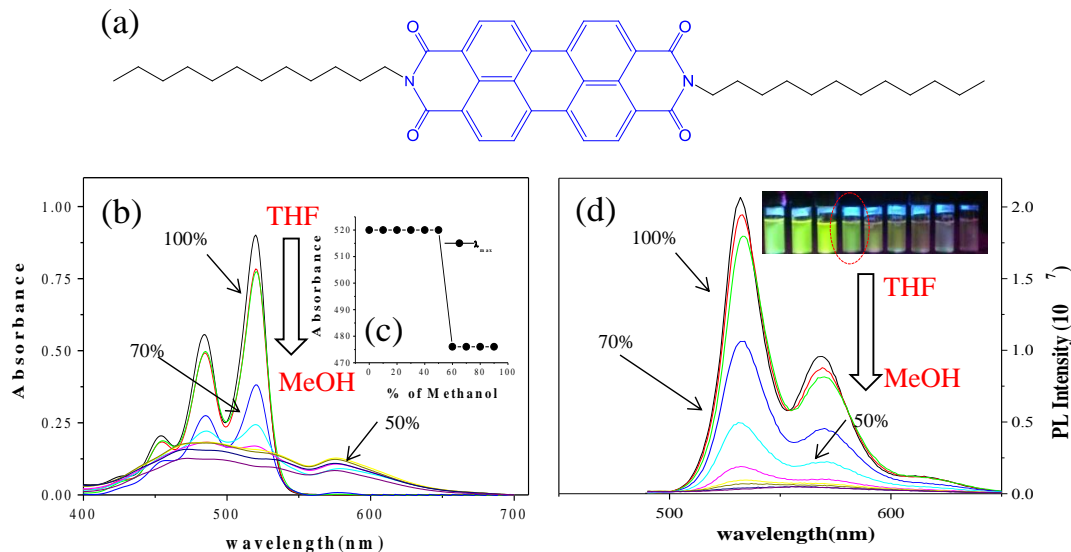


Figure 5.16. Chemical structure of PERY (a), absorption (b) plot of absorption maximum against amount of methanol in the solvent mixture (c) and emission spectra (d) at different solvent composition in THF/MeOH mixture (from 0 to 100% v/v).

The general chemical structure of PERY has been shown in the figure 5.16a. The number of carbon atoms in the terminal alkyl chains was kept equal to the alkyl segment length to promote alkyl chain-chain interactions. Figure 5.16b exhibited the absorption spectrum of PERY at different solvent composition of THF/MeOH (from 0 to 100% v/v). The absorption spectrum showed four well resolved absorption bands corresponding to 0–0 ($S_1 \leftarrow S_0$) at 520 nm, 0–1 ($S_1 \leftarrow S_0$) at 484 nm, 0–2 ($S_1 \leftarrow S_0$) at 456 nm, and 0–3 ($S_1 \leftarrow S_0$) at 425 nm. The areas under each of the absorption peaks were measured and the relative areas were calculated by dividing a particular peak area by total area of all the peaks. The relative areas corresponding to the peaks at 520 nm, 484 nm, 456 nm, and 425 nm were 50.8%, 35.4%, 11.4% and 2.4% respectively. Thus, a good spectral overlap with the emission spectra of the polymers was observed. As the concentration of methanol increased up to 60%, the molecules started aggregating and a new peak appeared at around 575 nm. The inset showed a plot of absorption maximum against amount of methanol in the solvent

mixture. A clear transition from molecularly dissolved PERY chromophores to aggregated state was observed above 40/60(v/v) THF/Methanol. Figure 5.16d shows the emission spectra at different solvent composition in THF/MeOH mixture (from 0 to 100% v/v). Emission maximum was observed at 531 nm corresponding to 0-0 transition. The peak at 569 nm corresponded to 0-1 transition. The above photophysical analysis suggested that PERY can form efficient donor-acceptor self-assemblies with segmented and rigid polymers.

The formation of these D-A arrays can be visualized in terms of the energy transfer or electron transfer that may occur when such donor acceptor molecules are in close vicinity of each other. After photoexcitation of the donor in D-A arrays, self-emission from the donor can be quenched by either a singlet-energy transfer reaction (k_{ET}) to the PERY chromophore or a charge separation (k_{CS}) to a charge-separated state (CSS) in which an electron is transferred from the donor to the acceptor unit. (see figure 5.17). The energy transfer from a singlet-excited donor to an acceptor occurs via dipole-dipole resonance interactions and is known as FRET (fluorescence resonance energy transfer). The Jablonski diagram explaining mechanism of fluorescence energy resonance transfer has been shown in the figure 5.17. The rate (k_{ET} or k_{CS}) at which these processes occur can give an estimate about the stability of these aggregates. Among several factors that determine the rate of energy transfer (k_{ET}), the spectral overlap between the emission spectrum of the donor and the absorption spectrum of the acceptor plays a crucial role.

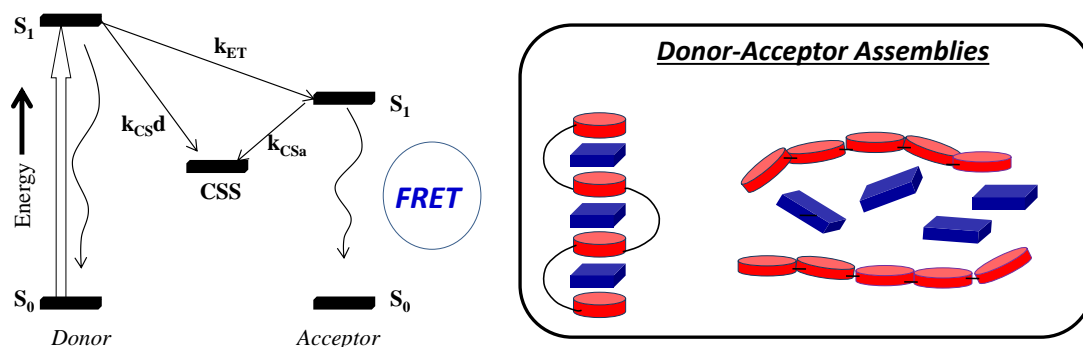


Figure 5.17. Schematic representation of energy levels of donor and acceptor molecules and FRET process.

Figure 5.18 exhibits the absorption and the emission spectra of PERY, Poly-12-PERY and m-PPV-PERY mixtures in 70/30 (THF/CH₃OH) solvent system. The concentration of PERY and polymers was kept fixed at 1.0×10^{-5} mol L⁻¹. The absorption maximum for OPV and perylene were observed at 393 nm and 520 nm, respectively. The transitions belonging to each of the chromophores could be easily distinguished in the absorption spectra of the mixtures. An important observation from the absorption spectra revealed that at 70/30 (THF/CH₃OH), PERY solution remained unaggregated, however, the mixtures showed aggregation peaks from both polymers and perylene. The emission spectra were recorded by exciting at the absorption maximum of donor. PERY did not emit strongly when excited at donor's maximum as seen from the intensity at 575 nm. But in the mixtures, strong emission from perylene at 575 nm was observed, which suggested energy transfer from donor to acceptor.

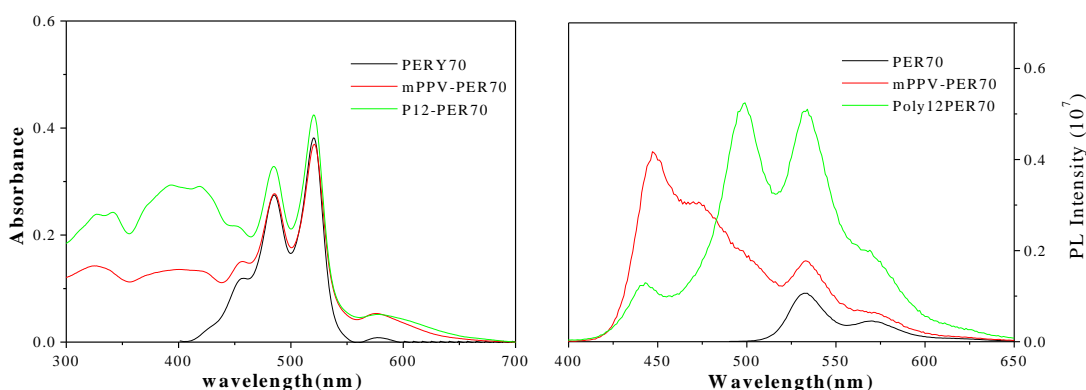


Figure 5.18. Absorption(a) and emission(b) spectra of Poly12-PERY, m-PPV-PERY and PERY in THF/MeOH mixture (70/30 v/v).

Photophysical analysis was done to find out and quantify the D-A arrays formed by these polymer-PERY systems. Figure 5.19a and 5.19b show the absorption and the emission spectra of Poly12-PERY mixtures by keeping concentrations of the donor (1.0×10^{-5} mol L⁻¹) and acceptor (1.0×10^{-5} mol L⁻¹) fixed and varying the THF/MeOH mixture (from 0 to 100% v/v). The absorption spectra

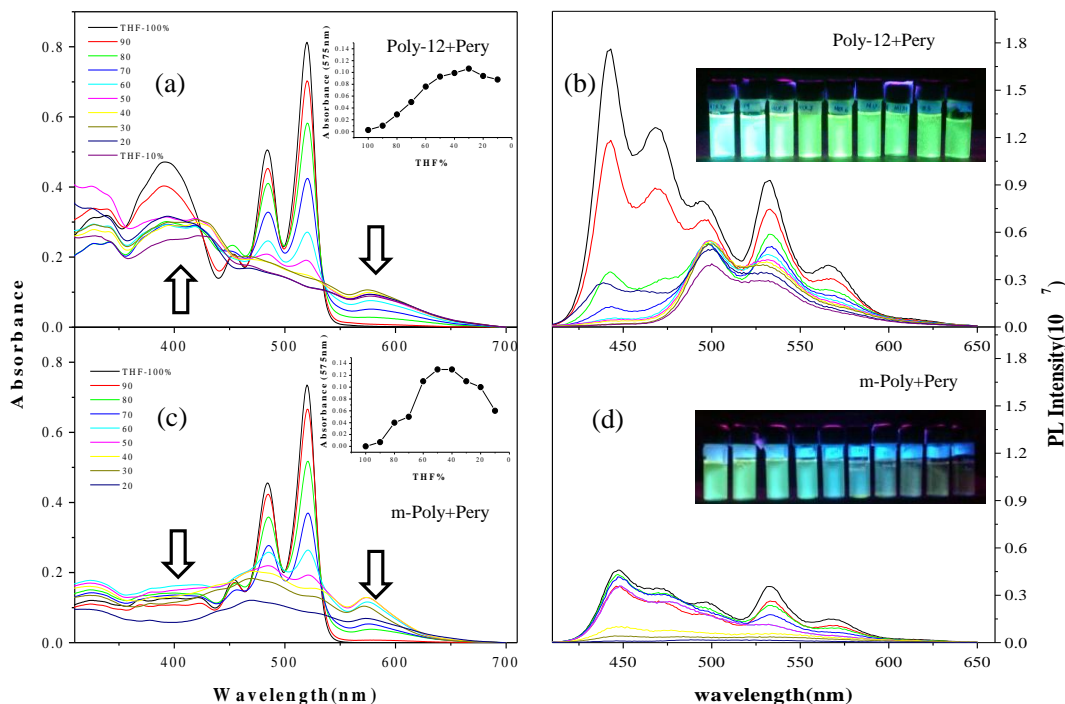


Figure 5.19. (a) Absorption and (b) emission spectra of Poly12-PERY. (c) Absorption and (d) emission spectra of m-PPV-PERY at different solvent composition in THF/MeOH mixture (from 0 to 100% v/v).

of Poly-12-PERY mixture in figure 5.19a exhibited a red shift and broadening of absorption band corresponding to OPV units confirmed aggregation of Poly-12. Similarly, a new peak at 575 nm appeared corresponding to perylene aggregation. Therefore, both Poly-12 and perylene aggregated in solution, but the aggregates were homogeneously dissolved. The inset in figure 5.19a exhibited a plot of absorbance recorded at 575 nm versus the concentration of THF in the solvent mixture. The absorbance intensity from the acceptor increased, even though the concentration of the acceptor was kept constant. This clearly revealed that energy was transferred from Poly-12 to PERY. On the other hand, the absorption spectrum of m-PPV-PERY mixture (see figure 5.19c) failed to show any significant spectral red shift or a clear isosbestic point. The emission for these D-A solutions have been shown in the 5.19b and 5.19d. The emission spectra in figure 5.19b showed that the self-emission from the donor traced at 444 nm underwent large decrease in Poly-12 as compared to m-

PPV. The other important observation was that the D-A mixtures were highly emissive even at higher methanol concentration in case of Poly-12 (see vials). Poly-12 chains prevented π - π stacking in PERY molecules by stabilizing them into D-A arrays, and hence precipitation of individual polymeric chains or perylene molecules was inhibited even on increasing polarity of the solvent. On the other hand, m-PPV-PERY mixtures exhibited large quenching (see photograph in the vials) suggesting precipitation of chromophores.

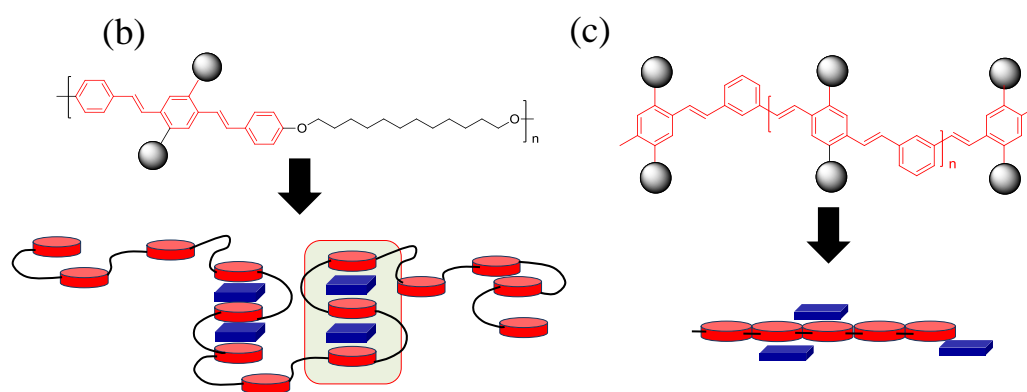


Figure 5.20. Models depicting D-A complexes in Poly-12 and m-PPV.

Based on the above analysis, a model for the formation of donor-acceptor arrays has been proposed in the figure 5.20. Poly-12 formed extended D-A aggregates in which the Poly-12 chains folded in helical fashion to accommodate acceptor units. The aggregates were uniformly dissolved in solution state. However, in the case of m-PPV, precipitation of chromophores resulted in large quenching in emission intensity resulting in weak donor- acceptor complexes scattered along the polymer chain.

5.3.7. Molar Ratio Method

The relative ratio of donor-acceptor units in the D-A arrays was found out by using Molar Ratio method. Detailed concentration dependent photophysical analysis was done, in which the solvent composition was fixed at THF/CH₃OH (70/30 (v/v))

and the concentration of polymer was varied from $1.0 \times 10^{-6} \text{ mol L}^{-1}$ (A) to $1.0 \times 10^{-4} \text{ mol L}^{-1}$ (I), keeping the concentration of perylene constant at $1.0 \times 10^{-5} \text{ mol L}^{-1}$, in all

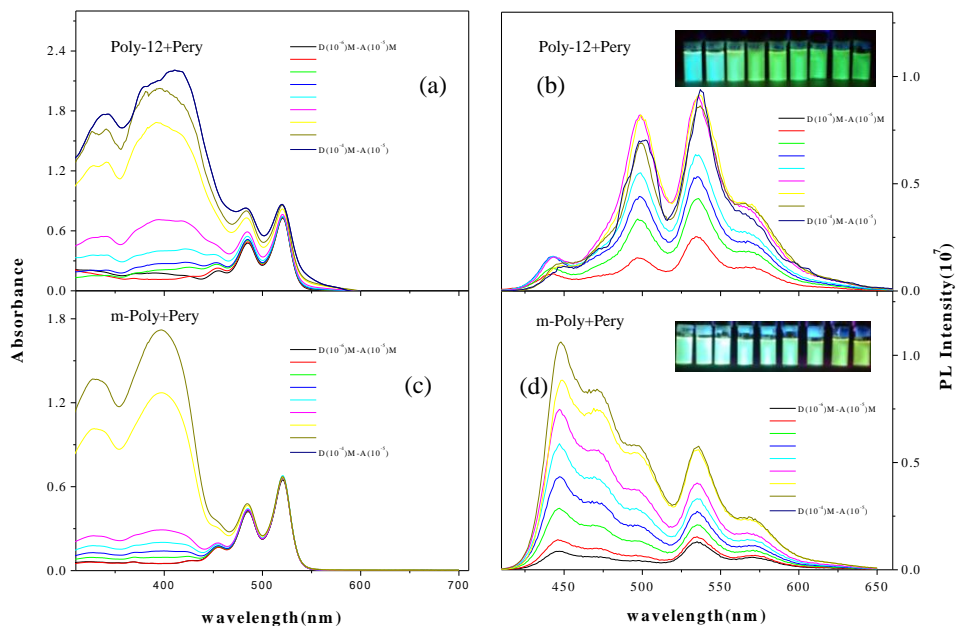


Figure 5.21. Absorption and Emission spectra of Poly12-PERY (a and b). Absorption and emission spectra of m-PPV-PERY mixtures (c and d) at different concentrations of polymer in THF/MeOH mixture (70/30, v/v).

the cases. Figure 5.21a exhibited the absorption spectra of Poly12-PERY mixtures. An intense absorption band was observed at 393nm, which was attributed to the OPV unit present in the polymer. The transitions corresponding to the PERY moiety were located at 520nm corresponding to 0–0 ($S_1 \leftarrow S_0$), with a vibronic shoulder at 486 nm. The transitions belonging to each of the chromophores could be easily distinguished in the absorption spectra and the absorption intensity of Poly-12 increased with increase in the polymer concentration. Figure 5.21b exhibited the emission spectra of these D-A mixtures by exciting at 393 nm to ensure selective excitation of the OPV units. It was found that with increase in the concentration of polymer, the fluorescence intensity at 535 nm, corresponding to 0-0 transition from perylene gradually increased, even though the amount of perylene was kept constant. This indicated that there was partial energy transfer from Poly-12 to PERY which

resulted in increase in emission from acceptor. This energy transfer also confirmed that there was indeed formation of donor-acceptor arrays because of electrostatic interactions between the electron rich donor molecules and the electron deficient acceptor PERY molecules. Figure 5.21c and 5.21d exhibited the absorption and the emission spectra of m-PPV and PERY mixtures under the same conditions. The trend was found to be the same, however the emission intensity from acceptor at 535 nm was significantly lower suggesting that the D-A complexes formed by m-PPV were relatively weak.

The composition (donor to acceptor ratio) in the above D-A complexes was calculated by using Molar Ratio method. The PL intensity at 535 nm of each solution (in figure 5.21b and 5.21d) was measured and the fluorescence intensity from PERY due to energy transfer from polymers was determined using the following equation:

$$I_{ET} = I_{DA} - [I_D + I_A]$$

where, I_{ET} = fluorescence intensity from A due to energy transfer; I_{DA} = total fluorescence intensity from D-A mixture at 535 nm; $I_D = [I_{495} \times \{I_{495}/I_{535}\}]$, theoretical fluorescence intensity from D at 535 nm, I_A = fluorescence intensity from A at 535 nm.

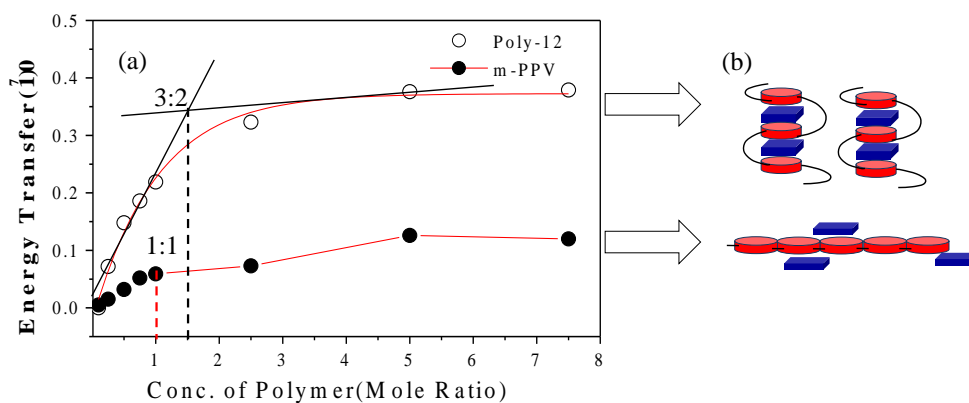


Figure 5.22. (a) Mole Ratio plots for polymers. (b) Models depicting D-A complexes in Poly-12 and m-PPV.

Figure 5.22 exhibits a plot of I_{ET} plotted versus the mole ratio of the polymers. The linear portions of the curves were extrapolated to locate the break point. The break

point in the slope of the curve gave the mole ratio corresponding to the combining ratio of the complex. The combining ratio for Poly-12-PERY and m-PPV- PERY complexes was found to be 3: 2 and 1:1, respectively. From above analysis, it can be concluded that Poly-12 formed extended D-A arrays in which the Poly-12 chains folded in helical fashion to accommodate acceptor units. The model depicting the formation of one such 3:2 complex has been shown in figure 5.22b. On the other hand, m-PPV formed only weak 1:1 complexes scattered along the polymer chains.

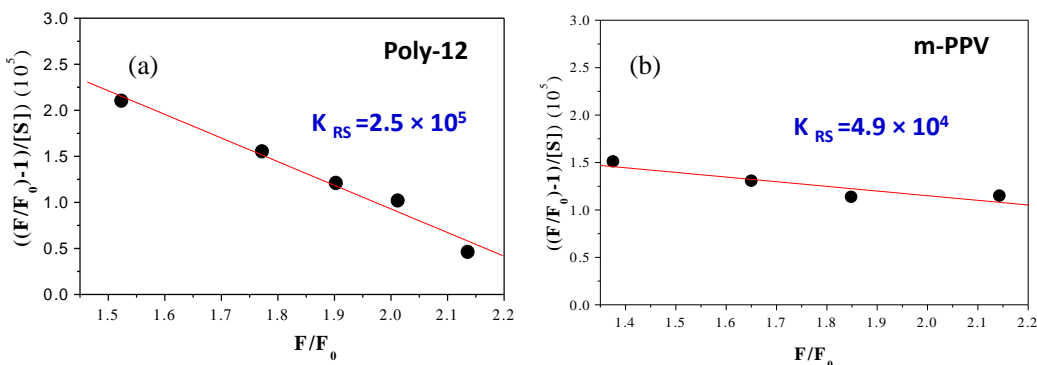


Figure 5.23. Scatchard plots for Poly-12(a) and m-PPV (b) for the determination of stability constants.

To further quantify the formation of these D-A arrays, the stability constant between the donor and the acceptor molecules was calculated by using a rearranged form of Benesi-Hildebrand equation known as the Scatchard equation.⁶⁰ This equation makes use of the fluorescence spectroscopic method for the evaluation of stability constants. According to the Scatchard Equation,

$$(F/F_0)-1/[S] = (k_{RS}/k_s) K_{RS} - K_{RS} (F/F_0),$$

where, F is the total intensity of fluorescence from donor, acceptor and complex; F_0 is the fluorescence intensity when both the complex and the acceptor are fluorescent and K_{RS} is the stability constant. According to this equation, from a linear plot of $(F/F_0)-1/[S]$ against (F/F_0) the stability constant can be calculated as the slope of the each plot. Figure 5.23a and 5.23b showed the Scatchard plots for Poly-12 and m-PPV and the determination of stability constants from the slopes of each plot. The stability constant for Poly12-PERY was found to be 2.5×10^5 , whereas the stability constant for m-PPV-PERY was determined to be 4.9×10^4 . These values suggested

that the D-A complexes formed in the case segmented polymer were ten times more stable as compared to the D-A arrays formed by rigid m-PPV. Above analysis clearly brought out the importance of an appropriate polymer scaffold i.e. the chemical structure, the flexibility and an optimum spacer length interconnecting the electron rich chromophores, that can fold to accommodate the electron deficient perylene bis imide molecules.

5.3.8. TCSPC Analysis

Time-dependent fluorescence decay measurements were carried out by the TCSPC technique by using a 375 nm diode laser as the excitation source. The fluorescence intensity decays were collected at emission maxima for polymer samples as shown in the figure 5.24a and 5.24c.

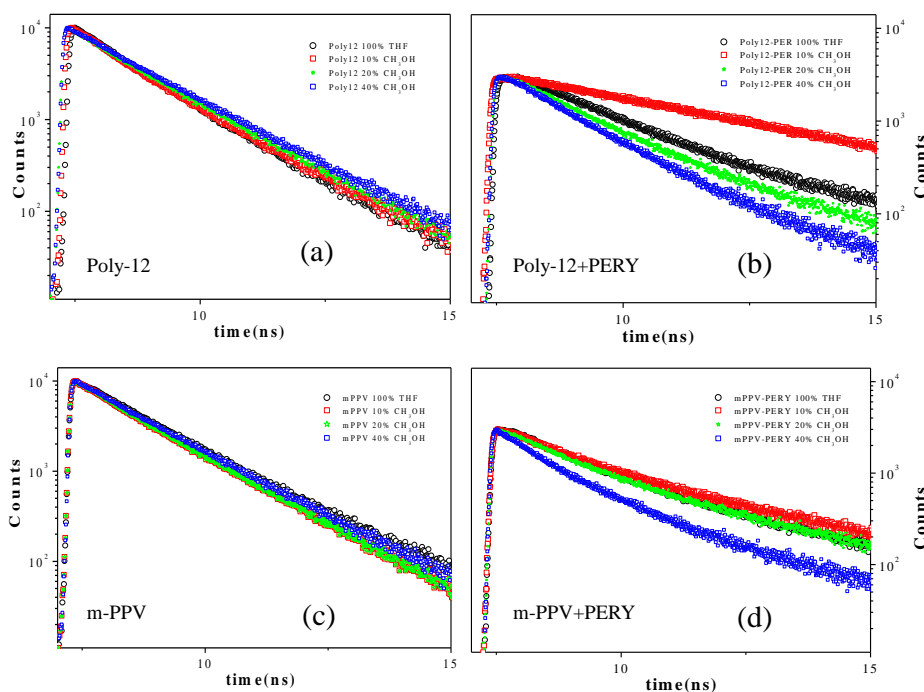


Figure 5.24. Life time decay profiles of Poly-12 (a) Poly12-PERY (b) m-PPV (c) and m-PPV-PERY (d) at different solvent composition in THF/MeOH mixture.

The D-A mixtures were excited at 393 nm to ensure selective excitation of the OPV units and fluorescence decays were collected at emission maximum of polymer as well as PERY. (see figures 5.24b and 5.24d). The decays were collected at four

different concentrations (in THF; 10%, 20% and 40% methanol in THF) for aggregated and non-aggregated states. The decay data were fitted using DAS 6 software and followed bi-exponential fit with $\gamma^2 \approx 1$. The lifetime data and γ^2 are summarized in table 5.3. The lifetime data suggests that Poly-12 exhibited a bi-exponential fit corresponding to the formation of a short lived and a longer lifetime species. At 0 and 10% concentration of methanol (in non- aggregated state), the lifetime values were low such that τ_1 and τ_2 values were 0.5 and 1.4 ns, respectively. As the concentration of methanol increased to 20% and 40%, there was a significant increase in the lifetime. On the other hand, the lifetime values remained almost unchanged in the case of m-PPV. In the case of mixtures, the solutions were excited

Table 5.3. life time data for polymers and donor-acceptor mixtures.

Sample	% (CH ₃ OH)	% (THF)	τ_1^a	τ_2^a	γ^2	τ_1^b	τ_2^b	γ^2
Poly-12	0	100	0.58	1.44	1.26	-	-	-
Poly -12	10	90	0.50	1.44	1.09	-	-	-
Poly-12	20	80	1.08	1.77	1.04	-	-	-
Poly- 12	40	60	0.95	1.75	1.04	-	-	-
m-PPV	0	100	0.77	1.71	1.46	-	-	-
m-PPV	10	90	0.41	1.47	1.14	-	-	-
m-PPV	20	80	0.37	1.48	1.13	-	-	-
m-PPV	40	60	0.33	1.53	1.36	-	-	-
Poly-12 -PERY	0	100	0.52	1.39	1.01	1.71	4.87	1.49
Poly-12 -PERY	10	90	0.59	1.51	1.07	1.73	4.60	1.45
Poly-12 -PERY	20	80	0.54	1.58	1.30	1.39	3.72	1.12
Poly-12 -PERY	40	60	0.45	1.46	1.51	1.22	2.96	1.13
m-PPV -PERY	0	100	0.58	1.54	1.05	1.32	4.0	1.04
m-PPV -PERY	10	90	0.34	1.42	1.06	1.23	4.02	1.08
m-PPV -PERY	20	80	0.32	1.44	1.02	1.21	3.92	1.07
m-PPV -PERY	40	60	0.28	1.50	1.01	0.92	3.14	1.11

(a) Fluorescent decay lifetime obtained by collecting at emission maximum for donor. (b) Fluorescent decay lifetime obtained by collecting at emission maximum for acceptor by fitting with multi-exponential decay. The data were collected by exciting with 375 nm Laser diode source.

at the absorption maximum of donor (393 nm) for selective excitation of OPV chromophore. The intensity decays were collected both at donor and acceptor's

emission maximum. This data has been summarized in the table 5.3. The lifetime data clearly indicated emission from acceptor PERY molecule on selective excitation of OPV chromophore in D-A mixtures. This observation further confirmed the formation of donor-acceptor self-assembly and energy transfer from OPV segmented polymers to PERY molecules. Thus in the present case, formation of donor-acceptor arrays was beautifully shown by TCSPC analysis.

In summary, the effects of chemical structures and polymer chain topology on donor-acceptor self-assemblies of OPV and perylenebisimide chromophores were studied using FRET mechanistic pathways. Segmented polymers were superior to rigid polymers and OPVs in forming strong inter-molecular aggregates in solution state. The flexible alkyl spacers facilitated chain folding in segmented polymers resulting in strong D-A arrays with electron deficient perylenebisimide based chromophores. Molar ratio method was used to determine the composition (donor to acceptor ratio) of D-A complexes and their stability or association constants. Poly-12 formed extended D-A arrays in which the polymer chains folded in helical fashion to accommodate acceptor PERY units in 3:2 (donor: acceptor) ratio. On the other hand, rigid m-PPV formed only weak 1:1 complexes scattered along the polymer chain backbone. The stability constants revealed that the donor and the acceptor complexes formed by segmented polymer were ten times more stable than their rigid counterparts. Fluorescence lifetime decay measurements further supported the formation of D-A arrays. Hence, donor-acceptor self-assembly of novel segmented polymers was traced through FRET mechanistic pathways.

5.4. Conclusion

A series of OPV segmented polymers with identical OPV optical chromophores but variable alkyl chain spacers ($n = 4, 8, \text{ and } 12$) were synthesised. A rigid polymer (m-PPV, $n = 0$) was also synthesised by introduction of m-linkages along the polymer back bone. The polymers were designed in such a way so that all the polymers had almost identical optical energy levels but differed in polymer chain topology. DSC analysis revealed that the macroscopic properties of polymers differ significantly from their oligomeric analogues. High molecular weight, polydisperse polymer chains were sluggish to crystallize and formed amorphous films; whereas, OPVs were found to have a strong tendency to self-assemble in to highly ordered crystalline domains. The effects of chemical structures and polymer chain topology on donor-acceptor self-assemblies of OPV and perylenebisimide chromophores was studied by photophysical analysis. Photophysical analysis revealed that segmented polymers were superior to rigid polymers and OPVs in forming strong intermolecular aggregates in solution state. The flexible alkyl spacers facilitated segmented polymer folding. Further, the Polymers were found to form D-A arrays with electron deficient perylenebisimide based chromophores. The stability and type of self-assembly in these arrays was highly dependent on the chemical structure and the topology of the polymer backbone. Molar ratio method was used to determine the composition (donor to acceptor ratio) of D-A complexes and their stability or association constants. Segmented polymer formed extended D-A arrays in which the chains folded in stacked fashion to accommodate acceptor perylene units in 3:2 (donor:acceptor) ratio. On the other hand, the rigid polymer was found to form only weak 1:1 complexes. The stability constants revealed that the donor and the acceptor complexes formed by segmented polymer were ten times more stable than their rigid counterparts. Thus, the role of chemical structure and polymer chain topology on donor-acceptor self-assembly was established using the segmented polymer approach.

5.5. References

1. Demas, J. N.; Crosby, G. A. *J. Phys. Chem.* **1971**, *75*, 991-1024.
2. Hunter, C. A.; Lawson, K. R.; Perkins, J.; Urch, C. J. *J. Chem. Soc., Perkin Trans.* **2001**, *2*, 651-669.
3. Ghosh, S.; Ramakrishnan, S. *Angew. Chem. Int. Ed.* **2004**, *43*, 3264-3268.
4. Lokey, R. S.; Iverson, B. L. *Nature* **1995**, *375*, 303-305.
5. Janietz, D. *J. Mater. Chem.* **1998**, *8*, 265-274.
6. Janietz, D. *Chem. Commun.* **1996**, 713-714.
7. Goldmann, D.; Mahlstedt, S.; Janietz, D.; Busch, P.; Schmidt, C.; Stracke, A.; Wendorff, J. H. *Liq. Cryst.* **1998**, *24*, 881-890.
8. Stracke, A.; Wendorff, J. H.; Janietz, D.; Mahlstedt, S. *Adv. Mater.* **1999**, *11*, 667-670.
9. Mahlstedt, S.; Janietz, D.; Stracke, A.; Wendorff, J. H. *Chem. Commun.* **2000**, 15-16.
10. Patrick, C. R.; Prosser, G. S. *Nature*, **1960**, 1021.
11. Kraft, A.; Grimsdale, A. C.; Holmes, A. B. *Angew. Chem. Int. Ed.* **1998**, *37*, 402.
12. Zgierski, M. Z.; Fujiwara, T.; Lim, E. C. *Acc. Chem. Res.* **2010**, *43*, 506.
13. Bowden, N. B.; Weck, M.; Choi, I. S.; Whitesides, G. M. *Acc. Chem. Res.* **2001**, *34*, 231.
14. Hoeben, F. J. M.; Jonkheijm, P.; Meijer, E. W.; Schenning, A. P. H. J. *Chem. Rev.* **2005**, *105*, 1491.
15. Muller, K.; Wegner, G. *Electronic Materials: The Oligomer Approach*: Wiley-VCH: Newyork, **1998**.
16. Osterbacka, R.; An, C. P.; Jiang, X. M.; Vardeny, Z. V. *Science* **2000**, *287*, 839-842.
17. Li, G.; Shrotriya V.; Huang, J.; Yao, Y.; Moriarty, T.; Emery, K.; Yang, Y. *Nat. Mater.* **2005**, *4*, 864.
18. Ma, W.; Yang, C.; Gong, X.; Lee, K.; Heeger, A. J. *Adv. Funct. Mater.* **2005**, *15*, 1617.

19. Tsuzuki, T.; Hirota, N.; Noma, N.; Shiota, Y. *Thin Solid Films* **1996**, *273*, 177-180.
20. Hiramoto, M.; Kumaoka H.; Yokoyama, M. *Synth. Met.* **1991**, *91*, 77-79.
21. Dittmer, J. J.; Marseglia, E. A.; Friend, R. H. *Adv. Mater.* **2000**, *12*, 1270-1274.
22. Petritsch, K.; Dittmer, J. J.; Marseglia, E. A.; Friend, R. H.; Lux, A.; Rozenberg, G. G.; Moratti, S. C.; Holmes, A. B. *Sol. Energy. Mater. Sol. Cells* **2000**, *61*, 63-72;
23. Dittmer, J. J.; Lazzaroni, R.; Leclere, P.; Moretti, P.; Granstrm, M.; Petritsch, K.; Marseglia, E. A.; Friend, R. H.; Bredas, J. L.; Rost, H.; Holmes, A. B. *Sol. Energy. Mater. Sol. Cells* **2000**, *61*, 53-61.
24. Ouali, L.; Krasnikov, V. V.; Stalmach, U.; Hadziioannou, G. *Adv. Mater.* **1999**, *11*, 1515-1518.
25. Guñes, S.; Neugebauer, H.; Sariciftci, N. S. *Chem. Rev.* **2007**, *107*, 1324-1338.
26. Eckert, J. F.; Nicoud, J. F.; Nierengarten, J. F.; Liu, S. G.; Echegoyen, L.; Barigelletti, F.; Armaroli, N.; Ouali, L.; Krasnikov, V.; Hadziioannou, G. *J. Am. Chem. Soc.* **2000**, *122*, 7467 -7479.
27. Peeters, E. V.; Hal, P. A.; Knol, J.; Brabec, C. J.; Sariciftci, N. S.; Hummelen, J. C.; Janssen, R. A. J. *J. Phys. Chem. B* **2000**, *104*, 10174 -10190;
28. Wang, L. H.; Chen, Z. K.; Xiao, Y.; Kang, E. T.; Huang, W. *Macromol. Rapid Commun.* **2000**, *21*, 897-900.
29. Neuteboom, E. E.; Meskers, S. C. J.; Van Hal, P. A.; Van Duren, J. K. J.; Meijer, E. W.; Janssen, R. A. J.; Dupin, H.; Pourtois, G.; Cornil, J.; Lazzaroni, R.; Bredas, J.-L.; Beljonne, D. *J. Am. Chem. Soc.* **2003**, *125*, 8625-8638.
30. Iqbal, R.; Moratti, S. C.; Holmes, A. B.; Yahioglu, G.; Milgrom, L. R.; Cacialli, F.; Morgado, J.; Friend, R. H. *J. Mater. Sci. Mater. El.* **2000**, *11*, 97-103.
31. Gong, X.; Ostrowski, J. C.; Moses, D.; Bazan, G. C.; Heeger, A. J. *Adv. Funct. Mater.* **2003**, *13*, 439-444; (b) Gong, X.; Ma, W.; Ostrowski, J. C.; Bazan, G. C.; Moses, D.; Heeger, A. J. *Adv. Mater.* **2004**, *16*, 615-619; (c) D'Andrade, B. W.; Holmes, R. J.; Forrest, S. R. *Adv. Mater.* **2004**, *16*, 624-628.

32. Morgado, J.; Cacialli, F.; Iqbal, R.; Moratti, S. C.; Holmes, A. B.; Yahsioglu, G.; Milgrom, L. R.; Friend, R. H. *J. Mater. Chem.* **2001**, *11*, 278-283.
33. Brunner, K.; van Haare, J. A. E. H.; Langeveld-Voss, B. M. W.; Schoo, H. F. M.; Hofstraat, J. W.; Dijken, A. *J. Phys. Chem. B* **2002**, *106*, 6834-6841.
34. Welter, S.; Brunner, K.; Hofstraat, J. W.; De Cola, L. *Nature* **2003**, *421*, 54-57.
35. E. E. Neuteboom, E. H. A. Beckers, S. C. J. Meskers, E. W. Meijer and R. A. J. Janssen, *Org. Biomol. Chem.*, **2003**, *1*, 198-203.
36. Wurthner, F.; Thalacker, C.; Sautter, A. *Adv. Mater.* **1999**, *11*, 754-758.
37. El-ghayoury, A.; Peeters, E.; Schenning, A. P. H. J.; Meijer, E. W. *Chem. Commun.* **2000**, 1969-1970.
38. Würthner, F.; Sautter, A.; Schmid D.; Weber, P. J. A. *Chem. Eur. J.* **2001**, *7*, 894-902.
39. Struijk, C. W.; Sieval, A. B.; Dakhorst, J. E. J.; Van Dijk, M.; Kimkes, P.; Koehorst, R. B. M.; Donker, H.; Schaafsma, T. J.; Picken, S. J.; van de Craats, A. M.; Warman, J. M.; Zuilhof, H.; Sudhölter, E. J. R. *J. Am. Chem. Soc.*, **2000**, *122*, 11057-11066.
40. Dimitrakopoulos, C. D.; Malenfant, P. R. L. *Adv. Mater.* **2002**, *14*, 99-117.
41. Jancy, B.; Asha, S. K. *Chem. Mater.* **2008**, *20*, 169-181.
42. Würthner, F.; Sautter, A. *Chem. Commun.* **2000**, 445-446.
43. Wurthner, F.; Chen, Z.; Dehm, V.; Stepanenko, V. *Chem. Commun.* **2006**, 1188-1190.
44. Haas, U.; Thalacker, C.; Adams, J.; Fuhrmann, J.; Riethmuller, S.; Beginn, U. Ziener, U.; Möller, M.; Dobraawa, R. and Würthner, F. *J. Mater. Chem.* **2003**, *13*, 767-772.
45. Wurthner, F.; Sautter, A. *Org. Biomol. Chem.* **2003**, *1*, 240-243.
46. Wurthner, F. *Chem. Commun.* **2004**, 1564-1579.
47. Sommer, M.; Huettnerab, S.; Thelakkat, M. *J. Mater. Chem.* **2010**, *20*, 10788-10797.
48. Herrikhuyzen, J.; Asha, S. K.; Schenning, A. P. H. J.; Meijer, E. W. *J. Am. Chem. Soc.* **2004**, *126*, 10021-10027.

49. Huettner, S.; Hodgkiss, J. M.; Sommer, M.; Friend, R. H.; Steiner, U.; Thelakkat, M. *J. Phys. Chem. B* **2012**, *116*, 10070-10078.
50. Lindner, S. M.; Thelakkat, M. *Macromolecules* **2004**, *37*, 8832.
51. Asha, S. K.; Schenning, A. P. H. J.; Meijer, E. W. *Chem. Eur. J.* **2002**, *8*, 3353-3361.
52. Balamurugan, A.; Reddy, M. L. P.; Jayakannan, M. *J. Phys. Chem. B* **2009**, *113*, 14128-14138.
53. Anish, C.; Amrutha, S.; Jayakannan, M. *J. Polym. Sci., Polym. Chem.* **2008**, *46*, 3241-3256.
54. Liao, L.; Pang, Y.; Ding, L.; Karasz, F. E. *Macromolecules* **2001**, *34*, 7300-7305.
55. Liao, L.; Pang, Y. *Synth. Met.* **2004**, *144*, 271-277.
56. Drury, A.; Maier, S.; Davey, A. P.; Dalton, A. B.; Coleman, J. N.; Byrne, H. J.; Blau, W. J. *Synth. Met.* **2001**, *119*, 151-152.
57. Liang, H.; Yan, J.; Lu, J. *Synth. Met.* **2004**, *142*, 143-145.
58. Mahler, A. K.; Schlick, H.; Saf, R.; Stelzer, F.; Meghdadi, F.; Pogantsch, A.; Leising, G.; Moller, K. C.; Besanhard, J. O. *Macromol. Chem. Phys.* **2004**, *205*, 1840-1850.
59. Chu, Q.; Pang, Y. *Macromolecules* **2003**, *36*, 4614. (b) Chu, Q.; Pang, Y. *Macromolecules* **2005**, *38*, 517.
60. Atwood, J. L.; Davies, J. E. D.; Macnicol, D. D.; Vogtle, F.; Lehn, J. M.; Suslick, K. S. *Comprehensive Supramolecular Chemistry*; Pergamon: Oxford, U.K., **1996**; Vol. 8, 439-441.

Conclusion and future directions

The thesis entitled “*Supramolecular Assemblies of π -conjugated Phenylenevinylenes in Solid State*” deals with design and development of new π -conjugated phenylenevinylenes and their segmented polymers that can self-assemble via weak non-covalent interactions in the solid state. A large number of custom designed oligophenylenevinylenes and segmented PPV polymers were synthesized for understanding π -conjugated self-assemblies in the solid state. The design principle was adopted in such a way such that the molecules were constructed using simple hydrocarbon anchoring units so that the molecular assemblies were driven by very weak non-covalent forces.

A homologous series of oligophenylenevinylenes (OPV- n) with tricyclodecanemethylene pendent units in the aromatic core and variable tail length in the longitudinal position was synthesized to trace the effect of vander Waals and π - π stacking interactions on self-assembly. Thermal (by DSC) and polarized light microscope analysis were done to understand the effect of the structure on solid state packing and mesophase morphologies. OPV molecules showed sigmoidal transition from crystalline solids ($n = 0-4$) to ring banded LC mesophases ($n = 10-15$) via fan shaped cholesteric textures ($n = 5-9$). Single-crystal X-ray structures of OPV molecules were resolved to trace the origin of sigmoidal self-assembly at the molecular level. The packing changed from herringbone (OPV- 4) to helical self-assembly (OPV-12), and, the presence of multiple CH/ π interactions (in OPV-12) was identified as the main driving force for helical suprastructures. Pitch and roll angles were determined to find out the existence of π - π stacking interactions. The large pitch and roll displacements completely destroyed the aromatic π -stacking interactions among this series of OPV chromophores. Circular dichroism studies on the OPVs confirmed that the helical structures were produced only on aligning the chromophores in the LC mesophases. The uniqueness of the present approach was that the type of self-assembly (herringbone or helical) could be tuned by just varying the number of carbon atoms in the tails.

To study the role of planarity, peripheral substitution and its orientation on solid state packing and intermolecular non-covalent forces in OPVs: a series of longitudinal, vertical and radial OPVs was synthesized by different alkyl side chains arrangements around the periphery. DSC analysis and PLM imaging revealed that horizontal isomers packed better than vertical isomers. Increasing n (no. of carbon atoms present in alkyl chain length) along the longitudinal direction favored liquid crystallinity as compared to vertical isomers, which were crystalline in nature. Radially substituted OPVs exhibited well-ordered two dimensional lamellar textures. Single crystal XRD analysis revealed that planar molecules were generally devoid of strong CH/ π and π - π interactions. However, non-planar molecules exhibited strong CH/ π interactions. Roll and pitch inclinations showed that non-planar molecules were more prone to show π - π stacking interactions. Further, OFET devices were constructed from OPVs by using LC and drop cast films. OPVs exhibited hundred folds increase in mobility in LC frozen state as compared to drop cast films. This preliminary result showed that the LC self-organization of molecules can be an effective tool for solid state packing in electronic devices.

To study the role of tail nature on LC mesophases, a series of OPVs were designed with hydrocarbon or fluorocarbon tails. Thermal analysis revealed that hydrocarbon tail OPVs packed better as compared to their fluorocarbon counterparts. PLM analysis revealed that fluorocarbon tail OPVs produced identical SmC LC mesophases irrespective of the pendent groups attached in the middle aromatic core. In contrast, for hydrocarbon tailed OPVs produced diverse self-assembly depending on pendent group present in the middle aromatic core. Variable temperature wide angle XRD patterns of fluorocarbon tail OPVs exhibited regular periodicity corresponding to equidistant planes formed in smectic LCs. Small angle variable temperature X-ray diffraction analysis confirmed transition from SmA to a more ordered SmC mesophase. Solid state photophysical analysis confirmed the formation of H and J aggregates in FC and HC-OPVs, respectively. Time resolved fluorescence decay measurements confirmed longer life time for H-type smectic OPVs compared to that of loosely packed one-dimensional nematic hydrocarbon tailed OPVs. Hence,

diverse molecular self-assembly of aromatic π -conjugated units via weak secondary forces was attained.

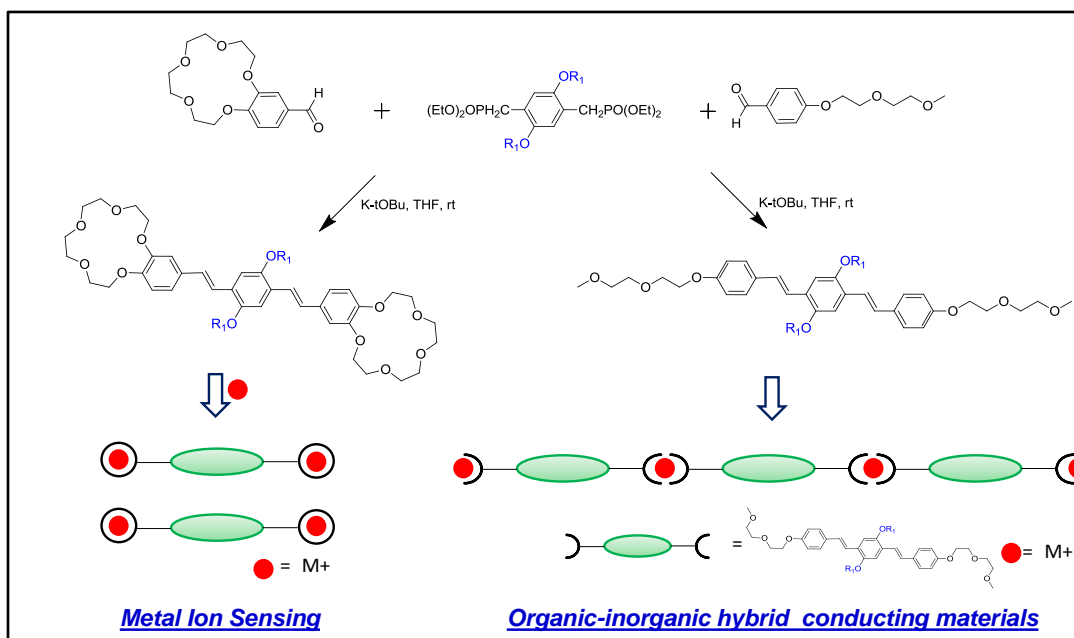
Towards the end, the effect of chemical structure and polymer chain topology on donor-acceptor self-assemblies of segmented OPV polymers and perylenebisimide chromophores was studied. A series of OPV segmented polymers (*Poly-n*) with identical OPV optical chromophores, but, different alkyl chain segments ($n = 4, 8, \text{ and } 12$) was synthesized. Poly-0 (rigid polymer without any alkyl segment) was synthesized as m-PPV having m-linkages along the polymer backbone. All the polymers had almost identical energy levels, but, differed in their topology. DSC analysis revealed that OPVs self-assembled in to highly order crystalline domains, but, polymers formed amorphous films. Photophysical analysis revealed that segmented polymers were superior to rigid polymers and OPVs in forming strong inter-molecular aggregates in solution state. The chemical structure and the topology of the polymer backbone determined the stability and type of donor-acceptor self-assembly perylene bisimide based chromophore. Segmented polymer formed extended D-A arrays to accommodate acceptor perylene units in 3:2 (donor: acceptor) ratio. In contrast, the rigid polymer was found to form only weak 1:1 complexes. The stability constant for D-A arrays formed by segmented polymer was ten times higher than rigid m-PPV. Hence, the role of chemical structure and topology of polymer chains on donor-acceptor self-assembly was established.

In short, this thesis work is focused on design and development of new π -conjugated phenylenevinylenes to trace the origin of supramolecular self-assembly at molecular level. The role of OPV backbone planarity, CH/ π hydrogen bond, and positional effect of peripheral substitution, alkyl chain lengths and its orientation were investigated on the various properties such as liquid crystallinity, solid state packing and so on. The OPV materials developed in the thesis are very important class of organic skeletons for understanding molecular self-assembly processes. LC-OPV molecules, FC-OPVs, segmented OPV polymers and their donor-acceptor assemblies can be explored for various applications in optoelectronics.

Future directions

π -Conjugated semiconducting oligomers and polymers are new generation electronic materials for potential applications in electronic devices such as light emitting diodes (LEDs), photovoltaics (PVs), field effect transistors (FETs), biological and chemical sensors etc. Solid state self-assembly of π -conjugated organic polymers and small molecules into hierarchical architectures is being extensively used for making molecular devices in solid state electronics. The optical and electronic features of devices such as organic field-effect transistors (OFETs) made up of these π -conjugated materials could be directly correlated to the precise arrangements of molecules in the solid state. Non-covalent forces such as hydrogen bonding, aromatic π - π stacking, hydrophilic/hydrophobic and van der Waals interactions are regularly employed as tools for obtaining self-assembled suprastructures used in these devices.

Regardless of the rapid progress of π -conjugated systems and their application in organic devices, there remain several challenges for the application of these materials in organic electronics. For example, the mobility of π -conjugated systems still lags behind their inorganic counterparts and designing π -conjugated

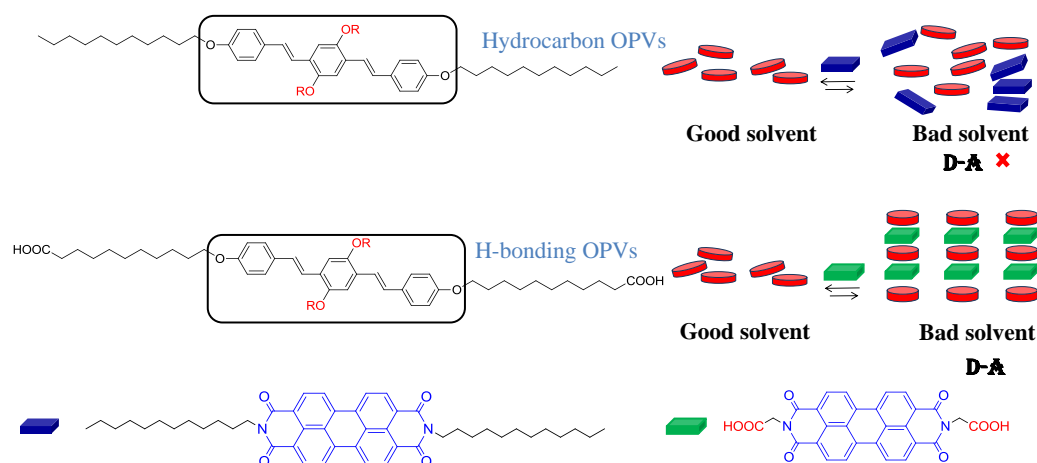


systems with even high mobility remains a hard task. In this attempt, synthesizing new hybrid materials having metal ions incorporated in organic π -conjugated molecules would be a useful concept to explore for highly conducting organic materials. OPVs with terminal polyethyleneglycol chains or with crown ether groups in the π -conjugated backbones can incorporate metal ions in the polymeric chain backbones. The resulting π -conjugated materials can show enhanced charge carrier mobility/conductivity due to the presence of metallic conductors and better processibility resulting due to soluble organic oligomers and polymers. Moreover, OPVs with crown ether functional groups can also be very useful for metal ion sensing applications.

Another important challenge to be addressed is the charge transport mechanism of π -conjugated systems in organic devices which requires an understanding of relationships among chemical structure, molecular packing, intermolecular interactions, and charge transport properties. In this thesis new π -conjugated phenylenevinylens were synthesized that self- assembled to produce well defined supra structures for applications in opto-electronics. Intense effort was put to optimize chemical structure, understanding the origin of self-assembly using single crystal XRD analysis and explore the role of non-covalent interactions in self-organization. It was understood that the mobility of the organic semiconductor is the key parameter for efficient electronic devices. This important parameter is extremely dependent on the packing (arrangement) of the organic molecules in the solid state. Therefore, the control of packing mode of the organic semiconductors in the solid state is a very important factor for better charge transport between molecules. The future research requires detailed understanding of structure property relationships and hence single crystal X-ray analysis of a large number of π - conjugated skeletons is very important for understanding precise molecular arrangements

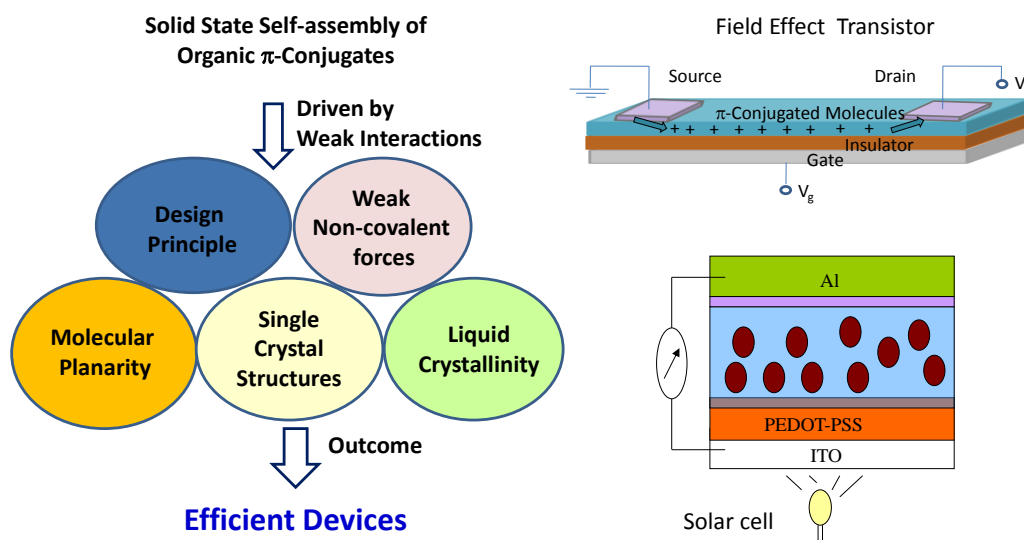
Typically, π -conjugated systems are comprised of two chemical units: (i) a rigid aromatic conjugated backbone and (ii) flexible alkyl chains anchored for solubility purpose. Without the alkyl chains, the aromatic molecules were found

insoluble which restrict their processability in devices. These aromatic-aliphatic systems self-organized via two in-built non-covalent forces: (i) π -stacking via rigid aromatic core backbone and (ii) van der Waals interactions among the alkyl chains. Most often, these two non-covalent forces were found not strong enough to bring the desired self-assembly in π -conjugated materials; for example purely hydrocarbon OPVs do not form D-A arrays with purely hydrocarbon perylene based molecules. Incorporation of secondary forces like strong hydrogen bonding units may result in strong donor acceptor self-assembly. Various donor acceptor self-assemblies can be studied by using different acceptor molecules such as naphthalene based dyes, Buckminster fullerene C_{60} and its derivative PCBM (1-(3-methoxycarbonyl) propyl-1-phenyl[6,6] C_{61}) for photovoltaic applications.



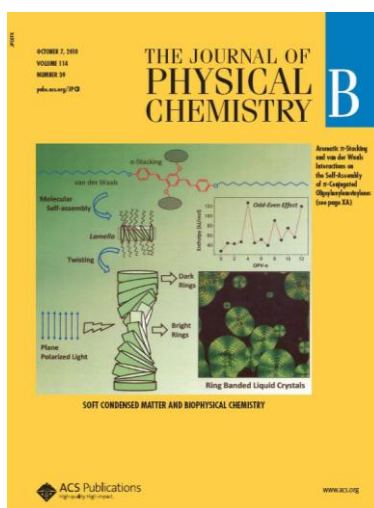
Building I-V measurement units and device fabrication setup for the OFETs fabrication and device characterization. Field effect mobility measurements provide direct information on structure property relations between molecular packing and charge carrier mobility for fundamental understanding and optimizing chemical structures. The liquid crystalline materials are particularly important since self-organized structures could be obtained in the solid state via melt crystallization process. Hence, the active transport layer in the solid state electronics like OFETs could be easily fabricated in the LC mesophase. Photovoltaic technology is another

important approach based on π -conjugated molecules for alternative source of electrical energy and offers great potential as a renewable and inexpensive energy sources. For the generation of electrical power by illumination, it is necessary to spatially separate the electron-hole pair generated in the absorption process before the recombination takes place.



Low cost homemade set up for making photovoltaic devices can be constructed which can be inexpensively used for directly measuring electrical and photovoltaic responses. The outcome of the research will fuel fundamental research in the area of solid state self-assembly and also their application in molecular electronics.

List of Publications



A part of Chapter-2 appeared as cover page on Oct 7, in 39th issue of JPCB 2010.

Publications in International Journals:

1. Goel, M.; Jayakannan, M. Herringbone and Helical Self-assembly of π -conjugated Molecules in Solid State through CH/ π Hydrogen Bond. *Chem. Eur. J.* **2012**, *18*, 11987-11994.
2. Goel, M.; Jayakannan, M. CH/ π Interaction Guided Molecular Self-assembly in π -conjugated Oligomers. *Chem. Eur. J.* **2012**, *18*, 2867-2874.
3. Goel, M.; Jayakannan, M. Supramolecular Liquid Crystalline π -Conjugates: The Role of Aromatic π -stacking and van der Waals Forces on the Molecular Self-assembly of Oligo-Phenylenevinylens. *J. Phys. Chem. B.* **2010**, *114*, 12508-12519.
4. Murthy, A. V. R.; Goel, M.; Patil, S.; Jayakannan, M. Probing the role of Chain length on the Diffusion Dynamics of π -conjugated Polymers by Fluorescence Correlation Spectroscopy. *J. Phys. Chem. B.* **2011**, *115*, 10779-10788. (*This work is not included in the thesis*).
5. Goel, M.; Jayakannan, M. Hierarchical Self-assembly of Structural Isomers and Homologues of π -Conjugated Skeletons: The Role of CH/ π Interactions and Planarity on the Solid State Molecular packing. *Manuscript under preparation*.
6. Goel, M.; Jayakannan, M. Donor-Acceptor Self-assembly of Segmented OPV π -Conjugated Polymers: Aggregation Induced FRET pathways and Mechanistic Aspects. *Manuscript under preparation*.

Publications in International Conference Proceedings:

7. Goel, M.; Jayakannan, M. Molecules to Materials via Self-assembly. *GLASGOW-IISER SYMPOSIUM 2012*, Pune, India, Dec. 10-12, **2012**.
8. Goel, M.; Jayakannan, M. π -Conjugated Liquid Crystals via Molecular Self-assembly, *CRSI-NCL 2009*, Pune, India, May 13-14, **2011**.

9. Goel, M.; Jayakannan, M. Liquid Crystalline π -Conjugates via Molecular Self-Assembly, IISER-Pune, India, Feb 28, **2011**. **(Selected for best Poster Award)**.
10. Goel, M.; Jayakannan, M. Self-Assembly of Liquid Crystalline π -Conjugated Materials. *INTERRA 2010*, Novosibirsk, Russia. Sep 21-26, **2010**.
11. Goel, M.; Jayakannan, M. Solid State Liquid Crystalline π -Conjugates. *RSC-Symposium 2010*, Goa, India, Aug 3-5, **2010**. **(Selected for best Poster Award)**.